VOLUME 33 DECEMBER 1955 NUMBER 12

Canadian Journal of Physics

Editor: G. M. VOLKOFF

Associate Editors:

L. G. ELLIOTT, *Atomic Energy of Canada, Ltd., Chalk River*
J. S. FOSTER, *McGill University*
G. HERZBERG, *National Research Council of Canada*
L. LEPRINCE-RINGUET, *Ecole Polytechnique, Paris*
R. W. PRINGLE, *University of Manitoba*
B. W. SARGENT, *Queen's University*
Sir FRANCIS SIMON, *Clarendon Laboratory, University of Oxford*
W. H. WATSON, *University of Toronto*

Published by THE NATIONAL RESEARCH COUNCIL
OTTAWA CANADA

CANADIAN JOURNAL OF PHYSICS

(*Formerly Section A, Canadian Journal of Research*)

Under the authority of the Chairman of the Committee of the Privy Council on Scientific and Industrial Research, the National Research Council issues THE CANADIAN JOURNAL OF PHYSICS and six other journals devoted to the publication, in English or French, of the results of original scientific research. Matters of general policy concerning these journals are the responsibility of a joint Editorial Board consisting of: members representing the National Research Council of Canada; the Editors of the Journals; and members representing the Royal Society of Canada and four other scientific societies.

EDITORIAL BOARD

Representatives of the National Research Council

A. N. Campbell, *University of Manitoba*
G. E. Hall, *University of Western Ontario*
E. G. D. Murray, *McGill University*
D. L. Thomson, *McGill University*
W. H. Watson (Chairman), *University of Toronto*

Editors of the Journals

D. L. Bailey, *University of Toronto*
T. W. M. Cameron, *Macdonald College*
J. B. Collip, *University of Western Ontario*
G. A. Ledingham, *National Research Council*
Léo Marion, *National Research Council*
R. G. E. Murray, *University of Western Ontario*
G. M. Volkoff, *University of British Columbia*

Representatives of Societies

D. L. Bailey, *University of Toronto*
Royal Society of Canada
T. W. M. Cameron, *Macdonald College*
Royal Society of Canada
J. B. Collip, *University of Western Ontario*
Canadian Physiological Society
R. G. E. Murray, *University of Western Ontario*
Canadian Society of Microbiologists
H. G. Thode, *McMaster University*
Chemical Institute of Canada
T. Thorvaldson, *University of Saskatchewan*
Royal Society of Canada
G. M. Volkoff, *University of British Columbia*
Royal Society of Canada; Canadian Association of Physicists

Ex officio

Léo Marion (Editor-in-Chief), *National Research Council*

Manuscripts for publication should be submitted to Dr. Léo Marion, Editor-in-Chief, Canadian Journal of Physics, National Research Council, Ottawa 2, Canada.
(For instructions on preparation of copy, see **Notes to Contributors** (inside back cover).)

Proof, correspondence concerning proof, and orders for reprints should be sent to the Manager, Editorial Office (Research Journals), Division of Administration, National Research Council, Ottawa 2, Canada.

Subscriptions, renewals, requests for single or back numbers, and all remittances should be sent to Division of Administration, National Research Council, Ottawa 2, Canada. Remittances should be made payable to the Receiver General of Canada, credit National Research Council.

The journals published, frequency of publication, and prices are:

Canadian Journal of Biochemistry and Physiology	Bimonthly	$3.00 a year
Canadian Journal of Botany	Bimonthly	$4.00 a year
Canadian Journal of Chemistry	Monthly	$5.00 a year
Canadian Journal of Microbiology*	Bimonthly	$3.00 a year
Canadian Journal of Physics	Monthly	$4.00 a year
Canadian Journal of Technology	Bimonthly	$3.00 a year
Canadian Journal of Zoology	Bimonthly	$3.00 a year

The price of single numbers of all journals is 75 cents.

*Volume 1 will combine three numbers published in 1954 with six published in 1955 and will be available at the regular annual subscription rate of $3.00.

"Reprinted in entirety by photo-offset from the original issue"

Canadian Journal of Physics

Issued by THE NATIONAL RESEARCH COUNCIL OF CANADA

VOLUME 33 DECEMBER 1955 NUMBER 12

NOTE ON THE USE OF NON-ORTHOGONAL WAVE FUNCTIONS IN PERTURBATION CALCULATIONS[1]

BY P. A. M. DIRAC

ABSTRACT

A method of first approximation is proposed for handling collision problems involving a chemical or ionic change, so that the interaction energy function is different at the beginning and end of the collision.

There are many transition problems in quantum mechanics for which the initial and final states belong to two different sets of orthogonal states, so that in the calculation one has to deal with a mixture of wave functions belonging to two different orthogonal sets. It then becomes necessary to take into account the lack of orthogonality of these wave functions in order to get an adequate basis for the calculation.

As an example we may consider a collision between two atoms resulting in the transfer of an electron from one atom to the other. For the initial state we have a neutral atom A and a positively ionized atom B^+, each moving with a definite momentum, and for the final state we have the atoms A^+ and B, each again having a definite momentum, such that the total momentum is conserved.

We now have to consider the total energy H from two points of view,

$$[1] \qquad H = H(A)+H(B^+)+V_1$$

$$[2] \qquad = H(A^+)+H(B)+V_2,$$

where $H(A)$, $H(B^+)$, . . . are the energies of the atoms A, B^+, . . . alone, V_1 is the interaction energy between A and B^+, and V_2 is the interaction energy between A^+ and B. Initially the state of the system is an eigenstate of $H(A)+H(B^+)$, and for the beginning of the interaction V_1 is the perturbing energy. But the final state is an eigenstate of $H(A^+)+H(B)$ and towards the end of the interaction the perturbing energy is V_2.

The wave equation is

$$H\psi = E\psi,$$

where E, a number, is the total energy of the state we are interested in. The initial wave function ψ_0 satisfies

$$\{H(A)+H(B^+)\}\psi_0 = E\psi_0.$$

[1]*Manuscript received August 25, 1955.*
Contribution from St. John's College, University of Cambridge, Cambridge, England.

Thus, putting

$$\psi = \psi_0 + \psi_1,$$

we have

[3] $$(H-E)\psi_1 = -(H-E)\psi_0 = -V_1\psi_0.$$

Let ϕ_λ denote the eigenfunctions of $H(A)+H(B^+)$, representing the atoms A and B^+ each in a stationary state and each having a definite momentum, such that the total momentum has the required value. Thus

[4] $$\{H(A)+H(B^+)\}\phi_\lambda = E_{1\lambda}\phi_\lambda,$$

where $E_{1\lambda}$ is a number. Different eigenfunctions are distinguished by different values for λ. Let χ_μ denote similarly the eigenfunctions of $H(A^+)+H(B)$, so that

[5] $$\{H(A^+)+H(B)\}\chi_\mu = E_{2\mu}\chi_\mu,$$

with $E_{2\mu}$ also a number.

The set of eigenfunctions ϕ_λ is far from being a complete set with the given total momentum, since it does not include any wave functions representing states with a free electron. Even the two sets ϕ_λ, χ_μ joined together will probably not be complete, so that an arbitrary wave function cannot be expanded in terms of them. We can, however, expand any wave function, such as $-V_1\psi_0$, in the form

[6] $$-V_1\psi_0 = \sum\int a_\lambda\phi_\lambda\,d\lambda + \sum\int b_\mu\chi_\mu\,d\mu + \psi_{res},$$

where ψ_{res}, the residual term, is made as small as possible, which requires that it shall be orthogonal to every ϕ_λ and every χ_μ.

Substituting [6] in [3], we get

[7] $$(H-E)\psi_1 = \sum\int a_\lambda\phi_\lambda\,d\lambda + \sum\int b_\mu\chi_\mu\,d\mu + \psi_{res}.$$

The work so far is exact. We now try to get an approximate solution of [7]. We discard ψ_{res} altogether, so that [7] may be written

$$\psi_1 = \sum\int a_\lambda(H-E)^{-1}\phi_\lambda\,d\lambda + \sum\int b_\mu(H-E)^{-1}\chi_\mu\,d\mu.$$

By neglecting the perturbation V_1 applied to ϕ_λ, we get

$$(H-E)^{-1}\phi_\lambda = \{H(A)+H(B^+)-E\}^{-1}\phi_\lambda$$

[8] $$= (E_{1\lambda}-E)^{-1}\phi_\lambda$$

from [4]. Similarly, by neglecting the perturbation V_2 applied to χ_μ, we get

[9] $$(H-E)^{-1}\chi_\mu = (E_{2\mu}-E)^{-1}\chi_\mu$$

from [5]. Thus an approximate solution of [7] is

[10] $$\psi_1 = \sum\int a_\lambda(E_{1\lambda}-E)^{-1}\phi_\lambda\,d\lambda + \sum\int b_\mu(E_{2\mu}-E)^{-1}\chi_\mu\,d\mu.$$

The solution [10] represents ingoing as well as outgoing waves. We can obtain from it a solution representing only outgoing waves in the standard way, by replacing the reciprocal $(E_{1\lambda}-E)^{-1}$ by $(E_{1\lambda}-E)^{-1}-i\pi\delta(E_{1\lambda}-E)$, and similarly for $(E_{2\mu}-E)^{-1}$. The various terms in the solution will then represent the various scattered waves that are produced by the collision process, and

their coefficients a_λ and b_μ will give us, when we take the squares of their moduli and multiply them by the appropriate factors, the transition probabilities for the various final states.

To calculate the coefficients a_λ and b_μ, we multiply [6] by $\bar{\phi}_\lambda$ and integrate over all values of the variables q that occur in the wave functions, thus

$$-\int \bar{\phi}_\lambda \, V_1 \psi_0 \, dq = \sum \iint a_{\lambda'} \, \bar{\phi}_\lambda \, \phi_{\lambda'} \, dq \, d\lambda' + \sum \iint b_\mu \, \bar{\phi}_\lambda \, \chi_\mu \, dq \, d\mu.$$

Assuming that the ϕ_λ are normalized, so that

$$\int \bar{\phi}_\lambda \, \phi_{\lambda'} \, dq = \delta(\lambda - \lambda'),$$

this reduces to

[11] $$a_\lambda + \sum \int \omega_{\lambda\mu} \, b_\mu \, d\mu = -\int \bar{\phi}_\lambda \, V_1 \psi_0 \, dq,$$

where $$\omega_{\lambda\mu} = \int \bar{\phi}_\lambda \, \chi_\mu \, dq.$$

Similarly, by multiplying [6] by $\bar{\chi}_\mu$ and integrating, we get

[12] $$b_\mu + \sum \int \omega_{\mu\lambda} \, a_\lambda \, d\lambda = -\int \bar{\chi}_\mu \, V_1 \psi_0 \, dq,$$

where $$\omega_{\mu\lambda} = \int \bar{\chi}_\mu \, \phi_\lambda \, dq = \bar{\omega}_{\lambda\mu}.$$

The equations [11], [12] may be solved for a_λ and b_μ. It is convenient to look upon these equations as a matrix equation. Introduce the square matrix

$$\Omega = \begin{pmatrix} 0 & \omega_{\lambda\mu} \\ \omega_{\mu\lambda} & 0 \end{pmatrix}$$

and consider the numbers a_λ, b_μ as forming a single-column matrix Y and the numbers $\int \bar{\phi}_\lambda \, V_1 \psi_0 \, dq$, $\int \bar{\chi}_\mu V_1 \psi_0 \, dq$ as forming a single-column matrix Z. Then [11] and [12] may be written

[13] $$(1+\Omega) Y = -Z.$$

The solution is thus

[14] $$Y = -(1+\Omega)^{-1} Z.$$

It is essential for the success of the method that the matrix $1+\Omega$ shall have a reciprocal. The condition for this is that there shall not exist a set of numbers α_λ, β_μ, not all zero, such that

[15] $$\begin{cases} \alpha_\lambda + \sum \int \omega_{\lambda\mu} \, \beta_\mu \, d\mu = 0, \\ \sum \int \omega_{\mu\lambda} \, \alpha_\lambda \, d\lambda + \beta_\mu = 0, \end{cases}$$

or such that

[16] $$\sum \int \alpha_\lambda \, \phi_\lambda \, d\lambda + \sum \int \beta_\mu \, \chi_\mu \, d\mu = 0.$$

This means that the wave functions ϕ_λ, χ_μ must be all independent. If this condition does not hold, the expansion [6] is not unique and the coefficients a_λ, b_μ are not determinate.

There does not seem to be any simple way of proving the independence of the ϕ_λ, χ_μ in examples of practical importance. It is a question for further study. If one should find in a particular example that the ϕ_λ, χ_μ are not independent, one might still be able to save the method by working with a smaller set of

functions ϕ_λ, χ_μ which are independent. One could get a smaller set, for example, by discarding those ϕ_λ, χ_μ that refer to one of the atoms being in a highly excited state.

A reduction in the number of ϕ_λ, χ_μ that one works with has the advantage not only of increasing the prospect for them to be independent, but also of simplifying the calculation, since it reduces the number of rows and columns of the matrix $1+\Omega$ whose reciprocal has to be worked out. It has the disadvantage that the accuracy of the method is probably diminished, since it makes ψ_{res} larger.

The foregoing work arose from a discussion with Dr. T. Y. Wu and others at the National Research Council, Ottawa.

RADIO OBSERVATIONS OF THE IONOSPHERE AT OBLIQUE INCIDENCE[1]

By J. H. Chapman, Kenneth Davies, and C. A. Littlewood

ABSTRACT

A description is given of an automatic method of using the radio pulse technique at oblique incidence to investigate the structure of the ionosphere. Sweep frequency photographic records were taken for the path Ottawa–Saskatoon (2355 km.). The records obtained confirm the validity of the theory relating vertical incidence to oblique incidence propagation. Sweeps showing such phenomena as *E* layer cutoff, transmission of the Pedersen ray, multiple reflections, are shown. It is found that the *F*1 layer is the important propagating layer rather than the *F*2 layer under certain conditions. Hence conventional methods of predicting frequencies over long distances require modification in these circumstances.

1. INTRODUCTION

During the last thirty years or so most high frequency radio observations on the ionosphere have been carried out at normal incidence. The data obtained from such observations have been applied to the calculation of maximum usable frequencies for radio communication purposes and some measurements have been made to check the relationship between vertical incidence and oblique incidence data. It appears that, in general, the theories are correct to a first approximation. Since most oblique pulse measurements have been made at short distances (less than 1000 km.) it was decided to make investigations at greater distances and especially at high latitudes, where the ionospheric characteristics differ from those at low latitudes.

The present soundings, made over a distance of 2355 km., are part of a comprehensive investigation of oblique incidence ionospheric radio propagation in Canada (2). Owing to the nature of much of the country it is difficult to obtain vertical incidence ionospheric observations at many points in high latitudes and so oblique incidence soundings offer a means of investigation of the ionosphere over these relatively inaccessible regions.

2. EXPERIMENTAL PROCEDURE

The equipment used at each station was a slightly modified LG17 Automatic Ionospheric Recorder (manufactured by the Marconi Company of Canada). A block diagram, illustrating the principle of operation of this recorder, is reproduced in Fig. 1. A variable frequency oscillator serves to tune both the transmitter and receiver. A variable frequency (f Mc.) in the range 30.6 Mc. to about 55 Mc. is mixed with a fixed frequency of 30.0 Mc. and the difference frequency ($f-30$ Mc.) is amplified and used to control and excite the transmitter at the desired frequency. The received signal is again mixed with the frequency f Mc. and the difference frequency $f-(f-30)$ Mc. $= 30$ Mc. is amplified and mixed with a frequency of 28.6 Mc. to yield a second intermediate

[1]*Manuscript received July 8, 1955.*
Contribution from the Radio Physics Laboratory, Defence Research Board, Ottawa. Work carried out under Project D48-95-11-02.

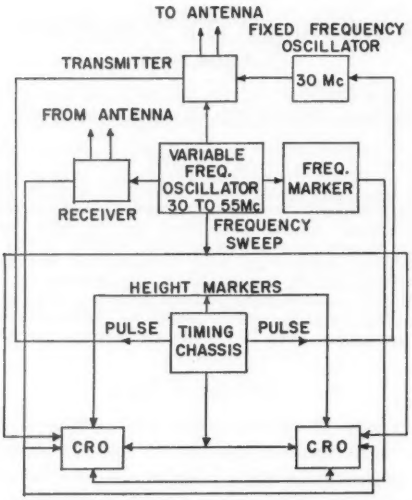

FIG. 1. Block diagram of LG17 Automatic Ionospheric Recorder.

frequency of 1.4 Mc. which is amplified, detected, and displayed on cathode ray tubes in the conventional manner.

In this experiment pulses of 50 μsec. duration were transmitted at the rate of 20 per second, which was also the repetition frequency of the time base. All the timing features (repetition frequency, time base, height markers, etc.) were obtained by counting down from a 100 kc. crystal standard having a stability of a few parts in 10^9. To enable the pulses from the distant transmitter to be set at convenient positions on both time bases, a variable frequency oscillator at Ottawa could be switched in to permit adjustment of the equipment triggering time. The frequency of this oscillator could be varied continuously from about 99 kc. to about 101 kc.

To keep the frequencies of both equipments exactly the same the variable frequency oscillator in the LG17 was replaced by an oscillator in which the frequency was increased in steps of about 100 kc. To ensure very accurate frequency control, auxiliary circuits were included which 'pulled' the frequency to that of the nearest harmonic of the 100 kc. frequency standard. A description of these auxiliary circuits will be given elsewhere. The oscillator remained on any single frequency for a period of two seconds and then 'stepped' quickly to the next frequency. The period for one complete sweep of the LG17 was 320 sec. so that a frequency sweep of 16.0 Mc. could be obtained. The frequency ranges generally used were:

2.0 Mc. to 18.0 Mc. by night, and
5.0 Mc. to 21.0 Mc. by day.

In this way the high daytime and the low nighttime maximum usable fre-

quencies could be covered. Sweeps were taken once every 20 min. The transmitting and receiving antennas were horizontal rhombics. The sweeps were recorded photographically on 35 mm. film; each photographic sweep record was either 2 or 4 in. in length.

The computation of the equivalent path of a signal between sender and receiver can be made as follows. Referring to Fig. 2,

let P_A = the interval (expressed in kilometers, where 1 km. = 3.3 μsec.) between the triggering of the equipment at A and the reception at A of a signal from B,

P_B = the interval between the triggering of the equipment at B and the reception at B of a signal from A,

P_{AB} = the equivalent path between A and B,

P_{BA} = the equivalent path between B and A.

Then

[1] $$P_A+P_B = P_{AB}+P_{BA}.$$

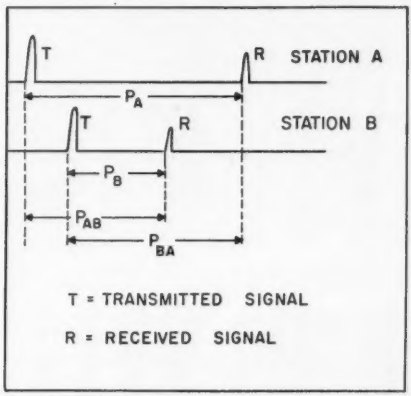

FIG. 2. Timing cycle.

Assume that the equivalent paths are equal in the two directions. Then

[2] $$P_{AB} = P_{BA}$$

[3] $$= \tfrac{1}{2}(P_A+P_B).$$

To assist in obtaining comparable records at both ends of the path, P_A and P_B were kept nearly equal. In practice, since P is approximately 2500 km., the Ottawa equipment was adjusted so that the signals received from Saskatoon were within the range 2200 km. to about 2800 km.

3. TYPICAL SWEEPS

Experiments were conducted in the summer and in December of 1954. Some typical sweeps are shown in Figs. 3 to 8. Fig. 3 was taken near noon and shows

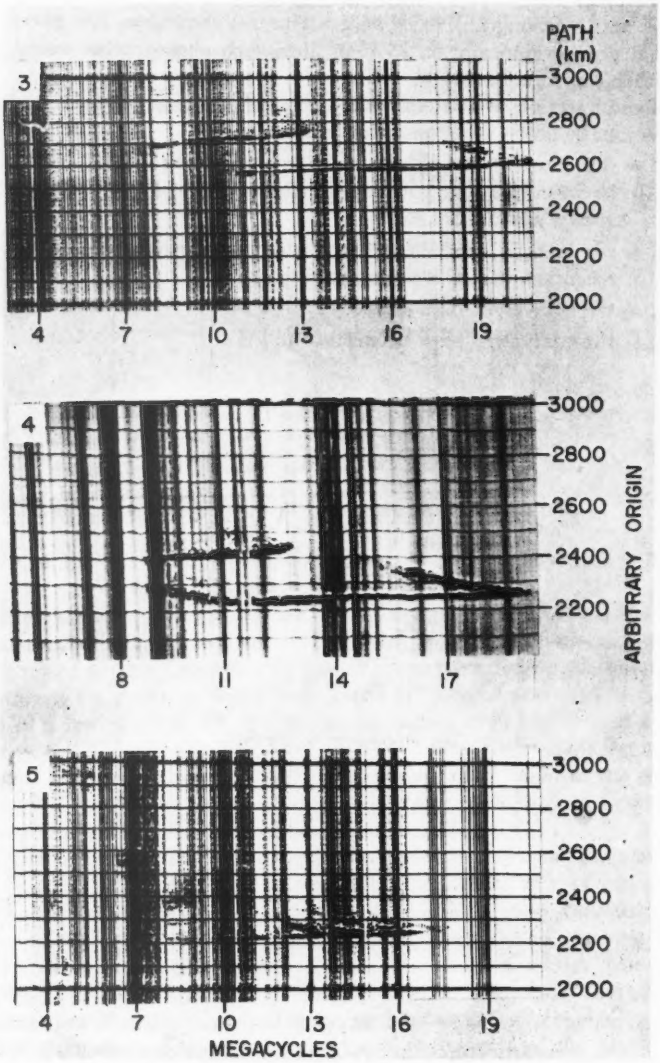

FIG. 3. A typical winter day equivalent path versus frequency sweep. Saskatoon, 6 December, 1954, 13:21 E.S.T.

FIG. 4. Winter day sweep showing *E* layer cutoff phenomenon. Ottawa, 12 December, 1954, 14:01 E.S.T.

FIG. 5. Sweep taken during slightly disturbed period. Saskatoon, 8 December, 1954, 17:21 E.S.T.

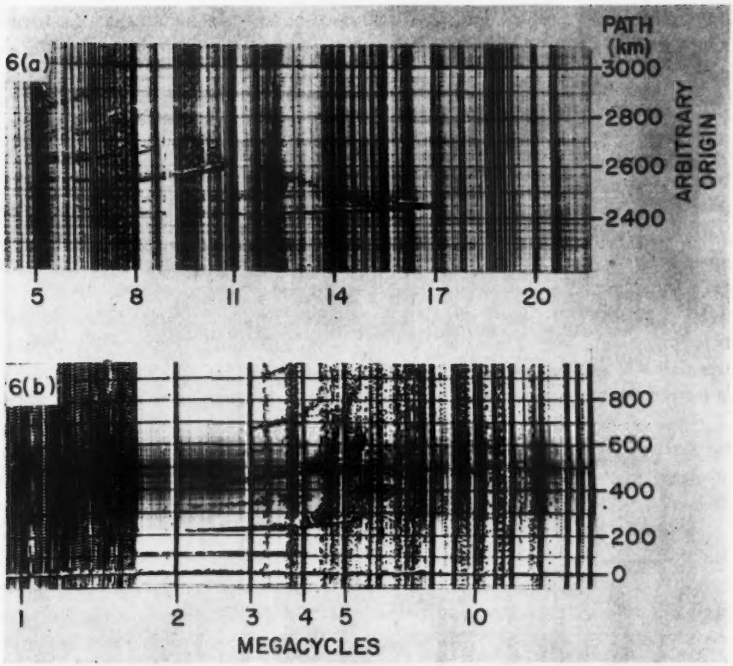

FIG. 6. (*a*) Sweep showing the influence of sporadic *E* and a relatively strong Pedersen ray. Saskatoon, 14 December, 1954, 17:01 E.S.T.

(*b*) Vertical incidence sweep near mid-point of Ottawa–Saskatoon path. Note the presence of *Es* echoes. Kakabeka Falls, 14 December, 1954, 17:05 E.S.T.

reflections from the *F*2 layer with both the once-reflected signal and the twice-reflected signal present. The once-reflected signal extends from 11 Mc. to 22 Mc. and, at its high frequency end, shows the more strongly retarded Pedersen or high angle ray. The twice-reflected signal is not transmitted at frequencies above 13.5 Mc. owing to the acute angle of incidence on the ionosphere. The changes in equivalent paths near the lower frequency limits of both traces are probably due to the *F*1 layer which, in winter, is not separated from the *F*2 layer. It may be noted that the double-hop trace is more spread near the maximum frequency than the corresponding portion of the one-hop trace. This feature appears to be true in general.

A somewhat similar sweep is shown in Fig. 4. Here there is an interesting feature, namely, the retardation in the *E* layer of the once-reflected *F*2 echo near its low frequency limit. The lower cutoff frequency of about 9 Mc. agrees quite well with the values calculated from the vertical incidence critical frequency near the mid-point of the circuit.

A more complicated sweep is that shown in Fig. 5. It is difficult to determine the maximum usable frequency (MUF) with accuracy because a weak signal is

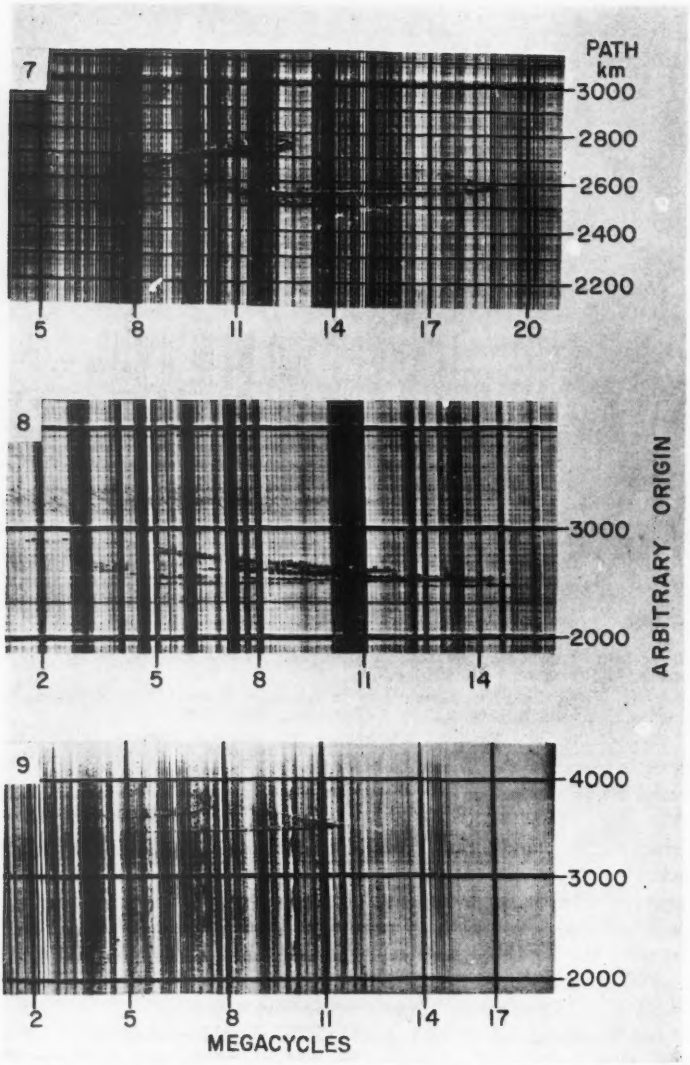

FIG. 7. Sweep with reflection from the *E* region. Saskatoon, 15 December, 1954, 12:41 E.S.T.
FIG. 8. Typical September day sweep. Ottawa, 19 September, 1954, 13:21 E.S.T.
FIG. 9. Sweep taken on a September evening. Note the close resemblance to winter sweeps. Compression of frequency scale between 14 and 17 Mc. is due to camera. Saskatoon, 10 September, 1954, 21:01 E.S.T.

present at frequencies above the so-called 'classical MUF'. This phenomenon was noticed frequently and it was found that the maximum observable frequency depended, to some extent, on the characteristics of the equipment. A much spread two-hop reflection is also present. An intermediate echo can be seen at about 2290 km. between 8.0 and 9.0 Mc.

Another sweep of considerable interest is shown in Fig. 6(*a*). It will be noticed that the single-hop Pedersen ray* has appreciable strength at frequencies well below the maximum frequency. Between 5.0 Mc. and 8.0 Mc. there is little sign of the once-reflected signal whereas the multiple reflected signals are quite strong. In addition to the one-hop, two-hop, and three-hop reflections, there are several traces which are produced by reflections from the *F*2 layer followed by reflections from the *Es* layer. Evidence that this is the case is provided by vertical incidence sweeps obtained near the mid-point of the circuit (see Fig. 6(*b*)) which show *N* type reflections, i.e., an echo received after a reflection from the *F* layer followed by a reflection at the ground and finally from the *E* layer.

Fig. 7 shows one of the relatively rare winter sweeps when reflections were obtained below the main *F*2 echo. It was found that such echoes were only obtained when sporadic *E* ionization was present at heights greater than about 130 km.

A typical September day sweep is shown in Fig. 8. This sweep is typical of summertime conditions and is more complicated than most winter sweeps. The maximum frequency observed, about 15 Mc., is reflected from the *E* layer. The signal received after two reflections from the *E* layer can also be seen, having a maximum frequency near 10 Mc. It will also be noticed that the maximum frequency reflected from the *F*1 layer is greater than the maximum frequency reflected from the *F*2 layer. The importance of the Pedersen rays relative to the low angle rays is clearly evident in Fig. 8. Note also the splitting of the *F*2 layer Pedersen ray into ordinary and extraordinary components near its lower frequency limit.

A record taken on a September evening is shown in Fig. 9. The *E* and *F*1 layers had disappeared, thus giving the sweep the appearance of a winter's day sweep.

4. RECIPROCITY

It has not yet been adequately demonstrated that propagation of radio signals in the ionosphere is completely reciprocal. Indeed, the influence of the earth's magnetic field may be such that the principle of reciprocity may not always hold. Hence this point is worthy of investigation.

In section 2 it was assumed that reciprocity was valid, i.e.,

(i) that the transmission times are the same in both directions, and

(ii) that the sweeps obtained at both ends of the circuit are identical.

Unfortunately, it is not possible to make a direct test of (i) since there is no

**This ray, also known as the high angle ray, has smaller angles of incidence on the reflecting layer than the low angle ray and is reflected from regions of higher electron density. As the frequency is increased these two paths come closer together and are identical at the maximum frequency of transmission.*

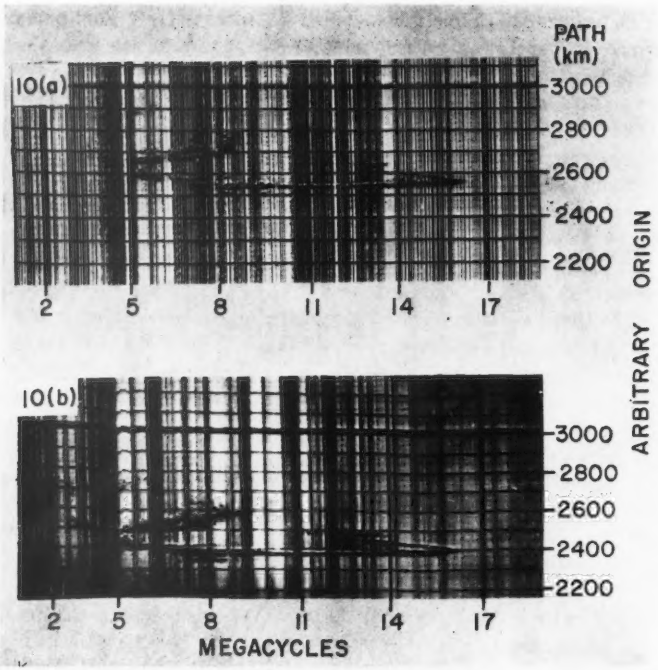

FIG. 10. (*a*) and (*b*) Simultaneous sweeps taken at Ottawa and at Saskatoon to illustrate the principle of reciprocity. 16 December, 1954, 10:41 E.S.T. (*a*) Saskatoon, (*b*) Ottawa.

common time reference. However, by taking the low angle one-hop trace as reference it is possible to compare the time delays of the one-hop Pedersen ray and of the multi-hop modes of transmission. Figs. 10(*a*) and 10(*b*) show that, in this respect, the patterns at Ottawa and at Saskatoon are very similar.

5. OBSERVED AND CALCULATED MAXIMUM USABLE FREQUENCIES

From the point of view of practical radio communication the maximum usable frequencies for any circuit are of great importance. Various methods have been developed for relating vertical incidence $h'f$ data to oblique transmission problems. For present purposes the theory developed by Millington (3) has been used to convert vertical sweeps to oblique sweeps. Beynon (1) in England has shown that over a distance of 715 km. there is a fairly close correspondence between vertical and oblique sweeps. Sultzer and Ferguson (4) have verified this for a distance of 1150 km.

Owing to the inaccessibility of the country at the mid-point of the circuit it was decided to locate an ionospheric recorder at Kakabeka Falls, Ontario, situated about 200 km. south of the mid-point.

Examination of the records obtained at Kakabeka Falls showed that, near midday, the minimum height of reflection of the *F*2 layer was between about

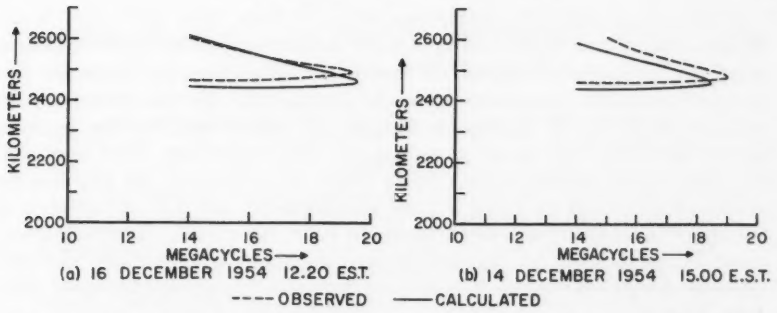

FIG. 11. (*a*) and (*b*) Comparison between observed sweeps and sweeps calculated from vertical incidence data.

190 km. and about 210 km. Since the true height of reflection must be less than this, a value for H of 180 km. was used to calculate the transmission curve, where H is the height of the bottom of the layer. Two examples of oblique sweeps calculated from vertical sweep data are shown in Figs. 11(*a*) and 11(*b*). The observed curves were obtained by averaging the values for Saskatoon and for Ottawa (see Section 2). Considering that Kakabeka Falls is about 200 km. from the mid-point together with the simplifying assumptions that are used in the theory, the agreement between deduced and observed curves is reasonable. The maximum frequencies are usually in fair agreement, but the observed path delays appear consistently to be greater than those calculated.

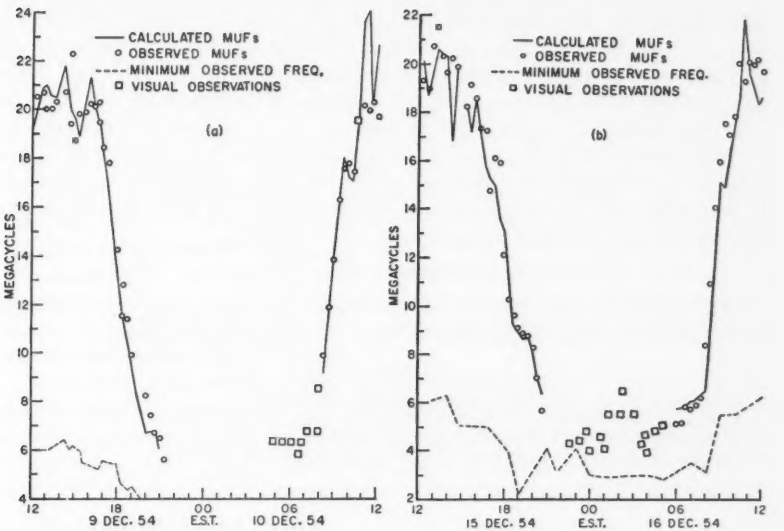

FIG. 12. (*a*) and (*b*) Comparison between observed and calculated maximum frequencies.

Observed and calculated MUFs are shown in Figs. 12(*a*) and 12(*b*). It will be seen that, on the whole, the agreement is reasonably good, again bearing in mind the limitations involved. It should be noted that the maximum frequencies generally were scaled from the photographic records. However, the frequencies at which the signals disappeared were noted by the operator during the sweep and the latter values are included in Figs. 12(*a*) and 12(*b*) for cases where photographic records could not be scaled. By plotting the minimum frequency on which echoes were observed, the diurnal variation of the useful frequency spectrum is emphasized. During the day, communications could be established on frequencies between about 6.0 Mc. and 20.0 Mc. whereas at night the usable frequency spectrum is compressed between about 4 Mc. and 6 Mc.

It has been noted that the station at Kakabeka Falls is about 200 km. south of the mid-point of the Ottawa–Saskatoon path. By comparing the values of f_0 *F*2 obtained at Ottawa, Kakabeka Falls, and Winnipeg it was found that, on the average, the difference between the values obtained at stations separated by 1180 km. was 0.38 Mc. and at a distance of 570 km. the difference was 0.2 Mc. Hence it is reasonable to expect that for a separation of about 200 km. the average difference would be about 0.07 Mc. That is, the data from Kakabeka Falls are not significantly different from those which would have been obtained at the precise mid-point. The differences between the Ottawa data and the Winnipeg data are sufficiently great to render these data unsuitable for determining ionospheric conditions at the mid-point.

Owing to the curvature of the earth there is a limit to the distance over which a wave may be propagated by the single-hop mode of transmission. This limiting distance depends on the height of reflection. It is of interest to note that, over much of Canada, on summer days the heights of reflection of the *F*1 layer are about 200 km. and on winter days the heights of reflection of the *F*2 layer are about 210 km. Now for a height of reflection of 210 km. the limiting distance for single-hop transmission is about 3300 km., whereas in problems concerning the prediction of maximum usable frequencies, it is customary to assume that one-hop transmission is effective up to 4000 km. This implies a height of reflection of about 320 km., a value appropriate to equatorial, but not to polar, regions.

ACKNOWLEDGMENT

The authors wish to thank the Department of Physics of the University of Saskatchewan for providing the necessary facilities at Saskatoon.

REFERENCES

1. Beynon, W. J. G. Wireless Engineer, 25: 322. 1948.
2. Cox, J. W. and Davies, K. Wireless Engineer, 32: 35. 1955.
3. Millington, G. Proc. Phys. Soc. 50: 810. 1938.
4. Sultzer, P. G. and Ferguson, E. E. Proc. I.R.E. 40: 1124. 1952.

A MATHEMATICAL ANALYSIS OF SOLUTE REDISTRIBUTION DURING SOLIDIFICATION[1]

By V. G. Smith, W. A. Tiller, and J. W. Rutter

ABSTRACT

A mathematical analysis is made of the redistribution of solute which occurs during the solidification, without convection, of a single-phase alloy. Calculations of solute distributions are carried out for steady state conditions, and for the transient changes in solute concentration, both in the solid and in the liquid, which occur at the beginning and end of solidification and as a result of a change in the speed of solidification. The solute distributions in the transient regions are considered for the case of two solutes present in the melt. It is shown that, under certain conditions, *p–n* junctions may be produced in the transient regions of solidification in germanium or silicon melts containing two suitable solutes.

INTRODUCTION

It is well known that, if a melt of impure metal of uniform composition is solidified under non-equilibrium conditions, a redistribution of the impurity occurs, so that the resulting solid is not of uniform composition; that is, segregation occurs during solidification. The problem of calculating the impurity distribution which will be obtained by solidifying a single-phase alloy under specified conditions has been treated by Pfann (6) and others under the assumption that mixing is complete at all points in the melt at all times during solidification. This problem has also been treated by Tiller *et al.* (10) under the alternative assumption that there is no convective mixing; rather, it is assumed that the only mixing is due to diffusion of the impurity in the melt. Wagner (11) has given an analysis of the problem, taking into consideration both convection and diffusion in the liquid. He has calculated the effect of natural convection on segregation, and has shown that, for a wide range of solidification rates commonly used in the freezing of castings and the growth of single crystals, natural convection has little effect on the segregation. These calculations have recently received some support by the work of Walton *et al.* (12) who have studied experimentally the conditions of solidification corresponding to the breakdown of a macroscopically smooth solid–liquid interface to a "cellular" interface of the type studied by Rutter and Chalmers (8). The conditions of solidification corresponding to this transition were predicted from the theoretical considerations of Tiller *et al.* (10), which are based on the assumption of no convection in the liquid. The fact that the experiments were in agreement with this theory indicates that convection was absent during solidification, thus substantiating the work of Wagner.

Since natural convection appears to play a small part in the segregation over a wide range of practical conditions of solidification, it is, therefore, useful to treat the problem in considerable detail under the assumption that convection is negligible. Accordingly, the present paper constitutes an extension of the work of Tiller *et al.*, giving a more precise and more complete calculation of the

[1]*Manuscript received August 11, 1955.*
Contribution from the Department of Metallurgical Engineering, University of Toronto, Toronto, Ontario.

segregation which will be obtained under various conditions of solidification. The results will be plotted for various conditions of solidification of practical interest.

MATHEMATICAL ANALYSIS

Assumptions

In order to treat the problem quantitatively, it is necessary to employ more specific assumptions than those given in the introduction. The problem which will be considered is that of the end-to-end segregation which accompanies the solidification of an impure metal melt which is of uniform cross-section (Fig. 1).

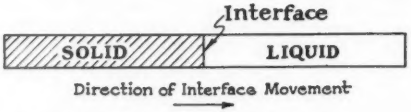

FIG. 1. Directional solidification of melt having uniform cross-section.

The case in which a single-phase alloy is formed will be considered. The following assumptions will be used:

1. Diffusion in the solid is negligible.
2. Convective mixing in the liquid is negligible.
3. The distribution coefficient, k, defined as the ratio of the concentration of impurity in the solid being formed to the concentration in the liquid from which it forms, is a constant. Attention will be directed to the case of k less than unity.
4. The interface separating solid and liquid is plane and perpendicular to the axis of the specimen.

The rate of diffusion of impurity in the liquid is specifically taken into account.

The Equation

Under the assumptions made, growth proceeds by the movement of an interface separating solid and liquid. This interface is considered to be plane and perpendicular to the axis of the specimen. The problem here is clearly a linear one, since growth takes place in one direction only.

Since the concentration of impurity appearing in the solid is related to that in the liquid adjacent to the interface by the factor k, the distribution in the solid resulting from solidification may be obtained by calculating the concentration in the liquid at the interface for all positions occupied by the interface during freezing. It has been assumed that the only factor causing movement of solute in the liquid is diffusion and, therefore, the equation which must be solved is the one-dimensional diffusion equation.

With regard to a fixed co-ordinate system, this equation may be written as:

$$D\frac{\partial^2 C_L}{\partial x^2} = \frac{\partial C_L}{\partial t} \qquad [1]$$

where D = the coefficient of diffusion of the solute in the melt,
C_L = the concentration of solute in the melt,
x = distance,
t = time.

However, the solute distribution relative to the moving solid–liquid interface is required and it is, therefore, convenient to use a co-ordinate system which moves with the interface. Transformed into this co-ordinate system, equation [1] becomes:

$$D\frac{\partial^2 C_L}{\partial x'^2}+R\frac{\partial C_L}{\partial x'}=\frac{\partial C_L}{\partial t} \qquad [2]$$

where R = rate of movement of the interface, assumed to be constant,
x' = distance measured from the interface into the liquid.

A solution for equation [2], giving the distribution of solute both in the liquid and in the solid, will be obtained for a semi-infinite sample in the following cases:

1. The initial transient rise in concentration of solute which occurs in the first part of the sample to freeze.
2. The steady state which is reached after the solidification has proceeded for some distance from the beginning.
3. The terminal transient change in concentration which occurs in the last portion of the sample to freeze.
4. The transient change in concentration which occurs as a result of a change in the speed of solidification.

The Steady State Solution

For the case of a distribution coefficient which is less than unity, the solid which forms will be purer than the liquid from which it freezes and, as a result, rejection of solute into the liquid will occur at the solid–liquid interface. Owing to the finite rate of diffusion of impurity in the liquid, a layer of high impurity concentration will build up adjacent to the advancing interface. As the concentration rises in the liquid at the interface, it must also rise in the solid being produced, since the two concentrations are related by the distribution coefficient k. If the original melt is of uniform concentration C_0 then, clearly, the layer of high impurity concentration must build up until the concentration appearing in the solid is also C_0; the concentration in the liquid at the interface will then be C_0/k. When this condition has been attained, the layer of high concentration will have reached a steady state, and no further variation with time will take place as long as the conditions of growth are not altered. Since time has been eliminated as a variable, the steady state distribution of impurity in the liquid may be found from a solution of the equation:

$$D\frac{d^2 C_L}{dx'^2}+R\frac{dC_L}{dx'}=0 \qquad [3]$$

subject to the boundary conditions:

$$C_L = C_0 \qquad \text{at } x' = \infty,$$
$$C_L = C_0/k \qquad \text{at } x' = 0.$$

The solution has been obtained by Tiller *et al.* (10) and may be written:

$$\frac{C_L}{C_0} = 1+\frac{q}{k}\epsilon^{-(R/D)x'} \tag{4}$$

where $q = (1-k)$.

A natural variable of this equation is the dimensionless quantity $(R/D)x'$. Equation [4] is plotted in the form C_L/C_0 vs. $(R/D)x'$ for various values of the parameter k in Fig. 2. It will be noted that the concentration falls off from the interface into the liquid more rapidly for higher rates of growth and that the amount of impurity carried ahead of the interface, obtained by integration of equation [4], is greater for lower rates of growth.

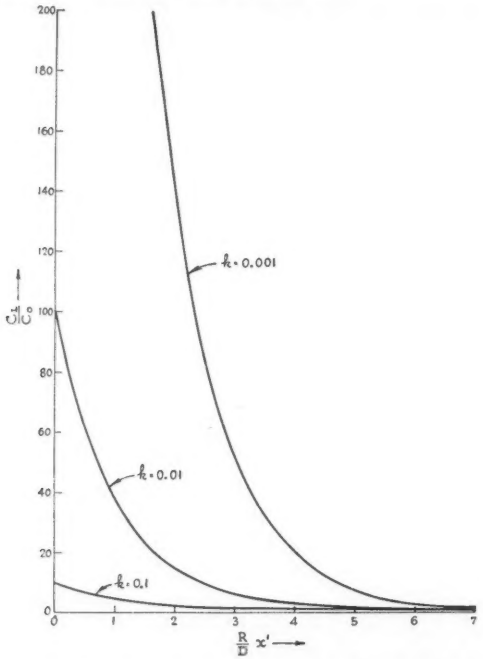

FIG. 2. Steady state solute distribution in the liquid ahead of the advancing solid–liquid interface.

The Initial Transient

In order to calculate the way in which the region of high solute concentration builds up adjacent to the interface during the first part of the solidification and the resulting transient rise of concentration to the steady state value, C_0, in the solid produced, it is necessary to solve the time-dependent equation [2].

The solution will be carried out for the case of a semi-infinite sample in which solidification is initiated at one end at time $t = 0$, and proceeds at constant speed, R.

Equation [2] must be solved subject to the following boundary conditions:

[5] $$C_L = C_0 \text{ at } x' = \infty \text{ for all } t,$$

[6] $$C_L = C_0 \text{ at } t = 0 \text{ for all } x' > 0,$$

[7] $$\frac{\partial C_L}{\partial x'} + \frac{R}{D} qC_L = 0 \text{ at } x' = 0 \text{ for all } t.$$

The boundary condition given by equation [7] expresses the fact that the concentration must remain finite at the solid–liquid interface at all times. The solution of equation [2] which satisfies the above constraints will describe the distribution of solute in the liquid at all times.

By the use of a Laplace transform, equation [2] may be transformed from a partial differential equation in x' and t into an ordinary differential equation in x'. This is accomplished by replacing C_L by:

[8] $$\bar{C} = \int_0^\infty C_L \epsilon^{-st} dt.$$

Substitution of [8] in equation [2] gives:

$$\frac{d^2\bar{C}}{dx'^2} + \frac{R}{D}\frac{d\bar{C}}{dx'} = \frac{1}{D}\int_0^\infty \frac{\partial C_L}{\partial t} \epsilon^{-st} dt$$

$$= \frac{1}{D} C_L \epsilon^{-st} \Big]_0^\infty + \frac{S}{D}\int_0^\infty C_L \epsilon^{-st} dt.$$

Rearranging terms, we get

[9] $$\frac{d^2\bar{C}}{dx'^2} + \frac{R}{D}\frac{d\bar{C}}{dx'} - \frac{S}{D}\bar{C} = -\frac{C_L(x', 0)}{D} = -\frac{C_0}{D}.$$

Equation [9] may now be solved for $\bar{C}$, and by operating on $\bar{C}$ with the inverse Laplace transformation, the time dependent solution, $C_L(x', t)$, is restored. The solution is carried out in Appendix I, and gives the concentration, C_L, throughout the liquid at any time, t.

The impurity concentration appearing in the solid is equal to k times the concentration in the liquid at $x' = 0$ at any time. Therefore, the impurity distribution resulting from solidification of the initial transient region may be obtained from $C_L(x', t)$ by putting $x' = 0$, multiplying by k, and introducing the co-ordinate $x = Rt$, which represents distance measured from the beginning of the sample. As derived in Appendix I, the concentration, $C_S(x)$, in the solid, is given by:

[10] $$\frac{C_S(x)}{C_0} = \frac{1}{2}\left\{1 + \operatorname{erf}\left(\frac{\sqrt{(R/D)x}}{2}\right) + (2k-1)\, \epsilon^{-kq(R/D)x} \operatorname{erfc}\left[\frac{(2k-1)}{2}\sqrt{(R/D)x}\right]\right\}.$$

Again, a natural variable of the solution is the dimensionless quantity

$(R/D)x$. $C_S(x)/C_0$ is plotted against $(R/D)x$ for various values of the parameter k in Fig. 3.

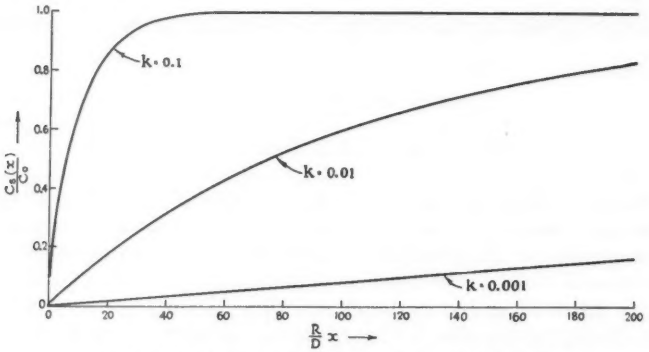

FIG. 3. Initial transient solute distribution in the solid.

Sudden Change in the Rate of Solidification, R

Suppose that the steady state distribution, C_L, of solute in the liquid has been established by growth at rate R. The rate of growth is then abruptly changed to $R_1 > R$. Since the amount of solute carried ahead of the interface in the steady state case is smaller for R_1 than for R, there will be a transient rise in the concentration in the liquid near the interface, and hence in the solid formed, as the adjustment to the new steady state is made (10). If time is measured from the instant at which the speed change occurs, this transient may be found by solving equation [2] subject to the following boundary conditions:

$$C_L = C_0 \text{ at } x' = \infty \text{ for all } t \geqslant 0,$$

$$C_L = C_0[1+(q/k)\,\epsilon^{-(R/D)x'}] \text{ at } t = 0 \text{ for all } x' \geqslant 0,$$

$$\frac{\partial C_L}{\partial x'}+\frac{R_1}{D}\,q\,C_L = 0 \text{ at } x' = 0 \text{ for all } t \geqslant 0.$$

This problem may be solved by the use of a Laplace transformation, in a manner similar to that employed for the initial transient case. The solution is derived in Appendix II. The concentration distribution produced in the solid as a result of the speed change is given by:

$$[11]\quad \frac{C_S(x_1)}{C_0} = 1-\frac{1}{2}\operatorname{erfc}\left(\sqrt{\frac{(R_1/D)x_1}{2}}\right)$$
$$+q\left(\frac{\frac{1}{2}-R/R_1}{k-R/R_1}\right)\exp\left[-\frac{R}{R_1}\left(1-\frac{R}{R_1}\right)\frac{R_1}{D}\,x_1\right]\operatorname{erfc}\left[\left(\frac{R}{R_1}-\frac{1}{2}\right)\sqrt{(R_1/D)x_1}\right]$$
$$+\left(\frac{2k-1}{2}\right)\left(\frac{1-R/R_1}{k-R/R_1}\right)\epsilon^{-kq(R_1/D)x_1}\operatorname{erfc}[(k-\tfrac{1}{2})\sqrt{(R_1/D)x_1}]$$

where x_1 = distance from the point at which the speed change occurred.

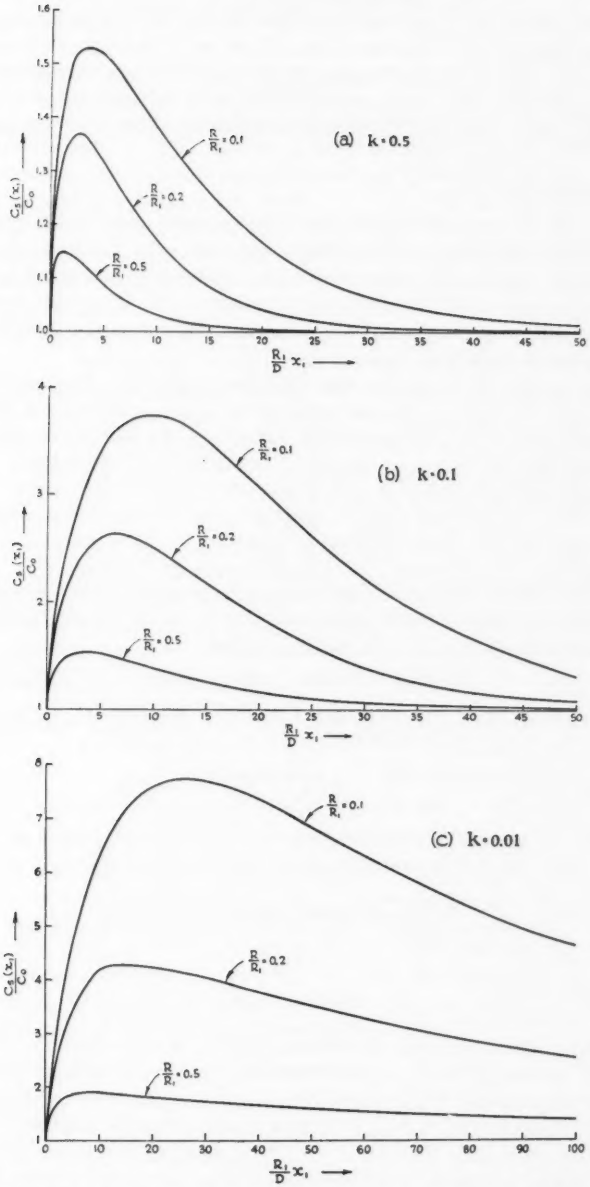

FIG. 4. Transient solute distribution in the solid caused by a change in the rate of solidification.

As in the case of the initial transient distribution, this equation may be put in dimensionless form by plotting $C_S(x_1)/C_0$ against $(R_1/D)x_1$ as the independent variable. However, since equation [11] contains two parameters, k and R/R_1, a family of curves, each corresponding to a different value of R/R_1, is obtained for each value of k. Three such families are shown in Figs. 4(*a*), 4(*b*), and 4(*c*).

The Terminal Transient

Let the advancing solid–liquid interface, carrying ahead of it the steady state impurity distribution, C_L, approach the end of the specimen at constant speed, R. The solute represented by the area under the C_L curve must appear in this last part to solidify, producing a transient rise in concentration. The impurity distribution in this terminal transient portion of the sample may be calculated in the following manner.

Take the origin at the end of the specimen, and let x_2 represent distance measured from this origin. Let the interface be at a distance y from the origin. This co-ordinate system is fixed with respect to the specimen, rather than moving with the interface and, therefore, the differential equation to be satisfied in the region of liquid $0 < x_2 < y$ is:

$$\frac{\partial^2 C_L}{\partial x_2^2} = \frac{1}{D}\frac{\partial C_L}{\partial t}. \qquad [12]$$

In order that the concentration shall remain finite at the interface and the end of the specimen during solidification of the terminal transient region, the following boundary conditions must be satisfied:

$$\partial C_L/\partial x_2 = 0 \text{ at } x_2 = 0 \text{ for all } t, \qquad [13]$$

$$\partial C_L/\partial x_2 = (R/D)q\, C_L \text{ at } x_2 = y \text{ for all } t. \qquad [14]$$

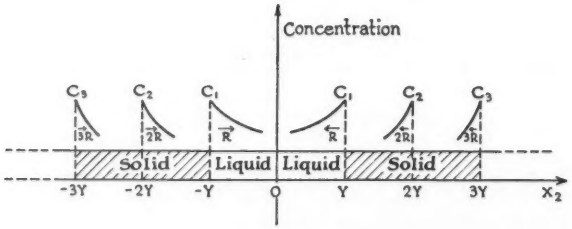

FIG. 5.

The first of these boundary conditions may be met by extending the sample to the left, as shown in Fig. 5, and assuming that two interfaces exist, one at $x_2 = y$ moving to the left at speed R and another at $x_2 = -y$ moving to the right with the same speed. It is clear that for this "double specimen" the same terminal transient as a function of x_2 will be obtained as for the "single specimen". The solute distribution ahead of each interface is known to be the steady state distribution until the interfaces get close enough to interfere with the second boundary condition. The steady state distributions are given by:

[15] $$C_L/C_0 = 1+(q/k)\,\epsilon^{-(R/D)(y-x_s)},$$

and

[16] $$C_L/C_0 = 1+(q/k)\,\epsilon^{-(R/D)(y+x_s)}.$$

In order to simplify the considerations, these distributions may be regarded as waves of strength $(q/k)C_0$ moving at speed R on the constant concentration C_0. As the two waves approach each other, a time will come when they seriously disturb the second boundary condition. This may be corrected by placing a source of properly chosen strength C_2 at $x_2 = 2y$ and at $x_2 = -2y$ moving to the left and right respectively with velocity $2R$, as indicated in Fig. 5. The double speed keeps the spacings equal and also balances the double distance of the original sources. At a later stage, the sources C_2 interfere, and it is necessary to add sources at $x_2 = \pm 3y$, of strength C_3, moving at speed $3R$. This argument may be repeated indefinitely and ultimately yields an infinite sequence of sources for which

[17] $$\frac{C_L}{C_0} = 1+\sum_{n=1}^{\infty} C_n[\epsilon^{-n(R/D)(ny-x_s)}+\epsilon^{-n(R/D)(ny+x_s)}].$$

As outlined in Appendix III, the coefficients C_n can be determined such that the second boundary condition, equation [14], is satisfied; the first boundary condition, equation [13], is satisfied for any values of C_n. The analysis given in Appendix III results in an expression for the concentration of solute in the liquid at any point for any interface position. By considering the concentration at the interface, as was done in the cases of the initial transient and the change in speed, the concentration produced in the solid as a result of the freezing of the terminal transient region may be obtained. It is given by:

[18] $$\frac{C_S(x_2)}{C_0} = 1+3\left(\frac{1-k}{1+k}\right)\epsilon^{-2(R/D)x_s}+5\,\frac{(1-k)(2-k)}{(1+k)(2+k)}\,\epsilon^{-6(R/D)x_s}+\ldots$$
$$+(2n-1)\,\frac{(1-k)(2-k)\ldots(n-k)}{(1+k)(2+k)\ldots(n+k)}\,\epsilon^{-n(n+1)(R/D)x_s}+\ldots.$$

If k is less than unity, this series diverges to infinity for $x_2 = 0$. For all other values of x_2 the series converges, and does so quite rapidly for larger values of x_2.

If k is equal to unity, there is no transient, while if k is greater than unity, the series converges even for $x_2 = 0$, though perhaps quite slowly.

As in the case of the initial transient, equation [18] contains the dimensionless quantity $(R/D)x_2$ as a natural variable. $C_S(x_2)/C_0$ is plotted against $(R/D)x_2$ for various values of the parameter k in Fig. 6.

DISCUSSION

The Extent of the Transient Regions of Solidification

It is frequently desirable to produce, by solidification from the melt, a specimen which is of uniform composition. If this is to be accomplished, all transient regions of solidification must be avoided or subsequently removed from the solid sample. Consequently, it is of interest to know how large the

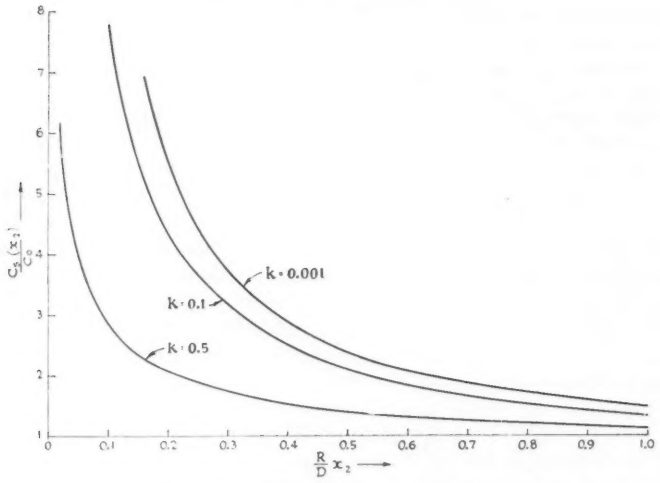

FIG. 6. Terminal transient solute distribution in the solid.

transient regions of solidification will be. As a basis for comparison of the lengths of the transients, the distance, measured from the beginning (or end, as the case may be) of the transient region, at which half of the transient change has occurred may be used. For example, in the case of the initial transient, the area between the $C_S(x)/C_0$ curve and the $C_S(x)/C_0 = 1$ line represents the solute deficiency in the transient region. The value of $(R/D)x$ corresponding to one-half of this area will be used as a measure of the extent of the distribution. A number of such "half-area values" are given in Table I.

TABLE I

COMPARISONS OF EXTENTS OF SOLUTE DISTRIBUTIONS

Distribution coefficient	Steady state, $(R/D)x'$	Initial transient, $(R/D)x$	Terminal transient, $(R/D)x_2$
0.5	0.693	1.4	0.8
0.1	0.693	7.6	<0.01
0.01	0.693	67	<0.01
0.001	0.693	670	<0.01

It will be noted that the half-area value for the steady state distribution is a constant; it is, in fact, equal to ln 2, as may be shown by direct integration of equation [4]. The half-area values for the initial transient were obtained graphically. In the case of the terminal transient, precise computation of half-area values is not feasible for values of k smaller than about 0.5 because of the slow rate of convergence of equation [18].

It is of interest to compare the precise equation for the distribution in the initial transient region, equation [10], with the approximate equation given by Tiller *et al.* (10). Their equation for the initial transient distribution may be

written: $$C_S(x)/C_0 = 1-q\,\epsilon^{-k(R/D)x}.$$

This equation is plotted in Fig. 7, along with equation [10] for comparison. It will be seen that the approximate equation is, in fact, quite accurate; the maximum error appears to be about 20 per cent. Hence, the approximate equation may be used with good accuracy.

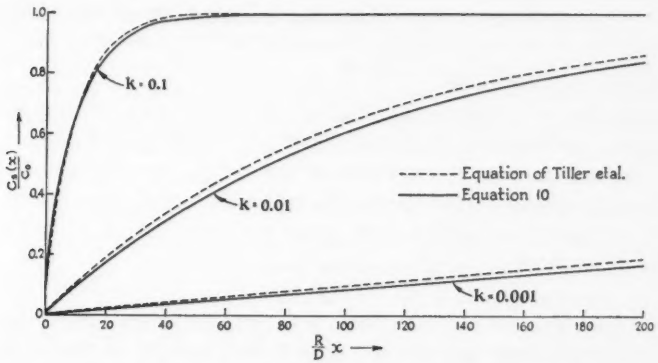

FIG. 7. Comparison of equation [10] for initial transient distribution with that given by Tiller *et al.*

Two methods may be used for the production of a specimen of uniform composition by solidification. If mixing in the liquid is complete at all times, the process of zone levelling (6) may be used. If there is no convection in the liquid (or a constant amount of convection) growth under steady state conditions as outlined in this paper may be employed. However, if this latter method is chosen, care must be taken to avoid the formation of the prismatic substructure described by Rutter and Chalmers (8), since the formation of this substructure is accompanied by a segregation of impurities into the boundaries of the elements of the structure. In practice, this means that the steady state method is restricted to cases of distribution coefficients close to unity or low solute concentrations (10).

The Nature of the Transient Regions of Solidification When Two or More Solutes Are Present in the Melt

If two or more solutes are present in low concentrations in a melt, it may be assumed that they will behave independently. If this is the case, the theory presented in this paper may be applied to each solute individually in order to calculate the distribution resulting from solidification under a given set of conditions. For simplicity, the discussion will be limited to the case of two solutes.

Let two solutes, having different distribution coefficients, be distributed uniformly throughout the melt, the concentration of one being greater than that of the other. As will be shown below, it is possible, during transient

regions of solidification, to produce solid in which the major solute is the one which was present to the smaller extent in the original melt. If the parent material in the melt is germanium and one of the solutes will produce n-type germanium while the other produces p-type germanium, then such a reversal of the predominant impurity in the solid will result in a change of conductivity type with the consequent production of a p–n junction. Because of the general interest in the production of p–n junctions, the effect will be discussed in this context.

(1) *The Initial Transient*

Suppose that two solutes, which shall be numbered 1 and 2, having different distribution coefficients, are added to a melt of pure germanium. Let:

$C_0(1)$ = concentration of impurity 1 in the melt,

$C_0(2)$ = concentration of impurity 2 in the melt,

k_1 = distribution coefficient of impurity 1,

k_2 = distribution coefficient of impurity 2.

It will be assumed that k_1 is greater than k_2.

By proper choice of concentrations, it is possible to have $C_0(1)$ less than $C_0(2)$ and at the same time $k_1 C_0(1)$ greater than $k_2 C_0(2)$. If this is the case, impurity 1 will appear in the solid in greater concentration than impurity 2 during the first part of the initial transient region of solidification; impurity 2 will be in excess throughout the rest of the initial transient as well as the steady state which follows. If the impurities are, for example, gallium ($k_1 = 0.12$) (7), which produces p-type germanium, and antimony ($k_2 = 0.007$) (7), which produces n-type germanium, then the sample will be p-type in the first portion of the initial transient and n-type thereafter. A p–n junction will be formed in the sample at the point where the atomic concentrations of antimony and

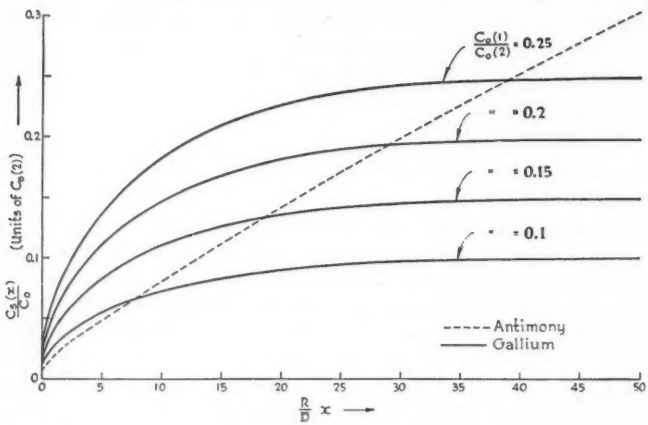

FIG. 8. Production of p–n junctions by crossover of initial transients for two solutes (gallium and antimony).

gallium are equal. The distributions of antimony and gallium, calculated from equation [10], in the portion of the initial transient region of interest here are shown in Fig. 8. The antimony and gallium concentrations are plotted as a fraction of $C_0(2)$, the initial concentration of antimony in the melt, vs. $(R/D)x$ for various values of the concentration ratio $C_0(1)/C_0(2)$. As Fig. 8 shows, both the thickness of the p-layer and the difference between the concentration gradients of the two solutes at the junction depend upon the rate of solidification and the starting concentrations. As a result, the rate of change of the difference in concentration, which may be called the differential concentration gradient, across the junction may be controlled by suitable choice of the rate of solidification and the starting concentrations in the melt. The difference between the antimony and gallium concentrations, obtained by subtracting corresponding values in Fig. 8, is plotted in Fig. 9; the slope of this curve at the p–n junction gives the differential concentration gradient across the junction.

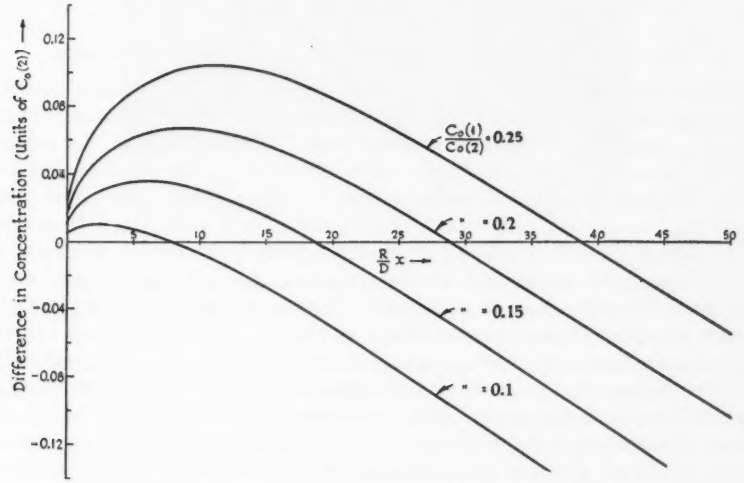

FIG. 9. Concentration difference across p–n junctions of Fig. 8.

A number of p–n junctions may be produced in one sample by the following method. Suppose that solidification has passed the initial p-region, as described above, so that the solid being formed is n-type germanium. Distributions of gallium and antimony will have built up in the liquid adjacent to the interface to the extent corresponding to the stage of solidification which has been reached. If these solute distributions in the liquid are now destroyed, for example by stopping solidification and stirring the liquid, the first material to solidify when growth is continued will be p-type germanium. That is, the initial transient region of solidification will be repeated and a p-region will be formed between two n-regions, as indicated in Fig. 10. The p–n junction formed at the point where growth resumes will be a step junction, while the other

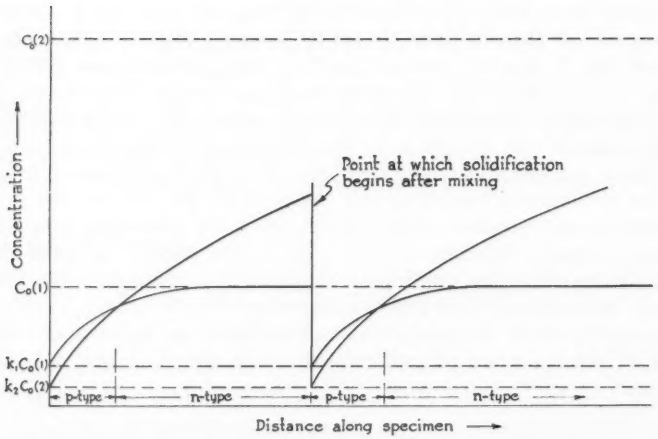

FIG. 10. Production of n–p–n distribution by repetition of initial transient.

junction, formed in the manner described above, will be a graded junction. This process could be repeated several times in a sample of sufficient length, thereby producing a series of p–n junctions. The thickness of the p-layers produced by this method could be controlled by varying the speed of solidification and the starting concentrations employed. Theoretically, there is no reason why the p-layer could not be made thin enough to produce a sample from which a transistor could be made. In producing a p-layer of requisite thickness for this purpose, the possibility of choosing solutes having more suitable distribution coefficients must be considered. The requirement here is to have the point of equal atomic concentrations of the two solutes occur as close as possible to the point at which solidification is resumed. It is clear that this will be favored by a rise of the concentration of impurity 2 from $k_2\,C_0(2)$ which is as rapid as possible and a rise of impurity 1 from $k_1\,C_0(1)$ which is as slow as possible. On the basis of the approximate equation of Tiller *et al.*, it may be shown that the maximum rate of rise will occur for a distribution coefficient of 1/2. Therefore, production of a thin p-layer will be favored by the use of two impurities, one of which has a distribution coefficient of 1/2 and the other of which has a distribution coefficient greater than unity. In the case of germanium, the closest available approach to this situation appears to lie in the use of arsenic ($k = 0.04$) (1) as n-type impurity and boron ($k > 1$) (1) as p-type impurity.

An example of a p-layer produced by the method described above in a sample of germanium containing antimony and gallium as impurities is shown in Fig. 11. This sample was solidified in a horizontal graphite boat to approximate the conditions of the theory. The step junction appears as a line running across the etched sample. The location of the graded junction is not revealed by etching, but can be found by using a hot copper probe. The operation of the probe is based on the fact that the thermal e.m.f. generated between copper

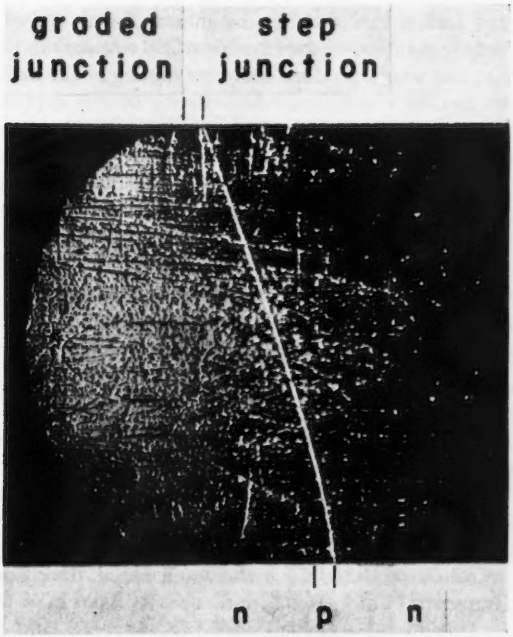

FIG. 11. p-Layer in germanium crystal containing antimony and gallium. 25×.

and n-type germanium is of opposite polarity to that generated between copper and p-type germanium. The width of the p-layer contained in the sample of Fig. 11 is approximately 0.005 in.; it was measured using the hot probe mounted in a micromanipulator. Similar samples have also been produced by this technique using boron and arsenic as impurities in germanium.

Owing, first, to lack of accurate information concerning such quantities as the diffusion coefficients, the distribution coefficients, and the concentrations of the solutes and, second, to the impossibility of producing the ideal experimental conditions required by the theory, it has not been possible to obtain an accurate comparison of theory and experiment. The theoretical values for p-layer width are larger than but, on the average, within one order of magnitude of those obtained experimentally.

Layers of p-type material between regions of n-type material have also been produced in germanium by Hall (4, 5) and in silicon by Tanenbaum *et al.* (9). The method used by these workers has been called the "rate growing" technique. It consists essentially of varying the crystal pulling rate or the melt temperature or both while growing a crystal from a properly doped melt. These workers have attributed the production of regions of different conductivity types in their samples to a variation of the distribution coefficients of the impurities with speed of solidification, the amount of variation depending upon the particular solute. This explanation is based on the experiments of Hall

(4, 5), who found such a variation in germanium crystals pulled from a melt which was stirred by rotation of the crystal at 200 revolutions per minute. It was believed that this would produce complete mixing of the melt at all times. However, doubt has been cast upon the validity of this explanation by the work of Burton *et al.* (1, 2), which shows that Hall probably did not have complete stirring of the melt during his experiments.

In addition to the method of crystal growth employed, the technique used by these workers to produce *p*-layers differs in other respects from that described in the present paper. Hall (4, 5) and Tanenbaum *et al.* (9) used "closely compensated melts" (9) which were stirred during growth, whereas the present technique employs a melt which is not compensated and in which precautions are taken to avoid convective mixing during growth.

(2) *A Change in the Rate of Solidification*

As shown by Fig. 4, the extent of the transient change in concentration produced by a given change in speed depends upon the distribution coefficient of the solute concerned; a smaller distribution coefficient results in a larger increase in concentration for a given change in speed. Therefore, it is possible, when solidifying a melt containing two solutes which have different distribution coefficients such as antimony and gallium in germanium, to change the major impurity appearing in the solid from one to the other over a limited region of the transient produced by a change in speed. This is illustrated by Fig. 12, where impurity 1 has $k_1 = 0.5$, and impurity 2 has $k_2 = 0.1$; the curves

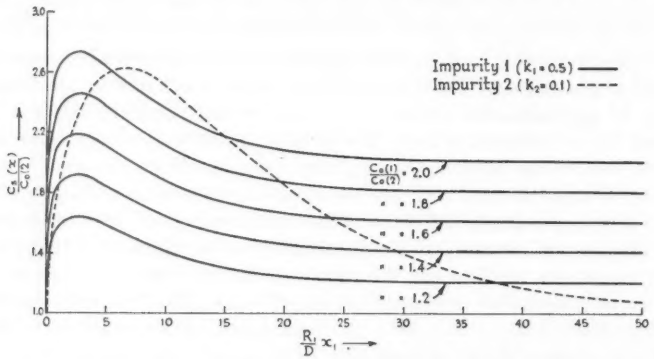

FIG. 12. Production of *p–n–p* distribution by change in rate transients of two suitable solutes.

are plotted for $R/R_1 = 0.2$. In the case of the change in rate transient, both the junctions produced in a germanium sample would be graded junctions.

ACKNOWLEDGMENTS

The authors gratefully acknowledge the financial assistance of Canadian Patents and Developments, Ltd., and The National Research Council of Canada throughout the course of this work.

APPENDIX I

The differential equation to be solved is the transformed equation

$$\frac{d^2\bar{C}}{dx'^2}+\frac{R}{D}\frac{d\bar{C}}{dx'}-\frac{S}{D}\bar{C} = -\frac{C_0}{D} \quad [19]$$

derived from the original equation, [2], by the substitution

$$\bar{C} = \int_0^\infty C_L\, \epsilon^{-St} dt.$$

The boundary conditions, equations [5] and [7], transform to

$$\bar{C} = C_0/S \text{ at } x' = \infty \text{ for all } t \quad [20]$$

and

$$d\bar{C}/dx' = -(R/D)q\bar{C} \text{ at } x' = 0 \text{ for all } t. \quad [21]$$

Try a solution of the form

$$\bar{C} = A\, \epsilon^{-ax'}+C_0/S \quad [22]$$

where A and a are constants. Substitution of [22] in the equation [19] gives a:

$$a = \frac{1}{2}\frac{R}{D} \pm \sqrt{1/D}\left(S+\frac{R^2}{4D}\right)^{\frac{1}{2}}. \quad [23]$$

By using the second boundary condition, [21], A is found to be

$$A = \frac{q}{(D/R)a-q}\frac{C_0}{S}. \quad [24]$$

Substitution of the values of a, [23], and A, [24], in equation [22] gives

$$\bar{C} = \frac{C_0}{S}\left\{1+q\,R\sqrt{1/D}\,\epsilon^{-(R/2D)x'} \times \exp\left[-\sqrt{1/D}\left(S+\frac{R^2}{4D}\right)^{\frac{1}{2}}x'\right]\Big/\left[(\tfrac{1}{2}-q)\,R\sqrt{1/D}+\left(S+\frac{R^2}{4D}\right)^{\frac{1}{2}}\right]\right\}. \quad [25]$$

The time-dependent solution may now be obtained by transforming $\bar{C}$ back to the required $C_L(x', t)$ through the inverse Laplace transform. The required transform has been given by Campbell and Foster (3). Incorporating their solution, the solute concentration at any point in the liquid for any time is found to be given by

$$C_L = C_0\left\{1+\frac{q}{2k}\epsilon^{-(R/D)x'}\operatorname{erfc}[\tfrac{1}{2}\sqrt{1/Dt}(x'-Rt)]-\tfrac{1}{2}\operatorname{erfc}[\tfrac{1}{2}\sqrt{1/Dt}(x'+Rt)] +\frac{q}{2}\left(\frac{1}{q}-\frac{1}{k}\right)\epsilon^{-q(R/D)(x'+kRt)}\operatorname{erfc}[\tfrac{1}{2}\sqrt{1/Dt}(x'+\overline{2k-1}\,Rt)]\right\}. \quad [26]$$

Since the convergence domain of the transform is violated in this problem, it is necessary to check the results of the computations. That equation [26] is the correct solution to the problem has been verified by showing that it satisfies the following conditions:

(1) When $t = \infty$, $C_L = C_0[1+(q/k)\epsilon^{-(R/D)x'}]$.

(2) At $t = 0$, $C_L = C_0$ for all $x' > 0$.

(3) At $x' = \infty$, $C_L = C_0$ for all t.

(4) At $x' = 0$, it may be shown by direct differentiation and substitution that

$$(\partial C_L/\partial x')_{x'=0} = -q(R/D)C_L(0, t) \text{ for all } t.$$

(5) By direct differentiation and substitution, it may be shown that the solution satisfies the original differential equation.

The concentration in the solid may be found by putting $x' = 0$ in equation [26] and multiplying by k. By putting $x = Rt$ and rearranging terms, the concentration in the solid may be expressed as a function of distance, x, from the beginning of the specimen, in the following form:

$$[27] \quad C_S(x) = \tfrac{1}{2} C_0 \left\{ 1 + \operatorname{erf}\left(\frac{\sqrt{(R/D)x}}{2} \right) + (2k-1)\, \epsilon^{-kq(R/D)x} \operatorname{erfc}\left[\frac{(2k-1)\sqrt{(R/D)x}}{2} \right] \right\}.$$

The following additional checks as to the correctness of this solution have been verified:

(1) When $x = 0$, $C_S(x) = kC_0$.

(2) When $x = \infty$, $C_S(x) = C_0$.

(3) The quantity of solute carried ahead of the interface must equal the solute deficiency below C_0 in the initial transient region of the solid. Therefore, the following equation must hold:

$$\int_0^\infty [C_0 - C_S(x)]\, dx = \int_0^\infty C_L(x')\, dx'.$$

By direct integration, it has been shown that this relation is satisfied.

APPENDIX II

In this case, the differential equation to be satisfied by the concentration, $C_L(x', t)$, in the liquid is

$$[28] \quad \frac{\partial^2 C_L}{\partial x'^2} + \frac{R_1}{D}\frac{\partial C_L}{\partial x'} = \frac{1}{D}\frac{\partial C_L}{\partial t}.$$

The boundary conditions are:

$$[29] \quad C_L = C_0 \text{ at } x' = \infty \text{ for all } t,$$

$$[30] \quad C_L = C_0[1 + (q/k)\epsilon^{-(R/D)x'}] \text{ at } t = 0 \text{ for all } x' > 0,$$

$$[31] \quad \partial C_L/\partial x' = -q(R_1/D)C_L \text{ at } x' = 0 \text{ for all } t.$$

As in Appendix I, the equation may be transformed by using

$$[32] \quad \bar{C} = \int_0^\infty C_L\, \epsilon^{-st} dt.$$

Substituting [32] in [28] yields the transformed equation

[33] $$\frac{d^2\bar{C}}{dx'^2}+\frac{R_1}{D}\frac{d\bar{C}}{dx'}-\frac{S}{D}\bar{C} = -R\,C_L(x',0) = -R\,C_0\left[1+\frac{q}{k}\,\epsilon^{-(R/D)x'}\right].$$

The particular integral of this equation is

[34] $$\bar{C} = \frac{C_0}{S}-C_0\,\frac{q}{k}\,\frac{\epsilon^{-(R/D)x'}}{(R/D)(R-R_1)-S}.$$

Therefore, try as a solution

[35] $$\bar{C} = A\epsilon^{-ax'}+\frac{C_0}{S}+C_0\,\frac{q}{k}\,\frac{\epsilon^{-(R/D)x'}}{S-(R/D)(R-R_1)}.$$

Applying the third boundary condition, equation [31], form the quantity

$$\left[\frac{d\bar{C}}{dx'}+\frac{R_1}{D}\,q\,\bar{C}\right]_{x'=0} = 0.$$

This gives

[36] $$A\left(\frac{R_1}{D}\,q-a\right)+\frac{R_1}{D}\,q\,\frac{C_0}{S}+\frac{C_0 q}{Dk}\,(R_1 q-R)\,\frac{1}{S+(R/D)(R-R_1)} = 0.$$

Solving equation [36] for A yields

[37] $$A = \frac{C_0\,q}{(aD/R_1)-q}\left[\frac{1}{S}-\frac{1}{k}\left(\frac{R}{R_1}-q\right)\frac{1}{S+(R/D)(R_1-R)}\right].$$

As in Appendix I, a is given by

[38] $$a = \frac{1}{2}\,\frac{R_1}{D}+\sqrt{1/D}\left(S+\frac{R^2}{4D}\right)^{\frac{1}{2}}.$$

Substituting [37] and [38] in [35] gives $\bar{C}$ in the form

[39] $$\bar{C} = \frac{C_0\,q\,R_1\sqrt{1/D}\,\exp[-(1/2D)\,R_1x']\exp\left[-\sqrt{1/D}\left(S+\frac{R_1^2}{4D}\right)^{\frac{1}{2}}x'\right]}{S\left[(\frac{1}{2}-q)\,R_1\sqrt{1/D}+\left(S+\frac{R_1^2}{4D}\right)^{\frac{1}{2}}\right]}$$

$$-\frac{1}{k}\left(\frac{R}{R_1}-q\right)\frac{C_0\,q\,R_1\sqrt{1/D}\,\exp[-(1/2D)\,R_1x']\exp\left[-\sqrt{1/D}\left(S+\frac{R_1^2}{4D}\right)^{\frac{1}{2}}x'\right]}{\left[S+\frac{R}{D}(R_1-R)\right]\left[(\frac{1}{2}-q)\,R_1\sqrt{1/D}+\left(S+\frac{R_1^2}{4D}\right)^{\frac{1}{2}}\right]}$$

$$+\frac{C_0}{S}+\frac{C_0 q}{k}\,\frac{\exp[-(R/D)x']}{S+(R/D)(R_1-R)}.$$

It will be seen that the first and third terms of this expression are, except for R_1 in place of R, the initial transient given in Appendix I. The second and fourth terms give rise to new transients. By applying the appropriate inverse Laplace transforms, as given by Campbell and Foster (3), to the terms of equation [39], the time-dependent solution may be obtained. The fourth term gives

[40] $$C_0(q/k)\exp[-(R/D)(x'+\overline{R_1-R}\,t)].$$

$$C_2 = \frac{q(1+q)}{k(1+k)},$$

$$C_3 = \frac{q(1+q)(2+q)}{k(1+k)(2+k)},$$

and, in general,

$$[48] \qquad C_n = \prod_0^{n-1}(m+q) \Big/ \prod_0^{n-1}(m+k).$$

Therefore, substituting [48] in [44],

$$[49] \quad \frac{C_L}{C_0} = 1+\sum_{n=1}^{n=\infty}\left[\prod_0^{n-1}(m+q) \Big/ \prod_0^{n-1}(m+k)\right][\epsilon^{-(R/D)n(ny-x')}+\epsilon^{-(R/D)n(ny+x')}].$$

It may easily be shown that each term of the above series satisfies the differential equation, noting that $\partial y/\partial t = R$. Hence, the above expression satisfies all the requirements of the problem.

Putting $x' = y$ gives the concentration at the interface for any interface position y. Multiplying by k gives the concentration in the solid at the position y from the end of the specimen. Replacing y by x_2 to agree with previous notation:

$$[50] \quad \frac{C_S(x_2)}{C_0} = k+k\sum_{n=1}^{n=\infty}\left[\prod_0^{n-1}(m+q) \Big/ \prod_0^{n-1}(m+k)\right] \times[\epsilon^{-n(n-1)(R/D)x_2}+\epsilon^{-n(n+1)(R/D)x_2}].$$

Combining terms in [50] which have the same exponentials:

$$[51] \quad \frac{C_S(x_2)}{C_0} = k+k\frac{q}{k}+k\sum_{n=1}^{n=\infty}\left[\prod_0^{n-1}(m+q) \Big/ \prod_0^{n-1}(m+k)\right] \times\left[1+\frac{n+q}{n+k}\right]\epsilon^{-n(n+1)(R/D)x_2}$$

$$= 1+\sum_{n=1}^{n=\infty}(2n+1)\left[\prod_0^{n-1}(m+q) \Big/ \prod_1^{n}(m+k)\right]\epsilon^{-n(n+1)(R/D)x_2}$$

$$= 1+\sum_{n=1}^{n=\infty}(2n+1)\left[\prod_1^{n}(m-k) \Big/ \prod_1^{n}(m+k)\right]\epsilon^{-n(n+1)(R/D)x_2}.$$

Written out in full, [51] becomes:

$$[52] \quad \frac{C_S(x_2)}{C_0} = 1+3\frac{(1-k)}{(1+k)}\epsilon^{-2(R/D)x_2}+5\frac{(1-k)(2-k)}{(1+k)(2+k)}\epsilon^{-6(R/D)x_2}+\ldots +(2n+1)\frac{(1-k)(2-k)\ldots(n-k)}{(1+k)(2+k)\ldots(n+k)}\epsilon^{-n(n+1)(R/D)x_2}+\ldots.$$

REFERENCES

1. Burton, J. A., Kolb, E. D., Slichter, W. P., and Struthers, J. D. J. Chem. Phys. 21: 1991. 1953.
2. Burton, J. A., Prim, R. C., and Slichter, W. P. J. Chem. Phys. 21: 1987. 1953.
3. Campbell, G. A. and Foster, R. M. Bell Telephone System, Tech. Publs. Monograph B-584. Sept. 1931. *Reprinted in* Collected Papers of George A. Campbell. American Telephone & Telegraph Co., New York. 1931.

4. HALL, R. N. Phys. Rev. 88: 139. 1952.
5. HALL, R. N. J. Phys. Chem. 57: 836. 1953.
6. PFANN, W. C. J. Metals, 4: 747. 1952.
7. PFANN, W. C. J. Metals, [illegible]. 1952.
8. RUTTER, J. W. and CHALM[illegible]. Can. J. Phys. 31: 15. 1953.
9. TANENBAUM, M., VALDES, L. B., BUEHLER, E., and HANNAY, N. B. J. Appl. Phys. 26: 686. 1955.
10. TILLER, W. A., JACKSON, K. A., RUTTER, J. W., and CHALMERS, B. Acta Metallurgica, 1: 428. 1953.
11. WAGNER, C. J. Metals, 6: 154. 1954.
12. WALTON, D., TILLER, W. A., RUTTER, J. W., and WINEGARD, W. C. J. Metals. 7: 1023. 1955.

$$C_2 = \frac{q(1+q)}{k(1+k)},$$

$$C_3 = \frac{q(1+q)(2+q)}{k(1+k)(2+k)},$$

and, in general,

$$[48] \qquad C_n = \prod_0^{n-1}(m+q) \Big/ \prod_0^{n-1}(m+k).$$

Therefore, substituting [48] in [44],

$$[49] \quad \frac{C_L}{C_0} = 1+\sum_{n=1}^{n=\infty}\left[\prod_0^{n-1}(m+q) \Big/ \prod_0^{n-1}(m+k)\right][\epsilon^{-(R/D)n(ny-x')}+\epsilon^{-(R/D)n(ny+x')}].$$

It may easily be shown that each term of the above series satisfies the differential equation, noting that $\partial y/\partial t = R$. Hence, the above expression satisfies all the requirements of the problem.

Putting $x' = y$ gives the concentration at the interface for any interface position y. Multiplying by k gives the concentration in the solid at the position y from the end of the specimen. Replacing y by x_2 to agree with previous notation:

$$[50] \quad \frac{C_S(x_2)}{C_0} = k+k\sum_{n=1}^{n=\infty}\left[\prod_0^{n-1}(m+q) \Big/ \prod_0^{n-1}(m+k)\right] \times[\epsilon^{-n(n-1)(R/D)x_2}+\epsilon^{-n(n+1)(R/D)x_2}].$$

Combining terms in [50] which have the same exponentials:

$$[51] \quad \frac{C_S(x_2)}{C_0} = k+k\frac{q}{k}+k\sum_{n=1}^{n=\infty}\left[\prod_0^{n-1}(m+q) \Big/ \prod_0^{n-1}(m+k)\right] \times\left[1+\frac{n+q}{n+k}\right]\epsilon^{-n(n+1)(R/D)x_2}$$

$$= 1+\sum_{n=1}^{n=\infty}(2n+1)\left[\prod_0^{n-1}(m+q) \Big/ \prod_1^{n}(m+k)\right]\epsilon^{-n(n+1)(R/D)x_2}$$

$$= 1+\sum_{n=1}^{n=\infty}(2n+1)\left[\prod_1^{n}(m-k) \Big/ \prod_1^{n}(m+k)\right]\epsilon^{-n(n+1)(R/D)x_2}.$$

Written out in full, [51] becomes:

$$[52] \quad \frac{C_S(x_2)}{C_0} = 1+3\frac{(1-k)}{(1+k)}\epsilon^{-2(R/D)x_2}+5\frac{(1-k)(2-k)}{(1+k)(2+k)}\epsilon^{-6(R/D)x_2}+\ldots +(2n+1)\frac{(1-k)(2-k)\ldots(n-k)}{(1+k)(2+k)\ldots(n+k)}\epsilon^{-n(n+1)(R/D)x_2}+\ldots .$$

REFERENCES

1. Burton, J. A., Kolb, E. D., Slichter, W. P., and Struthers, J. D. J. Chem. Phys. 21: 1991. 1953.
2. Burton, J. A., Prim, R. C., and Slichter, W. P. J. Chem. Phys. 21: 1987. 1953.
3. Campbell, G. A. and Foster, R. M. Bell Telephone System, Tech. Publs. Monograph B-584. Sept. 1931. *Reprinted in* Collected Papers of George A. Campbell. American Telephone & Telegraph Co., New York. 1931.

4. HALL, R. N. Phys. Rev. 88: 139. 1952.
5. HALL, R. N. J. Phys. Chem. 57: 836. 1953.
6. PFANN, W. C. J. Metals, 4: 747. 1952.
7. PFANN, W. C. J. Metals, 4: 861. 1952.
8. RUTTER, J. W. and CHALMERS, B. Can. J. Phys. 31: 15. 1953.
9. TANENBAUM, M., VALDES, L. B., BUEHLER, E., and HANNAY, N. B. J. Appl. Phys. 26: 686. 1955.
10. TILLER, W. A., JACKSON, K. A., RUTTER, J. W., and CHALMERS, B. Acta Metallurgica, 1: 428. 1953.
11. WAGNER, C. J. Metals, 6: 154. 1954.
12. WALTON, D., TILLER, W. A., RUTTER, J. W., and WINEGARD, W. C. J. Metals. 7: 1023. 1955.

COSMIC-RAY EXPERIMENTS WITH A PROTON VELOCITY SELECTOR[1]

By K. W. Ogilvie[2]

ABSTRACT

Experiments with a selector of slow heavy cosmic-ray particles are described. The pressure coefficient of protons at sea level in the momentum region 700 to 1100 Mev./c is found to be $0.64 \pm 0.08\%$ per mb. Points are obtained on the differential momentum spectrum of protons at sea level between 650 and 1250 Mev./c, in agreement with the results of Mylroi and Wilson. This spectrum is discussed in connection with the experiments of Filthüth between 200 and 900 Mev./c.

INTRODUCTION

Duerden and Hyams (3) in 1952 described an apparatus designed to study the heavy particles in the cosmic-ray beam. This utilizes the fact that, under the appropriate conditions, a liquid Cerenkov counter will detect with very high efficiency particles passing through it with a velocity greater than the Cerenkov critical velocity. This critical velocity is c/n, where c is the velocity of light in free space, and n is the refractive index of the medium. Fig. 1 shows

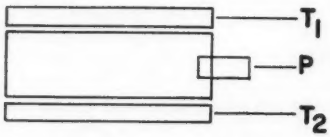

FIG. 1. Illustrating the principle of the velocity selector.

the arrangement in principle. The tank containing the liquid used as the Cerenkov radiator is placed between the two trays of Geiger counters T_1 and T_2. Light, generated by the passage of fast particles through the tank, is detected by the photomultiplier P and gives rise to an output pulse from it in coincidence with the pulses from the Geiger counters. An anticoincidence of the type T_1+T_2-P denotes the passage of a particle moving with less than the critical velocity. It can be arranged that μ mesons, electrons, etc., having great enough range to penetrate the apparatus, will have velocities greater than the critical, so that the recording of an anticoincidence denotes the passage of a heavy particle. This apparatus thus selects particles able to penetrate it, but unable to emit Cerenkov light. The majority of such particles in the cosmic-ray beam at sea level are protons.

In their paper, Duerden and Hyams show that the velocity of a μ meson is greater than the Cerenkov velocity in water if its residual range in water is greater than about 20 gm./cm.[2] They also show that the effect of knock-on

[1]*Manuscript received September 1, 1955.*
Contribution from the Division of Pure Physics, National Research Council, Ottawa, Canada. Issued as N.R.C. No. 3767.
[2]*National Research Laboratories Postdoctorate Fellow.*

electrons produced in water by the passage of protons moving with velocity below the critical velocity is negligible. A non-accidental anticoincidence with the arrangement of Fig. 1 thus indicates the passage of a heavy particle. We shall call R_1 the range equivalent to the apparatus and R_2 the residual range of a particle of velocity c/n. It is, thus, particles with ranges between R_1 and R_2 which will be of interest to us.

DESCRIPTION OF APPARATUS

In practice, it is necessary to collect a sufficient fraction of the light, due to the passage of a fast particle, at the photocathode of the phototube. It is also necessary to be sure that no light is emitted by fluorescence, excited by particles moving slowly through the tank. The refractive index of the liquid must be low enough to include between the limits R_1 and R_2 a sufficiently wide band of energies. These three requirements place stringent conditions on the substances to be used as Cerenkov radiators. One such suitable liquid is distilled water, the energy of protons corresponding to the range R_2 being then 480 Mev.

The absorption coefficient of water for light in the spectral region of the maximum response of the photocathode is such that 10% is absorbed in a path length of 3 meters (10). Studies of the spectral distribution of the Cerenkov light excited in water by the gamma rays from Co^{60} indicate that fluorescence is negligible (Rich and Slovaceck, 16). In this apparatus, the tank containing the water is made of brass, and two E.M.I. type 6262 phototubes are mounted in watertight glands, similar to those described by Harrison (9), at the center of opposite sides. The photocathodes of these tubes are of the end-window type, and also cover a strip $\frac{1}{2}$ in. wide around the periphery adjacent to the end. The tubes are therefore mounted so as to project $\frac{1}{2}$ in. into the tank.

The output pulses from the phototubes are applied to a conventional amplifier, of gain approximately 80, to which they are connected in parallel. At the output of this amplifier the pulses have a rise time of 1 μsec., and a duration of approximately 5 μsec. The inside surfaces of the tank are coated with a white waterproof paint, developed in the paint research laboratories of the National Research Council (Harris and Ogilvie (8)). Between the wavelengths 4250Å and 7000Å, the reflection coefficient of this paint is 94%, the pigment used being zinc oxide.

Examination of those pulses from the phototubes that are in coincidence with the Geiger counters shows that they have a considerable spread in amplitude, the average pulse corresponding to the emission of about 15 electrons from the cathode, Fig. 2. Since a μ meson, moving with a velocity c, emits 250 photons per cm., this indicates a collection efficiency of 6% per tube, compared to Duerden and Hyams value of 15% for a tank having a volume of 45% of this one and containing one multiplier, and agreeing closely with calculations based on the theory of Mando (12). In the present experiment two tubes were found to be necessary, and the combined gain of each, together with the following amplifier, is sufficient to deliver to the coincidence circuit a pulse from one photoelectron that will operate it.

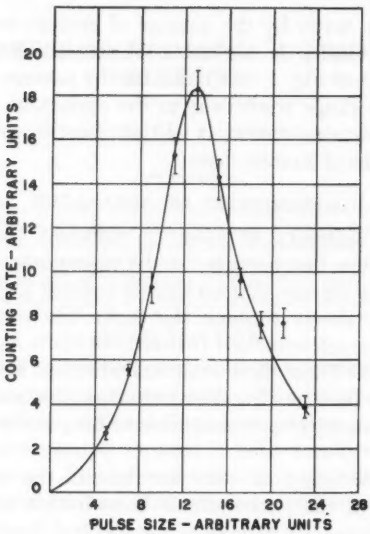

FIG. 2. Pulse height spectrum of pulses from the phototubes in coincidence with triple Geiger counter coincidences.

A block diagram of the apparatus is given in Fig. 3 in the form in which it was used to study the heavy particle beam. The circuits used were for the most part conventional, the coincidence mixer C_2, between the photo and Geiger tube circuits, where a large spread of input pulse sizes is encountered, being of the type described by Garwin (5). The Geiger counter trays were 16 in. square, and the extreme ones were separated by a distance of 21 in.

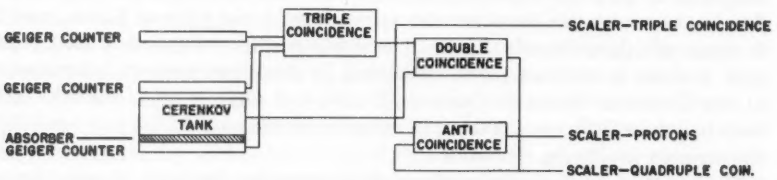

FIG. 3. Block diagram of the experimental arrangement.

ACCIDENTAL ANTICOINCIDENCES

An anticoincidence could occur because of an accidental triple coincidence, leading to too high a proton rate. Accidental quadruple coincidences can be neglected since they cannot be recorded as protons. The expression for the number of accidental coincidences between three counters is

$$3N_1N_2N_3T^2+2N_{12}N_3T+2N_{13}N_2T+2N_{23}N_1T$$

where T is the resolving time of the coincidence circuit and N_{12}, N_{13}, and N_{23} represent the real coincidence rates between pairs of counters. Owing to

the high efficiency of the Cerenkov counter for the detection of μ mesons, the contributions of the third and fourth terms are negligible, since in each case a particle must cross the tank, leading to a quadruple coincidence. The term in T^2 is likewise very small, with a triple coincidence circuit resolving time of 2 μsec. Experiments without the lead absorber below the tank (see below) show that a relativistic particle must cross only 20% of the depth of the tank to be recorded. The second term is thus the only one of interest to us, and it has been shown (15) to be small. As a further check on this the proton anticoincidence counting rate has been measured while the resolving time was varied, and the results indicate that accidental triple coincidences account for less than 5% of the proton counting rate where the resolving time is 2 μsec., as used in the measurements described here. They will, therefore, be neglected below.

RESULTS OF MEASUREMENTS

With the 1½ in. thick layer of lead below the Cerenkov tank, which is necessary to exclude slow μ mesons, the apparatus records particles with a mass greater than 550 electron masses and, in particular, protons in the energy range 230–480 Mev. It was decided to study the nature of the anticoincidence counts both by measuring their barometric pressure coefficient and by comparing the flux with the proton flux in this energy range, as measured by Mylroi and Wilson (14).

THE BAROMETER COEFFICIENT

The apparatus was run for a period of several months at Ottawa, (altitude 320 ft.), and the results of a linear correlation of counting rate with pressure are given in Table I below.

TABLE I

BAROMETER COEFFICIENT DETERMINATION

No. of readings (hourly)	940	348	476
Average pressure (mb.)	1003.54	999.13	1002.83
Counting rate per hour	47.1	47.15	45.28
Barometer coefficient, %/mb.	-0.58 ± 0.1	-0.78 ± 0.2	-0.63 ± 0.1

The weighted mean barometer coefficient is 0.64 ± 0.08% per mb.

An identical piece of equipment was also used in an aircraft at altitudes up to 25,000 ft., Ogilvie (15), and the absorption length determined. The result was 128 ± 12 gm./cm.^{2}, in agreement with the absorption length found by Tinlot (19) for the variation of penetrating shower rate with atmospheric depth. The results are set out in Table II, together with the pressure coefficient and corresponding absorption length obtained by Simpson (18) for the slow neutron component.

It will be noted that the pressure coefficients for protons obtained in the two different experiments are not equal. Such a small discrepancy could probably be explained by a change in the angular distribution of the protons with altitude.

TABLE II

ABSORPTION LENGTHS

Method	Pressure coefficient	Absorption length, gm./cm.^{2}
Slow neutrons (<700 gm./cm.^{2}) (18)	0.72±0.03	140±3
Protons, sea level	0.64±0.08	158±20
Protons, aircraft (15)	0.78±0.06 (calculated)	128±10

If we suppose the whole of the discrepancy between the sea level slow neutron and proton pressure coefficients to be due to the admixture of some slow μ mesons with the latter, taking the μ meson pressure coefficient to be $\backsim$0.15%/mb. (Rose, 17), the minimum proportion of protons is 85%. A plot of some results obtained during one of the barometer coefficient experiments is given in Fig. 4, showing daily mean values and the slope of the best-fit line.

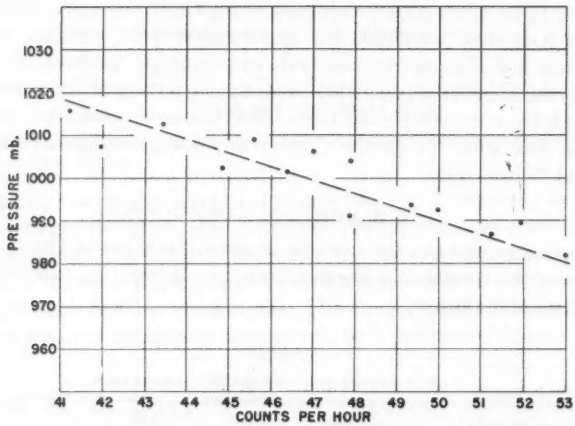

FIG. 4. Some results of pressure coefficient experiments. Daily mean results are plotted.

THE PROTON FLUX

The proton spectrum, obtained by Mylroi and Wilson (14), has been redrawn as a differential energy spectrum by Ballam and Lichtenstein (1). In the region of interest, 230 to 480 Mev. (700–1100 Mev./c), the proton flux is 3.03×10^{-5} particles/cm.^{2}/sec./steradian.

In the present experiments the observed anticoincidence rate was 46.9 per hour, when corrected to a barometric pressure of 1000 mb. This value is the mean of the results obtained during the pressure coefficient experiments, and during the same period the mean meson, triple coincidence, rate was 16,100 per hour. Thus, taking the absolute intensity of the vertical hard component, with 20 cm. of water and 3.8 cm. of lead in the telescope, as 9.0×10^{-3} particles/cm.^{2}/sec./steradian, we obtain an uncorrected value for the proton intensity of 2.62×10^{-5} particles/cm.^{2}/sec./steradian. Applying a correction

for the scattering loss between 230 and 350 Mev., as detailed by Ogilvie (15), amounting to $(19\pm5)\%$, we arrive at the value $3.14\pm0.15\times10^{-5}$ particles/cm.^{2}/sec./steradian, in agreement with Mylroi and Wilson (14). In view of the foregoing, we may conclude that the apparatus counts heavy particles, that it excludes slow μ mesons with high efficiency, and that a large proportion of the particles counted are protons.

An estimate for the proton flux in the energy region 150 to 230 Mev. can be derived, and at the same time an estimate of the minimum distance that a relativistic particle must move in the tank in order to be detected can be made.

The minimum energy required by a proton to pass through the telescope with no lead absorber in it being 150 Mev., in order to find the number of protons recorded in the range 150–480 Mev. we therefore require the counting rate with no lead absorber together with an estimate of the number of mesons which produce anticoincidences when no lead is present below the tank. If N_2 is the anticoincidence counting rate of the apparatus with the 3.8 cm. of lead absorber below the tank, and N_1 with it above the tank, then

N_1-N_2 = number of protons in the energy range 480 to 540 Mev. + number of such protons lost in the absorber owing to interactions $-N_m$.

Here N_m is the number of mesons counted as protons where the absorber is in the upper position, namely, those which are slowed by the absorber so as to be travelling with $\beta < 0.75$ for a large fraction of their path through the tank. The number of protons in the range 480 to 540 Mev., Mylroi and Wilson (14), accounts for approximately seven counts per hour. The observed counting rates with the lead in different positions are shown in Table III.

TABLE III

COUNTING RATES FOR DIFFERENT ABSORBER POSITIONS

Position of absorber	Counting rate, per hour
Above tank	$N_1 = 54.5$
Below tank	$N_2 = 41.6$
None	98.3

Thus $N_1-N_2 = 13$ counts per hour, and assuming that the number of protons lost in the 3.8 cm. Pb is small, $N_m = 6$ per hour approximately. Noting that the differential range spectrum of low energy mesons at sea level obtained by Lichtenstein (11) is closely constant in this region, to obtain the number of slow mesons recorded with no absorber, we need only multiply N_m by the ratio of the range intervals in the two cases. In this way we arrive at a counting rate of 80 protons per hour in the energy range 150 to 540 Mev., and thus 38 per hour in the region 150 to 230 Mev., $= 2.1\times10^{-5}$ particles/cm.^{2}/sec./steradian or 2.6×10^{-7} particles/cm.^{2}/sec./steradian/Mev.

From the value of N_m and the meson spectrum referred to above, we can deduce that the highest energy with which an undetected meson enters the

water from the absorber is about 80 Mev. ($\beta \approx 0.8$), and that it traverses one quarter of the tank before going below the Cerenkov threshold. It emits on the average about 120 photons per cm. in this path, a total of 600 photons. Thus a relativistic particle, emitting 250 photons per cm., must only traverse 15–20% of the depth of the tank, 20 cm., in order to be detected.

ABSORPTION CURVE

After these experiments had been performed, increasing quantities of lead were placed above the bottom Geiger-counter tray, which had been moved to about 8 in. below the bottom of the tank. The uncorrected column in Table IV shows the counting rates then obtained. When there is a large gap between the tank and the lower tray, the error due to accidental triple coincidences and showers increases, and the correction for them was found in the following way. The position of the bottom tray, and thus the solid angle, remained the same during the whole of the measurements of the absorption curve. Thus the anticoincidence rate in this position, P_2, should be equal to P_1T_2/T_1, where P_1 is the proton rate with the same quantity, 3.8 cm., of lead and the bottom tray immediately under the tank, and T_1 and T_2 are the triple coincidence counting rates. Actually $P_2 = P_1T_2/T_1+C$ where C respresents the accidental and shower correction. In this way it was found that $C = 12.5$ counts/hour. This will remain substantially the same as lead is added above the lower tray. In Table IV the counting rates for various thicknesses of lead

TABLE IV

ABSORPTION MEASUREMENTS

Inches of lead absorber	Uncorrected rate, hour^{-1}	Corrected rate, hour^{-1}
6.5	18.1±1.0	5.6±2
6	19.1±0.8	6.6±1.5
5.5	19.9±0.8	7.4±1.5
5	20.4±1	7.9±1.5
4.5	20.2±1	7.7±1.2
4	22.3±1	9.8±1.2
3.5	23.8±1	11.3±1
3	25.3±1	12.8±1
2.5	30.0±1	17.5±1
2	37.1±1	24.6±1
1.5	43.6±1	31.1±1

are given. The corrected rates, obtained by subtracting C from the observed rates, are shown in the table and plotted in Fig. 5. The rate of 31.1 counts per hour, in conjunction with a meson rate of 11,147 per hour, corresponds to a proton flux of $3.0\pm0.1\times10^{-5}$ particles/cm.^{2}/sec./steradian.

The range of protons of 480 Mev. in lead is 225 gm./cm.^{2} Thus, with a total absorber of 7.8 in. of lead equivalent comprising the telescope, tank, and lead absorber (6.5 in.), no protons should be counted. The residual rate, 5.6±2 counts/hour, equal to 15% of the proton flux, is provisionally assumed to represent an upper limit for the flux of deuterons in the appropriate energy range, 460 Mev. to 960 Mev.

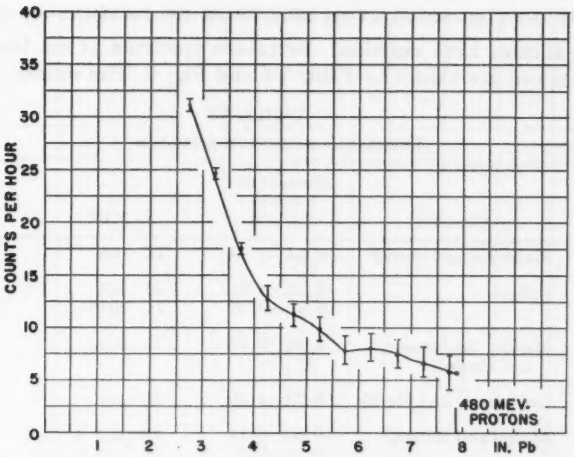

FIG. 5. Absorption curve for protons obtained with the apparatus.

The above procedure for obtaining C neglects scattering, which is the same in the two positions of the bottom tray, since the 3.8 cm. lead absorber is moved with it. It also assumes that the difference between the angular dependence of protons and mesons does not introduce an appreciable error. A set of measurements of the angular dependence of protons, made with an apparatus of the present type, gives a $\cos^n w$ law with n approximately equal to 3.

THE PROTON FLUX AT HIGHER ENERGIES

In order to obtain information about the proton spectrum at energies above 480 Mev., increasing quantities of lead were placed above the apparatus. The usual 1.5 in. of lead was in place below the tank. The results of these experiments are summarized in Table V.

TABLE V

COUNTING RATES WITH LEAD ABOVE THE APPARATUS

Inches of lead	Energy band, Mev.			Counting rate, hour^{-1}	Intensity, particles/cm.^{2}/ sec./sterad./Mev.
	Lower	Mean	Upper		
½	280	415	550	34.0±1	0.92×10^{-7}
1	300	437	575	32.0±1	0.915
1½	320	459	597	29.2±0.9	0.85
2	345	477	610	27.7±0.9	0.88
2½	370	500	630	23.8±0.9	0.81
3	395	522	650	22.8±0.8	0.82
3½	415	542	670	21.9±0.8	0.83
4	440	565	690	19.5±0.8	0.80
4½	465	582	700	18.1±0.8	0.81

N.B.—Intensity corrected on the basis of the absorption length in Pb being 300 gm./cm.^{2} (Bernardini et al. (2) and George and Jason (6)).

THE DIFFERENTIAL MOMENTUM SPECTRUM OF PROTONS AT SEA LEVEL

Several authors have examined the proton spectrum at sea level and the results obtained are shown in Table VI and Fig. 6. The results up to 1952

TABLE VI

THE PROTON MOMENTUM SPECTRUM

No.	Observer	Momentum interval, $\times 10^{-9}$ ev./c	$I_v \times 10^8$	Date
1	Rochester and Bound*	0.34 –0.40	14 ±5	1940
2	Ballam	0.42 –0.91	30 ±8	
		0.51 –0.96	31 ±14	
3	Merkle, Goldwasser, and Brode	0.48 –0.88	23 ±3	1950
4	Goldwasser and Merkle	0.78 –1.10	20 ±5	1951
5	Mylroi and Wilson*	0.53 –0.71	20 ±5.3	1951*
		0.71 –0.93	10.7±1.9	
		0.93 –1.35	6.6±1.1	
6	York	0.55 –0.75	28 ±3	1952
		0.75 –0.88	10.7±0.8	
7	Filthüth†	0.18 –0.21	2.2±0.3	1954
		0.21 –0.236	$3.7^{+0.5}_{-0.1}$	
		0.236–0.26	$3.3^{+0.5}_{-0.1}$	
		0.275–0.312	6.5±0.7	
		0.332–0.358	8.0±1	
		0.432–0.446	8.3±1	
		0.456–0.469	11 ±1	
		0.615	10.0±1	
		0.730	8.4±1	
		0.887	4.8±1	
8	Ogilvie‡	0.59 –0.70	14 ±4	1955
		0.70 –1.10	7.8±1	
		0.85 –1.240	6.5±0.5	
		0.95 –1.300	6.0±0.7	
		1.050–1.400	5.5±0.7	

Corrected by York (20).

†Uncorrected for absorption and production of secondary protons. This would increase three high energy points by about 20%.

‡Not all points given in Table V are plotted, in interest of clarity.

have been discussed by York. Those of Ballam; Merkle, Goldwasser, and Brode (13); and Goldwasser and Merkle (7) are early measurements. The other points divide themselves into two classes, namely, those due to Filthüth (4), and the others. Both suggest a maximum in the region of 500 to 600 Mev./c, but since the results of Filthüth constitute almost the only information available below about 500 Mev./c, it is worth while enquiring as to the cause of the discrepancy between the two classes at higher energies, amounting to a factor of about two. In view of the good agreement between the results of

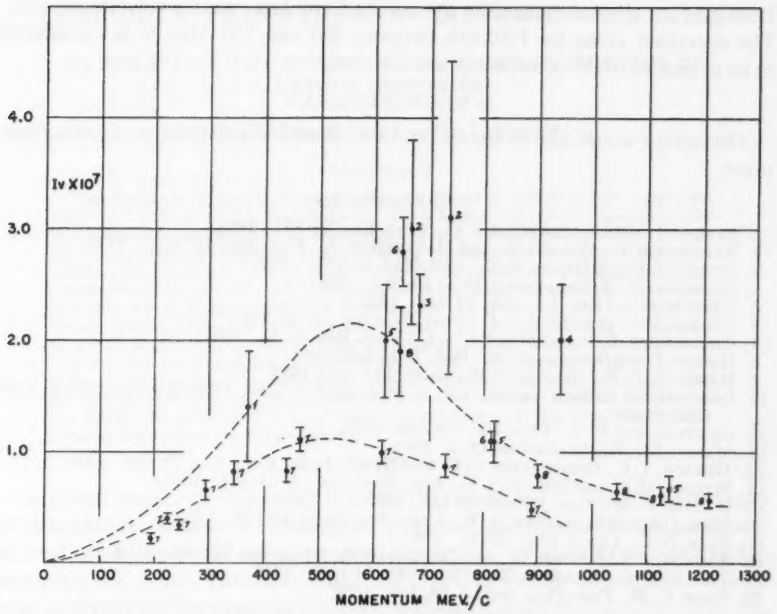

FIG. 6. The differential momentum spectrum of protons. Numbered points refer to Table V.

Mylroi and Wilson, York, and the present author, we shall consider the experiment of Filthüth to see if a possible systematic error might be found.

The value of the proton intensity, I_P, in this type of experiment is given by

$$I_P = \frac{C_P}{C_m} \frac{I_m}{\Delta E}$$

where I_m is the meson intensity, and C_m and C_P are the meson and proton counting rates under the same conditions. ΔE is the energy (momentum) range covered by the experiment. Thus an accurate knowledge of ΔE is decisive for the determination of the proton intensity, but a careful consideration leads Filthüth to the conclusion that his points would not be in error owing to this cause by more than 10%. Since the whole curve drawn through the points marked 7 in Fig. 6 appears to be displaced in the direction of lower intensities, the cause must be at least approximately independent of incoming proton momentum. An estimate of the scattering of protons by the absorbers in the experimental arrangement used by Filthüth indicates that scattering might be sufficiently large to account for the observed discrepancy.

CONCLUSIONS

The momentum spectrum of protons at sea level is considered to agree with that given by Mylroi and Wilson in the momentum range between 600 and

1250 Mev./c, when measured by means of a Cerenkov counter velocity selector. The spectrum given by Filthüth between 200 and 700 Mev./c is considered to be displaced in the direction of low intensity.

ACKNOWLEDGMENT

The author would like to thank Dr. D. C. Rose for discussion and encouragement.

REFERENCES

1. BALLAM, J. and LICHTENSTEIN, P. G. Phys. Rev. 93: 851. 1954.
2. BERNARDINI, G., CORTINI, G., and MANFREDINI, A. Phys. Rev. 76: 1792. 1949.
3. DUERDEN, T. and HYAMS, B. D. Phil. Mag. 43: 717. 1952.
4. FILTHÜTH, H. Z. Naturforsch. Pt.a., 10: 219. 1955.
5. GARWIN, R. L. Rev. Sci. Instr. 24: 618. 1953.
6. GEORGE, E. P. and JASON, A. C. Proc. Phys. Soc., A, 62: 243. 1949.
7. GOLDWASSER, E. L. and MERKLE, T. C. Phys. Rev. 83: 43. 1951.
8. HARRIS, J. and OGILVIE, K. W. 1955. To be published.
9. HARRISON, F. B. Nucleonics, 10 (No. 6): 40. June, 1952.
10. International Critical Tables. Vol. 5. McGraw-Hill Book Company, Inc., New York. 1929. p. 269.
11. LICHTENSTEIN, P. G. Phys. Rev. 93: 858. 1954.
12. MANDO, M. Nuovo cimento, 12: 5. 1954.
13. MERKLE, T. C., GOLDWASSER, E. L., and BRODE, R. B. Phys. Rev. 79: 926. 1950.
14. MYLROI, M. G. and WILSON, J. G. Proc. Phys. Soc., A, 64: 404. 1951.
15. OGILVIE, K. W. Can. J. Phys. 33: 555. 1955.
16. RICH, J. A. and SLOVACECK, R. E. J. Opt. Soc. Amer. 43: 750. 1953.
17. ROSE, D. C. Can. J. Phys. 29: 97. 1951.
18. SIMPSON, J. A., FONGER, W., and TREIMAN, S. B. Phys. Rev. 90: 934. 1953.
19. TINLOT, J. H. Phys. Rev. 73: 1476. 1948; 74: 1197. 1948.
20. YORK, C. M. Proc. Phys. Soc., A, 65: 559. 1952.

FORBIDDEN TRANSITIONS IN DIATOMIC MOLECULES

IV. THE $a'^1\Sigma^+ \leftarrow X^1\Sigma^+$ AND $e^3\Sigma^- \leftarrow X^1\Sigma^+$ ABSORPTION BANDS OF CARBON MONOXIDE[1]

By G. Herzberg and T. J. Hugo[2]

ABSTRACT

Two examples of forbidden electronic transitions in heteronuclear molecules, $^3\Sigma^+ - {}^1\Sigma^+$ and $^3\Sigma^- - {}^1\Sigma^+$, are studied in the spectrum of the CO molecule. The bands have been obtained in absorption in the region 1750 to 1230 Å with absorbing paths up to 400 cm-atm., using the fourth and fifth orders of a 3 meter vacuum spectrograph. In most of the $^3\Sigma^+ - {}^1\Sigma^+$ bands all four predicted branches are observed. For the $^3\Sigma^- - {}^1\Sigma^+$ bands, a somewhat unusual structure is predicted: two branches of O and S form and three branches of Q form. In the best-resolved bands, four branches are observed which closely fit the predicted branches, two of the Q branches being very nearly coincident and unresolved in the present spectra. The rotational and vibrational constants of the upper states, $a'^1\Sigma^+$ and $e^3\Sigma^-$, of the two band systems have been determined. Some of these data had previously been obtained from perturbations in other band systems of CO. On the whole, the perturbation data agree satisfactorily with the more precise data obtained directly in the present study.

A. INTRODUCTION

In earlier papers of this series (13, 15, 17), examples of four different types of forbidden transitions of *homonuclear* molecules were discussed and analyzed. Several other types had been discussed previously by various authors (for a summary see (16)). Thus far, only two types of forbidden transitions have been analyzed for *heteronuclear* diatomic molecules, viz., $^3\Pi - {}^1\Sigma^+$ and $^4\Sigma^- - {}^2\Pi$. The best-known example of a $^3\Pi - {}^1\Sigma^+$ transition is the Cameron bands of CO first observed in absorption and recognized as a $^3\Pi - {}^1\Sigma^+$ transition by Hopfield and Birge (19) and later analyzed in detail by Gerö, Herzberg, and Schmid (10), Gerö (8), and Rao (22). Several other examples of this type are known, particularly for heavier molecules for which the selection rule $\Delta S = 0$ is less strong. The only example of a $^4\Sigma^- - {}^2\Pi$ transition is the red bands of GeH analyzed recently by Kleman and Werhagen (20).

In an investigation of the ultraviolet absorption spectrum of carbon monoxide under high resolution, we have analyzed examples of two further types of forbidden transitions of heteronuclear diatomic molecules, namely $^3\Sigma^+ - {}^1\Sigma^+$ and $^3\Sigma^- - {}^1\Sigma^+$.

The absorption spectrum of CO in the vacuum ultraviolet was previously investigated by Leifson (21) and Hopfield and Birge (19). Leifson (21) observed only the simple progression of the fourth positive group starting at 1546 Å while Hopfield and Birge, with higher resolution and longer absorbing paths, observed a number of additional band systems including the very much weaker Cameron bands[3] which start at 2063 Å. Between the start of the

[1] *Manuscript received August 19, 1955.*
Contribution from the Division of Pure Physics, National Research Council, Ottawa, Canada. Issued as N.R.C. No. 3778.

[2] *National Research Laboratories Postdoctorate Fellow, on leave of absence from the South African Council for Scientific and Industrial Research.*

[3] *Unfortunately the work of Hopfield and Birge has never been fully published. However, through the courtesy of Professor Birge, one of us (G.H.) received many years ago prints of their fine spectrograms.*

Cameron bands and that of the fourth positive group, they observed another very weak progression which they designated $a'-X$ to distinguish it from the Cameron bands $a-X$. Later, Asundi (1) found in the red and infrared the $a'-a$ transition (Asundi bands). From work on these bands and perturbations in other emission bands in the visible and ultraviolet regions, it was shown by various authors (4, 25, 2, 11) that the a' state is a $^3\Sigma^+$ state.

The dispersion used by Hopfield and Birge was not sufficient to resolve the $a'-X$ bands nor to follow them through the much stronger $A-X$ (fourth positive) bands. This was done in the present investigation and in this way an example of a $^3\Sigma^+-{}^1\Sigma^+$ transition is supplied. In addition, a new weak absorption band system was found among the much stronger bands of the fourth positive group. The bands of this new system have a very peculiar structure and have been assigned to a $^3\Sigma^--{}^1\Sigma^+$ transition. The upper state is identical with the $e^3\Sigma^-$ state whose existence had already been derived from perturbations in the $A^1\Pi$ state by Coster and Brons (4) and Schmid and Gerö (26).[4] Much improved rotational and vibrational constants of both the $a'^3\Sigma^+$ and the $e^3\Sigma^-$ states have been derived.

B. EXPERIMENTAL

The absorption spectrum of CO was photographed in the fourth and fifth orders of the 3 meter vacuum spectrograph previously described (3). The reciprocal dispersion was 0.63 and 0.50 Å/mm., respectively. The light source, as previously, was a Lyman discharge through argon at 70 mm. pressure. The lower orders were eliminated by the use of an LiF prism (5, 3).

For most spectra an absorption tube of 40 cm. length was used which was filled with CO at pressures ranging from 7 to 760 mm. In order to obtain longer path lengths for the weaker bands of the forbidden transitions, the whole spectrograph was filled with CO to a pressure of 400 mm., thus reaching an absorbing path of 400 cm-atm.

A few experiments were also carried out with an absorption tube of 20 cm. length entirely cooled by liquid nitrogen. A diagram of this tube is shown in Fig. 1. Considerable difficulty was experienced in obtaining a tight seal

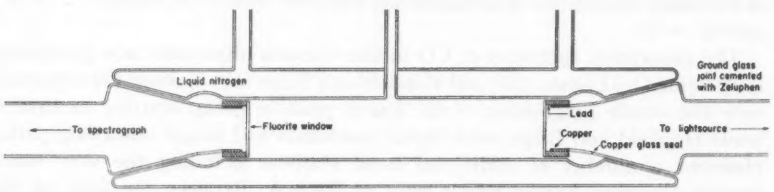

FIG. 1. Low temperature absorption tube.

between the LiF windows and the absorption tube at low temperature because of the difference in the coefficients of expansion of LiF and the material of the tube. This difficulty was finally overcome by using Cu-glass joints, the Cu

[4]*This state should not be confused with the state called e in Fig. 197 of Ref. (14). The latter is the upper state of the Kaplan bands and should perhaps be renamed f.*

part of which was fused to a lead cylinder which in turn was sealed by Zeluphen cement (supplied by Zeh and Company, Chemische Fabrik, Ludwigsburg, Württ., Germany) to the windows.

As in the previous work on oxygen (3), Fe lines of second order served as wavelength standards. The wavelengths were converted to vacuum by means of Edlén's tables (6) except in the case of the exposures with CO in the spectrograph. For these exposures, since the index of refraction of CO in the vacuum region is not known, a correction curve was established from spectral features that could be measured accurately both with a proper absorption tube and with CO in the spectrograph. This method introduces an uncertainty of up to 1 cm^{-1} in the absolute values of some wave numbers, but the relative accuracy is estimated to be well within 0.1 cm^{-1}.

The most conspicuous feature of the absorption spectrum of CO in the region 1800 to 1200 Å is the $v'' = 0$ progression of the fourth positive system. This progression masks a considerable part of the region at the absorbing paths necessary to observe the forbidden transitions. In addition, the $v'' = 1$ progression of the fourth positive system which appears with considerable intensity overlaps a number of the forbidden bands. It was the object of the low temperature absorption spectra to reduce this overlapping by eliminating completely the $v'' = 1$ progression of the fourth positive system and by reducing the extent of the individual bands of the $v'' = 0$ progression. In this way, some of the new bands could be recognized much more clearly. However, most of the measurements were made from the plates taken at normal temperature since these plates were of a somewhat better quality.

C. THE $a'\,^3\Sigma^+ - X\,^1\Sigma^+$ SYSTEM

The $a'^3\Sigma^+ - X^1\Sigma^+$ transition of CO forms one of the band systems known as the Hopfield–Birge bands. These bands, as mentioned earlier, were discovered in absorption by Hopfield and Birge (19). They assigned the first band observed by them, at 58927 cm^{-1}, as the 0–0 band of the system. On the basis of an additional band found by Birge at 57763 cm^{-1}, Estey (7) raised the vibrational quantum numbers in the $a'^3\Sigma^+$ state by one unit. The final assignment was deduced by Beer (2) from rotational perturbations in the $b^3\Sigma^+ - a^3\Pi$ system caused by the $a'^3\Sigma^+$ state. According to the perturbation data, the vibrational quantum numbers proposed by Hopfield and Birge have to be raised by three units. The expected position of the 0–0 band is then at 55380 cm^{-1}. Some fairly accurate data about the rotational structure of the $a'^3\Sigma^+$ state have already been obtained by Gerö (9) and Gerö and Lörinczi (11) from a study of the fine structure of a few of the Asundi bands $a'^3\Sigma^+ - a^3\Pi$. In addition, from the numerous perturbations produced by the $a'^3\Sigma^+$ state in the $A^1\Pi$, $b^3\Sigma$, and $a^3\Pi$ states, Schmid and Gerö (25) and Beer (2) have obtained further information about the constants of the $a'^3\Sigma^+$ state. Beer (2) gives $B_e = 1.320$ cm^{-1}, $\alpha = 0.0135$ cm^{-1}, $\omega_e = 1210$ cm^{-1}, $\omega_e x_e = 9.5$ cm^{-1} while Gerö and Lörinczi (11) give $B_e = 1.331$ cm^{-1} and $\alpha = 0.016$ cm^{-1}.

In the present investigation, the $a'^3\Sigma^+$ state is reached in absorption from the ground state $X\,^1\Sigma^+$. A single long v'-progression (with $v'' = 0$) of single-

TABLE I

BAND HEADS, BAND ORIGINS, AND B_v VALUES OF THE $a'\,^3\Sigma^+ - X\,^1\Sigma^+$ SYSTEM

$v'-v''$	Band head (cm^{-1})	Intensity	Band origins, ν_0 (cm^{-1})			$B_{v'}$ values (cm^{-1})			Remarks
			Observed	From perturbations	Calculated	Observed	From perturbations	Calculated	
0–0	55363	0		55380	55353.91		1.31	1.3360	Fine structure too weak to measure
1–0	56570	0			56562.77			1.3177	Fine structure too weak to measure
2–0	57756	1	57750.16		57750.23	1.2995		1.2997	
3–0	58922	2	58916.49		58916.69	1.2823		1.2821	
4–0	60068	4	60062.64		60062.50	1.2658		1.2648	Rotational perturbation by $v = 7$ $a\,^3\Pi$ level at $J \simeq 20$
5–0	61192	8	61187.65		61187.99	1.2478		1.2477	
6–0	62299	20	62293.64		62293.47	1.2307		1.2309	
7–0	63384	40	63379.44		63379.22	1.2140		1.2143	
8–0			(64446.8)[a]		64445.48	(1.195_0)[a]		1.1979	Masked by 0–0 $A\,^1\Pi - X\,^1\Sigma^+$
9–0	65495	80	65492.28		65492.48	1.1816[b]		1.1816	
10–0	66523	100	66520.39	66525	66520.41	1.1655[b]	1.17	1.1654	
11–0			(67529.2)[a]		67529.44	(1.147_0)[a]		1.1494	Masked by 2–0 $A\,^1\Pi - X\,^1\Sigma^+$
12–0	68522	80			68519.71			1.1334	
13–0	69494	100	69491.25	69480	69491.32	1.117_8	1.13	1.1174	Overlapped by 3–0 $A\,^1\Pi - X\,^1\Sigma^+$
14–0					70444.37			1.1014	Masked by 4–0 $A\,^1\Pi - X\,^1\Sigma^+$
15–0				71339	71378.91		1.10	1.0854	Masked by 5–0 $A\,^1\Pi - X\,^1\Sigma^+$
16–0	72298	50	72295.14	72234	72294.96	1.0692	1.09	1.0693	Overlapped by 7–1 $A\,^1\Pi - X\,^1\Sigma^+$
17–0	73194	50			73192.54			1.0532	Overlapped by 6–0 $A\,^1\Pi - X\,^1\Sigma^+$ and 11–0 $d\,^3\Pi - X\,^1\Sigma^+$
18–0				73995	74071.60		1.07	1.0369	Masked by 7–0 $A\,^1\Pi - X\,^1\Sigma$ and 12–0 $d\,^3\Pi - X\,^1\Sigma^+$
19–0	74934	30	74932.04	74883	74932.10	1.0206	1.06	1.0204	
20–0	75776	20	75773.91	75753	75773.96	1.003_7	1.06	1.0038	
21–0					76597.06			0.9869	Masked by 9–0 $A\,^1\Pi - X\,^1\Sigma^+$
22–0	77408	20			77401.27			0.9698	Overlapped by 10–0 $A\,^1\Pi - X\,^1\Sigma^+$
23–0	78186	10	78184.8	78165	78186.43	0.95_8	1.00	0.9524	Overlapped by 10–0 $A\,^1\Pi - X\,^1\Sigma^+$

[a] *From the Asundi bands according to Gerö and Lörinczi (11).*
[b] *Gerö and Lörinczi (11) give* $B_9 = 1.178_9\ cm^{-1}$, $B_{10} = 1.163_1\ cm^{-1}$.

PLATE I

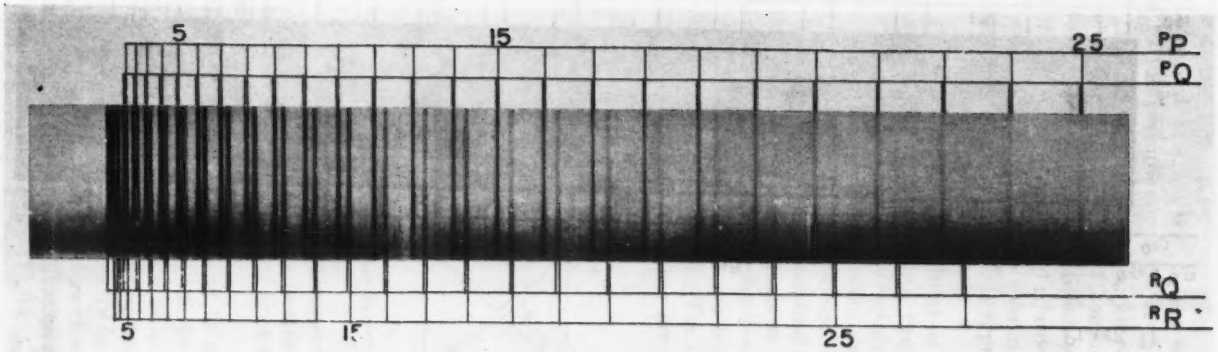

FIG. 2. The 5–0 band of the $a'\,^3\Sigma^+ - X\,^1\Sigma^+$ system. ($\lambda_A = 1634.2$ Å.)

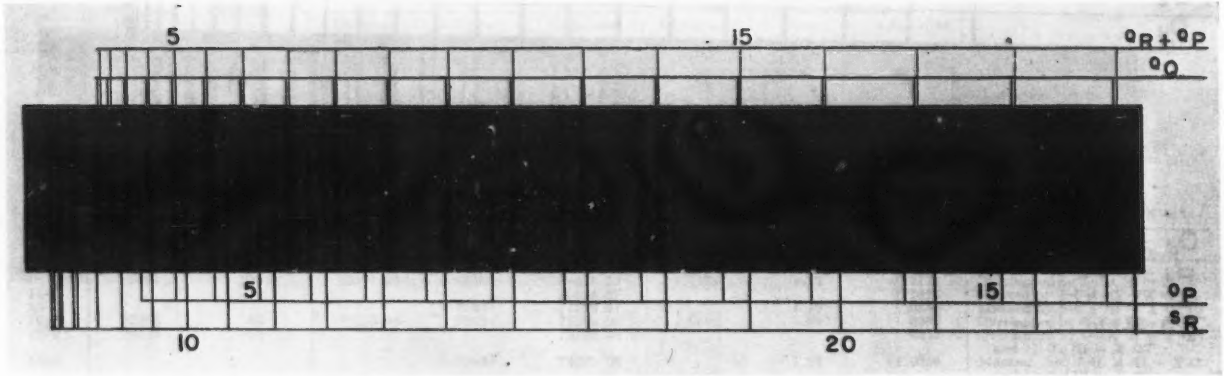

FIG. 3. The 3-0 band of the $e\,^3\Sigma^- - X\,^1\Sigma^+$ system. ($\lambda_A = 1471.0$ Å.)

headed, red-degraded bands is observed. It starts with a very weak band at 55363 cm^{-1}, which, according to the perturbation data, is the 0–0 band. The intensity increases fairly rapidly to shorter wavelengths, reaches a flat maximum at about the 15–0 band, and then drops again. The last band that could be observed under the available experimental conditions was the 23–0 band at 78190 cm^{-1}. The band heads, with their estimated relative intensities, are listed in Table I. The absorption intensity of the overlapping fourth positive system, which is an allowed electronic transition, is approximately a thousand times higher.

In Fig. 2 a greatly enlarged spectrogram of the 5–0 band at 1632.4 Å is reproduced. It shows clearly the presence of four branches, two P branches and two R branches giving the appearance of a doublet structure. At shorter wavelengths, because of the smaller wave number dispersion, the doublet P branches (which have the smaller splitting) are no longer resolved.

The observed structure of the bands is immediately understood on the basis of the diagram Fig. 4 which indicates the possible transitions on the basis of electric dipole selection rules. According to the selection rules $+ \leftrightarrow -$, $\Delta J = 0, \pm 1$ we obtain two branches of R form ($\Delta N = +1$) and two branches of P form ($\Delta N = -1$), but no branches of Q form ($\Delta N = 0$). The designations of the branches follow from the values of ΔJ and ΔN. They are (see Fig. 4)

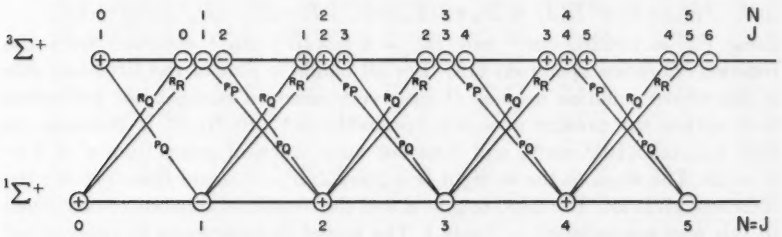

FIG. 4. Branches of a $^3\Sigma^+ - {}^1\Sigma^+$ band. The quantum number N was formerly called K.

^RR, ^RQ, ^PP, ^PQ, the two Q branches having R and P form respectively. The structure of the bands is entirely similar to that of the atmospheric oxygen bands ($^1\Sigma_g^+ - {}^3\Sigma_g^-$) except that the symmetries are reversed since the oxygen bands represent a magnetic dipole transition with $+ \leftrightarrow -$.

As shown by Fig. 4, the separation of the branches ^PQ and ^PP corresponds to the separation of the sublevels F_1 and F_2 of the $^3\Sigma^+$ state while the separation of ^RQ and ^RR corresponds to the separation of F_2 and F_3 just as in the case of the O_2 bands. The order of the levels F_1, F_2, F_3, corresponding to $J = N+1$, N, $N-1$ respectively, is normally not that shown for simplicity in Fig. 4, but F_2 lies either below or above the two others which, in turn, are close together. Which case applies here can be ascertained from the combination differences: only $^RR(J-1) - {}^PP(J+1)$ and not $^RQ(J-1) - {}^PQ(J+1)$ give $\Delta_2 F''$ values that agree with those known for the ground state. In this way, the numbering given in Fig. 2 was established.

As in other $^3\Sigma$ states, the triplet splitting is very nearly constant for N values above 5. Near the band origin, for $N < 5$, the bands are not well resolved and the deviations from a constant value, expected from the Schlapp (24) formulae, cannot be detected. However, Gerö and Lörinczi (11) from the analysis of the Asundi bands have established the variation at low N. The sum of the splittings in corresponding members of P and R branches gives the constant $2\lambda+\gamma$ (see (15)). In the present case, this constant is found to be -2.37 ± 0.05 cm^{-1} for $v' = 2$ and -2.13 ± 0.25 for $v' = 19$, that is, unlike the case of the $A^3\Sigma_u^+$ and $B^3\Sigma_u^-$ states of O_2 (15, 3), there is only a very slight, if any, change of λ with vibrational quantum number. The negative sign of $2\lambda+\gamma$ indicates that, unlike the ground state of O_2, the F_1 and F_3 levels are above F_2 with F_3 the highest.

In Table II are given the wave numbers of the lines of all $a'-X$ bands that could be measured with reasonable accuracy. Lines marked by an asterisk are blends or are very faint and are therefore not as accurately determined as the others.

Because of the unfavorable wave number dispersion in the vacuum region, the accuracy with which the rotational constants B'' and D'' of the lower state could be determined is much inferior to that obtained from infrared and microwave spectra. Therefore, no attempt was made to evaluate them. Rather, the B' and D' values were determined from the combination sums

$$^RR(J-1)+{}^PP(J) = 2\nu_0+2(B_v'-B_v'')\,J^2-(D_v'-D_v'')\,J^2(J^2+1)$$

using $B_0'' = 1.9226_5$ cm^{-1} and $D_0'' = 6.4_5\times10^{-6}$ cm^{-1} obtained from the rotation–vibration spectrum (18). For all bands, a plot of the left-hand side of the above equation against J^2 gave very nearly a straight line indicating that within the present accuracy (probably $\pm1\times10^{-6}$), D' is the same as D_0'', i.e., 6.5×10^{-6} cm^{-1}, and does not vary much in going from $v' = 2$ to $v' = 23$. The slope of the straight line gives $2(B'-B'')$ and therefore B'; the intercept gives $2\nu_0$. The band origins ν_0 and the rotational constants determined in this way are included in Table I. The ν_0 and B_v values can be represented by the following two equations:

$$\nu_0 = 55823.0_7+1230.65_1(v'+\tfrac{1}{2})-11.013_0(v'+\tfrac{1}{2})^2 +0.0737_8(v'+\tfrac{1}{2})^3-0.0011_5(v'+\tfrac{1}{2})^4-1081.74,$$

$$B_v = 1.3453-0.0187_2(v+\tfrac{1}{2})+0.00020_5(v+\tfrac{1}{2})^2-0.000005_1(v+\tfrac{1}{2})^3.$$

Here the quantity 1081.74 cm^{-1} is the zero point energy in the ground state of CO. The ν_0 and B_v values calculated from these equations as well as the values obtained by Schmid and Gerö (25) and Beer (2) from the perturbation data are included in Table I for comparison with the observed values.

Even though the $a'^3\Sigma^+$ state causes many perturbations in the $A^1\Pi$, $a^3\Pi$, and $b^3\Sigma^+$ states, only one clear perturbation was found in it, namely in the $v' = 4$ level at $J' \approx 20$. The perturbing state is the $v = 7$ level of the $a^3\Pi$ state which has not been observed directly. The reason for the apparent absence of the other perturbations in the $a'-X$ bands is the fact that these perturbations occur mostly at high J values which were not observed in absorption.

TABLE II

WAVE NUMBERS OF THE LINES IN THE $a'\,^3\Sigma^+ - X\,^1\Sigma^+$ SYSTEM OF CO

J	$R(J)$	$P(J)$	$^RQ(J)$	$^PQ(J)$	$R(J)$	$P(J)$	$^RQ(J)$	$^PQ(J)$
	2–0 band, $\lambda_{\text{Å}}$ = 1731.4 Å				3–0 band, $\lambda_{\text{Å}}$ = 1697.2 Å			
0	57753.02*				58919.18*			
1	754.29*		57755.78*		920.54*	58912.81*	58922.11*	58913.39
2	754.29*		755.78*		920.54*	907.62*	922.11*	908.48
3	753.02*	57734.99	754.29*	57735.95*	919.18*	901.23*	920.54*	902.23*
4	750.73	—	752.06	728.30*	916.63	893.52*	918.07	894.76*
5	747.03	718.53	748.43	719.48	912.81*	884.56*	914.21	885.79*
6	742.13	708.44	743.51	709.39	907.62*	874.32*	908.98	875.49*
7	735.95*	697.09	737.38	698.08	901.23*	862.77*	902.52*	863.99*
8	728.57*	684.58	730.00	685.53	893.52*	849.95*	894.76*	851.17*
9	720.04	670.74	721.40	671.75	884.56*	835.83*	885.79*	837.04*
10	710.15	655.68	711.51	656.68	874.32*	820.49*	875.49*	821.68*
11	699.05	639.35	700.37	640.37	862.77*	803.80*	863.99*	805.06*
12	686.68	621.84	688.04	622.83	849.95*	785.88*	851.17*	787.03*
13	673.06	603.04	674.40	604.07	835.83*	766.64*	837.04*	767.83*
14	658.18	583.00	659.51	584.04	820.49*	746.13*	821.68*	747.32*
15	642.05	561.66	643.40	562.75	803.80*	724.36*	805.06*	725.56*
16	624.71	539.12	626.05	540.18	785.88*	701.28*	787.03*	702.50*
17	606.06	515.43	607.46	516.46	766.64*	677.00*	767.83*	678.14
18	586.19*		587.62*		746.13*	651.47	747.32*	652.54
19					724.36*	624.55	725.56*	625.68
20					701.28*	596.45	702.50*	597.51
21					677.00*	566.95		568.02
	4–0 band, $\lambda_{\text{Å}}$ = 1664.8 Å				5–0 band, $\lambda_{\text{Å}}$ = 1634.2 Å			
0	60065.05*							
1	066.41*		60068.15*		61191.29*	61183.55*	61192.50*	61184.28
2	066.41*	60053.76*	068.15*	60054.50	191.29*	178.44*	192.50*	179.21
3	065.05*	047.22*	066.41*	048.19	189.53	172.01	—	172.77
4	062.22	039.49*	063.65	040.50	186.58	164.19	187.85	164.89
5	058.15	030.25*	059.59	031.44	182.37	154.89	183.55	155.66
6	052.81	019.75*	054.15	021.06	176.76	144.29	177.93*	145.13
7	046.08	008.06	047.55	009.34	169.80	132.45	170.96	133.18
8	038.12	59995.09	039.49*	59996.31	161.51	119.13	162.70	119.92
9	028.85	980.78	030.25*	982.02	151.86	104.47	153.07	105.26
10	018.24	965.12	019.75*	966.32	140.82	088.54	142.04	089.30
11	006.28	948.10	007.68	949.31	128.50	071.20	129.69	071.94
12	59993.07	929.85	59994.40	931.12	114.80	052.45	115.96	053.24
13	978.49	910.22	979.79	911.58	099.72	032.40	100.93	033.28
14	962.64	889.33	963.89	890.64	083.27	011.07	084.52	011.89
15	945.41	867.10	946.66	868.41	065.48	60988.31	066.77	60989.17
16	927.00	843.58	928.12	844.91	046.42	964.24	047.66	965.12
17	907.30	818.76	908.30	820.27	025.96	938.82	027.24	939.74
18	886.39	792.68	887.16	793.59	004.10	912.05	005.39	912.96
19	864.70*	765.30	864.70*	766.42	60980.96	883.97	60982.24	884.80
20	836.61	736.78	840.93	737.76	956.41	854.43	957.76	855.37
21	813.44	707.69*	815.92	707.69*	930.54	823.66	931.88	824.53
22	787.55	671.73	789.47	676.88	903.32	791.48	904.22	792.39
23	760.24	640.94	762.04	643.75	874.73	757.99	876.00	758.92
24		607.40		610.27	844.83	723.16	846.14	724.09
25					813.49*		814.92*	
	6–0 band, $\lambda_{\text{Å}}$ = 1605.2 Å				7–0 band, $\lambda_{\text{Å}}$ = 1577.7Å			
0								
1	62297.08*	62289.85	62298.63*	62290.85			63384.15*	63376.20
2	297.08*	284.51	298.63*	285.51	63382.33*		384.15*	370.85
3	294.98*	277.92	—	278.92	380.43	63363.58	382.33*	364.29
4	292.06	269.96	293.49	270.96	377.23	355.63	378.73	356.29
5	287.43	260.61	288.94	261.61	372.65	346.23	373.93	346.78
6	281.80	249.83	283.07	250.83	366.59	335.16	367.91	335.87
7	274.60	237.67	275.87	238.67	359.18	322.77	360.36	323.50
8	265.97	224.11	267.26	225.11	350.27	308.99	351.44	309.77
9	256.00	209.27	257.27	210.27	340.00	293.86	341.10	294.62
10	244.62	192.90	245.89	193.90	328.20	277.15	329.41	278.01
11	231.85	175.22	233.13	176.16	314.99	259.30	316.27	260.11
12	217.64	156.19	218.97	157.11	300.38	239.69	301.66	240.75
13	202.08	135.76	203.08	136.65	284.41	218.94	285.61	219.85
14	185.20	113.89	186.52	114.90	267.03	196.76	268.15	197.67
15	166.86	090.72	168.19	091.74	248.11	173.07	249.35	173.94
16	147.19	066.12	148.57	067.11	227.83	148.04	229.19	148.98
17	126.10	040.16	127.48	041.13	206.05	121.39	207.54	122.35
18	103.64	012.83	105.04	013.81	183.10	093.72	184.35	094.58
19	079.77	61984.06	081.14	61985.08	158.45	064.05	160.09	065.21
20	054.52	953.97	055.90	955.04	132.78		134.14	034.21
21	027.93	922.52	029.29	923.52	103.55			001.81
22	61999.86	889.64	001.31	890.68				
23	970.50	855.38	61971.87	856.48				
24	939.78	819.78	941.06	820.79				
25	907.57		908.91					
26	873.93		875.37					

TABLE II (*concluded*)

WAVE NUMBERS OF THE LINES IN THE $a' {}^3\Sigma^+ - X {}^1\Sigma^+$ SYSTEM OF CO (*concluded*)

J	$R(J)$	$P(J)$[5]	$^RQ(J)$	$^PQ(J)$[5]	$R(J)$	$P(J)$[5]	$^RQ(J)$	$^PQ(J)$[5]
	9–0 band, λ_A = 1526.7 Å				10–0 band, λ_A = 1503.2 Å			
0								
1		65489.21*						
2	65494.83*	484.06*		65485.53*	66522.71			
3	492.87	477.08*	65494.40*	477.66*	520.63			
4	489.21*	468.03	490.60	469.04	516.87		66518.12	
5	484.06*	458.15	485.53*	459.15	511.66	66485.90	512.79	66486.81*
6	477.66*	447.01	479.18	448.02	504.93	474.41	—	475.46*
7	469.72	434.26	470.94	435.30	496.60	—	—	462.57*
8	460.27	419.96	461.51	420.96	486.81*	447.10	487.94	448.18*
9	449.19	404.33	450.55	405.25	475.46*	431.06	476.65	432.26*
10	436.65	387.24	437.89	388.18	462.57*	—	464.00	414.84*
11	422.82	368.39	423.98	369.48	448.18*	394.76	449.51	395.92*
12	407.30	348.38	—	349.36	432.26*	374.14	433.73	375.32*
13	390.54	326.68	391.80	327.73	414.84*	352.11	416.28	353.19*
14	372.17	303.76	373.29	304.80	395.92*	328.67	—	329.76*
15	352.53		353.57		375.32*	303.59	376.99	304.64*
16			331.93		353.19*	277.08	353.80*	278.15*
17					329.76*		331.49	
18					304.64*		305.56	
19					278.15*		279.05	
	13–0 band, λ_A = 1439.0 Å				16–0 band, λ_A = 1383.2 Å			
0	69493.65*							
1	494.09*	69487.63*			72297.53*			
2	493.37*	481.91*	69494.46*	69482.70	296.43	72285.78*	72297.53*	72286.38*
3	490.44	474.85*	491.96	475.81	293.47	278.67	294.69	279.23
4	486.33	466.19	487.63*	467.11	288.77	269.73	289.99	270.25
5	480.63	455.89	481.91*	456.80	282.36	259.07	283.56	259.50
6	472.82	444.06	474.59*	445.00	274.25	246.41	275.54	247.28
7	464.03	430.70	465.32	431.48	264.49	231.88	265.65	233.61*
8	453.59	415.42	454.62	416.30	253.28*	216.53	253.95*	217.66
9	441.09	398.81	442.36	399.62	239.48	198.94	240.73	199.96
10	427.21	380.45	428.54	381.37	224.94	180.05	226.13	180.63
11	411.73	360.50	412.99	361.48	208.06	158.84	209.15	159.75
12	394.63	338.98	395.90	339.69	189.85	136.59	190.84	137.08
13	375.92		377.24		169.81	112.19	170.61	113.00
14	355.53		356.84		147.89	086.21	149.10	086.99
15	333.60		334.94		124.33	058.42	126.56*	059.22
16					099.29	029.06	100.37	029.72
17					072.19	71997.81	073.50	71998.67
18					043.74	964.96	044.93	965.75
19					013.47		014.63	
20					71981.27		71982.73	
	19–0 band, λ_A = 1334.5 Å				20–0 band, λ_A = 1319.7 Å			
0								
1	74934.25*				75775.82*			
2	932.79	74923.01*	74934.25*	74924.26*	774.30		75775.82*	
3	929.19	914.97*	930.47	915.68*	770.70	75757.21*	772.05	75758.21*
4	924.26	905.90*	925.57	906.88*	765.14	747.64*	767.00	748.64*
5	917.15	894.79*	918.46	895.50*	—	735.95*	—	736.95*
6	908.32	881.83*	909.56	882.85*	—	723.20*	—	724.20*
7	897.90	867.43*	899.03	868.03*	738.33	708.44*	739.64	709.44*
8	885.41	850.85*	886.73	851.66*	725.62	691.68*	726.69	692.68*
9	871.20	832.47*	872.56	833.19*	711.13	673.32*	712.37	674.32*
10	855.17	812.46*	856.82	813.25*	694.90	652.31*	695.88	653.31*
11	837.34	790.54*	838.68	791.48*	676.66		677.82	
12	817.86	766.80*	819.08	767.71*	656.76		657.88	
13	795.89	741.46*	797.49*	742.23*				
14	773.07	714.30*	774.34	715.16*				
15	748.19		749.28					
16	721.25		722.46					

[5]*For the 19–0 and 20–0 bands, the P and ^PQ branches are no longer properly resolved. However, each of the unresolved broad blends has been measured as two lines.*

D. THE $e {}^3\Sigma^- - X {}^1\Sigma^+$ SYSTEM

The second system here under discussion has not previously been observed even under low resolution. The reason is that this system is wholly submerged in the far stronger fourth positive group and can be separated from it only on spectra of high resolving power. Some of the bands can only be seen on the low temperature plates since they are overlapped by $v'' = 1$ bands of the fourth positive group and others are unobservable because of overlapping by the $v'' = 0$ bands of this system.

Like the $a'^3\Sigma^+ - X^1\Sigma^+$ system, the $e^3\Sigma^- - X^1\Sigma^+$ system consists of a single progression of weak bands which are degraded to the red and show single heads only. The progression starts with a relatively strong band at 64816 cm^{-1} of which only the head could be observed because the rest of the band is masked by the 0–0 band of the fourth positive system. Because of the relative strength of this band and the absence of further bands in this progression toward longer wavelengths, it was assumed that it is the 0–0 band of the system. To be sure, at longer paths and higher pressures, an extremely weak feature is observed at 63686 cm^{-1} which might be a band preceding 64816 cm^{-1} in the progression. However, it is 40 cm^{-1} off the expected position and was therefore not considered to belong to it. The $v'' = 0$ progression of the $e^3\Sigma^- - X^1\Sigma^+$ system could be identified with certainty as far as the 10–0 band at 74709 cm^{-1}. At shorter wavelengths, the bands are either completely masked or badly overlapped by the fourth positive and $a'^3\Sigma^+ - X^1\Sigma^+$ systems. Band heads could, however, be recognized at the expected positions of the 12–0, 13–0, and 17–0 bands of the progression. The band heads, with their vibrational assignments and estimated intensities, are listed in Table III.

On casual inspection the fine structure of the bands of the $e - X$ system, exemplified by the 3–0 band in Fig. 3, gives the appearance of a $^1\Pi - ^1\Sigma$ transition with a P, Q, and R branch. It turns out, however, that on this assumption no agreement with the well-known combination differences of the ground state of CO can be obtained. Rather the differences $R(J-1) - P(J+1)$ are about twice what they should be. This, together with the observation that in the best-resolved bands the Q branch is double, led to a search for other interpretations of the fine structure. It was found that a $^3\Sigma^- - ^1\Sigma^+$ transition accounts in all details for the observed band structure. In Fig. 5 a diagram of the expected rotational transitions is shown. Considering the electric dipole

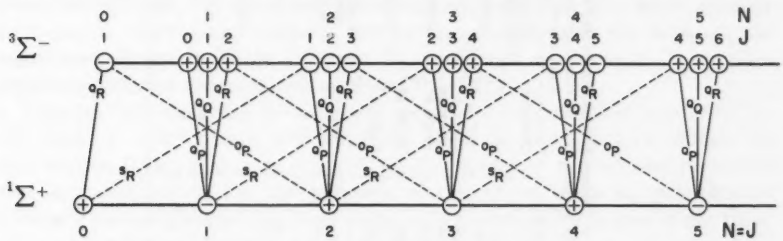

FIG. 5. Branches of a $^3\Sigma^- - ^1\Sigma^+$ band. The quantum number N was formerly called K.

selection rules ($+ \leftrightarrow -$, $\Delta J = 0, \pm 1$), five branches are to be expected, viz., three branches of Q form ($\Delta N = 0$) ^QQ, ^QP, and ^QR, and one branch each of $S(\Delta N = +2)$ and $O(\Delta N = -2)$ form: ^SR and ^OP. Since in a $^3\Sigma$ state the F_1 and F_3 levels ($J = N \pm 1$) lie close together and somewhat above or below the F_2 levels ($J = N$), the ^QP and ^QR branches will nearly coincide, but will be separated from the ^QQ branch. This conclusion agrees with the observation in the best-resolved band shown in Fig. 3. In most other bands, the three Q branches are entirely unresolved.

TABLE III

BAND HEADS, BAND ORIGINS, AND B_v VALUES OF THE $e\,^3\Sigma^- - X\,^1\Sigma^+$ SYSTEM

$v'-v''$	Band head (cm^{-1})	Intensity	Band origins, ν_0 (cm^{-1})			$B_{v'}$ values (cm^{-1})			Remarks
			Observed	From perturbations	Calculated	Observed	From perturbations	Calculated	
0–0	64816	50		64802	64802.91		1.24	1.2574	Masked, except for head, by 0–0 $A\,^1\Pi - X\,^1\Sigma^+$
1–0	65891	30	65877.82		65877.77	1.2399		1.2397	
2–0	66955	20	66933.26		66933.52	1.2221		1.2222	
3–0	67982	50	67970.31	67968	67970.21	1.2048	1.22	1.2049	
4–0					68987.86			1.1878	Masked by 3–0 $A\,^1\Pi - X\,^1\Sigma^+$
5–0	69992	30	69986.39		69986.51	1.172_9		1.1709	
6–0				70950	70966.21		1.17	1.1542	Masked by 6–1 $A\,^1\Pi - X\,^1\Sigma^+$
7–0	71925	25	71926.47		71926.97	1.136_0		1.1377	Overlapped by 5–0 $A\,^1\Pi - X\,^1\Sigma^+$ at high rotation
8–0				72794	72868.84		1.13	1.1214	Masked by 6–0 $A\,^1\Pi - X\,^1\Sigma^+$
9–0	73792	20	73792.28	73777	73791.86	1.105_2	1.12	1.1053	
10–0	74709	20		74673	74696.06		1.12	1.0894	Weak band observed on low temperature plates only
11–0					75581.47			1.0737	Masked by 8–0 $A\,^1\Pi - X\,^1\Sigma^+$
12–0	76448?	20			76448.12			1.0582	Overlapped by 9–0 $A\,^1\Pi - X\,^1\Sigma^+$
13–0	77303?	15			77296.07			1.0429	Overlapped by 22–0 $a'\,^1\Sigma^+ - X\,^1\Sigma^+$
14–0				78112	78125.33		1.06	1.0278	Masked by 23–0 $a'\,^1\Sigma^+ - X\,^1\Sigma^+$ and 10–0 $A\,^1\Pi - X\,^1\Sigma^+$
15–0					78935.95			1.0129	Masked by 11–0 $A\,^1\Pi - X\,^1\Sigma^+$
16–0					79727.95			0.9982	Masked by 12–0 $A - X$ band of $C^{13}O$
17–0	80523?	5			80501.38			0.9837	

It is readily seen from Fig. 5 that the following combination relations hold for $^3\Sigma^- - {}^1\Sigma^+$ bands:

$$^sR(J-1) - {}^qP(J+1) = {}^qR(J-1) - {}^oP(J+1) = \Delta_2F''(J).$$

Table IV shows these differences obtained from the 3–0 band as well as the $\Delta_2F''(J)$ values from the infrared bands. Considering the facts that the

TABLE IV

COMPARISON OF Δ_2F'' VALUES OBTAINED FROM THE 3–0 $e\,^3\Sigma^- - X\,^1\Sigma^+$ BAND AND THE 4–0 ROTATION–VIBRATION BAND OF CO

J	$\Delta_2F''(J)$		
	From $e^3\Sigma^- - X^1\Sigma^+$		From rot. vib. spectrum
	$^qR(J-1) - {}^oP(J+1)$	$^sR(J-1) - {}^qP(J+1)$	$R(J-1) - P(J+1)$
1		11.39	11.53
2	19.22	19.06	19.22
3	26.83	27.20	26.91
4	34.56	34.50	34.60
5	42.39	42.44	42.28
6	50.02	50.06	49.97
7	57.66	57.60	57.69
8	65.34	65.14	65.35
9	72.99	73.06	73.03
10	80.63	80.61	80.66
11	88.27	88.25	88.37
12	96.16	96.19	96.03
13	103.83	103.74	103.70
14	111.28	111.36	111.36
15	119.02	119.11	118.99
16		126.77	126.66
17		134.35	134.31
18		142.05	141.95

branches ^qP and ^qR have not been resolved and that the wave number accuracy in the vacuum region is not by far as good as in the infrared, the agreement shown in Table IV must be considered as excellent. It supplies definite proof that the transition really is $^3\Sigma^- - {}^1\Sigma^+$.

Schlapp (23) has given the intensity factors for the branches both in $^3\Sigma^+ - {}^1\Sigma^+$ and $^3\Sigma^- - {}^1\Sigma^+$ bands. For the latter these intensity factors contain, in addition to J, two constants A and C which depend on the detailed nature of the electronic states. For the purposes of this paper, since no quantitative intensity measurements have been made, only the intensity factors of the three Q form branches are of interest. Schlapp gives

$$\text{for } {}^qQ: \quad 2A^2(2J+1),$$

$$\text{for } {}^qR: \quad [2A^2(J+1)^2 + C^2J^2]/[2J+1],$$

$$\text{for } {}^qP: \quad [2A^2J^2 + C^2(J+1)^2]/[2J+1].$$

According to these formulae, if C were small compared to A, the ^qQ branch would be about four times as intense (at large J) as the ^qR or ^qP branch while, if $C^2 \approx 2A^2$, ^qQ would be about twice as strong as ^qR or ^qP. The observation that the sum of ^qR and ^qP is about as strong as ^qQ (see Fig. 3) is thus not in disagreement with theory.

In Table V the wave numbers of the observed lines in the bands are listed. Blended and very weak lines are again indicated by asterisks.

According to Schlapp's formula (24), only the F_2 levels of a $^3\Sigma$ state follow the standard formula

$$F_2'(J) = B'J(J+1)-D'J^2(J+1)^2.$$

However, this level, according to Fig. 5, is not involved in the O and S form branches, but only in the ^QQ branch. Therefore, the best way to determine B' and D' is from the ^QQ branch which is represented by

$$^QQ(J) = \nu_0+(B_v'-B_v'')J(J+1)-(D_v'-D_v'')J^2(J+1)^2.$$

Plotting $^QQ(J)$ against $J(J+1)$, one obtains very nearly a straight line indicating that $D'-D''$ is small, i.e., $D' \simeq D''$. The slope of the line gives $B_v'-B_v''$ and, since B_v'' is known, B_v' is obtained. The intercept gives ν_0. The ν_0 and B_v' values obtained in this way are given in Table III.

The magnitude of the doubling in the Q form branch, that is, the separation between ^QQ and $(^QP+^QR)$, is approximately constant and nearly equal to $\lambda+\frac{1}{2}\gamma$. The average of this quantity from the bands in which the Q branch is resolved is 0.84 cm^{-1}. In order to get the correct ν_0 for the bands in which the Q branch is not resolved, the quantity 0.42 cm^{-1} has to be added to the value obtained from the Q lines. This assumes that the measured position of the unresolved Q lines is half-way between the true positions of ^QQ and $(^QP+^QR)$, that is, that ^QQ has the same intensity as $(^QP+^QR)$ (see above). The correction 0.42 cm^{-1} has been taken into account for the 1–0, 5–0, and 7–0 bands in Table III.

The B_v' values and the band origins ν_0 can be represented by the formulae

$$B_v' = 1.266_3-0.0179(v+\tfrac{1}{2})+0.0001(v+\tfrac{1}{2})^2,$$

$$\nu_0 = 65340.0_5+1093.9_{93}(v'+\tfrac{1}{2})-9.5_{78}(v'+\tfrac{1}{2})^2 +0.005_{87}(v'+\tfrac{1}{2})^3-1081.74 \text{ cm}^{-1}$$

where again the quantity 1081.74 cm^{-1} is the zero point energy in the ground state of CO. The values given by the above formulae are included in Table III.

As mentioned before, the existence of the $^3\Sigma^-$ state of CO has previously been derived by Coster and Brons (4) and Schmid and Gerö (26) from perturbations in the Ångström bands and the fourth positive group. From these data, approximate positions of the vibrational levels and approximate B_v values were derived by the authors mentioned. These values are included in Table III. Considering that these data are often based on a very few perturbed lines, the agreement with the more precise values here obtained is quite striking, particularly for the ν_0. This agreement gives support to other molecular constants which have been derived from perturbation data only.

Apart from the $a'-X$, $e-X$, and the strong $A-X$ bands (fourth positive group), two other long progressions appear on our plates, the $a-X$ bands (Cameron system) and the $d-X$ (Hopfield–Birge) bands, both $^3\Pi-^1\Sigma$

TABLE V

WAVE NUMBERS OF THE LINES IN THE $e\,^3\Sigma^- - X\,^1\Sigma^+$ SYSTEM OF CO

	1–0 band, λ_A = 1517.7 Å				2–0 band, λ_A = 1493.7 Å			
J	$Q_Q(J)$	$Q_R(J)+Q_P(J)$	$S_R(J)$	$O_P(J)$	$Q_Q(J)$	$Q_R(J)+Q_P(J)$	$S_R(J)$	$O_P(J)$
0			65884.42				66939.75*	
1	65876.11		888.53		66931.55*	66931.55*	943.13*	
2	872.70		890.66		929.13	928.31*	945.28*	
3	869.18		890.66	65856.89*	924.92	924.07	946.13	66911.73*
4	863.62		890.66	846.18	919.16	918.42	945.28*	901.19*
5	856.89*		888.53	834.37	911.73*	911.73*	943.13*	889.39
6	848.71*		885.54	821.22	903.86	902.93	939.75*	875.94
7	839.11		880.91	806.76	894.01	893.27	934.92	861.30
8	828.14		874.99	790.83	882.81	882.05	928.31*	845.38
9	815.98		867.54	773.68	869.78*	869.78*	920.80	—
10	802.23		858.89	755.07	856.14	855.48	911.73*	809.05
11	788.25		848.71*	735.04	840.77	840.00	901.19*	788.54
12	770.81		837.38	713.71*	823.99	823.17		—
13	753.03		824.46	691.26	805.78*	805.78*		743.90
14	734.31		810.26	666.93	786.23	785.30		
15	713.71*		794.65	641.70	764.71*	764.71*		
16	692.01		777.88	615.67	742.64	741.63		
17	668.99		759.48	586.54				
18	643.58		739.84	557.14				
19	617.69		718.76					
20	590.23		696.39					
21	561.70		672.78					
22	531.77							

	3–0 band, λ_A = 1471.0 Å				5–0 band, λ_A = 1428.9 Å			
J	$Q_Q(J)$	$Q_R(J)+Q_P(J)$	$S_R(J)$	$O_P(J)$	$Q_Q(J)$	$Q_R(J)+Q_P(J)$	$S_R(J)$	$O_P(J)$
0			67976.53					
1	67968.84	67968.10	979.91*					
2	966.02	965.14	982.48*	67958.17				
3	961.80	960.85	982.48*	948.88				
4	955.88	955.28*	981.81*	938.31	69971.13			
5	948.88	947.98	979.32*	926.29	963.45			
6	940.15	939.37	975.40	912.89	954.26			
7	930.10	929.26	969.98	897.96	943.89			
8	918.54	917.80	963.51	881.71	932.07			
9	905.66	904.84	955.28*	863.92	918.29			
10	891.38	890.45	945.85	844.81	903.58			
11	875.55	874.67	934.93	824.21	886.74			
12	858.34	857.50	922.46	802.18	868.76			
13	839.66	838.74	908.55	878.51	849.42			
14	819.55	818.72	893.24	753.67	828.36			
15	797.99	797.19	876.53	727.46				
16	775.05	774.13	858.34	699.70				
17	750.67	749.76	838.74					
18	724.84	723.99	817.57					
19	697.51	696.69	795.09					
20			770.94					
21			745.70					
22			718.76					
23			690.78					

	7–0 band, λ_A = 1390.1 Å				9–0 band, λ_A = 1355.2 Å			
J	$Q_Q(J)$	$Q_R(J)+Q_P(J)$	$S_R(J)$	$O_P(J)$	$Q_Q(J)$	$Q_R(J)+Q_P(J)$	$S_R(J)$	$O_P(J)$
0								
1	71924.52				73790.45*	73790.45*		
2	921.23				786.95*	786.95*		
3	916.62				782.06*	782.06*		
4	910.35				775.58*	775.58*		
5	902.46				767.40*	767.40*		
6	893.12				758.23	757.40	73790.45*	
7	882.01				746.15	745.05	—	73717.69*
8	869.06				732.99*	732.99*	—	699.75
9	855.33				718.51	717.69	764.16	680.23*
10	839.45				702.02*	702.02*	752.53*	659.71*
11	822.22				683.92*	683.92*		636.93*
12					664.73	664.11		
13					643.16*	643.16*		
14					620.40	619.42		
15					596.01	595.19		
16					569.98	569.08		
17					542.70	541.37		

systems. The fine structure of the former has been well studied (10, 22) while that of the latter has not yet been studied in detail.

In addition to these band systems, one further band progression was observed

extending from 1348 to 1234 Å. This progression was found to represent the $v'' = 0$ progression of the fourth positive group of $C^{13}O$. It has been observed from $v' = 7$ to $v' = 13$. Most of the isotopic bands could only be measured on the low temperature plates on which the strong fourth positive bands of $C^{12}O$ are reduced in width.

E. DISCUSSION AND CONCLUSION

The rotational and vibrational constants of the $a'^3\Sigma^+$ and $e^3\Sigma^-$ states of CO obtained in the foregoing analysis are summarized in Table VI. In both cases,

TABLE VI

VIBRATIONAL AND ROTATIONAL CONSTANTS OF THE $a'^3\Sigma^+$ AND $e^3\Sigma^-$ ELECTRONIC STATES OF CO

Constant	$a'^3\Sigma^+$	$e^3\Sigma^-$	
B_e	1.3453 ± 0.0003	$1.266_2 \pm 0.0010$	cm^{-1}
α_e	$0.0187_2 \pm 0.00010$	0.0179 ± 0.0003	cm^{-1}
γ_e	0.000205	0.0001	cm^{-1}
δ_e	5.1×10^{-6}	—	cm^{-1}
D	$\sim 6.5 \times 10^{-6}$	$\sim 6.5 \times 10^{-6}$	cm^{-1}
$\lambda + \frac{1}{2}\gamma$	-1.1_2	$+0.8_4$	cm^{-1}
I_e	$2.080_5 \times 10^{-40}$	$2.210_2 \times 10^{-40}$	gm. $cm.^2$
r_e	$1.351_8 \times 10^{-8}$	$1.393_3 \times 10^{-8}$	cm.
ν_{00}	55353.9_1	64802.9_1	cm^{-1}
T_e	55823.0_7	65340.0_5	cm^{-1}
ω_e	1230.65_1	1093.9_{93}	cm^{-1}
$\omega_e x_e$	11.013_0	9.5_{78}	cm^{-1}
$\omega_e y_e$	$+0.0737_8$	$+0.005_{87}$	cm^{-1}
$\omega_e z_e$	-0.0011_5		cm^{-1}

the B_e and ω_e values are considerably smaller than in the ground state. This accounts for the length of the observed progressions. Further bands of the $a'-X$ and $e-X$ systems would most probably be found at shorter wavelengths if this region were studied. This was not possible in the present work because of the lack of transmission of the LiF windows at wavelengths shorter than 1200 Å.

The transitions $^3\Sigma^+ - {}^1\Sigma^+$ and $^3\Sigma^- - {}^1\Sigma^+$ of heteronuclear molecules are in many ways complementary to each other: The branches possible in one transition according to the electric dipole selection rules ($\Delta J = 0, \pm 1, + \leftrightarrow -$) cannot occur for the other. Both transitions are made possible by spin–orbit interaction. The selection rule that Σ^- states do not combine with Σ^+ states does not apply to intercombinations as was shown by Schlapp (23) and does, therefore, not introduce an additional degree of forbiddenness for $^3\Sigma^- - {}^1\Sigma^+$. Indeed the intensities of the two band systems are of the same order. $\Sigma^- - \Sigma^+$ transitions between Σ states of the same multiplicity are much weaker, like the $^3\Sigma_u^+ - {}^3\Sigma_g^-$ bands of O_2 (see (15)). No $^1\Sigma^+ - {}^1\Sigma^-$ bands have yet been found. Examples in homonuclear molecules of $^3\Sigma^+ - {}^1\Sigma^+$ (or $^1\Sigma^- - {}^3\Sigma^-$) transitions of electric dipole type have been observed for O_2 (see the paper III of this series (17)) and N_2 (Vegard–Kaplan bands). They are very much weaker than the $^3\Sigma^+ - {}^1\Sigma^+$ CO bands and, in the case of N_2, have not yet been observed in absorption in spite of many attempts.

The ground state electron configuration of CO can be written

[1] $$KK(\sigma 2s)^2(\sigma^*2s)^2(\pi 2p)^4(\sigma 2p)^2$$

where KK stands for the two K shells. The two lowest unoccupied orbitals are π^*2p and σ^*2p, both of antibonding type. Since, as shown by the spectrum of CO^+, the orbital $\pi 2p$ has an energy not much below $\sigma 2p$, the lowest excited states of CO would be expected to belong to the following configurations (omitting $KK(\sigma 2s)^2(\sigma^*2s)^2$ which is the same for all):

[2] $(\pi 2p)^4(\sigma 2p)(\pi^*2p)$; $^1\Pi$, $^3\Pi$

[3] $(\pi 2p)^3(\sigma 2p)^2(\pi^*2p)$; $^1\Sigma^+$, $^1\Sigma^-$, $^1\Delta$, $^3\Sigma^+$, $^3\Sigma^-$, $^3\Delta$

[4] $(\pi 2p)^4(\sigma 2p)(\sigma^*2p)$; $^1\Sigma^+$, $^3\Sigma^+$

[5] $(\pi 2p)^3(\sigma 2p)^2(\sigma^*2p)$; $^1\Pi$, $^3\Pi$

These configurations give rise to the electronic states given at the right. There is no question that the $^1\Pi$ and $^3\Pi$ states of [2] are to be identified with the observed $A^1\Pi$ and $a^3\Pi$ states (upper states of the fourth positive and Cameron systems). The upper states of the two band systems here under discussion $a'^3\Sigma^+$ and $e^3\Sigma^-$ must, in all probability, be correlated with configuration [3]. The $^1\Sigma^+$ state of the same configuration is presumably the $B^1\Sigma^+$ upper state of the Ångström bands, (compare the energy level diagram Fig. 197 of (14)). The $^1\Sigma^+$ and $^3\Sigma^+$ states of [4] may be readily identified with the observed $C^1\Sigma^+$ and $b^3\Sigma^+$ states and the $^1\Pi$ and $^3\Pi$ states of [5] with the observed $F^1\Pi$ and $d^3\Pi$ states.

The electronic configurations [1]–[5] are entirely analogous to the low-lying configurations of the N_2 molecule (see (12)). In particular, the upper $^3\Sigma_u^+$ state of the Vegard–Kaplan bands is the analogue of the $a'^3\Sigma^+$ state of CO here considered. It is remarkable that in spite of the great similarity in electron configuration, there is such a large difference of intensity. Further theoretical work on the intensities of forbidden transitions is indicated.

ACKNOWLEDGMENT

We are greatly indebted to Mr. J. Shoosmith for his care in taking all the plates on which this study is based and to Miss Lila Howe for efficient help in the computations. We also wish to thank Dr. A. E. Douglas for critical comment.

REFERENCES

1. Asundi, R. K. Proc. Roy. Soc. (London), A, 124: 277. 1929.
2. Beer, B. S. Z. Physik, 107: 73. 1937.
3. Brix, P. and Herzberg, G. Can. J. Phys. 32: 110. 1954.
4. Coster, D. and Brons, F. Physica, 1: 634. 1934.
5. Curry, J. and Herzberg, G. Ann. Physik, 19: 800. 1934.
6. Edlén, B. J. Opt. Soc. Amer. 43: 339. 1953.
7. Estey, S. Phys. Rev. 35: 309. 1930.
8. Gerö, L. Z. Physik, 109: 204. 1938.
9. Gerö, L. Z. Physik, 109: 216. 1938.
10. Gerö, L., Herzberg, G., and Schmid, R. Phys. Rev. 52: 467. 1937.
11. Gerö, L. and Lörinczi, K. Z. Physik, 113: 449. 1939.
12. Herzberg, G. Phys. Rev. 69: 362. 1946.
13. Herzberg, G. Can. J. Research, A, 28: 144. 1950.

14. HERZBERG, G. Molecular spectra and molecular structure. I. Spectra of diatomic molecules. 2nd ed. D. Van Nostrand Company, Inc., New York. 1950.
15. HERZBERG, G. Can. J. Phys. 30: 185. 1952.
16. HERZBERG, G. Trans. Roy. Soc. Can. 46: 1. 1952.
17. HERZBERG, G. Can. J. Phys. 31: 657. 1953.
18. HERZBERG, G. and RAO, K. N. J. Chem. Phys. 17: 1099. 1949.
19. HOPFIELD, J. J. and BIRGE, R. T. Phys. Rev. 29: 922. 1927.
20. KLEMAN, B. and WERHAGEN, E. Arkiv Fysik, 6: 399. 1953.
21. LEIFSON, S. W. Astrophys. J. 63: 73. 1926.
22. RAO, K. N. Astrophys. J. 110: 304. 1949.
23. SCHLAPP, R. Phys. Rev. 39: 806. 1932.
24. SCHLAPP, R. Phys. Rev. 51: 342. 1937.
25. SCHMID, R. and GERÖ, L. Z. Physik, 105: 36. 1937.
26. SCHMID, R. and GERÖ, L. Z. Physik, 106: 205. 1937.

AURORAL HEIGHTS OVER WEST-CENTRAL CANADA[1]

By B. W. Currie

ABSTRACT

A complete analysis of the parallactic photographs of aurora taken at Chesterfield, N.W.T., (63.3°N., 90.7°W.) in 1933 show (*a*) a marked maximum in the heights of the lower limits of both homogeneous arcs and bands and auroral structures with rays between 100 and 110 km., (*b*) a mean height of the lower limit of arcs and bands of 108.2 km., (*c*) a mean height of the lower limit of auroral structures with rays of 113.4 km., (*d*) a decrease of height with increasing intensity, and (*e*) no definite evidence of a change of height with time after sunset. The results suggest that heights of aurora as observed from Northern Canada are slightly higher than of aurora observed from Norway. This may be due to the locations of the two regions relative to the zone of maximum auroral occurrence. No exceptionally low heights were observed at Chesterfield. Remeasurements of the 1933 photographs for Saskatoon (52.1°N., 106.6°W.) indicate that one arc was definitely below the 70-km. level, and possibly below the 60-km. level.

INTRODUCTION

The numerous measurements of height made by Størmer, Vegard and Krøgness, and Harang (8, 9, 10, 11) on aurora observed from Norway have shown characteristics that are assumed generally to apply to all regions. Data in support of this assumption are exceedingly scanty, only small numbers of measurements having been made over other regions. During the Second International Polar-Year, 1932–33, about a thousand pairs of parallactic photographs of aurora were taken at Chesterfield, N.W.T., (63.3°N., 90.7°W.). Height measurements were made shortly after on 200 pairs that were selected roughly at random from the group. The results showed heights for the lower limit of aurora that were substantially the same as for Norway (2). At the same time, Alty and Wilson (1) made a small number of height measurements at Saskatoon (52.1°N., 106.6°W.). A number of these were much lower (50–70 km.) than any reported previous to or since that time. In view of the approaching International Geophysical Year, 1957–58, it seems worth while to report on the complete analysis of the Chesterfield photographs, and on remeasurements of the Saskatoon photographs. The Chesterfield measurements are also the only ones in any number from a place well inside the zone of maximum auroral occurrence.

The length of the Chesterfield base-line was 32.14 km. The orientation (6.3°E. of N.) was particularly good for height measurements on arcs and bands because of their horizontal extent from east to west. They were taken during three periods of major auroral activity—January 22–27, February 26–28, and March 21–27—and mostly in the evening hours. A definite effort was made to get photographs of auroral structures satisfactory for height measurements. This meant that rapidly changing forms and ones with poor orientations for measurement relative to the base-line were not photographed.

[1]*Manuscript received August 11, 1955.*
Contribution from the Department of Physics, University of Saskatchewan, Saskatoon, Saskatchewan.

As a result, only about one out of every two pairs had to be rejected because of unsatisfactory orientation, too low an angular altitude, motion during photographing, unsatisfactory exposure times, and so on.

The length of the Saskatoon base-line was 112.5 km., orientated slightly north of east. The long base-line resulted in large parallactic displacements even for forms at low angular altitudes. The orientation was unsatisfactory for structures with an east–west extent, the parallactic displacements running nearly parallel to the edges of arcs and bands. Photographs were taken on January 30, February 25–26, and April 16 and 20. Only 55 were considered suitable for height measurements.

The methods used in measuring heights from parallactic photographs have been described in detail in auroral publications (6). They consist essentially of projecting the auroral photographs on tracing paper (1 cm. on the tracing corresponding to one angular degree) and using the star backgrounds to fit the tracings to "nets" which are projections on plane surfaces of orthogonal systems of small and great circles for the celestial sphere. By means of these, the altitude, the azimuth, and the parallactic displacement for selected auroral points are determined. Graphical methods are used also to determine the height and the distance along the earth's surface from the primary photographic station to the vertical projection on the earth's surface of each auroral point.

The heights of several points (three or four or five depending on the angular extent) along the lower edge of each arc or band, and of the apparent lower and upper limits of rays, are usually measured. The upper limits of arcs and bands cannot be determined with any accuracy because of the lack of brightness contrast between the upper edges and the sky background. Intermediate heights of auroral structures are sometimes useful for determining the orientation in space of auroral structures, but serve no other purpose as far as height characteristics are concerned.

A fairly critical attitude must be taken toward the measurements on each form. If the values along the lower edge of an arc or band vary irregularly and by large amounts, or if a ray structure is not approximately parallel to the lines of the earth's magnetic field, it is probable that the set of photographs was not suitable for height measurements. Sometimes the parallactic angles are at fault because of low altitudes or poor orientations relative to the base-line of the auroral structures. More frequently a volume effect is responsible, edges that apparently correspond on the two photographs being actually different ones because of folds and depth in the auroral structures. A set of photographs yielding consistent values that are much smaller or larger than normal is more difficult to eliminate. This situation is most likely to occur with rapidly changing auroral forms when a failure to take the two photographs simultaneously can result in large errors in the parallactic angles.

Both the Chesterfield and Saskatoon measurements were examined with these sources of error in mind. All values for particular structures were discarded whenever there was definite evidence that one or more of these errors had appreciably affected the results. Some measurements were retained

that were suspect, since discarding them could mean the loss of significant information. Cases with heights departing appreciably from the expected ones will be discussed later.

RESULTS

The pertinent information on 1378 heights of the lower limits of homogeneous arcs and bands as observed from Chesterfield are given in Table I

TABLE I

FREQUENCIES OF MEASURED HEIGHTS OF THE LOWER LIMITS OF HOMOGENEOUS ARCS AND BANDS, AND OF AURORAL STRUCTURES WITH RAYS

Heights, km.	Homogeneous arcs and bands				Structures with rays, total
	Jan.	Feb.	Mar.	Total	
75–79	3	1	0	4	1
80–84	16	5	6	27	17
85–89	50	8	11	69	28
90–94	84	14	22	120	38
95–99	106	30	32	168	46
100–104	126	36	46	208	79
105–109	143	43	42	228	80
110–114	108	35	28	171	57
115–119	50	38	31	119	69
120–124	49	23	16	88	43
125–129	33	14	13	60	21
130–134	22	8	10	40	29
135–139	7	10	10	27	19
140–144	8	9	6	23	23
145–149	4	4	2	10	10
150–154	2	3	4	9	4
155–159	3	0	1	4	6
160–164	1	1	1	3	6
165–169	0	0	0	0	4
170–174	0	0	0	0	4
175–179	0	0	0	0	2

and are shown graphically in Fig. 1. In preparing the table, heights were grouped in ranges of 5 km., starting upward from 75 km. The number occurring in each height interval is plotted against the median height for the interval. Included in Table I are the height frequencies of the lower limits of arcs and bands for each of the three periods during which photographs were taken (January, February, and March), and of the lower limits of auroral structures with rays. Because of the smaller number of measurements on ray structures they are not subdivided into monthly groupings.

Heights in the ranges 100–104 and 105–110 km. are definitely more numerous than for other ranges. The average height of the lower limits of the arcs and bands is 108.2 km.; of the structures with rays, 113.4 km. Both the frequencies of occurrence and the average values suggest heights for Canada to the north of the auroral zone that are slightly greater than for Norway (6, 8, 9, 10). Since less energetic particles can penetrate to greater depths of the atmosphere inside than outside the auroral zone this difference may actually exist. Other factors, such as tidal effects in the upper atmosphere, intensity of the aurora,

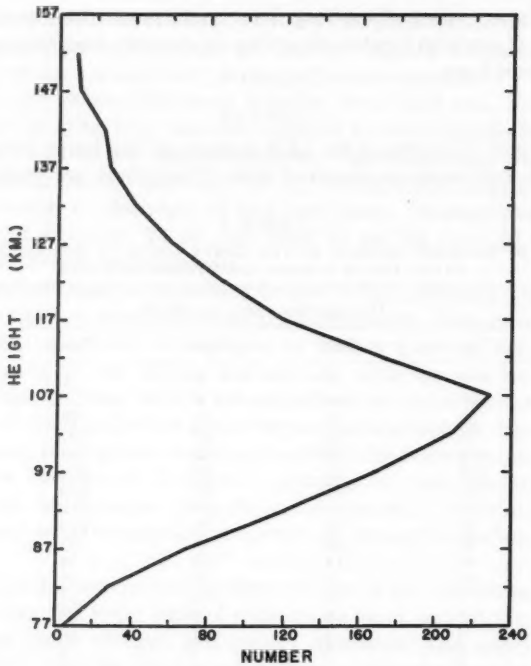

FIG. 1. The frequency distribution of the heights of the lower limits of homogeneous arcs and bands. The number of measurements in 5-km. ranges, starting from 75 km., are plotted against the median height for the range.

and time from sunset, affect auroral heights to such an extent that not much weight can be attached to the slightly larger values from the Chesterfield measurements.

The frequency distributions for some of the Norwegian measurements show two maxima (6, 11). Egedal (3) and Harang (4) have shown that the maximum for the larger height is associated with flood-time, and the maximum for the smaller height with ebb-time of the lunar tide. The Chesterfield photographs for January were taken almost entirely during times when the tides were low; for February, when high; and for March, partly when high and partly when low. The average height of the arcs and bands for January is 106.1 km.; for February, 112.0 km.; and for March, 110.0 km. These values support the belief that a lunar tide is present in the atmosphere at auroral levels. Since most of the Chesterfield heights are for times of low tide, the most frequent and the average values that have been deduced may be smaller than normal for the region. It should also be noted that this supports the possibility of larger auroral heights inside than outside the auroral zone.

The Norwegian measurements indicate lower heights for the brighter or more intense auroral forms (5). This is also evident from the Chesterfield

measurements. A visual intensity figure for aurora, ranging from 0 for the weakest to 4 for the strongest, had been entered in the photographic logbook. All forms with three or more height determinations along their lower edges were divided into two groups according to intensities—weak and moderate. Measured forms of strong intensity were too few to be worth separating from the ones of moderate intensity. Each of these groups was again divided into height ranges of 10 km. A form was considered as belonging in a particular height range if the majority of the heights for it fell within the range. Forms with heights scattered over more than two ranges were not included. This procedure eliminated from consideration both individual heights and forms where the measurements were probably in error. The results of these groupings are shown in Table II. It is apparent from the table that forms of moderate intensity are relatively more frequent at the lower heights than ones of low intensity.

TABLE II

NUMBERS OF HOMOGENEOUS ARCS AND BANDS, AND OF AURORAL STRUCTURES WITH RAYS OF WEAK AND OF MODERATE INTENSITY HAVING THEIR LOWER LIMITS LARGELY WITHIN THE INDICATED HEIGHT RANGES. FORMS OF MODERATE INTENSITY ARE RELATIVELY MORE FREQUENT AT LOWER HEIGHTS THAN ONES OF WEAK INTENSITY

Heights, km.	Homogeneous arcs and bands		Structures with rays	
	Weak	Moderate	Weak	Moderate
<90	5	16	3	6
90–99	15	48	7	21
100–109	38	41	17	30
110–119	32	15	16	15
120–129	16	3	17	5
130–139	7	0	12	2
>140	0	0	3	0

A progressive decrease in height with time after sunset, as shown by Egedal and by Størmer (page 44 of Ref. 6), could not be deduced from the Chesterfield measurements. Figure 2 shows a plot of the average heights of arcs and bands

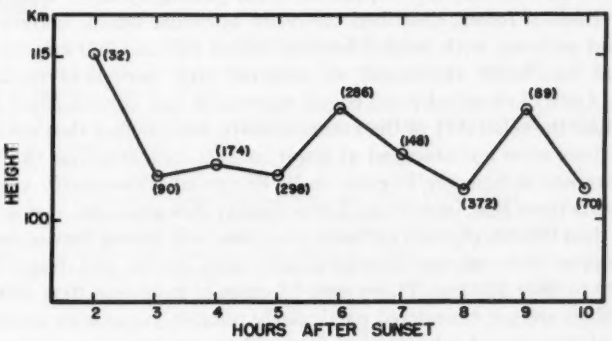

FIG. 2. The mean heights of the lower limits of homogeneous arcs and bands for hourly periods centered on the indicated number of hours after sunset. The quantities in brackets are the number of heights used in evaluating each mean.

for each hourly interval centered on the indicated hours after sunset. The variations are possibly due to intensity changes. As mentioned previously, the photographs were taken during periods of above normal auroral activity. Each night the aurora went through several periods of maximum and minimum activity, each lasting for an hour or more but occurring irregularly from night to night. Subdivisions of the data for Fig. 2 according to intensity were equally inconclusive, and are not included.

An attempt was also made to detect a change of height with geomagnetic latitude, as has been demonstrated by Størmer (9, 10) for latitudes to the south of the auroral zone. Heights of arcs and bands to the south of Chesterfield were compared with those to the north of Chesterfield. No significant differences could be detected. Again, intensity variations may be an obscuring factor. Displays at Chesterfield developed in much the same way as they do to the south of the auroral zone—building up in the direction toward the auroral zone and spreading overhead and into the part of the sky away from the zone at the peak of their activity. Obviously, any increase of height due to decreasing geomagnetic latitude could be balanced by the decrease of height due to the higher intensities at such times.

There was one case of unusually low aurora. This occurred on January 27 for an arc-like structure of intensity 3 and with pink and red shades. The heights for five points separated by about 5-degree intervals of azimuth were 77, 76, 71, 72, and 71 km. The parallactic angles varied from 4.5 to 5.2 degrees—values sufficiently large to give reasonably reliable height measurement. The only criterion that might be used for discarding these measurements is the possible lack of simultaneity in taking the two photographs, since such forms develop and change rapidly. Similar forms have been measured at heights below 70 km. by Harang and Bauer (7). The values for this arc are not included in Table I and Fig. 1.

Unexpectedly large heights were not numerous. Most of those associated with arcs and bands were probably due to volume effects which could not be detected with certainty by inspection of the photographs. In addition there were 11 cases of forms, described variously as diffuse bands, corona-like surfaces, and surfaces, with heights between about 150 and 300 km. All of these had large parallactic angles and all occurred after periods of much auroral activity. Lack of clearly defined edges, movement and volume effect undoubtedly reduce the reliability of the measurements, but the fact that similar types of structures were not observed at lower heights indicates that the measurements are not sufficiently in error to be discarded. Presumably some of the diffuse structures that form as an active display dies away are at much greater heights than the sharply defined forms preceding and during the display.

The upper limits of rays associated with arcs, bands, and draperies varied from 130 to over 300 km. There were 11 cases of rays exceeding 400 km., but these values are not considered particularly reliable. None were sunlit. Photographs of rays completely isolated from other structures were not obtained.

The Saskatoon values were checked by having an assistant remeasure all the plates. Where his values of the heights departed appreciably from the

original values, the writer measured the heights once again. The agreement with the original values was reasonably good for all cases where twists and rays in the auroral structures had been used to determine the parallactic angles. For structures with regular lower edges, nearly parallel to the plane of the parallactic displacements, there was a notable lack of agreement. If the same criteria as for the Chesterfield photographs had been used, these structures would have been discarded. Three sets of successive photographs of the same arc with heights reported by Alty and Wilson (1) as between 52 and 61 km. are not exclusively in this group. The exposures were long for this type of work (between 40 and 50 sec.), but the lower edges on the photographs are well defined and show no evidence of motion during the exposures. The directions of the edges are not particularly favorable to the determination of reliable parallactic angles, but their values are internally consistent for the three sets of photographs. Repeated measurements indicate that this arc was definitely below 70 km. and possibly below 60 km. Unless some unsuspected reason can be found for discarding these measurements, it must be accepted that auroras occasionally occur to the south of the auroral zone at much lower levels than is usually assumed.

ACKNOWLEDGMENTS

Many individuals contributed in various ways to the work reported in this paper. These include Mr. F. T. Davies who selected the forms to be photographed and operated one of the cameras; Mr. C. K. Jones who constructed some of the "nets" that were needed for the later measurements; Mr. E. D. Micklewright and Mr. R. E. Jensen who did all of the computations and many of the graphical manipulations for the later measurements; and Miss K. Noyce who tabulated pertinent details concerning the measurements from the working sheets. Their help is gratefully acknowledged. The photographs were taken and the earlier measurements were made under the auspices of the Meteorological Service of Canada. Grants from the National Research Council and the Defence Research Board of Canada helped to defray some of the later costs.

REFERENCES

1. Alty, T. and Wilson, F. Canadian Polar Year Expeditions, 1932–33. Vol. 2. Meteorological Service, Ottawa. 1939.
2. Currie, B. W. Canadian Polar Year Expeditions, 1932–33. Vol. 2. Meteorological Service, Ottawa. 1939. Terrestrial Magnetism and Atm. Elec. 20: 289. 1934.
3. Egedal, J. Nature, 124:913. 1929.
4. Harang, L. Geofys. Publikasjoner, Vol. 12, No. 1. 1937.
5. Harang, L. Geofys. Publikasjoner, Vol. 13, No. 14. 1944.
6. Harang, L. The aurorae. John Wiley & Sons, Inc., New York. 1951.
7. Harang, L. and Bauer, W. Gerlands Beitr. Geophys. 37: 109. 1932.
8. Harang, L. and Tonsberg, E. Geofys. Publikasjoner, Vol. 9, No. 5. 1930.
9. Størmer, C. Geofys. Publikasjoner, Vol. 4, No. 7. 1926.
10. Størmer, C. Terrestrial Magnetism and Atm. Elec. 54: 251. 1948.
11. Vegard, L. and Krøgness, O. Geofys. Publikasjoner, Vol. 1, No. 1. 1920.

THE INTENSITY AT THE BOTTOM OF THE FRAUNHOFER *D* LINES[1]

By J. A. Scrimger and D. M. Hunten

ABSTRACT

The line profiles were measured by scanning a photomultiplier and exit slit in the second order of a 21-ft. grating. The large distortions resulting from finite resolution were evaluated by means of an absorption cell containing sodium vapor with helium at a pressure of 170 mm. This produced an artificial line whose central intensity was known to be zero. By matching its profile carefully to that of the solar line the central intensities of D_1 and D_2 were found to be $(5.0\pm0.6)\%$ and $(4.8\pm0.6)\%$ in terms of the nearby continuum.

1. INTRODUCTION

One of the most valuable results coming from studies of the twilight sodium emission is an estimate of the number of free sodium atoms per square centimeter column in the upper atmosphere (1, 5). The data required are the scattered intensity, the scattering power of a sodium atom, and the intensity of the incident sunlight. The first two are known with reasonable accuracy, but the last is very uncertain. The intensity of the continuous spectrum is well known (6), but the radiation active in exciting the twilight scattering is at the bottom of the Fraunhofer *D* lines. The ratio of the central intensity to the continuous intensity (which we will call p) is not known with any accuracy. The best and most recent measurement is that of Priester (8) who used a Lummer plate crossed with a high dispersion spectrograph to observe the line profiles. The recording was done photographically, and separate measurements were made for various parts of the sun's disk. Substantial corrections had to be made for finite resolution and scattered light.

It was felt that an independent measurement by a different method, using light from the whole sun, would be desirable. This consisted of a measurement of the line profiles using a 21-ft. concave grating, and a second measurement under similar conditions but with the central intensity reduced to zero by a sodium vapor absorption tube. The difference then gave the central intensity directly. Direct photoelectric photometry was used in order to eliminate uncertainties in the standardization of photographic plates. The agreement of our results with Priester's is highly satisfactory.

2. PRELIMINARY MEASUREMENTS

It was thought at first that direct photometry with the grating would yield the required accuracy. The spectrograph is an Eagle type using a 15,000 lines per inch grating 5 in. wide. A photomultiplier and exit slit were mounted so that they could be scanned for a short distance tangent to the Rowland circle in the second order. A coelostat was arranged to bring in the sunlight without forming an image, so that the results were for the whole sun.

[1]*Manuscript received July 21, 1955.*
Contribution from the Department of Physics, University of Saskatchewan, Saskatoon, Saskatchewan. Sponsored by The Geophysics Research Directorate of the Air Force Cambridge Research Center, Air Research and Development Command, under Contract AF 19(122)-152.

A simple double monochromator was set up ahead of the grating instrument and adjusted to pass about a 20 Å band. Errors caused by scattered light were thus greatly reduced. The detector was a 1P21 photomultiplier followed by a simple but stable and linear direct-current amplifier. A similar system at a fixed position in the first order served as a monitor for changes in the incident intensity. The circuit of the amplifier was similar to one already published (4), but with the electrometer stage omitted since the photomultiplier load resistance was only 50 megohms. A two-pen recording potentiometer allowed both signals to be recorded on one chart.

The theoretical resolving power of the grating in the second order is 180,000; in practice we were able to achieve 100,000. The resulting distortion of the *D* line profiles should be small; however the values of p were about 20% rather than about 6%. Because of the double monochromator this could not be attributed to scattered light. The instrumental line profile was therefore measured using the 5790 Å line of mercury 198. (The loan of the source was kindly arranged by Dr. A. E. Douglas of the National Research Council and Dr. A. Vallance Jones of this Department.) The width halfway down was about 0.06 Å, giving the resolving power already quoted, but there were faint wings extending nearly 0.4 Å out from the center. These would have very little effect on the sharpness of lines in emission spectroscopy, but would result in a serious filling-in of the absorption lines, as was observed.

An attempt was made to correct the observed profiles by a method resembling that of Hardy and Young (3). For D_1 and D_2 the resulting values of p were 8.5% and 7.7%. These cannot be considered at all accurate, since the correction is about twice the final result.

3. THE SODIUM VAPOR TUBE

The correction at the center of a line was evaluated directly by forming an absorption line whose shape matched that of the solar line but whose central intensity was known to be zero. Any observed intensity was spurious and was of course equal to the required correction. The artificial line was produced by passing sunlight through a tube containing sodium vapor and helium at the correct pressures. The helium was required to make the line broad enough and smooth enough, since pure sodium vapor gives a very narrow line in the pressure range that was used.

Since glass is attacked by hot sodium vapor, the tube was lined with a glaze used for vapor lamps by the General Electric Company (generously given by Mr. R. W. Schmies). This is normally used with a special glass of matching thermal expansion, but was found satisfactory with Pyrex. The glaze must be fired at a temperature in the softening range of the glass, and it is difficult to keep the flat glass for the windows from distorting. This problem was solved by making a layer about 1 mm. thick of powdered graphite on an iron plate and packing it by pressure with the window blank. Heat could then be applied from above and below. The uncoated surface remained adequately smooth and kept its polish. The coated surface was finely pebbled and had to be polished with rouge on a felt pad. The two windows were found to remove about half the light from a collimated beam.

The diameter of the tube was 34 mm. and the length 92 mm. Many of the first attempts failed when the tubes cracked after the windows were sealed on, because of strains introduced when the glaze was fired. This difficulty was removed by annealing the parts in an oven before assembly. The completed tube was also annealed. Because a considerable pressure of helium was to be used, the tube was not carefully outgassed. It was evacuated by a single-stage oil diffusion pump, flushed with helium, evacuated again, and filled to the final pressure of 170 mm. Sodium purified by vacuum melting and distillation was introduced from a thin-walled ampoule.

The profile of the absorption line at different temperatures was calculated from equation (97) of MZ (book by Mitchell and Zemansky, Reference 7). This equation assumes Lorentz broadening, but should give a good approximation at the pressure used. For the pressure of helium used and for a temperature near 180°C., equations (104) and (96) of MZ give a Lorentz damping ratio $a' = 1.5$. Some lines were also calculated for $a' = 0.5$ and 1.0 to find the effect of a' on the line shape. To a very good approximation a temperature giving the same shape could be found for each value. Since there is no optimum value of a' the largest was used, so that the temperature could be kept relatively low. Calculations were made with the aid of Appendix IX in MZ. The vapor pressures used were those of Edmondson and Egerton (2).

4. MEASUREMENTS AND INTERPRETATION

The observing procedure was very simple once the spectrograph had been adjusted to give the sharpest possible lines. The two D lines were observed in different runs, since too much time would otherwise have been lost in scanning between them. The line was scanned several times as the sodium tube slowly cooled. Another measurement was made with the tube removed from the optical path. The position of the continuum was estimated by drawing a line through the trace about 1 Å from the center. The observed

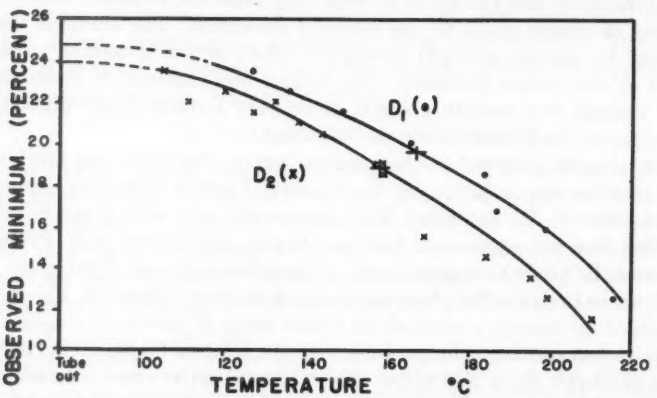

FIG. 1. The observed central intensities for D_1 and D_2 as a function of the temperature of the sodium vapor tube. The temperatures found from Figs. 2 and 3 are marked on the curves.

residual intensity was the ratio of the minimum deflection to the deflection for the continuum. The results are plotted in Fig. 1 as a function of temperature of the tube. Since there is no break in the curves indicating the desired point, it is necessary to estimate this point with the aid of the calculated absorption line profiles.

The line desired has the same shape as the solar line but is displaced downward so that its central intensity is essentially zero. The shape used was that found by Priester (8) for $\sin \theta = 0.60$; θ is the angle between the line of sight and the normal to the sun's surface. An average shape for the whole disk would be preferable, but did not seem worth the considerable labor of calculat-

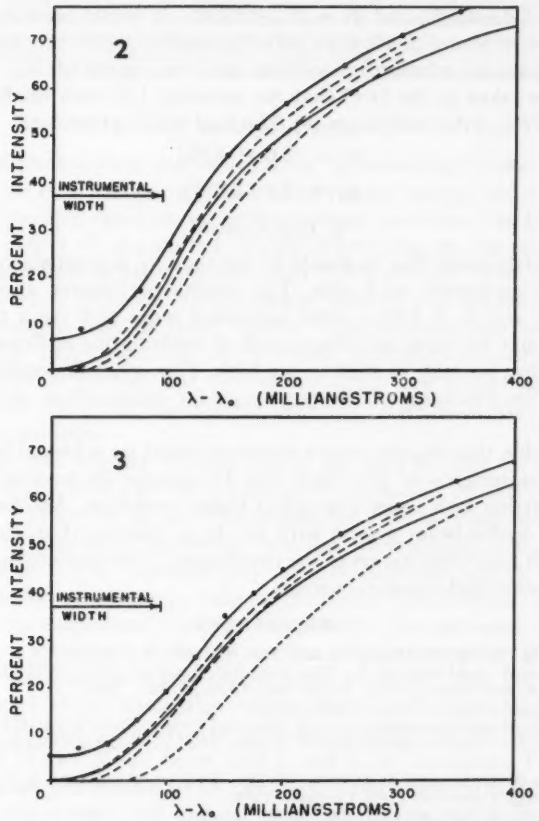

FIG. 2. Profiles of the D_1 line 5896 Å. The upper solid curve with points is Priester's measurement. The lower is the same displaced down. The three dotted curves are calculated for sunlight passing through the sodium vapor tube at 160, 170, 180°C. (left to right).

FIG. 3. Profiles of the D_2 line 5890 Å. The upper solid curve with points is Priester's measurement. The lower is the same displaced down. The three dotted curves are calculated for sunlight passing through the sodium vapor tube at 150, 160, 180°C. (left to right).

ing it. However, the average central intensity was calculated, allowing for the contribution of each region to the total area and for limb darkening. The latter was represented by the approximation suggested by Minnaert (6), with a coefficient $\beta = 1.6$. For D_1 and D_2 the results were $p_1 = 6.6\%$ and $p_2 = 5.8\%$. As would be expected, these are close to the values observed at $\sin\theta = 0.60$.

The line shapes actually achievable are shown by the dotted curves in Figs. 2 and 3. Also shown are the shape of the solar line as found by Priester and the same curve displaced down until it touches the horizontal axis. The dotted curve most nearly matching the desired curve in the region of the instrumental profile is the one desired. The best temperatures are 167°C. for D_1 and 158° for D_2, with uncertainty of about $\pm 2°$ in both cases. Reference to Fig. 1 then gives $p_1 = (5.4\pm0.3)\%$ and $p_2 = (5.2\pm0.3)\%$. It would seem reasonable to double the error figures to allow for uncertainties in temperature measurement, the vapor pressure relation for sodium, and the curves of Fig. 1. Account must also be taken of the fact* that the intensity 1 Å from the line center is only about 92% of the continuum (9). The final result is therefore

$$p_1 = (5.0\pm0.6)\%,$$

$$p_2 = (4.8\pm0.6)\%.$$

5. DISCUSSION

There is little doubt that p_2 should be less than p_1; it is satisfactory that our result is in agreement with this. The results of Priester already quoted ($p_1 = 6.6\%$ and $p_2 = 5.8\%$) differ somewhat more and are a little higher. Our values may be taken as giving a general confirmation of Priester's, but as indicating that his may be slightly too high. This is not impossible, since the corrections for instrumental effects, though far smaller than ours, were still appreciable.

It is possible that slightly better accuracy might be achieved by averaging several measurements of this type, but far greater improvement could be made by starting with a spectrograph of higher resolution. Another possibility is to use a double-beam system with one beam passing through the sodium cell and with rapid alternation of the two beams on the phototube. A measurement by this method is now in progress.

REFERENCES

1. BATES, D. R. Terrestrial Magnetism and Atm. Elec. 52: 71. 1947.
2. EDMONDSON, W. and EGERTON, A. Proc. Roy. Soc. (London), A, 113: 520. 1928.
3. HARDY, A. C. and YOUNG, F. M. J. Opt. Soc. Amer. 39: 265. 1949.
4. HUNTEN, D. M. Can. J. Phys. 31: 681. 1953.
5. HUNTEN, D. M. and SHEPHERD, G. G. J. Atm. and Terrest. Phys. 5: 57. 1954.
6. MINNAERT, M. The sun. *Edited by* G. P. Kuiper. The University of Chicago Press, Chicago. 1953.
7. MITCHELL, A. C. G. and ZEMANSKY, M. W. Resonance radiation and excited atoms. Cambridge University Press, London. 1934.
8. PRIESTER, W. Z. Astrophys. 32: 200. 1953.
9. SHANE, C. D. Lick Observatory Bull. No. 507. 1941.

We are grateful to the referee for pointing out this correction.

ENERGY AND ANGULAR DISTRIBUTIONS OF PHOTONEUTRONS PRODUCED BY 70-MEV. X-RAYS[1]

By W. R. Dixon[2]

ABSTRACT

The angular distributions of the photoneutrons produced by 70-Mev. X-rays in seven elements have been measured with a zinc sulphide – lucite scintillation detector. For the heavy elements the distributions are essentially isotropic, indicating the predominance of the evaporation process, while for the light elements there is also an anisotropic component peaked at 90°. The energy distributions of the photoneutrons produced in copper and lead targets have been determined with nuclear emulsions. It is shown that most of the neutrons can be attributed to an evaporation process which is governed by a constant nuclear temperature, the temperature found for copper being 1.2 Mev., and for lead being 1.0 Mev. A high-energy tail on the energy distributions is attributed to direct interactions.

I. INTRODUCTION

Studies of photonuclear reactions can be conveniently divided into studies of the reaction cross section as a function of photon energy, and studies of the energy and angular distributions of the emitted particles. The latter type of experiment is first of all expected to yield information on the relative importance of compound-nucleus formation and direct ejection. The study of the compound-nucleus processes is of particular value in that the excitation of the compound nucleus may be more "gentle" with photons than with incident particles. The direct ejections are of course intimately connected with the photon-absorption process, and their study is expected to give more detailed information on the absorption process than can be obtained from total cross-section measurements.

The energy and angular distributions of particles emitted by a compound nucleus are characteristically different from those ejected by direct interaction. The energy distribution of particles evaporated from a compound nucleus is expected to be somewhat maxwellian in shape, while directly-ejected particles are expected to follow approximately an inverse power law (5, 13). Direct particles thus form high-energy tails on the energy distributions. The angular distribution for evaporated particles is expected to be isotropic, unless there are only a few states of the residual nucleus available, in which case however the angular distribution is still symmetrical about 90° (10, 25). For direct ejection (electric dipole absorption) the angular distribution is expected to be of the form $(a+b\sin^2\theta)$, where θ is the angle at which the neutron is emitted with respect to the X-ray beam and a and b are constants. For protons, dipole–quadrupole interference can give rise to a peak forward of 90°.

Although the energy and angular distributions are characteristic of the interaction process, it should be noted that an unambiguous separation of the evaporation and direct processes is often experimentally impossible. Indeed

[1]*Manuscript received August 2, 1955.*
Contribution from the Department of Physics, Queen's University, Kingston, Ontario.
[2]*Present address: Radiology Laboratory, National Research Council, Ottawa, Ontario.*

it may be futile to seek a sharp delineation, since processes intermediate between conventional compound-nucleus formation and direct interaction undoubtedly occur.

There have been several studies of the energy and angular distributions of photoprotons, but relatively few of photoneutrons, probably owing to the difficulty of measuring neutrons in the unfavorable conditions which exist experimentally. In Section II angular-distribution measurements made here with a zinc sulphide – lucite detector are described and in Section III energy distributions for copper and lead are presented.

II. ANGULAR DISTRIBUTIONS

Experimental Arrangement

In measuring photoneutrons one must contend with very large background intensities of secondary electrons and gamma-rays which originate in the target placed in the X-ray beam to produce the photoneutrons. These intensities exceed the neutron intensity by a factor of roughly 1000. However it is possible to obtain the required discrimination against gamma-rays from the fact that the specific ionization of recoil protons is much higher than that of secondary electrons, provided that counting rates are kept low enough to avoid a pile-up of pulses during the high-intensity bursts of X-rays from the synchrotron. A suitable detector has been described by Hornyak (11). Grains of zinc sulphide of diameters in the range of 8–25 microns are molded in lucite, which serves to produce recoil protons and to transmit the emitted light to a photomultiplier. The sensitivity of this detector is found to increase almost linearly with neutron energy (24). This increase seems to be due to the fact that the average range of the recoil protons increases with neutron energy at a greater rate than the cross section for neutron–proton scattering decreases.

The experimental apparatus used here consisted of a target placed in the X-ray beam, a zinc sulphide – lucite detector at a distance of 25 cm. from the target, an EMI 6262 photomultiplier, a turntable to rotate the detector about the target, and associated electronic apparatus. A large shield of lead and paraffin was used to shield against the field of stray X-rays and neutrons from the donut of the synchrotron. A lead collimator with half-angle about 1°16′ was used to define the X-ray beam. Lead shielding of thickness approximately 2 in. was used about the photomultiplier.

In order to reduce the pile-up of small pulses, lead absorbers were also used between the target and detector. Aluminum absorbers alone, intended to reduce the electron intensity incident on the detector, were not sufficient. Some integral bias curves illustrating the effect of absorbers are shown in Fig. 1. Since the electron and gamma-ray intensities are strongly forward in their angular distributions, the thickness of absorber required must be determined experimentally for the smallest angle for which it is proposed to take measurements. For the present work this angle was 45°; from Fig. 1 it was decided that 2 in. of lead absorber was ample at this angle.

A further measure against pile-up was taken by maintaining the length of the X-ray pulse at a large value (about 200 μsec.) and thereby reducing the

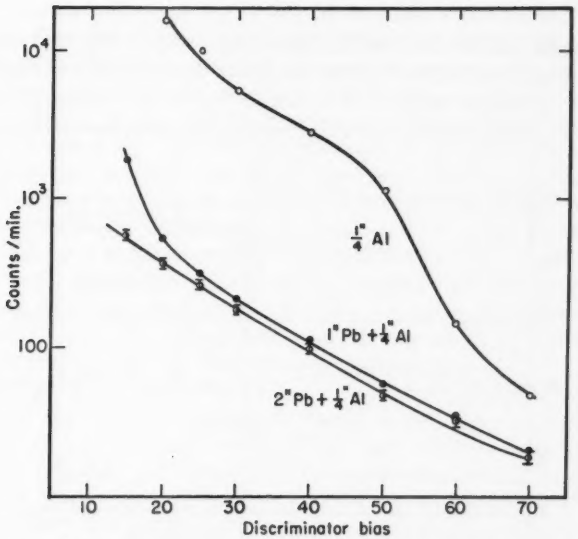

FIG. 1. Integral bias curves with the zinc sulphide – lucite detector at an angle of 45° to the X-ray beam. The source of photoneutrons was a lead target. The curve for an absorber of 1/4 in. aluminum shows the effect of a pile-up of small pulses.

instantaneous intensities. This was accomplished by cutting off the synchrotron r.f. when the magnetic field was near its peak value. A "beam-spilling" circuit was also tried, but it did not prove to be necessary.

Large targets were required to produce reasonable neutron counting rates. The targets used are listed in Table I. Two different beryllium targets were

TABLE I

TARGETS USED IN ANGULAR DISTRIBUTION MEASUREMENTS

Element	Radius (cm.)	Length (cm.)	Weight (gm.)
Lead	1.21	7.9	328
Tin	1.30	9.1	306
Copper	1.44	7.1	408
Iron	1.26	7.7	306
Aluminum	1.25	8.0	108
Carbon	2.37	8.4	246
Beryllium (1)		10.2	490
Beryllium (2)		5.08	91.3

used. In the first, which had dimensions 2 in. × 2 in. × 4 in., there was a considerable smearing of the emergent neutrons due to scattering of the neutrons within the target. A second target, in the form of a hollow cylinder of length 2 in., inside diameter 2.4 cm., and outside diameter 4.3 cm., was then obtained in order to reduce this effect.

Results

The angular distributions of the photoneutrons from the lead, tin, copper, iron, aluminum, and carbon targets are shown in Fig. 2, and the distributions for the two beryllium targets are shown in Fig. 3. The counting rates shown

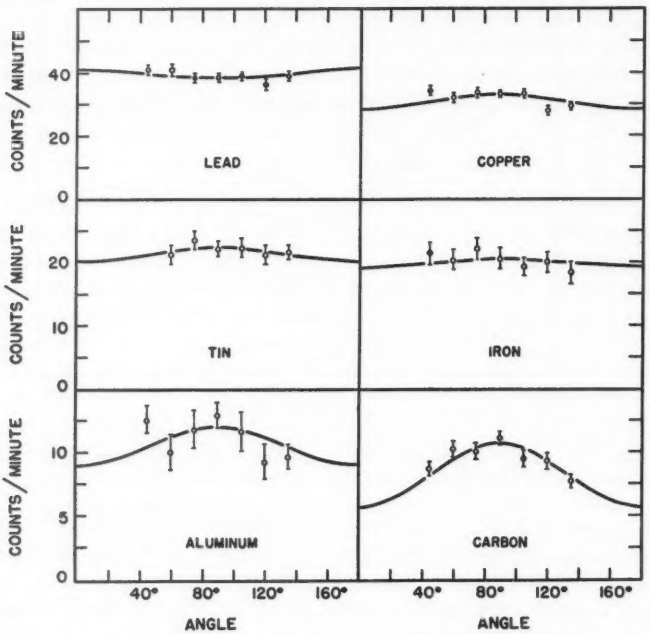

FIG. 2. The angular distributions of photoneutrons as measured with the zinc sulphide – lucite detector.

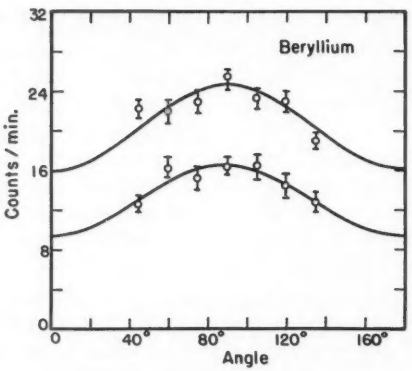

FIG. 3. The angular distribution of photoneutrons from beryllium targets as measured with the zinc sulphide – lucite detector. The upper curve is for the rectangular target, and the lower curve is for the hollow cylinder.

for the various elements have not all been normalized to one another. Angular distributions for most of the targets were obtained on several different days, and these results were then averaged. A single day's run consisted of two or three complete surveys of the angular positions, this being preferred to one survey with longer counting periods in order that any systematic drifts in the counting rate would be apparent. The X-ray beam intensity was monitored with an ionization chamber, and the output recorded on a moving chart. The counting rates with the X-ray beam on, but with no target, have been subtracted from the total counting rates to give the net rates shown in Figs. 2 and 3. The no-target background rate amounted to about half the total counting rate for the carbon target, and was relatively less important for the other targets. The errors assigned to the experimental points in Figs. 2 and 3 are root mean square deviations which include the effects of statistical uncertainties in both the total and background counting rates.

The solid curves shown in Figs. 2 and 3 have been obtained from least-squares fits of the experimental data to curves of the form $(a+b\sin^2\theta)$. The accuracy of the data does not warrant attempts to fit them to more complicated curves, although a forward shift in the peak seems to be present in most of the angular distributions. (This shift may be due in part to pile-up of gamma-ray pulses.) There is a theoretical as well as a practical reason for fitting the data to a simple curve. This is based on the theorem that if the absorbed photon has angular momentum $l\hbar$ the outgoing intensity distribution may contain spherical harmonics up to Y_{2l} only, provided that both the incident beam and the target are unpolarized. (See for example Sachs (22).) Since only photons of small angular momentum are absorbed appreciably, a simple angular distribution of the outgoing particles is expected.

A quantitative measure of the anisotropy is provided by the ratio b/a, although the accuracy of this quantity is low, particularly when b is small. The values obtained from the present results are summarized in Table II.

TABLE II

EXPERIMENTAL VALUES FOR b/a

Target	Correction factor for self-scattering	Corrected b/a
Lead	1.10	-0.08 ± 0.08
Tin	1.08	0.12 ± 0.17
Copper	1.48	0.23 ± 0.15
Iron	1.35	0.09 ± 0.25
Aluminum	1.17	0.36 ± 0.29
Carbon	1.8	$1.6\ \pm0.8$
Beryllium (1)	2.6	$1.2\ \pm0.4$
Beryllium (2)	1.35	

Corrections for the self-scattering of the photoneutrons within the targets have been made by assuming that one can replace the actual problem with a point source of neutrons located at the center of a spherical target and emitting according to $(a+b\sin^2\theta)$. The corrections obtained in this manner are also

given in Table II. It can be shown that in the particular geometry employed here the loss of angular resolution due to the finite size of the target, the finite size of the detector, and scattering in the lead absorbers is small compared to the effect of self-scattering.

In the heavy elements the angular distributions are seen to be nearly isotropic, indicating the predominance of the evaporation process. These results are in general agreement with the results of Price and Kerst (20) and of Palmer (17), both obtained with detectors involving the moderation of the fast neutrons and the subsequent capture of thermal neutrons. Geller, Halpern, and Yergin (7) have obtained similar results with a zinc sulphide – lucite detector. On the other hand, Price (19) and Poss (18) with Al(n, p) "threshold detectors", and Johannson (12) with a zinc sulphide – lucite detector have observed $b/a \approx 1$ in some heavy elements. In order to explain these various results, it is only necessary to suppose that the anisotropic neutrons on the average have a much higher energy and are much fewer in numbers than the isotropic neutrons. Then if the detector is sensitive at all to low-energy neutrons, the observed b/a ratio is essentially zero, while if the detector is sensitive only to high-energy neutrons, the observed b/a ratio is characteristic of the anisotropic process.

The variation of the observed b/a with mass number A can also be understood on this basis. With an Al(n, p) detector Price (19) found b/a to increase with increasing A. Since the evaporated neutrons tend to have lower energies in heavy nuclei, owing to the lower nuclear temperatures, this trend is probably caused by the rapidly decreasing sensitivity of his detector to evaporated neutrons, rather than by a change in the b/a value for the direct interactions alone. If the present results can be said to show a trend with A at all, it is that b/a decreases with increasing A. Since the response of the detector used here is not critically dependent on the energy of the evaporated neutrons, the present results can be interpreted as giving a qualitative indication of the relative importance of the evaporation and direct processes over a wide range of nuclei.

A large anisotropic component in carbon has been found in the present investigation, in contrast with previous results obtained with the moderator type of detector (17, 23). Both this large anisotropic component and the long tail observed on the high-energy side of the $C^{12}(\gamma, n)$ cross section curve (1) probably can be attributed to a rather large direct process. The remarks of Mann, Stephens, and Wilkinson (15) on the angular distribution of the photoprotons produced by 24-Mev. X-rays should also be noted in this connection.

A large peak has been found for beryllium in the present work and by Johannson (12). Since the b/a value found with zinc sulphide – lucite ($\backsim 1$) is greater than that found with the moderator type of detector ($\backsim 0.3$), it appears that the anisotropic neutrons are on the average more energetic than the isotropic neutrons. This result suggests that the effect of the low-energy anisotropic component, known to be present upon the absorption of 2.76-Mev. photons (9), has been masked by the usual behavior at high photon energies. The angular distributions of neutrons resulting from the absorption

of photons of intermediate energies are not known, although the disintegration processes found by Carver, Kondaiah, and McDaniel (4) make it seem unlikely that there would be marked anisotropy, at least for 6-Mev. photons.

Photoneutron Yields

The experimental data on the angular distributions were also used to give information on photoneutron yields as a function of atomic number. In making this analysis it was necessary to normalize the various counting rates. Corrections were applied for the absorption of the X-ray beam in the targets and for the lateral variation of the beam across the target. No attempt was made to correct for the effect of inelastic scattering of the photoneutrons within the target; inelastically scattered neutrons were detected with a reduced efficiency. It was found that the yield per mole varied approximately as Z^n, with $n = 1.7 \pm 0.2$. This result is in accord with other measurements: with the moderator type of detector, the yield per mole is found to vary approximately as Z^2 (20, 17, 23), while if only high-energy neutrons are counted, the yield is found to vary as $(A-Z)$ (12).

III. ENERGY DISTRIBUTIONS

Experimental Procedure and Results

In many methods for the determination of the energy distribution of neutrons it is necessary to measure the total ionization loss of recoil protons. For photoneutrons it is also necessary to provide sharp discrimination against gamma-rays. These requirements often place a lower limit on the neutron energy which can be measured. For example a proton telescope in which both E and dE/dx are measured cannot be successfully used below about 5 Mev. Roughly the same energy limitation applies to a two-crystal delayed-coincidence spectrometer in which the discrimination against gamma-rays is achieved by arranging that the second pulse due to a scattered neutron occurs at a time appreciably later than the second pulse due to a scattered gamma-ray. Nuclear emulsions seem to the author to be the best means presently available for measuring the complete spectrum of the photoneutrons produced by high-energy X-ray beams.

Ilford C2 plates of dimensions 1 in. $\times$ 3 in. and emulsion thickness 200 μ were exposed to neutrons produced in copper and lead targets irradiated in the X-ray beam. The plates were exposed at angles of 60°, 90°, and 120° and at a distance of 22 cm. from the target to the center of the plate. Background exposures were made with the target removed. A lead shield of thickness 1/8 in. was interposed between the target and plates in order to reduce the electron intensity incident on the plates, no correction to the observed energy distributions being required for this thickness. The large shield of lead and paraffin and the collimator mentioned above were used.

The targets were chosen small enough that no correction to the observed energy distribution would be necessary because of inelastic scattering in them. The copper target was a cylinder of length 1 in. and radius 3/8 in. The lead target was roughly spherical in shape, with the radius corresponding to about 0.05 of a mean free path for inelastic scattering.

The following criteria were used for the selection of recoil-proton tracks. Each track had to lie in a square pyramid of half-angle 20° in the unprocessed emulsion, the axis of the pyramid being parallel to the edge of the plate, and the apex being located at the beginning of the track. The track had to start and stop in the emulsion. Individual calculations were made on each track, both because of the rather large acceptance angles, and in order to make sure that no "good" tracks were lost. The range–energy relation of Rotblat (21) was used to ascertain the proton energies, and the neutron energies were then calculated using the known angle of the track. All tracks due to neutrons of energies less than 0.5 Mev. were ultimately discarded, because of the non-agreement of different observers in this energy range. The experimental distributions were corrected for the escape of proton tracks through the sides of the emulsion, and for the neutron–proton scattering cross section. The areas scanned and the total numbers of acceptable tracks are given in Table III.

TABLE III

TRACKS USED IN ENERGY-DISTRIBUTION MEASUREMENTS

Target	Area scanned ($mm.^2$)	Number of acceptable tracks
Copper	217	991
Lead	140	259
None	166	60

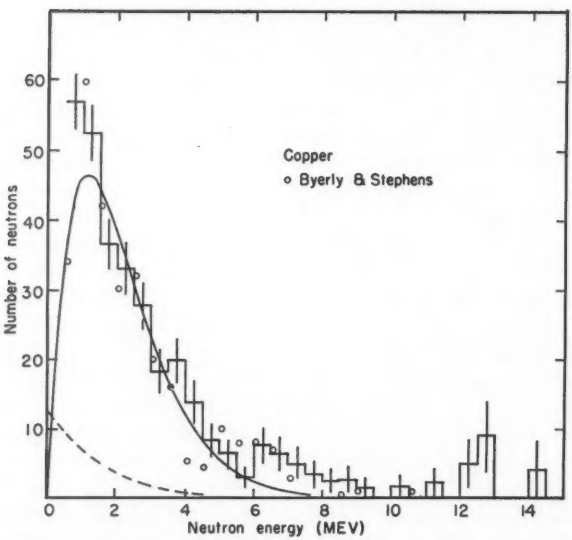

FIG. 4. The energy distribution of photoneutrons from copper. The histogram represents the present results, and the circles the results of Byerly and Stephens. The solid and dashed curves are calculated for the evaporation of first and second neutrons, respectively, their sum being normalized to the histogram.

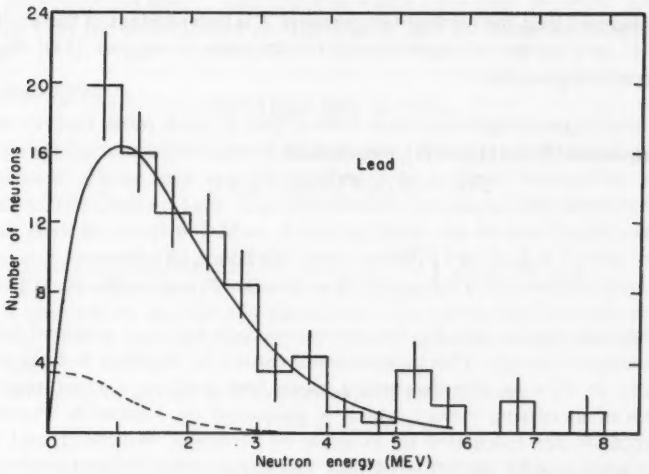

FIG. 5. The energy distribution of photoneutrons from lead. The solid and dashed curves are calculated for the evaporation of first and second neutrons, respectively.

The experimental neutron energy distribution for copper* is shown in Fig. 4, and the distribution for lead is shown in Fig. 5. These distributions have been corrected for the no-target background, which was found to be appreciable only in the energy interval 0.5–1.0 Mev. The errors shown are root mean square deviations based on the number of tracks observed. The data shown for copper are averages of results obtained at angles of 90° and 60°, there being no significant differences between the two distributions in the energy range 0.5–5 Mev. For higher energies there seemed to be more tracks in the 90° plate. The data shown for lead were obtained at 120°.

The Evaporation Process

From formulae given by Blatt and Weisskopf (2), the energy distribution for evaporated photoneutrons is expected to be of the form

$$[1] \qquad J(\eta)\,d\eta = d\eta\,\frac{2M}{\hbar^2}\,\eta\sigma(\eta)\int_{B+\eta}^{E_{\max}} \frac{I_\gamma(E)\,\sigma_{\gamma,n}(E)\,\omega(E-B-\eta)}{F_n(E-B)}\,dE,$$

where η is the neutron energy, M is the neutron mass, $\sigma(\eta)$ is the cross section for formation of the compound nucleus by absorption of a neutron of energy η, B is the photoneutron threshold, E is the photon energy, $E_{\max}$ is the maximum photon energy, I_γ is the spectral distribution of X-rays, $\sigma_{\gamma,n}$ is the sum of the partial cross sections for which the first particle evaporated is a neutron, $\omega(U)$ is the level density of the residual nucleus at excitation U, and finally

$$[2] \qquad F_n(E-B) = \frac{2M}{\hbar^2}\int_0^{E-B} \eta\sigma(\eta)\,\omega(E-B-\eta)\,d\eta.$$

*The author wishes to acknowledge the generous assistance of Dr. D. L. Livesey in measuring the tracks used for this distribution.

If it is assumed that the nuclear temperature T is independent of the excitation energy U, as a variety of experimental results seem to suggest (14), then the level density is given by

$$\omega(U) = \omega(0) \exp(U/T). \quad [3]$$

Using equation [3] in [1] and [2], one obtains

$$J(\eta) = f_1(\eta, T) \exp(-\eta/T), \quad [4]$$

where

$$f_1(\eta, T) = \frac{\eta}{T^2} \int_{B+\eta}^{E_{\max}} \frac{I_\gamma(E)\, \sigma_{\gamma,n}(E)\, dE}{1-[1+(E-B)/T] \exp[-(E-B)/T]}. \quad [5]$$

Here the cross section $\sigma(\eta)$ for the inverse reaction has been assumed independent of neutron energy. This independence cannot be expected to hold strictly, especially in view of the decreasing mean free path in nuclear matter for nucleons of increasing energy which is envisaged by Feshbach, Porter, and Weisskopf (6) and calculated for example by Morrison, Muirhead, and Rosser (16). It must also be remembered that this cross section refers to the capture of neutrons by the residual nucleus when it is in an excited state.

Equations [4] and [5] can be used to determine the nuclear temperature from the experimental data by a process of successive approximations. The first approximation is to consider the incident photons to be monoenergetic, so that f_1 varies linearly with η. From a plot of $\log[J_{\text{exp}}/\eta]$ vs. η one obtains a first approximation to the temperature, which can then be used to evaluate f_1, and hence to obtain the next approximation to T. The integral in f_1 is not sensitive to T, so that the process is rapidly convergent.

The procedure can be modified to include the second neutrons emitted in $(\gamma, 2n)$ reactions, if it is assumed that the residual nucleus after the emission of two neutrons has the same temperature as the nucleus left after the emission of the first neutron. One obtains a double integral similar to [5], which we denote by f_2; for the determination of the nuclear temperature one now replaces f_1 by (f_1+f_2). For copper we estimate that $f_2 < 0.15\, f_1$ for $\eta > 1$ Mev., so that higher order reactions probably can be neglected.

The nuclear temperature found in this way for copper is $T = 1.2 \pm 0.1$ Mev., and for lead is $T = 1.0 \pm 0.2$ Mev. These values of the temperatures seem to be significantly higher than those found by Graves and Rosen (8) for the inelastic scattering of 14-Mev. neutrons, namely $T = 0.77 \pm 0.08$ Mev. for copper and $T = 0.76 \pm 0.08$ for lead.

The neutron energy distributions, calculated from equations [4] and [5] with the above values of the nuclear temperatures, are shown as the solid curves in Figs. 4 and 5. The dashed curves represent the results of the analogous calculations for the second neutrons. The sums of the two curves have been normalized to the experimental distributions. The results of Byerly and Stephens (3) for copper are shown as circles in Fig. 4. The agreement with the present results is very good, except possibly at high energies; this can be attributed to their relatively low maximum X-ray energy (24 Mev.). The only

other photoneutron energy distributions which have been reported are those of Price (19) for silver, based on 129 tracks, and for bismuth, based on 196 tracks.

The Direct Effect

It is evident from Figs. 4 and 5 that there are high-energy tails on the energy distributions which cannot be accounted for by a conventional evaporation process. These tails can be attributed to a direct interaction process, possibly of the Courant type. The distribution for copper also appears to have a broad peak at about 6–7 Mev. A similar peak can be seen in the results of Byerly and Stephens at a slightly lower energy. For lead a similar peak at 5–6 Mev. is observed, but since there are only seven tracks represented in this peak, it may not be statistically significant. The results for bismuth, reported by Price, show a similar peak at 6–7 Mev., while his results for silver are inconclusive.

It is tempting to assume that this broad peak has the form

$$J(\eta) \backsim I_\gamma(B+\eta)\, \sigma_{\gamma,n}(B+\eta), \tag{6}$$

so that the energy of the peak corresponds to the energy of the giant resonance relative to the photoneutron threshold. When $\sigma_{\gamma,n}$ is weighted with I_γ, the peak given by equation [6] is shifted by about one Mev. towards the low-energy end. Equation [6] is based on the assumption that the shape of the cross-section curve for the photoemission of these neutrons is approximately the same as that observed for the total (γ, n) reaction; this is consistent with the view that even when a compound nucleus is formed, the primary absorption process involves one nucleon only. Further detailed speculation does not seem to be warranted until further experimental evidence is forthcoming.

IV. CONCLUSIONS

From the angular distributions it is possible to conclude that in heavy nuclei, the evaporation of photoneutrons from a compound nucleus is much more important than direct ejection. The results for carbon and beryllium probably indicate large direct effects in these nuclei. The relative neutron yields agree with previous results.

The energy distributions in copper and lead can be largely accounted for by an evaporation process governed by a constant nuclear temperature rather than by a temperature which increases with the excitation energy of the residual nucleus. The temperature found for copper is 1.2 Mev. and for lead is 1.0 Mev., both slightly higher than the temperatures found from the inelastic scattering of 14-Mev. neutrons. The high-energy tails on the energy distributions are attributed to a direct effect, possibly of the Courant type, while broad peaks at about 6 Mev. may be due to a special direct process.

ACKNOWLEDGMENTS

This work has formed part of the synchrotron program under the general supervision of Professor B. W. Sargent. It is a pleasure to thank Professor Sargent for suggesting this investigation, Professor L. E. H. Trainor and

Dr. D. L. Livesey for many valuable discussions, and Mr. H. Janzen for operating the synchrotron. The author gratefully acknowledges financial assistance from the National Research Council of Canada and a Fellowship from the Shell Oil Company of Canada. Financial support for the synchrotron program has been received from the Atomic Energy Control Board.

REFERENCES

1. BARBER, W. C., GEORGE, W. D., and REAGAN, D. D. Phys. Rev. 98:73. 1955.
2. BLATT, J. M. and WEISSKOPF, V. F. Theoretical nuclear physics. John Wiley & Sons, Inc., New York. 1952.
3. BYERLY, P. R. and STEPHENS, W. E. Phys. Rev. 83:54. 1951.
4. CARVER, J. H., KONDAIAH, E., and MCDANIEL, B. D. Phil. Mag. 45:948. 1954.
5. COURANT, E. D. Phys. Rev. 82:703. 1951.
6. FESHBACH, H., PORTER, C. E., and WEISSKOPF, V. F. Phys. Rev. 96:448. 1954.
7. GELLER, K., HALPERN, J., and YERGIN, P. F. Phys. Rev. 95:659. 1954.
8. GRAVES, E. R. and ROSEN, L. Phys. Rev. 89:343. 1953.
9. HAMERMESH, B., HAMERMESH, M., and WATTENBERG, A. Phys. Rev. 76:611. 1949.
10. HAUSER, W. and FESHBACH, H. Phys. Rev. 87:366. 1952.
11. HORNYAK, W. F. Rev. Sci. Instr. 23:264. 1952.
12. JOHANNSON, S. Phys. Rev. 97:434. 1955.
13. LEVINGER, J. S. Phys. Rev. 84:43. 1951.
14. LIVESEY, D. L. Can. J. Phys. 33:391. 1955.
15. MANN, A. K., STEPHENS, W. E., and WILKINSON, D. H. Phys. Rev. 97:1184. 1955.
16. MORRISON, G. C., MUIRHEAD, H., and ROSSER, W. G. V. Phil. Mag. 44:1326. 1953.
17. PALMER, J. F. M.Sc. Thesis, Queen's University, Kingston, Ont. 1955.
18. POSS, H. L. Phys. Rev. 79:539. 1950.
19. PRICE, G. A. Phys. Rev. 93:1279. 1954.
20. PRICE, G. A. and KERST, D. W. Phys. Rev. 77:806. 1950.
21. ROTBLAT, J. Nature, 167:550. 1951.
22. SACHS, R. G. Nuclear theory. Addison-Wesley Publishing Company, Inc., Cambridge, Mass. 1953.
23. TERWILLIGER, K. M., JONES, L. W. and JARMIE, W. N. Phys. Rev. 82:820. 1951.
24. WHITEHEAD, W. D. and SNOWDON, S. C. Phys. Rev. 92:114. 1953.
25. WOLFENSTEIN, L. Phys. Rev. 82:690. 1951.

THE ZERO-POINT KINETIC ENERGY OF LIQUID HELIUM[1]

By D. G. Henshaw and D. G. Hurst

ABSTRACT

The zero-point kinetic energy of liquid helium has been calculated from the interatomic potential, the latent heat of vaporization, and atomic distributions derived from neutron diffraction measurements. Calculations were carried out for two liquid temperatures and several published interatomic potential functions. The resulting values of the "zero-point temperature" lie between 9.0°K. and 12.6°K.

An experimental value of the zero-point kinetic energy of liquid helium can be obtained[2] from the radial distribution function, the interatomic potential, and the latent heat of vaporization. If the energy of a system of helium atoms is taken as zero when they are at rest and well separated, and the departure from an ideal gas neglected for the moment, the internal energy per atom of gaseous helium at temperature T is $3kT/2$ and the enthalpy per atom is

[1] $$H_{gi} = \tfrac{3}{2}kT + PV_g = \tfrac{5}{2}kT$$

where P is the pressure and V_g the volume per atom. The non-ideal character of the gas was taken into account by using

$$\begin{aligned} H_g &= H_{gi} + kT(B - T\,dB/dT)/U \\ &= H_{gi} + \Delta H \end{aligned}$$

where B is the second virial coefficient per mole, U is the molar volume, and ΔH stands for the correction term.

The kinetic energy per atom of liquid helium at a temperature T can be expressed as $\frac{3}{2}k\Phi$ where Φ is a temperature. In the cases to be considered the temperature T is small compared to the Debye characteristic temperature. Under these conditions Φ is nearly equal to the "zero-point temperature" (6). The potential energy per atom is

$$\frac{1}{2}\int_0^\infty 4\pi r^2 \rho(r) V(r)\, dr$$

where r is the radial distance from an atom, $\rho(r)$ is the atomic density, and $V(r)$ is the interatomic potential of helium.

The enthalpy per atom of the liquid is equal to

[2] $$H_l = \frac{3}{2}k\Phi + \frac{1}{2}\int_0^\infty 4\pi r^2 \rho(r) V(r)\, dr + PV_l$$

where V_l is the volume per atom of the liquid. The latent heat of vaporization per atom is

[3] $$L = H_g - H_l.$$

[1]*Manuscript received July 29, 1955.*
Contribution from Division of Physics, Atomic Energy of Canada Limited, Chalk River, Ontario. Issued as A.E.C.L. No. 247.
[2]*This was pointed out to us by Professor J. G. Kirkwood.*

Equations [1], [2], and [3] yield

$$[4] \qquad \Phi = \frac{5T}{3} - \frac{2L}{3k} - \frac{1}{3k}\int_0^\infty 4\pi r^2 \rho(r) V(r)\, dr + \frac{2}{3k}(\Delta H - PV_l).$$

It is convenient to write equation [4] in the form

$$\Phi = A + I$$

with

$$A = 5T/3 - 2L/3k + 2\Delta H/3k - 2PV_l/3k,$$

$$I = -(1/3k)\int_0^\infty 4\pi r^2 \rho(r) V(r)\, dr.$$

A is independent of the interatomic potential chosen for the calculation; I, which represents the potential energy in the same way as Φ represents the kinetic energy, depends directly on the potential function and the atomic distribution. Calculations have been carried out with the potential functions listed in Table I where the notation follows Reference (3) and using $4\pi r^2\rho(r)$

TABLE I

LIST OF POTENTIAL FUNCTIONS

Form	Designation	ϵ/k, °K.	α	r_m, Å
$V(r) = \frac{\epsilon}{1-(6/\alpha)}\left[\frac{6}{\alpha}\exp[\alpha(1-r/r_m)] - \left(\frac{r_m}{r}\right)^6\right]$	MR-1	9.16	12.4	3.135
	MR-5	7.5628	12.4	3.1894
	S-K	9.25	13.54	2.943
$V(r) = \epsilon\left[\left(\frac{r_m}{r}\right)^{12} - 2\left(\frac{r_m}{r}\right)^6\right]$	LJ-1	10.22		2.86911

determined experimentally (2) at 4.24°K. and at nominally 2°K. (average of results at 1.65, 1.95, and 2.25°K.). The values of A are given in Table II.

TABLE II

VALUES OF A

Helium temperature, °K.	$5T/3$, degrees	$2L/3k$, degrees	$2\Delta H/3k$, degrees	$2PV_l/3k$, degrees	$A = 5T/3 - 2L/3k + 2\Delta H/3k - 2PV_l/3k$, degrees
2	3.33	7.47	−0.1	0.00	−4.24
4.24	7.07	7.00	−1.86	0.26	−2.05

Latent heat contributions were deduced from 23.2 joules/gm. at 2°K. and 21.8 joules/gm. at 4.24°K. (5). The values of B required for ΔH were taken from Reference (4).

The resulting values of Φ at 2°K. and 4.24°K. are given in Table III. Because the potentials increase very rapidly as r decreases below the finite root of $V(r) = 0$, small errors in $\rho(r)$ in this region can contribute appreciably to the integral. Inspection of the experimental $r\rho(r)$ curves suggested that the non-zero values for $r \leqslant 2.2$Å are spurious. Accordingly most of the integrals were

TABLE III

VALUES OF Φ FOR VARIOUS POTENTIALS

Potential type	$T = 2°K.$, $A = -4.24°$		$T = 4.24°K.$, $A = -2.0°$	
	I, degrees	$\Phi = A+I$, degrees	I, degrees	$\Phi = A+I$, degrees
MR-1	15.9	11.7	14.4	12.4
MR-5	13.1	8.9	12.0	10.0
S-K	13.4	9.2	11.8	9.8
LJ-1	14.3	10.1	12.4	10.4
LJ-1*	13.3	9.1	12.1	10.1

calculated with $\rho(r) = 0$ for $0 \leqslant r \leqslant 2.2$Å. To check this assumption, Morse potentials were fitted to MR-5 and LJ-1, and the wave mechanical density of a diatomic combination was calculated for each of these potentials. Comparison of the calculated and observed $\rho(r)$ justified the cutoff at $r = 2.2$Å for MR-5, but showed that perhaps the observed $\rho(r)$ should be used at $r = 2.2$Å for LJ-1. The results of retaining the observed $\rho(r)$ at $r = 2.2$Å are shown starred in Table III. These are preferred over the unstarred values for LJ-1.

More figures are given than the accuracy warrants in order to show the variation caused by the different potentials. Errors are difficult to assess but may well be 1 or 2 degrees. There is some doubt about the latent heat at the higher temperature. If instead of Kistemaker's result we use a lower value (1) of 20.3 joules/gm. the effect is to increase Φ for 4.24°K. by 0.5°.

The quantity Φ represents the kinetic energy of the liquid at the temperature of the measurement. Because it includes some temperature excitation Φ is slightly larger than the zero-point temperature and is expected to increase with temperature. The 4.24°K. values in Table III exceed the 2°K. values by an average of 0.7° which is more than would be predicted for a simple structure. For example, if liquid helium behaved like a simple Debye solid with a characteristic temperature of 26°K. (a value commonly assumed for helium) about one half the heat content at constant volume would contribute to the temperature excitation. Expressed in degrees in a manner comparable with Φ the heat contents for the Debye model are 0.035° at 2°K. and 0.626° at 4.24°K., giving a predicted change of $(0.626-0.035)/2 = 0.3°$ in Φ between these two temperatures. Some or all of the difference between 0.7° and 0.3° may arise from experimental error. On the other hand the energy associated with the lambda transition may contribute to the difference.

An upper limit of 0.5° for the amount by which Φ at 2°K. is larger than the zero-point temperature is obtained from the integral of specific heat under saturated vapor pressure from 0 to 2°K. This is possibly a gross overestimate and in view of the experimental errors the 2°K. values of Φ in Table III may be considered to represent also the zero-point temperature.

ACKNOWLEDGMENTS

We should like to thank Professor J. G. Kirkwood and Dr. Robert M. Mazo for helpful criticisms and suggestions during the preparation of this paper.

REFERENCES

1. BERMAN, R. and POULTER, J. Phil. Mag. 43: 1047. 1952.
2. HURST, D. G. and HENSHAW, D. G. Phys. Rev. In press. 1955.
3. KILPATRICK, J. E., KELLER, W. E., and HAMMEL, E. F. Phys. Rev. 97: 9. 1955.
4. KILPATRICK, J. E., KELLER, W. E., HAMMEL, E. F., and METROPOLIS, N. Phys. Rev. 94: 1103. 1954.
5. KISTEMAKER, J. Physica, 12: 281. 1946.
6. MAZO, R. M. and KIRKWOOD, J. G. Proc. Natl. Acad. Sci. U.S. 41: 204. 1955.

THE SPECTRUM OF THE Si_2 MOLECULE[1]

By A. E. Douglas

ABSTRACT

Two band systems attributed to the Si_2 molecule have been excited in a discharge tube. The first of these is a $^3\Pi - {}^3\Pi$ system of red-shaded bands with heads at 3489, 3556, 3626, and 3696 Å. The second is an extensive system of $^1\Sigma - {}^1\Sigma$ bands in the visible and near ultraviolet region. High resolution spectra have been analyzed and the rotational and vibrational constants have been determined.

I. INTRODUCTION

The electronic structures of silicon and carbon are similar and the Si_2 molecule might be expected to show a spectrum similar to that of the well-known C_2 spectrum. The only published account of a spectrum attributed to Si_2 is a short note on some flame bands which were photographed at low resolution by Downie and Barrow (1). Recently in this laboratory two new band systems have been excited in an electric discharge and it has been shown that these bands are due to Si_2. The method of excitation and the analyses of the bands are discussed in this paper.

II. EXPERIMENTAL

Silane at a few millimeters pressure was admitted into a discharge tube with aluminum electrodes and a discharge passed through the gas. This process deposited a grayish film (presumably Si) on the walls of the tube and on the electrodes. The residue of the SiH_4 was then pumped out and a few millimeters pressure of xenon admitted to the tube. By means of a small centrifugal pump, the xenon was circulated over a heated mixture of active uranium and uranium hydride (4) which served the dual purpose of purifying the xenon and maintaining a small constant partial pressure of hydrogen in the discharge tube. When a discharge of low current density was passed through the tube, the bands, described below, were observed.

The spectrum was photographed first on a Hilger medium quartz spectrograph and later on a 35-ft. concave grating spectrograph. Because the bands were weak, a wide slit was used with the large spectrograph and the resolving power was limited to about 150,000. This resolving power proved to be quite sufficient to resolve the fine structure of the bands. For the stronger bands an exposure time of one hour was sufficient but for the weaker bands even an exposure time of thirty hours proved insufficient.

Besides the very strong bands of the $^2\Delta - {}^2\Pi$ system of SiH, which will be discussed in a later paper, the low resolution plates showed four double-headed red-shaded bands with their short wavelength heads at 3489.1, 3556.5, 3625.9, and 3695.5 Å. In addition, a number of weak and almost headless bands could be seen extending from 3980 Å into the red. Subsequent analysis of the two band systems from high resolution plates showed that the stronger bands

[1]*Manuscript received August 25, 1955.*
Contribution from the Division of Pure Physics, National Research Council, Ottawa 2, Ontario. Issued as N.R.C. No. 3791.

are due to a $^3\Pi - ^3\Pi$ transition of Si_2 and the weaker bands are due to a $^3\Sigma - ^3\Sigma$ transition of the same molecule.

III. THE $^3\Pi - ^3\Pi$ BAND SYSTEM

A reproduction of the band at 3626 Å is shown in Fig. 1. The bands at 3489, 3556, and 3697 Å are similar in appearance and it was at once apparent that these bands form a lower state progression. The structure of the bands is, however, most unusual since they show only two distinct heads, but a large number of branches, many of which end abruptly. The fact that some of the branches in the bands show a "staggering" (see (2), p. 268) indicates that the bands arise from a homonuclear molecule with zero nuclear spin. Close to the strong band heads, two weaker heads can be seen (see Fig. 1) and the positions and intensities of these heads leave no doubt that they arise from the less abundant isotopes of silicon. Thus it was quite apparent that the bands arose from a transition of an Si_2 (or Si_2^+) molecule, but, because of the unusual appearance of the bands, it was not at all apparent what type of electronic transition was involved. It was only by a detailed investigation of the common combination differences of the upper state of the bands that it was shown that each band possesses three P and three R branches and that they can be readily interpreted as bands resulting from a $^3\Pi - ^3\Pi$ transition. The peculiar appearance arises from the fact that only portions of two of the subbands are present and only the subband of longest wavelength is essentially complete. The wave numbers of the lines of the (0, 1), (0, 2), and (0, 3) bands and their rotational numberings are given in Table I. The excellent agreement of the combination differences of the upper state leaves no doubt that this assignment is correct and that the large number of missing lines arises from some unusual sort of predissociation.

For a $^3\Pi$ state with Hund's case *a* coupling, the three spin components $^3\Pi_2$, $^3\Pi_1$, and $^3\Pi_0$ can be treated independently and to each component can be assigned an effective B value designated by B^*. The component with the largest effective B value (that is, the component whose energy levels lie highest) is designated as the F_3 component. In the Si_2 band it is found that the subband lying at longest wavelength has the largest effective B values in both the upper and lower electronic states and therefore involves the F_3 components.

It is well known that, for a homonuclear molecule with zero nuclear spin, the Λ-doubling of the rotational levels of a Π state shows up in the bands of a $\Pi - \Pi$ transition as a staggering of the lines of the branches. For a $^3\Pi$ state (case *a*), the Λ-doubling is largest for the $^3\Pi_0$ component. In the observed Si_2 bands, the subband lying at longest wavelength has much the largest staggering band and, therefore, is most probably the $^3\Pi_0 - ^3\Pi_0$ subband. It appears, therefore, that in both the upper and lower electronic states, the $^3\Pi_0$ component is the F_3 component or, in other words, both $^3\Pi$ states are inverted.

The spin coupling constants A cannot be determined accurately from a $^3\Pi - ^3\Pi$ transition in which only transitions with $\Delta\Sigma = 0$ are observed. Rough values of A can be found from the approximate equation

$$B^* = B_e[1 \pm (2B/A)]. \qquad [1]$$

TABLE I

WAVE NUMBERS OF THE LINES OF THE $^3\Pi - ^3\Pi$ SYSTEM OF Si_2

J	$P_1(J)$	$R_1(J)$	$P_2(J)$	$R_2(J)$	$P_3(J)$	$R_3(J)$
			(0, 1) Band			
5	28103.98					
6	03.18					
7	02.34					
8	01.46					
9	00.51					
10	28099.52					
11	98.48	28108.96				
12	97.36	08.76				
13	96.19	08.51				
14	94.98	08.15				
15	93.69	07.75			27999.28	
16	92.33				98.32	
17	90.91				97.09	28013.97
18					96.08	13.97
19					94.76	13.59
20					93.70	13.44
21					92.28	13.00
22					91.14	12.79
23					89.67	12.26
24					88.48	12.00
25					86.89	11.41
26					85.61	11.08
27					83.97	10.36
28					82.62	09.96
29					80.95	09.20
30					79.46	08.72
31					77.69	07.88
32					76.16	07.33
33					74.30	06.42
34					72.71	05.78
35					70.76	04.77
36					69.09	04.07
37				28046.33	67.08	02.99
38		28089.13	28009.00**	45.24	65.29	02.16
39		87.61	06.85	44.01	63.22	01.02
40		86.11	04.77*	42.85	61.38	00.13
41		84.64	02.38*	41.59	59.22	27998.88
42	44.01	83.10	00.31	40.32	57.28	97.09
43	41.41	81.52	27997.79*	38.91	55.03	96.59
44	38.91	79.88	95.72	37.61	53.03	95.53
45	36.18	78.23	93.34	36.18	50.69	94.13
46	33.59	76.55	90.98	34.75	48.61*	92.94*
47	30.93	74.80	88.48	33.20	46.18	91.39
48	28.24	73.00	86.08	31.68	43.99	89.91
49	25.47	71.18	83.51	30.04		
50	22.67	69.33	80.95	28.44		
51	19.88	67.43	78.37			
52	16.99	65.49	75.74			
53		63.49	72.96			
54		61.50	70.14			
55						
56						
57						
58						
59						
60						
61						
62					08.02	
63					04.85	
64					02.06	
65					27898.91	

TABLE I (*continued*)

WAVE NUMBERS OF THE LINES OF THE $^2\Pi - ^2\Pi$ SYSTEM OF Si_2 (*continued*)

J	$P_1(J)$	$R_1(J)$	$P_2(J)$	$R_2(J)$	$P_3(J)$	$R_3(J)$
			(0, 1) Band			
66					27896.04	
67					92.84	
68					89.90	
69					86.59	
70					83.60	
71					80.20	
72					77.13	
73					73.61	
			(0, 2) Band			
4	27566.59					
5	65.80					
6	65.05					
7	64.25					
8	63.36					
9	62.45					
10	61.50					
11	60.47					
12	59.41	27570.81				
13	58.28	70.60				
14	57.10	70.35				
15	55.86	69.92			27461.38	
16	54.56				60.59	
17	53.17				59.40	27476.26
18					58.46	76.26
19					57.18	75.95
20					56.17	75.95
21					54.85	75.49
22					53.79	75.49
23					52.38	74.95
24					51.24	74.79
25					49.75	74.22
26					48.54	74.01
27					47.00	73.40
28					45.72	73.09
29					44.11	72.38
30					42.76	72.03
31					41.07	71.28
32					39.64	70.81
33					37.88	69.99
34				27513.97	36.40	69.46
35				12.24	34.56	68.59
36				11.33	33.01	67.97
37				10.30	31.09	67.00
38			27473.09*	09.36	29.45	66.32
39			71.04	08.30*	27.74	65.25
40			69.02	07.20	25.78	64.50
41		49.07	66.82	06.06	23.72	63.40
42	08.30**	47.63	64.89	04.94	21.94	62.58
43	06.06*	46.21	62.72*	03.67	19.81	61.38
44	03.67*	44.73	60.46	02.49	17.95	60.46
45	01.18*	43.19	58.18	01.18*	15.75	59.21
46	27498.71	41.64	56.17	27499.88	13.81*	58.18
47	96.19	40.02	53.79	98.52	11.52	56.77
48		38.37	51.51	97.13	09.49	
49	90.96	36.72	49.12	95.66		
50	88.33	35.00	46.75	94.21		
51	85.67	33.25	44.25			
52	82.95	31.48	41.78			
53	80.21	29.67				
54	77.43	27.76				

TABLE I (*concluded*)

WAVE NUMBERS OF THE LINES OF THE $^3\Pi - ^3\Pi$ SYSTEM OF Si_2 (*concluded*)

J	$P_1(J)$	$R_1(J)$	$P_2(J)$	$R_2(J)$	$P_3(J)$	$R_3(J)$
			(0, 3) Band			
6	27031.78					
7	30.96					
8	30.12					
9	29.26					
10	28.31					
11	27.35					
12	26.30					
13	25.19	27037.51				
14	24.05	37.28				
15	22.87					
16	21.62				26927.75	
17	20.24				26.56	
18					25.77	
19					24.49	26943.29
20					23.57	43.21
21					22.28	42.87
22					21.31	42.87
23					19.91	42.39
24					18.89	42.39
25					17.41	41.97
26					16.36	41.81
27					14.95	41.29
28					13.71	41.08
29					12.16	40.48
30					10.91	40.17
31					09.32	39.52
32					08.02	39.19
33					06.34	38.47
34					04.95	38.04
35					03.22	37.26
36					01.81	36.77
37					00.04	35.95
38					26898.50	35.37
39					96.61	34.40
40		19.59			95.07	33.77
41		18.34			93.14	32.82
42		17.02			91.46	32.09
43		15.72			89.48	31.07
44		14.37	26930.29	26972.23	87.76	30.29
45	26970.99	12.95	28.25	70.99	85.70	29.14
46	68.64	11.52	26.13	69.90	83.88*	28.25*
47	66.15	10.08	23.97	68.64	81.76	26.98
48	63.79	08.60	21.81	67.45	79.89	
49	61.34	07.09	19.57	66.15		
50	58.85	05.50	17.41	64.84		
51	56.40	03.91	14.95			
52	53.78	02.29	12.72	61.84		
53	51.21	00.63				
54	48.59	26998.95				
55	45.93					

* *Overlapped.*
***Calculated value; seen but not measured.*

For the (0, 1) band it was found (by comparing $\Delta_2 F(J)$ values at $J \sim 46$) that the difference in the effective B values of the $^3\Pi_0$ and $^3\Pi_2$ components is 0.0036_5 in the lower electronic state and 0.079_7 in the upper. These differences combined with the observed B^* values give $A'' = 71.6$ and $A' = 27.6$. The A'' value is probably the best value that can be obtained from the observed experimental

data. On the other hand, A' is sufficiently small that for $J = 46$ we no longer have case a coupling and equation [1] is not valid. A more accurate value can be determined by finding a value of A which, when substituted into Budó's equations (2, p. 235) for the energy levels, will give the observed differences between $\Delta_2F(J)$ of the $^3\Pi_0$ and $\Delta_2F(J)$ of the $^3\Pi_2$ component. When calculated in this way, A' is found to be 16.5 cm^{-1}. Neither A' nor A'' is determined accurately since not only is this method of finding A quite inaccurate, but, in the Si_2 bands, predissociations in the $^3\Pi_2$ component make it impossible to compare very accurately the $\Delta_2F'(J)$ values of the two components. The difference in the positions of the origins of the $^3\Pi_0$ and $^3\Pi_2$ subbands should be given by $2(A'-A'')$. The observed difference in the band origins is 98.1 cm^{-1} while the value calculated from the above A values is 110.2 cm^{-1}.

The B values of both electronic states can best be determined from the $^3\Pi_0$ subband since here long P and R branches are observed. For the lower state where A is large, the effective B value of the $^3\Pi_0$ component was found by assuming

$$\Delta_2F(J) = 4B^*(J+\tfrac{1}{2})-8D(J+\tfrac{1}{2})^3.$$

From this $B^{*\prime\prime}$ value and from A'', the true B'' value was determined by Eq. [1]. For the upper electronic state where A is small, the true B value was obtained directly by fitting the observed $\Delta_2F'(J)$ values to an expression for $\Delta_2F(J)$ calculated from the Budó formula using the previously obtained value of A. B values were obtained from the (0, 1) and (0, 2) bands and α'' was found from the differences in the B'' values. The measurements of the (0, 3) band are less accurate. The rotational constants are given in Table II.

TABLE II

MOLECULAR CONSTANTS OF Si_2

State	T_0	ω_e	ω_ex_e	A	B_e	α	r_e
$L^3\Pi_u$	E+28059.1			−16.5	0.2370[a]		2.255[a]
$H^3\Sigma_u^-$	24075.70[b]	271.32[b]	1.99		0.1699[b]	0.00135	2.663[b]
$D^3\Pi_g$	E	547.94	2.43	−71.6	0.2596	0.00155	2.155
$X^3\Sigma_g^-$	0	506.72[c]	1.97		0.2376[c]	0.00135	2.252[c]

[a] *These numbers are B_0 and r_0 values.*
[b] *The vibrational numbering is not known and these values are obtained by assuming that the lowest observed level is the $v = 0$ level.*
[c] *The vibrational numbering of this state is not certain.*

The origins of the $^3\Pi_0$ subbands could be determined quite accurately and fairly good values could also be obtained for the origins of the $^3\Pi_2$ subband. The mean of these two subband origins was taken to be the band origin. The vibrational constants of the upper electronic state could not be determined since only one vibrational level was observed. The lower state $\Delta G(v+\frac{1}{2})$ values could be determined quite accurately for $v = 1$ and $v = 2$ from the (0, 1), (0, 2), and (0, 3) bands. These data are sufficient to determine T_0, ω_e'', and ω_ex_e'' which are given in Table II. The heads of the isotopic bands are useful in assigning the vibrational numbering and in giving a positive identification of the emitter of the bands, but are too weak to be measured accurately and therefore do not give a good value for ω'.

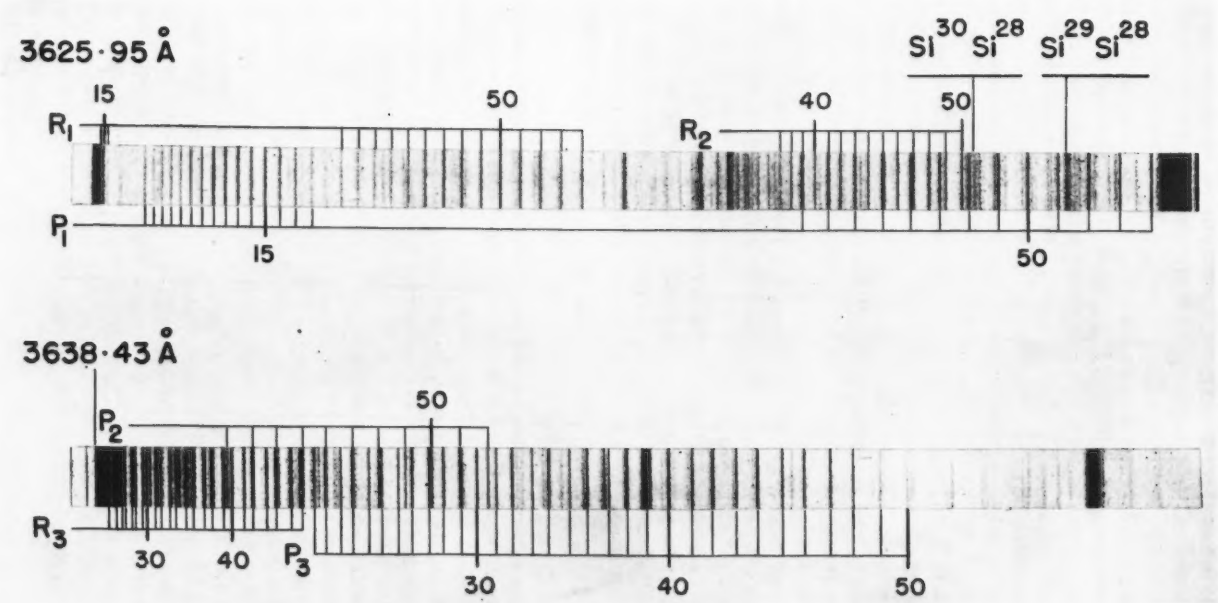

FIG. 1. The (0, 2) band of the $^3\Pi - {}^3\Pi$ system of the Si_2 molecule.

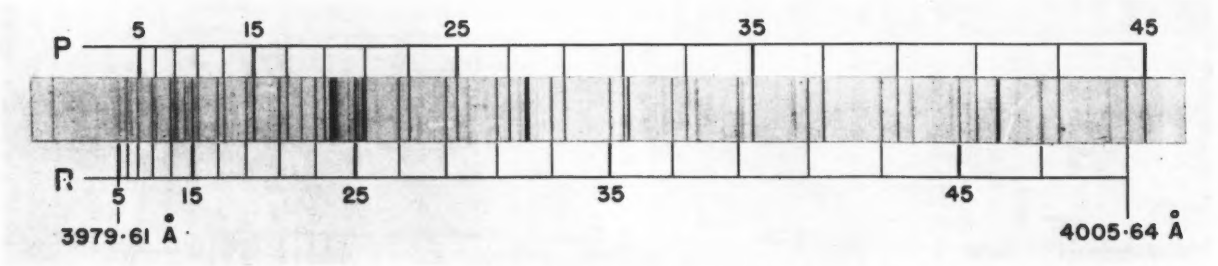

FIG. 2. The $(m+4, n)$ band of the $^3\Sigma - ^3\Sigma$ system of the Si_2 molecule.

The observed abrupt terminations of a number of the branches of the bands are unusual and are not understood. It is certain that the upper electronic state is responsible for the effect. It is probable that the effect arises from some type of predissociation and below it is discussed as such. The $^3\Pi_0$ component is least affected, but even in this component the predissociation is marked above $J = 47$. On overexposed plates, however, lines of the P branch arising from levels with J between 61 and 72 can be seen, but at $J' = 72$ the branch breaks off sharply a second time. In the $^3\Pi_1$ component, the predissociation affects all the low rotational levels and causes the $^3\Pi_1 - {}^3\Pi_1$ subband to be headless. Also, all $^3\Pi_1$ levels above $J' = 51$ are predissociated. The $^3\Pi_2$ component appears to be predissociated for $16 < J' < 39$ and again for $J' > 55$. Though these predissociations are probably of the nature of accidental predissociations, the fact that only one vibrational level of the upper state is observed seems to indicate that the higher vibrational levels are completely predissociated.

In addition to the striking predissociation, an unusual intensity alternation occurs in the lines of the $^3\Pi_0$ subband. This effect is especially marked at low J values where every other line is much weaker, but for J greater than about 40, the effect almost disappears and successive lines have almost the same intensity. This effect may also arise from a predissociation. If a $^3\Pi_0$ state is predissociated by a Σ state, then only one set of the Λ components is affected (see (2), p. 417). For homonuclear molecules with zero nuclear spin such as Si_2, one set of components accounts for alternate lines of $\Pi - \Pi$ bands. Thus a weak predissociation by a Σ state may reduce the intensity of alternate lines in the $^3\Pi_0$ component.

IV. THE $^3\Sigma - {}^3\Sigma$ BAND SYSTEM

The high resolution plates showed a number of simple bands extending over the region from 3980 Å into the red. A large difference between the upper and lower state B value causes the bands to be nearly headless. These bands are quite weak, and between 4090 and 4290 Å, where the very strong SiH bands occur, no bands of this system could be observed even though it appears that a number should occur in this region. One of the bands is shown in Fig. 2.

The bands have a simple P and R branch structure, but the analysis shows that alternate lines (those of even J value) are missing. This structure implies that the bands are $\Sigma - \Sigma$ bands of a homonuclear molecule of zero spin. At low J values the lines of the bands break up into two or three components which are just barely resolved and again at high J values the lines become broad as if they are composed of a number of unresolved components. This behavior is exactly what might be expected for bands of a $^3\Sigma - {}^3\Sigma$ transition. The B values of the upper and lower electronic states are about 0.17 and 0.24 cm^{-1} respectively. The magnitude of these B values together with the type of transition is sufficient to limit the emitter of the bands to S_2 or Si_2. The bands do not involve either of the well-known $^3\Sigma$ states of S_2 and the strong bands of S_2 do not appear in our discharge tube. Thus it seems certain that the new bands are emitted by the Si_2 molecule.

The rotational analysis of the bands presented no difficulty. A number of the bands had upper or lower state in common so that the correct J numbering

of the lines was not in doubt. The triplet structure of the lines was not sufficiently well-resolved to be measured, and the three components are measured as a single line. The wave numbers of the lines of the bands are given in Table III and the band origins and B and D values are given in Table IV.

TABLE III

WAVE NUMBERS OF THE LINES OF THE $^3\Sigma - {}^3\Sigma$ BANDS OF Si_2

	$(m+4, n)$		$(m+4, n+1)$		$(m+1, n+2)$		$(m+2, n+3)$		$(m+1, n+3)$	
N	$P(N)$	$R(N)$	$P(N)$	$R(N)$	$P(N)$	$R(N)$	$P(N)$	$R(N)$	$P(N)$	$R(N)$
3	25118.91			24618.76						
5	117.15	25120.99		618.21						
7	114.89	119.70		616.95						
9	111.79	117.90		615.14						
11	107.99	115.49	24605.23	612.76			23097.15			
13	103.62	112.46	600.97	609.82			093.26			
15	098.68	108.85	596.15	606.30		23330.66	088.66	23098.94	22825.87	22836.24
17	093.25	104.69	590.76	602.19		326.93	083.60	095.24	820.86	832.58
19	087.17	099.92	584.78	597.55	23309.43		078.05	091.01	815.45	828.42
21	080.51	094.58	578.23	592.31	303.49	317.91	071.95		809.33	823.77
23	073.28	088.64	571.12	586.49	296.87	312.60	065.31	080.88	802.79	818.58
25	065.44	082.13	563.42	580.10	289.65	306.75	058.13	075.08	795.76	812.87
27	057.04	075.00	555.16	573.12	281.97	300.38	050.43	068.71	788.20	806.60
29	048.03	067.29	546.30	565.58	273.70	293.45	042.20	061.77	780.11	799.82
31	038.45	059.02	536.88	557.43	264.91	286.00	033.46	054.32	771.45	792.57
33	028.25	050.13	526.86	548.73	255.59	277.98	024.13	046.32	762.32	784.73
35	017.49	040.64		539.43	245.72		014.31	037.84	752.64	776.38
37	006.15	030.58		529.57	235.35	260.37	003.93	028.77	742.43	767.50
39	24994.16	019.90	493.37	519.09	224.39	250.78	22992.99	019.18	731.69	758.10
41	981.65	008.68	481.03		212.94	240.64	981.53	009.01	720.44	748.13
43	968.51	24996.82	468.16	496.44	200.96	229.97	969.52	22998.34		737.71
45	954.81	984.40	454.66	484.23	188.42	218.77		987.12		726.74
47		971.36		471.45		207.01		975.31		715.21
49		957.73		458.08		194.73				
51						181.87				

	$(m+4, n+5)$		$(m, n+3)$		$(m+1, n+4)$		$(m, n+4)$	
N	$P(N)$	$R(N)$	$P(N)$	$R(N)$	$P(N)$	$R(N)$	$P(N)$	$R(N)$
3								
5								
7								
9								
11	22634.29							
13	630.26	22639.08				22348.39	22072.56	22081.66
15	625.80	635.92			22335.11	345.62	068.26	078.73
17	620.69	632.21	22558.81		330.31	342.08	063.40	075.28
19	615.18	627.90	548.53		324.90	337.97	058.13	071.33
21	609.07	623.13	542.62		319.01	333.41	052.33	066.88
23	602.39	617.77	536.17		312.61	328.36	046.04	061.93
25	595.23	611.92	529.25	22546.39	305.67	322.76	039.25	
27	587.60	605.50	521.76	540.36	298.24	316.63	031.92	050.48
29		598.57	513.83	533.72	290.31	310.03	024.15	044.00
31		591.05	505.36	526.57	281.84	302.92		037.04
33			496.35	518.92	272.85	295.26		029.59
35			486.85	510.79	263.38	287.11		021.63
37			476.82	502.09	253.38	278.46		
39			466.31	492.92	242.87	269.24		
41			455.24	483.20	231.83	259.53		
43			443.72		220.33	249.32		
45			431.63	462.20	208.21	238.56		
47				450.95		227.32		
49				437.62				
51								

Though the relative vibrational numbering of the bands is readily obtained, the absolute numbering is not at all certain. Unlike the $^3\Pi - {}^3\Pi$ bands, the $^3\Sigma - {}^3\Sigma$ bands have no strong band heads which show isotopic structure. Also, the lines of the bands are quite weak and no lines of the isotopic molecules (which have only about one twentieth the intensity) have been observed. Towards longer wavelengths the bands become progressively weaker until

TABLE IV

ORIGINS AND ROTATIONAL CONSTANTS OF THE $^3\Sigma - ^3\Sigma$ BANDS

Band	ν_0	B'	B''	$D' \times 10^7$	$D'' \times 10^7$
$m+4, n$	25121.17	0.1638	0.2369	2.8	2.1
$m+4, n+1$	24618.27	0.1639	0.2356	3.7	2.1
$m+1, n+2$	23341.23	0.1679	0.2342	3.0[b]	2.0[b]
$m+2, n+3$	23109.55	0.1665	0.2328	3.0[b]	2.0[b]
$m+1, n+3$	22846.48	0.1680	0.2331	3.0[b]	2.0[b]
$m+4, n+5$	22646.60	0.163_5	0.230_0		
$m, n+3$	22579.14	0.1692	0.2329	3.0[b]	2.0[b]
$m+1, n+4$	22355.50	0.1679	0.2315	3.1	2.0
$m, n+4$	22088.31	0.1692[a]	0.2315[a]		

[a] *These values were taken over from the better developed bands and used in the determination of* ν_0 *from the observed lines.*

[b] *These values were taken over from the better developed bands and used in the determination of* B.

they can no longer be observed. At the violet end of the band system, one of the strongest bands (here designated as the $m+4$, n band) is found at 3980 Å and no bands are observed at shorter wavelengths than this. The abrupt termination of the band system in the violet suggests that all levels above the $m+4$ level in the upper electronic state are predissociated or are not excited and that the n level is the $v = 0$ level of the lower electronic state. Thus it is probable that $n = 0$ but the true value of m is unknown.

The vibrational and rotational constants of the two Σ states together with those of the Π states are given in Table II.

V. DISCUSSION

The electron configurations of Si_2 may be expected to be similar to those of the C_2 molecule which have been discussed by Mulliken (3). Because the relative positions of the energy levels change slightly as the principal quantum number increases from 2 to 3, the lowest electronic configuration of Si_2 (see below) is one which is slightly excited in C_2 and the resulting ground state of Si_2 is expected to be a $^3\Sigma_g^-$ state (see (2), p. 343). Since the Si^{28} nucleus obeys Bose statistics and since the even rotational lines of the observed $^3\Sigma - ^3\Sigma$ bands are missing, the bands must arise from either a $^3\Sigma_g^+ - ^3\Sigma_u^+$ or a $^3\Sigma_u^- - ^3\Sigma_g^-$ transition. It seems reasonable therefore to associate the observed lower $^3\Sigma$ state with the ground state. The fact that the electron configurations show that the ground state is the only low-lying $^3\Sigma_g^-$ state and that no $^3\Sigma_g^+ - ^3\Sigma_u^+$ transitions are expected from low-lying states gives strong support to the assumption that the lower state of the observed $^3\Sigma - ^3\Sigma$ bands is the ground state. If it is accepted that the lower $^3\Sigma$ state is the ground state, then the upper $^3\Sigma$ state can be uniquely assigned to a definite electron configuration since there is only one $^3\Sigma_u^-$ state arising from low-lying configurations. The observed $^3\Pi$ bands can arise either from a $^3\Pi_g - ^3\Pi_u$ or from a $^3\Pi_u - ^3\Pi_g$ transition. No $^3\Pi_u - ^3\Pi_g$ transition can be expected from low-lying states and it is therefore assumed that the bands are due to a $^3\Pi_g - ^3\Pi_u$ transition. The electron configurations give only one low-lying $^3\Pi_u$ state, but at somewhat higher energy two $^3\Pi_u$ states. Because of the small change in the B values in the observed

transition, it is probable that these bands are analogous to the Swan band of C_2 which also shows a small value of $B'-B''$. From these assumptions, the probable electron configurations of the observed states are then as follows:

$$KKLL\ (\sigma_g 3s)^2(\sigma_u 3s)^2(\sigma_g 3p)^2(\pi_u 3p)^2 \qquad X^3\Sigma_g^-$$

$$KKLL\ (\sigma_g 3s)^2(\sigma_u 3s)^2(\sigma_g 3p)\ (\pi_u 3p)^3 \qquad D^3\Pi_u$$

$$KKLL\ (\sigma_g 3s)^2(\sigma_u 3s)^2(\sigma_g 3p)^2(\pi_u 3p)(\pi_g 3p) \qquad H^3\Sigma_u^-$$

$$KKLL\ (\sigma_g 3s)^2(\sigma_u 3s)(\sigma_g 3p)^2(\pi_u 3p)^3 \qquad L^3\Pi_g$$

With our present limited knowledge of Si_2, the assignment of the observed states to the configuration given above is not certain, but there appear to be no other low-lying configurations which can account for the spectrum equally well.

If the lower state of the $^3\Sigma-{}^3\Sigma$ bands is the ground state, as seems probable, then these bands may occur in astrophysical sources. The large value of $B'-B''$ for this transition causes the bands to be nearly headless and to spread over a large wavelength range. Therefore, even if the bands do occur in such sources, they will be difficult to find.

I am indebted to Dr. G. Herzberg for numerous helpful suggestions and to Miss Lila Howe for assistance in the calculations.

REFERENCES

1. DOWNIE, A. R. and BARROW, R. F. Nature, 160: 198. 1947.
2. HERZBERG, G. Molecular spectra and molecular structure. I. Spectra of diatomic molecules. D. Van Nostrand Company, Inc., New York. 1950.
3. MULLIKEN, R. S. Phys. Rev. 56: 778. 1939.
4. SPEDDING, F. H. Nucleonics, 4(No. 1): 4. 1949.

HIGH RESOLUTION RAMAN SPECTROSCOPY OF GASES

V. ROTATIONAL SPECTRA OF ALLENE, ALLENE-d_4, AND ALLENE-1,1-d_2 [1]

By B. P. Stoicheff

ABSTRACT

The pure rotational Raman spectra of allene, allene-d_4, and allene-1,1-d_2 were photographed in the second order of a 21 ft. grating. Two plates of each spectrum were analyzed yielding the following values for the rotational constants:

Allene: $B_0 = 0.2965_3 \pm 0.00008$ cm.$^{-1}$, $D_J = 11 \times 10^{-8}$ cm.$^{-1}$
Allene-d_4: $B_0 = 0.2323_0 \pm 0.0001$ cm.$^{-1}$, $D_J = 7.5 \times 10^{-8}$ cm.$^{-1}$
Allene-1,1-d_2: $B_0 = 0.2619_0 \pm 0.0001$ cm.$^{-1}$, $D_J = 7.0 \times 10^{-8}$ cm.$^{-1}$

These constants lead to the value r_0(C=C) $= 1.308_8 \pm 0.001$ Å. Also if a value of r_0(C—H) $= 1.07 \pm 0.01$ Å is assumed, then $\angle$HCH $= 117 \pm 1.5°$. It is noted that the length of the carbon–carbon double bond in allene is significantly shorter than that in ethylene.

A. INTRODUCTION

Although the structure of the allene molecule has been the subject of several investigations by electron diffraction and infrared spectroscopy, the geometrical parameters are not accurately known. Values for the CH distance and HCH angle have yet to be determined directly, and the existing values for the CC distance are not in satisfactory agreement. The most accurate data available at present were provided by recent investigations of the infrared spectra of allene and allene-d_4. These investigations, however, are not altogether without complications. Lord and Venkateswarlu (9) have carried out a detailed study on the perpendicular bands, and their results together with several plausible assumptions yield a value of $113 \pm 1°$ for the HCH angle. Also, high resolution studies on parallel bands by Overend and Thompson (10) lead to a value of 1.30 ± 0.005 Å for the length of the carbon–carbon double bond in allene. It is of interest that this value is considerably smaller than that found for the carbon–carbon bond length in ethylene (1.344 Å), thereby suggesting that the length of the carbon–carbon double bond is dependent on environment, a conclusion already well established for the carbon–carbon single bond (see, for example, Ref. 5). Since this result is of considerable importance for valence theory, an investigation of the rotational Raman spectrum of allene was undertaken.

The pure rotational Raman spectra of allene, allene-d_4, and allene-1,1-d_2 were photographed with high resolution. The rotational lines were well resolved and the analysis was straightforward, resulting in an accurate evaluation of the C=C distance. This bond length is shorter than that found in ethylene in agreement with the observation of Overend and Thompson. Also, a relationship between the CH distance and HCH angle was obtained, although it was not possible to evaluate these parameters independently.

[1]*Manuscript received September 2, 1955.*
Contribution from the Division of Pure Physics, National Research Council, Ottawa, Canada. Issued as N.R.C. No. 3792.

B. EXPERIMENTAL

Allene was prepared by the dehalogenation of pure 2,3-dibromopropene with zinc dust in alcoholic solution (7). Allene-d_4 and allene-1,1-d_2 of 88 mol. per cent and 96 mol. per cent purity respectively were prepared in a new synthesis by Leitch and Morse of the Division of Pure Chemistry (8). In the present investigation, the gas pressures were 35 cm. Hg for allene and 15 cm. Hg for allene-d_4 and allene-1,1-d_2.

The pure rotational Raman spectra of the three gases excited by the Hg 4358 line were photographed with the apparatus described in I of this series (14). A 21 ft. concave grating spectrograph was used giving a dispersion of 6.75 cm.$^{-1}$/mm. The slit width was 0.03 mm. Exposure times were of the order of 15–20 hr. with Eastman Kodak 103 a-0 photographic plates. Second- and third-order iron lines provided the necessary wavelength standards.

C. OBSERVED SPECTRA

Photographs of the pure rotational Raman spectra of allene and allene-d_4 are shown in Fig. 1. Approximately 50 lines are observed on each side of the

TABLE I

OBSERVED WAVE NUMBER SHIFTS OF THE ROTATIONAL RAMAN LINES OF ALLENE, ALLENE-d_4, AND ALLENE-1,1-d_2

J	$\lvert\Delta\nu\rvert$, cm.$^{-1}$ [a]			J	$\lvert\Delta\nu\rvert$, cm.$^{-1}$ [a]		
	Allene	Allene-d_4	Allene-1,1-d_2		Allene	Allene-d_4	Allene-1,1-d_2
5	—	6.02_1	6.81_0	30	37.33_6*	29.24_3*	32.98_9
6	—	6.95_7	7.87_0	31	38.50_5*	30.16_6	34.02_8
7	—	7.89_0	—	32	39.69_7	31.08_6	35.07_7
8	11.27_4*	—*	—	33	40.88_4	32.02_2	36.12_4
9	12.41_0*	—*	10.99_4	34	42.06_2	32.96_2	37.17_9
				35	43.25_1	33.89_5	38.23_0*
10	13.63_8	10.65_5	12.05_2*	36	44.42_9	34.83_6	39.26_3
11	14.83_7	11.59_7*	13.09_0	37	45.61_4	35.75_0	40.30_8
12	16.00_4	12.50_5*	14.13_2	38	46.79_7	36.69_6	41.36_4
13	17.20_3	13.46_0*	15.16_7	39	47.95_4*	37.62_7*	42.39_1
14	18.35_4*	14.37_5	16.25_4				
15	19.57_4*	15.32_3	17.28_7	40	49.15_8	38.51_8*	43.44_8
16	20.74_3	16.25_5	18.31_5*	41	50.34_7	39.44_2	44.48_7
17	21.93_9	17.18_6	19.33_5*	42	51.52_2	40.37_3	45.53_7
18	23.12_0	18.13_1*	20.42_0	43	52.72_4	41.29_3	46.56_8
19	24.31_8	19.07_0*	21.47_7	44	53.89_8	42.21_6	47.66_6*
				45	55.07_2	43.15_1	48.65_8
20	25.48_1	19.97_8	22.52_3	46	56.26_2[b]	44.08_2	49.67_7
21	26.67_9	20.91_2	23.56_7	47	57.27_9[b]*	44.96_5	50.75_8
22	27.86_0*	21.84_5	24.61_0	48	58.60_9[b]	45.92_4	51.79_6[b]
23	29.05_1*	22.76_6	25.65_2	49	59.77_9[b]	46.83_7	52.86_8[b]
24	30.22_7	23.68_7	26.71_2				
25	31.41_9	24.61_2	27.75_3	50	61.04_8[b]	47.74_0[b]*	53.88_0[b]
26	32.60_8	25.54_8	28.79_1*	51	62.13_1[b]	48.71_9[b]	
27	33.78_5	26.45_7	29.84_3	52	63.30_7[b]	49.64_1[b]	
28	34.97_5	27.39_5	30.88_6	53	64.49_1[b]	50.58_2[b]	
29	36.15_5	28.32_0*	31.93_5	54	65.63_8[b]	51.52_1[b]	

[a] *All values are averages of the Stokes and anti-Stokes lines measured on two plates, except the values marked* [b].

[b] *Stokes lines measured on one plate only.*

* *Lines blended with grating ghosts.*

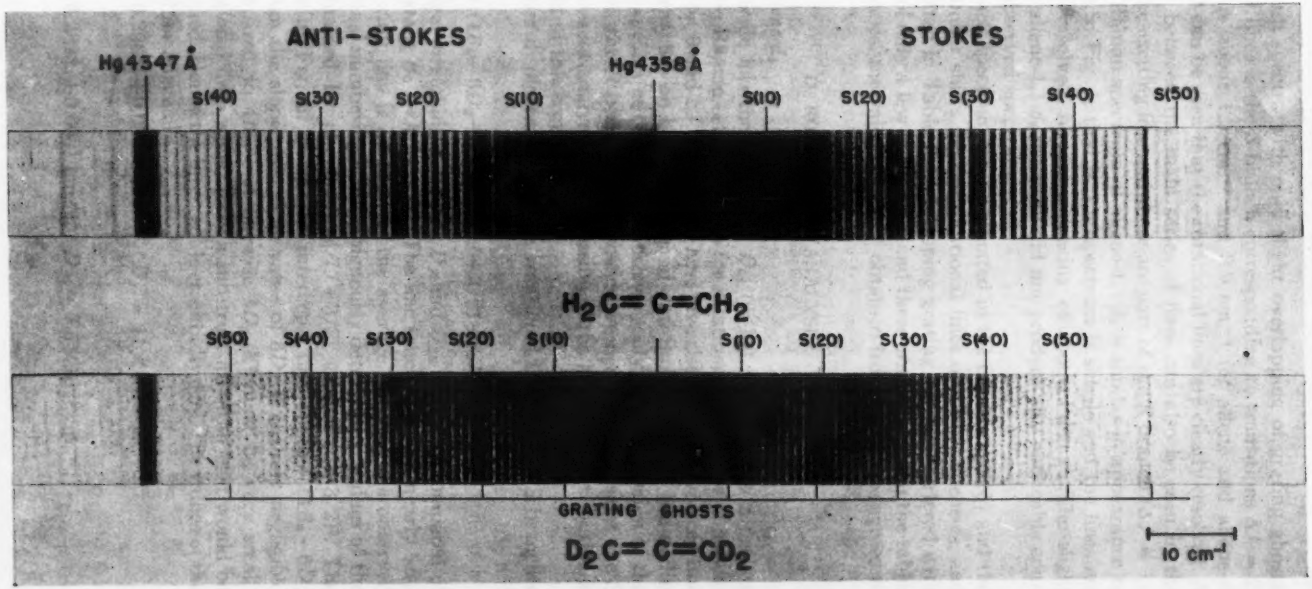

FIG. 1. Rotational Raman spectra of allene and allene-d_4 photographed in the second order of a 21 ft. grating.

exciting line in both spectra with only slight overlapping of grating ghosts. The main series of lines is the S branch corresponding to transitions $\Delta J = 2$. The line spacing is about 1.2 cm.$^{-1}$ and 0.9 cm.$^{-1}$ for allene and allene-d_4 respectively and it can be seen that the rotational lines are clearly resolved. A few lines midway between the main series of lines can also be seen in the neighborhood of the exciting line and these are part of the R branch ($\Delta J = 1$).

The rotational Raman spectrum of allene-1,1-d_2 is similar in appearance to the spectra shown in Fig. 1, that is, the spectrum is simple and the lines are sharp and clearly resolved, having a spacing of about 1 cm.$^{-1}$. The slight asymmetry of the allene-1,1-d_2 molecule did not produce any noticeable complications in the observed spectrum.

Two plates of each spectrum were evaluated in the usual way (15) and the observed wave number shifts for the rotational lines of allene, allene-d_4, and allene-1,1-d_2 are listed in Table I. Overlapping grating ghosts interfered with the measurement of only a few of the lines and these are indicated in the table. For all three molecules, the values of $|\Delta\nu_{\text{vac}}|$ obtained from two plates agreed to within ± 0.02 cm.$^{-1}$.

D. ROTATIONAL ANALYSIS

(a) *Allene and Allene-d_4*

The allene molecule has the symmetry D_{2d} ($= V_d$) and hence is a prolate symmetric top. The Raman selection rules for rotational transitions of a symmetric top are $\Delta K = 0$ and $\Delta J = 0, 1, 2$. These give rise to an undisplaced line and to R and S branches on both Stokes and anti-Stokes sides of the undisplaced line. In the spectra of the allenes, however, only a small fraction of the total intensity is in the R branches, and hence we need only consider the S branches for the present analysis. (A discussion of the intensity distribution is included at the end of this section.)

The wave number displacements of the rotational lines in the S branches are given by

$$[1] \qquad |\Delta\nu| = (4B_0 - 6D_J - 4D_{JK}K^2)(J+3/2) - 8D_J(J+3/2)^3$$

where the centrifugal stretching constants D_J and D_{JK} are small compared to the rotational constant B_0 ($= h/8\pi^2 cI_B$). The line spacing is very nearly $4B_0$, and when $|\Delta\nu|$ for any line is divided by the average value of the observed spacing, the rotational numbering is unambiguously determined. Values of the constants were obtained by plotting $|\Delta\nu|/(J+3/2)$ against $(J+3/2)^2$. The graphs are shown in Fig. 2. From the intercept, one obtains $(4B_0 - 6D_J - 4D_{JK}K^2)$ and from the slope, $8D_J$. The value of $6D_J$ is entirely negligible ($\sim 10^{-6} \times B_0$) compared to $4B_0$, and likewise $4D_{JK}K^2$ must be very small, otherwise the rotational lines would have a substructure or at least would be appreciably broadened. Hence the intercept is essentially $4B_0$. The values of the constants obtained for allene are

$$B_0 = 0.2965_3 \pm 0.00008 \text{ cm.}^{-1}, \quad D_J = 11 \times 10^{-8} \text{ cm.}^{-1}$$

and for allene-d_4

$$B_0 = 0.2323_0 \pm 0.0001 \text{ cm.}^{-1}, \quad D_J = 7.5 \times 10^{-8} \text{ cm.}^{-1}.$$

The B_0 values give the effective moments of inertia for the ground states:

$$I_B{}^0 = (94.38_9 \pm 0.03) \times 10^{-40} \text{ gm. cm.}^2 \text{ for allene, and}$$

$$I_B{}^0 = (120.48_7 \pm 0.05) \times 10^{-40} \text{ gm. cm.}^2 \text{ for allene-}d_4,$$

using the atomic constants of DuMond and Cohen (1).

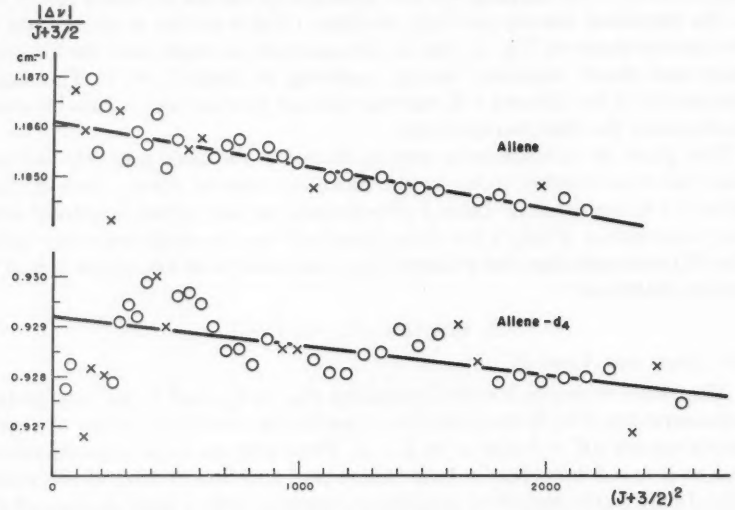

FIG. 2. $|\Delta\nu|/(J+3/2)$ graph for the ground states of allene and allene-d_4. (× lines blended with grating ghosts.)

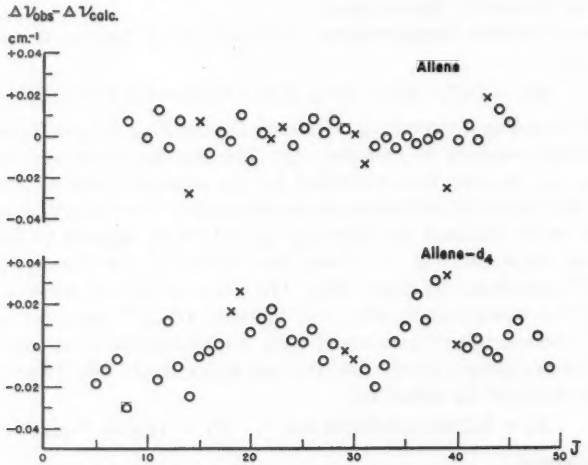

FIG. 3. Deviations of the observed wave number shifts of the rotational lines from those calculated with the derived constants. (× lines blended with grating ghosts.)

The rotational constants were then used to calculate the wave number displacements of the rotational lines and a comparison with the observed values is shown in the graph of Fig. 3. Almost all of the observed−calculated values lie within ±0.02 cm.$^{-1}$ in agreement with the estimated accuracy of ±0.03 cm.$^{-1}$. The scatter in the values for allene-d_4 is larger than for allene and is probably due to the presence of small amounts of partially deuterated molecules.

Although a calculation of D_J from force constants was not carried out, it was tempting to apply a formula of the type $D_J = 4B_0^3/\omega_{eff}^2$. When the B and D values just derived were substituted in this equation, the following values were obtained:

$$\omega_{eff} = 974 \text{ cm.}^{-1} \text{ for allene, and } 818 \text{ cm.}^{-1} \text{ for allene-}d_4.$$

These are within 10% of the observed C=C=C stretching frequencies 1076 cm.$^{-1}$ and 874 cm.$^{-1}$ (9).

The values of the rotational constants derived here differ slightly from those obtained from the parallel infrared bands by Overend and Thompson (10), $B_0 = 0.2974 \pm 0.0006$ cm.$^{-1}$ for allene, $B_0 = 0.2313 \pm 0.0005$ cm.$^{-1}$ for allene-d_4, and $D_J < 10^{-8}$ cm.$^{-1}$ for both. These differences may arise from complications in the infrared spectra which do not permit clear resolution of the lines, as is observed in the Raman spectra, or more probably may be due to the difficulty of determining the correct rotational numbering in such closely-spaced spectra.

The observed intensity distribution in the rotational Raman spectra of the allenes is quite regular with a continuous decrease in intensity at the outer extremities; there is no intensity alternation as is observed in the parallel infrared bands of allene (10). This difference in appearance is readily explained by considering the temperature of the gas samples in the two experiments. In the latter study, the gas was cooled to −100°C. so that a large fraction of the molecules would be in the rotational levels with $K = 0$ where the statistical weight factors are in the ratio 7:3 for J even:J odd (3). In the present experiment, the temperature was about 50°C. and rotational levels with K up to 10 were appreciably populated. Since no intensity alternation occurs for the subbands with $K > 0$, no intensity alternation is predicted for the Raman spectrum. Also, it must be pointed out that molecules which have been thermally excited into the lowest vibrational levels will contribute to the observed Raman spectrum and affect slightly the intensity distribution and line positions.[2]

Placzek and Teller (12) have calculated the intensity distribution in the rotational Raman spectrum of a symmetric top molecule and have shown that the intensity of the R branch decreases with decreasing value of the ratio of the least and largest moments of inertia (I_A/I_B). For allene, this ratio is less than 0.1 and the intensity of the R branch would be expected to be extremely small. It can also be shown from the equations of Placzek and Teller that the R branch lines with $J < 20$ will have the highest intensity. Both expectations

[2] *A qualitative discusssion is given in Section D of paper II in this series (15).*

are borne out here; only a few lines of the R branch can be seen in the spectra of allene and allene-d_4 and these are in fact confined to the neighborhood of the exciting line.

(*b*) *Allene-1,1-d_2*

The isotopic molecule allene-1,1-d_2 has the symmetry C_{2v} and has a slightly asymmetric structure. However, since the general appearance of the rotational spectrum is simple, this molecule must be very nearly a symmetric top and hence it was assumed that the wave number displacements of the S branch lines can be expressed by an equation similar to [1] above, but with B_0 replaced by $\bar{B}_0$ $(=\frac{1}{2}(B_0+C_0))$. An analysis based on this equation gave $\bar{B}_0 = 0.2619_0$ ± 0.0001 cm.$^{-1}$ and $D_J \sim 7.0\times10^{-8}$ cm.$^{-1}$, where $\bar{B}_0 = \frac{h}{8\pi^2 c}\left(\frac{1}{I_B}+\frac{1}{I_C}\right)$. These constants reproduce the observed displacements to within ± 0.02 cm.$^{-1}$.

E. MOLECULAR STRUCTURE OF ALLENE

The structure and the structural parameters of the allene molecule are shown in Fig. 4. The moment of inertia about any axis perpendicular to the C=C=C axis and passing through the center atom is given by the simple expression

[2] $$I_B = 2[m_C r_1^2 + m(2r_2^2+h^2)]$$

where $m = m_H$ or m_D. When the numerical values for the moments of inertia of allene and allene-d_4 are substituted in equation [2], one obtains

$$r_1 = r_0(C{=}C) = 1.308_8 \pm 0.001 \text{ Å}$$

and

$$2r_2^2+h^2 = 7.810_8 \pm 0.024 \text{ Å}^2.$$

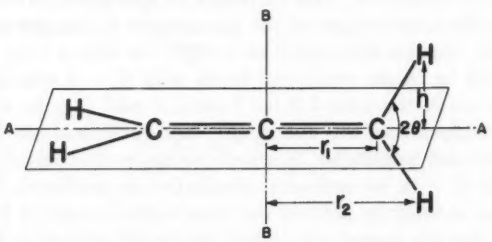

FIG. 4. The structure and structural parameters of the allene molecule.

The latter value gives a relationship for the CH distance, r_0(CH), and the HCH angle, 2θ, namely

[3] $$2[r_0(C{=}C)+r_0(CH)\cos\theta]^2+[r_0(CH)\sin\theta]^2 = 7.810_8 \pm 0.024 \text{ Å}^2.$$

Equation [3] is represented graphically by the shaded strip B–B in Fig. 5. The width of the shaded strip gives an estimate of the error in the values of the parameters based on the above experimental errors.

Initially it had been hoped that the investigation of allene-1,1-d_2 would provide sufficient information to determine r_0(CH) and $\angle$HCH independently.

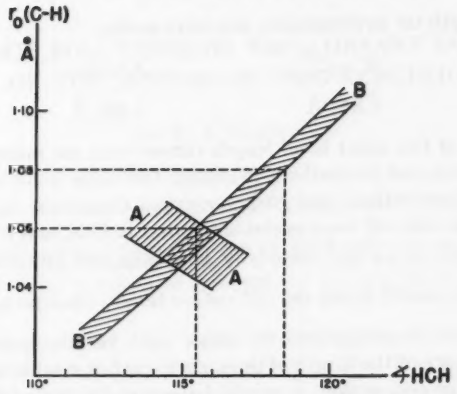

FIG. 5. Graphical determination of the CH distance and HCH angle in allene. The shaded band *B–B* represents the values that are consistent with the B_0 values for allene and allene-d_4; *A–A* represents the values consistent with the infrared value of *A* (9).

On the graph (Fig. 5) this would be represented by a line crossing *B–B* at some point, giving the values of these parameters consistent with the value of $\bar{B}_0$. However, the present data give a line which falls entirely within the shaded area *B–B*, thus confirming the right-hand side of Eq. [3], but without providing further useful information. This result can be understood if one recalls that Eq. [3] is evaluated from the difference of the moments of inertia of allene and allene-d_4. In order to obtain r_0(CH) and ∠HCH separately, it is necessary to find the second difference of the moments of inertia of the three isotopic molecules. For the three allene molecules, the second difference is a very small number and has a rather large uncertainty. With the present data, one can do no better than to assume a value of r_0(CH) = 1.07±0.01 Å (as found in ethylene (2)) and so obtain the value ∠HCH = 117±1.5° from the graph, Fig. 5.

In summary, the results of the present investigation of the rotational spectra of the allene molecules lead to the value r_0(C=C) = 1.309 Å, and are consistent with the values r_0(CH) = 1.07 Å and ∠HCH = 117°.

F. DISCUSSION

The value for the carbon–carbon distance in allene found here, 1.309 Å, is in good agreement with the value 1.30±0.005 Å found by Overend and Thompson (10) from the infrared spectra. While the electron diffraction result of Wierl (16) for this distance, 1.31±0.05 Å, is also in agreement, the value 1.34±0.02 Å quoted by Pauling and Brockway (11) for allene and ethylene is not in accord with the present results. As shown by Overend and Thompson and fully confirmed by the present results, the carbon–carbon double bond in allene is significantly shorter than that in ethylene.[3] To show the dependence

[3]*The value 1.344 Å for the carbon–carbon distance in ethylene was calculated from the most recent Raman value of* B_0 *(13) and the infrared value of* A_0 *(2).*

of the bond length on environment, one may write:

1.344 Å 1.309 Å

A confirmation of this short bond length comes from the microwave spectrum of ketene. Johnson and Strandberg (6) found the value 2.475±0.003 Å for the sum of the carbon–carbon and carbon–oxygen distances. In ketene the environment of the =C=O bond is similar to that in CO_2, and if one assumes the value of r_0(C=O) = 1.162 Å found by Herzberg and Herzberg (4) for CO_2, a value of 1.313±0.003 Å for the C=C= bond in ketene is obtained. Thus the spectroscopic investigations of allene and ketene have established a marked dependence of the length of the carbon–carbon double bond on adjacent bonds (5). In this connection, it would be especially desirable to investigate the structure of butatriene which has one carbon–carbon double bond with an environment different from that in allene, namely =C=C=. A bond length considerably shorter than that in allene would be expected for this bond.

The only evaluation of the least moment of inertia, I_A, for the allene molecule is that obtained by Lord and Venkateswarlu (9) from an analysis of the perpendicular infrared bands. From their value of $A = 5.28\pm0.1$ cm.$^{-1}$, one finds $I_A = (5.30\pm0.1)\times10^{-40}$ gm. cm.^{2} ($=4m_H r^2(\mathrm{CH})\sin^2\theta$). A graph, A–A, of this relation is included in Fig. 5. It can be seen that their value of A and the new B_0 are consistent with the values r_0(CH) = 1.053±0.01 Å and ∠HCH = 115±1°. Both values appear to be slightly low. A definitive value of the CH distance and HCH angle must await further high resolution studies of the infrared[4] and Raman rotation–vibration spectra of allene.

I am grateful to Dr. G. Herzberg for helpful discussions and to Dr. Leitch and Mr. Morse for preparing the deuterated allenes.

REFERENCES

1. DuMond, J. M. W. and Cohen, E. R. Revs. Mod. Phys. 25: 691. 1953.
2. Gallaway, W. S. and Barker, E. F. J. Chem. Phys. 10: 88. 1942.
3. der Heer, J. J. Chem. Phys. 20: 637. 1952.
4. Herzberg, G. and Herzberg, L. J. Opt. Soc. Amer. 43: 1037. 1953.
5. Herzberg, G. and Stoicheff, B. P. Nature, 175: 79. 1955.
6. Johnson, H. R. and Strandberg, M. W. P. J. Chem. Phys. 20: 687. 1952.
7. Kistiakowsky, G. B., Ruhoff, J. R., Smith, H. A., and Vaughan, W. E. J. Am. Chem. Soc. 58: 146. 1936.
8. Leitch, L. C. and Morse, A. T. To be published.
9. Lord, R. C. and Venkateswarlu, P. J. Chem. Phys. 20: 1237. 1952.
10. Overend, J. and Thompson, H. W. J. Opt. Soc. Amer. 43: 1065. 1953.
11. Pauling, L. and Brockway, L. O. J. Am. Chem. Soc. 59: 1223. 1937.
12. Placzek, G. and Teller, E. Z. Physik, 81: 209. 1933.
13. Romanko, J., Feldman, T., Stansbury, E. J., and McKellar, A. Can. J. Phys. 32: 735. 1954.
14. Stoicheff, B. P. Can. J. Phys. 32: 330. 1954.
15. Stoicheff, B. P. Can. J. Phys. 32: 339. 1954.
16. Wierl, R. Ann. Physik, 13: 453. 1932.

[4]*An improved value of A_0 for allene was given by K. N. Rao at the Symposium on Molecular Structure and Spectroscopy, Ohio, 1955. When his value of A_0 = 5.07 cm.$^{-1}$ is combined with the present B_0, the values r_0(CH) = 1.067 Å and ∠HCH = 116° 36′ are obtained.*

SOME EXACT SOLUTIONS OF THE LORENTZ INVARIANT PROBLEM OF THE MOTION OF TWO ELECTRIC FLUIDS[1]

By J. J. Gibbons

ABSTRACT

Methods of generating exact steady-state solutions for the flow of superimposed positive and negative fluids are developed for the cases of linear and cylindrical motion. The two fluids are assumed to be subject only to body forces arising from the total **E** and **B** fields. It is shown that the only axially symmetric solutions are of cylindrical symmetry, i.e. rotating spheres or rings of charge cannot satisfy the equations where the two fluids overlap.

The problem of the dynamics of ionized media has been attacked by various methods as it arises in different fields of investigation. This paper approaches the general problem not by attempting to find solutions with preassigned initial boundary conditions, but by seeking any exact solutions of the Maxwell equations coupled to the dynamical equations of motion. The resulting solutions may be interpreted as limiting cases of ion cloud motion, or may be interpreted in the sense of the "self-consistent electrodynamics" of Buneman (1).

We idealize the problem by representing the positive and negative charges by positive and negative perfect electric fluids, subject only to body forces arising from the total fields **E** and **B**, and not subject to forces arising from pressure gradients or viscosity. The general procedure is to assume some velocity field of simple symmetry. From the Maxwell and dynamical equations we then find the conditions on the velocity components which give possible solutions. These conditions usually resolve into differential inequalities, because the charge densities of the two fluids computed from $\nabla \cdot \mathbf{E}$ and $\nabla \times \mathbf{B}$ must be essentially positive or essentially negative quantities.

I. GENERAL EQUATIONS, M.K.S. SYSTEM

Symbols

$\mathbf{V}$ = velocity of positive fluid.
$\mathbf{W}$ = velocity of negative fluid.
$\mathbf{E}$ = electric field.
$\mathbf{B}$ = magnetic induction.
Φ = scalar potential.
p = charge density of positive fluid.
$-n$ = charge density of negative fluid.
P = rest charge–mass ratio of positive fluid.
N = rest charge–mass ratio of negative fluid.
$\boldsymbol{\alpha} = \mathbf{V}/\sqrt{(1-v^2c^2)}$.

[1]*Manuscript received in original form March 30, 1954, and, as revised, August 3, 1955.*
Contribution from the Ionosphere Research Laboratory, The Pennsylvania State University, University Park, Pennsylvania.
The research reported in this paper has been supported by the National Science Foundation under Grant G450 and, in part, by the Geophysics Research Directorate of the Air Force Cambridge Research Center under Contracts AF19(122)-44 and AF19(604)-1304.

$\alpha_4 = 1/\sqrt{(1-V^2/c^2)} = \sqrt{(1+\alpha^2/c^2)}$.
$\boldsymbol{\beta} = \mathbf{W}/\sqrt{(1-W^2/c^2)}$.
$\beta_4 = 1/\sqrt{(1-W^2/c^2)} = \sqrt{(1+\beta^2/c^2)}$.
ϵ_0 = electric permittivity of free space.
μ_0 = magnetic permeability of free space.

In Lorentz invariant form the dynamical equations governing the steady-state motion of the two fluids subject only to body forces due to **E** and **B** can be put in the form (2)

$$(\boldsymbol{\alpha}\cdot\text{grad})\boldsymbol{\alpha} = P[\mathbf{E}\alpha_4+(\boldsymbol{\alpha}\times\mathbf{B})],$$
$$\text{div}(p\boldsymbol{\alpha}) = 0,$$
$$(\boldsymbol{\beta}\cdot\text{grad})\boldsymbol{\beta} = -N[\mathbf{E}\beta_4+(\boldsymbol{\beta}\times\mathbf{B})],$$
$$\text{div}(n\boldsymbol{\beta}) = 0.$$

The Maxwell equations are

$$\text{curl}\,\mathbf{E} = 0, \qquad \text{div}\,\epsilon_0\mathbf{E} = p\alpha_4 - n\beta_4,$$
$$\text{curl}\,\mathbf{B} = \mu_0(p\boldsymbol{\alpha}-n\boldsymbol{\beta}), \qquad \text{div}\,\mathbf{B} = 0.$$

The continuity equations on $p\boldsymbol{\alpha}$ and $n\boldsymbol{\beta}$ are not independent of one another, since the conservation of total charge follows from the Maxwell equations.

II. STEADY-STATE LINEAR FLOW

As the simplest example consider that $\boldsymbol{\alpha}$ and $\boldsymbol{\beta}$ have only x components. For brevity we write α for α_x and β for β_x in this section. The dynamical equations give

$$\alpha\,\partial\alpha/\partial x = PE_x\,\alpha_4, \qquad \beta\,\partial\beta/\partial x = -NE_x\,\beta_4,$$
$$0 = E_y\,\alpha_4 - \alpha B_z, \qquad 0 = E_y\,\beta_4 - \beta B_z,$$
$$0 = E_z\,\alpha_4 + \alpha B_y, \qquad 0 = E_z\,\beta_4 + \beta B_y.$$

Then $\alpha = \beta$; otherwise the y and z components of **E** and **B** all vanish. With $\alpha = \beta$, $E_x = 0$ and $\partial\alpha/\partial x = 0$. It now follows that all quantities are functions of y and z only. The curl **B** equation gives $\partial B_x/\partial y = \partial B_x/\partial z = 0$, and thus B_x is at most a constant, which can be taken to be zero in this problem. Then in terms of the scalar potential Φ,

$$\alpha B_y = \alpha_4\,\partial\Phi/\partial z, \qquad \alpha B_z = -\alpha_4\,\partial\Phi/\partial y.$$

Substitution in the div **B** equation gives

$$\frac{\partial\Phi}{\partial z}\frac{\partial}{\partial y}(\alpha_4/\alpha) - \frac{\partial\Phi}{\partial y}\frac{\partial}{\partial z}(\alpha_4/\alpha) = 0,$$

with the solution $\Phi = F(\alpha)$.

The conditions so far imposed satisfy all equations except the two Maxwell equations now in the form

$$\text{div}\,\epsilon_0\mathbf{E} = (p-n)\alpha_4,$$
$$(\text{curl}\,B)_x = \mu_0(p-n)\alpha.$$

The first of these is solved for $(p-n)$ and substituted in the second. The resulting equation in α is then

$$\nabla^2\alpha+\{F''(\alpha)/F'(\alpha)-1/\alpha\}\ |\text{grad}\ \alpha|^2 = 0.$$

The substitution $q(\alpha) = \int (1/\alpha)F'(\alpha)d\alpha$ gives

$$\nabla^2 q = 0.$$

We can now generate any number of solutions to the steady-state linear flow problem. First, select any solution $q(y, z)$ of the two-dimensional Laplace equation; next, select any function $F(\alpha)$. This determines $\alpha(y, z)$ and $\Phi(y, z)$. From these the fields and charge density $(p-n)$ are derived. In the linear steady-state flow problem only $(p-n)$ appears; no reference is made to p and n individually.

One other type of non-accelerated linear flow was examined. It was assumed that the flow was in parallel straight lines in any plane perpendicular to the z-axis, but the direction of the parallel flow lines might vary from one such plane to another in a continuous way. It was found that no such solutions are possible with any actual variation of flow direction with z.

III. STEADY-STATE AXIAL SYMMETRY IN SPHERICAL COORDINATES

With $x = \rho \sin\theta \cos\phi$, $y = \rho \sin\theta \sin\phi$, $z = \rho \cos\theta$, we investigate the possibility of the flow of the superimposed positive and negative fluids in circles about the z-axis; that is, assume $\alpha_\rho = \alpha_\theta = \beta_\rho = \beta_\theta = 0$. The remaining α_ϕ and β_ϕ we here abbreviate to α and β. Further, $E_\phi = B_\phi = 0$ and all $\partial/\partial\phi$ are zero. The dynamical equations reduce to

$$\begin{aligned}
-\alpha^2/\rho &= P[E_\rho\, \alpha_4-\alpha B_\theta],\\
-\alpha^2 \cot\theta/\rho &= P[E_\theta\, \alpha_4+\alpha B_\rho],\\
-\beta^2/\rho &= -N[E_\rho\, \beta_4-\beta B_\theta],\\
-\beta^2 \cot\theta/\rho &= -N[E_\theta\, \beta_4+\beta B_\rho].
\end{aligned}$$

From these equations

$$\begin{aligned}
[B_\rho+B_\theta \cot\theta]\ \alpha/\alpha_4 &= E_\rho \cot\theta-E_\theta,\\
[B_\rho+B_\theta \cot\theta]\ \beta/\beta_4 &= E_\rho \cot\theta-E_\theta.
\end{aligned}$$

Then it follows that either $\alpha = \beta$ or $E_\rho \cot\theta-E_\theta = \beta_\rho+\beta_\theta \cot\theta = 0$. The first alternative leads to the trivial solution $\alpha = \beta = 0$. The second alternative states that in cylindrical coordinates (r, ϕ, z), $E_z = B_r = 0$, and that therefore complete cylindrical symmetry is the only symmetry possible. We cannot, for example, have rotating spheres of overlapping charge, or polarized toroidal rings rotating about the axis.

IV. CYLINDRICAL SYMMETRY

With $x = r \cos\phi$, $y = r \sin\phi$, $z = z$, we again assume steady motion in circles around the z-axis, i.e., α_r, α_z, β_r, β_z, E_ϕ, and B_ϕ are all zero, as well as all $\partial/\partial\phi$. The remaining α_ϕ and β_ϕ are then designated simply as α and β. The dynamical equations become

$$-\alpha^2/r = P[E_r\,\alpha_4+\alpha B_z],$$
$$-\beta^2/r = -N[E_r\,\beta_4+\beta B_z],$$

and the only necessary Maxwell equations are

$$\epsilon_0(1/r)\,d(rE_r)/dr = p\alpha_4-n\beta_4,$$
$$-dB_z/dr = \mu_0(p\alpha-n\beta)$$

with all quantities functions of r only. Eliminating E_r and B_z by means of the dynamical equations and solving for p and n we have p and n expressed as non-linear functions of α and β and their derivatives. The condition is now to be imposed that α and β be chosen such functions of r as to make p and n everywhere positive. Solutions to this problem have been obtained in two special cases.

Case I. $\alpha = -\beta$

Set $1/P-1/N = A$ and $1/P+1/N = D$, and consider the case in which A is positive. The expressions for p and n become

$$p\mu_0\sqrt{(1+\alpha^2/c^2)} = -(4c^2r)^{-1}\frac{d}{dr}\left[A\alpha^2/\sqrt{(1+\alpha^2/c^2)}\right] + \sqrt{(1+\alpha^2/c^2)}\left(\frac{1}{4\alpha}\right)\frac{d}{dr}\left(D\frac{\alpha}{r}\right) > 0,$$

$$n\mu_0\sqrt{(1+\alpha^2/c^2)} = +(4c^2r)^{-1}\frac{d}{dr}\left[A\alpha^2/\sqrt{(1+\alpha^2/c^2)}\right] + \sqrt{(1+\alpha^2/c^2)}\left(\frac{1}{4\alpha}\right)\frac{d}{dr}\left(D\frac{\alpha}{r}\right) > 0.$$

Addition of the two inequalities gives $(1/\alpha)\,d(\alpha/r)/dr > 0$, and if this condition is satisfied the inequality for n is also seen to be satisfied, since both terms are then positive. The equation for p may be written as

$$\frac{p\mu_0\sqrt{(1+\alpha^2/c^2)}+(A/4)\alpha^2/c^2(2+\alpha^2/c^2)(1+\alpha^2/c^2)^{-3/2}r^{-2}}{D-A\alpha^2/c^2(2+\alpha^2/c^2)(1+\alpha^2/c^2)^{-2}} = \sqrt{(1+\alpha^2/c^2)}(1/4\alpha)\frac{d}{dr}\left(\frac{\alpha}{r}\right).$$

The denominator of the left side is always positive. Then if p is taken to be any positive function and the resulting differential equation solved for α, the inequalities for p and n are simultaneously satisfied, because $(1/\alpha)\,d(\alpha/r)/dr$ is then positive. All solutions obtained in this special case $\alpha = -\beta$ have constant magnetic fields along the z-axis in addition to the fields produced by the moving fluid itself.

Case II. $N\alpha+P\beta = 0$

We have then $E_r = 0$, and

$$p\sqrt{(1+\alpha^2/c^2)} = n\sqrt{(1+\beta^2/c^2)}.$$

The resulting equation on β and n is

$$r\,d\beta/dr-\beta = \mu_0\,Nnr^2\beta[P/N(1+\beta^2/c^2)^{\frac{1}{2}}(1+P^2/N^2\cdot\beta^2/c^2)^{-\frac{1}{2}}+1]$$

from which it follows that

$$r\beta\, d\beta/dr - \beta^2 = f > 0$$

in order that n be positive. We may choose f to be any positive function of β or $\log r$ and integrate to get an allowed $\beta(r)$. These solutions also show constant applied magnetic fields.

Note that any exact solution for the fields and dynamical variables may now be subjected to Lorentz transformations, the cylindrical flow, e.g., going to helical flow.

Though the solutions so far obtained do not appear to describe any usual physical situations, it is felt that the methods used may be extended to situations of less simple symmetry, and in any case such solutions may be used as zero order solutions in perturbation problems, or as exact solutions against which to check approximation methods.

The solutions given are all steady state, but the same analysis may be applied to the general time-varying case, and this problem is now being worked on.

The author wishes to express his appreciation for the assistance of Mr. P. E. Bedient in some parts of this work.

REFERENCES

1. BUNEMAN, O. Proc. Cambridge Phil. Soc. Pt. I, 50: 77. 1954.
2. MØLLER, C. The theory of relativity. The Clarendon Press, Oxford. 1952. Chaps. VI and VII.

ON EQUATIONS OF MOTION IN GENERAL RELATIVITY[1]

By G. E. Tauber[2]

ABSTRACT

It has been shown that both the equations of motion of a charged particle in a gravitational field and the field equations can be obtained from *one* variational principle by suitably generalizing Dirac's classical theory of electrons.

1. INTRODUCTION

In addition to the field equations of general relativity, which connect the distribution of matter and energy with the resulting gravitational field described by the potentials $g_{\mu\nu}$, the motion of a particle in this field must be described by additional equations, the equations of motion. Although it has been shown in the case of weak fields (2, 3) that the latter can be derived from the former, a complete union has not been achieved. This is at least partially due to the fact that two separate sets of variables have to be employed. The field equations are functions of the g's and their derivatives, while the equations of motion employ co-ordinates x^μ (and their derivatives with respect to a parameter) themselves. This situation is fundamentally different from other field theories, say, the scalar meson field, where the same set of equations play the role of field equations and equations of motion and therefore only one set of field variables is necessary.

Although both, the field equations and equations of motion, can be obtained from an appropriate variational principle, it has not been possible to use only *one* to describe both. Recently Dirac (1) has shown how Lorentz's equations of motion and Maxwell's field equations can be both obtained from one variational principle for a stream of electrons characterized by a velocity field v^μ, and in this note his method is generalized for general relativity.

2. FIELD EQUATIONS AND EQUATIONS OF MOTION

Einstein's field equations are given by

$$G_{\mu\nu} = R_{\mu\nu} - \tfrac{1}{2}Rg_{\mu\nu} = -\kappa T_{\mu\nu} \tag{1}$$

where $R_{\mu\nu}$ are the components of the Riemann–Christoffel curvature tensor and $T_{\mu\nu}$ the components of the energy–momentum tensor. For the electromagnetic field the latter are given by

$$T_{\mu\nu} = -g_{\nu\beta}\, F_{\mu\alpha}\, F^{\beta\alpha} + \tfrac{1}{4}g_{\mu\nu}\, F_{\alpha\beta}\, F^{\alpha\beta} \tag{2}$$

where the $F_{\mu\nu}$ are the components of the field tensor, which can be defined in terms of the electromagnetic potentials A_μ as follows:

$$F_{\mu\nu} = \frac{\partial A_\mu}{\partial x^\nu} - \frac{\partial A_\nu}{\partial x^\mu}. \tag{3}$$

[1]*Manuscript received September 14, 1955.*
Contribution from the Division of Pure Physics, National Research Council, Ottawa, Canada. Issued as N.R.C. No. 3788.
[2]*Present address: Department of Physics, Western Reserve University, Cleveland, Ohio, U.S.A.*

In addition, the F's satisfy Maxwell's equations, which in the absence of any charge and current distributions are

$$\frac{\partial \mathfrak{F}^{\mu\nu}}{\partial x^{\nu}} = 0. \tag{4}$$

Here $\mathfrak{F}^{\mu\nu}$ denote tensor densities defined by $\mathfrak{F}^{\mu\nu} = \sqrt{-g}\, F^{\mu\nu}$. The other set of Maxwell's equations is automatically satisfied by writing the field in the form [3]. Both the field equations and Maxwell's equations can be obtained from a variational principle (5):

$$\delta \int (2G+\kappa M)\sqrt{-g}\, d\tau_4 = 0 \tag{5}$$

where for G we have to take

$$G = \tfrac{1}{2} g^{\mu\nu}[\Gamma^{\sigma}_{\mu\lambda}\, \Gamma^{\lambda}_{\nu\sigma} - \Gamma^{\sigma}_{\mu\nu}\, \Gamma^{\tau}_{\sigma\tau}], \tag{6}$$

where $\Gamma^{\lambda}_{\mu\nu}$ are the Christoffel symbols, and for M,

$$M = -\tfrac{1}{2} F_{\mu\nu}\, F^{\mu\nu}. \tag{7}$$

Variation with respect to $g^{\mu\nu}$ then results in the field equations [2] where each quantity is expressed as a tensor density, while variation with respect to A_{μ} gives Maxwell's equations [4].

Similarly the equations of motion of a *free* particle are given by

$$\frac{d^2x^{\mu}}{ds^2} + \Gamma^{\mu}_{\alpha\beta} \frac{dx^{\alpha}}{ds} \frac{dx^{\beta}}{ds} = 0 \tag{8}$$

which can be derived from a variational principle

$$\delta \int ds = 0 \tag{9}$$

where use has been made of the definition of the line element $ds^2 = g_{\mu\nu}\, dx^{\mu}\, dx^{\nu}$. In the following it will be necessary to use the covariant form of the equations of motion, which is given by

$$\frac{d^2x_{\mu}}{ds^2} + \frac{1}{2} \frac{\partial g^{\rho\sigma}}{\partial x^{\mu}} \frac{dx_{\rho}}{ds} \frac{dx_{\sigma}}{ds} = 0. \tag{10}$$

At this point it might be interesting to point out that the equations of motion can be expressed in Hamilton's canonical form (4), as we might have to use them in that form when going to the Hamiltonian form of the theory. This is achieved by defining a scalar *inertial function* $m(x, p)$ which will become numerically equal to the mass m_0 of the particle as a consequence of the equations of motion. Defining p_{μ} by the equations

$$p_{\mu} = m \frac{dx_{\mu}}{ds}, \qquad m(x, p) = \sqrt{g^{\mu\nu} p_{\mu} p_{\nu}} \tag{11}$$

(a consequence of $ds^2 = g^{\mu\nu}\, dx_{\mu}\, dx_{\nu}$), we obtain the canonical equations

$$\frac{dx^{\mu}}{ds} = \left(\frac{\partial m}{\partial p_{\mu}}\right)_{x=\text{const.}} = \frac{1}{m} p^{\mu}, \tag{12}$$

$$\frac{dp_{\mu}}{ds} = -\left(\frac{\partial m}{\partial x^{\mu}}\right)_{p=\text{const.}} = -\frac{1}{2m} \frac{\partial g^{\alpha\beta}}{\partial x^{\mu}} p_{\alpha} p_{\beta}. \tag{13}$$

3. LORENTZ'S EQUATIONS OF MOTION

Lorentz's equations of motion for a charged particle moving with velocity $v^\mu = dx^\mu/ds$ in an electromagnetic field $F_{\mu\nu}$ and in the presence of a gravitational field are

$$\frac{d^2x^\mu}{ds^2}+\Gamma^\mu_{\alpha\beta}\frac{dx^\alpha}{ds}\frac{dx^\beta}{ds}+\frac{1}{k}F^\mu_\alpha\frac{dx^\alpha}{ds}=0 \tag{14}$$

or in their covariant form

$$\frac{d}{ds}v_\mu+\frac{1}{2}\frac{\partial g^{\rho\sigma}}{\partial x^\mu}v_\rho v_\sigma+\frac{1}{k}F_{\mu\alpha}v^\alpha=0. \tag{15}$$

From the equation $v_\rho v_\sigma g^{\rho\sigma} = 1$ it follows that

$$\frac{\partial g^{\rho\sigma}}{\partial x^\mu}v_\rho v_\sigma+2\frac{\partial v_\rho}{\partial x^\mu}v^\rho=0$$

and for a stream of particles v_μ is a continuous function and thus

$$\frac{dv_\mu}{ds}=\frac{\partial v_\mu}{\partial x^\nu}v^\nu.$$

So [15] may be written as

$$v^\nu f_{\mu\nu}=0 \tag{16}$$

where

$$f_{\mu\nu}=F_{\mu\nu}+k\left(\frac{\partial v_\mu}{\partial x^\nu}-\frac{\partial v_\nu}{\partial x^\mu}\right). \tag{17}$$

From here on we follow Dirac's treatment (1) and finally obtain for the potentials A_μ*

$$A_\mu=-kv_\mu+\xi\frac{\partial\eta}{\partial x^\mu}. \tag{18}$$

4. THE ACTION PRINCIPLE

We are now in the position to write down the variational principle, which is to give both the equations of motion and the field equations. Let us take for the action

$$L=G+\frac{u}{4}F_{\mu\nu}F^{\mu\nu}+\frac{\kappa\lambda}{2}(v_\mu v^\mu-1) \tag{19}$$

where for G we use the function previously defined (Eq. [6]) and the $F_{\mu\nu}$ are derived from the potentials [18]. As independent field variables we take v_μ, λ, ξ, η, $g^{\mu\nu}$. Varying the action integral

$$I=\int L\sqrt{-g}\,d\tau_4 \tag{20}$$

over the whole of space–time we obtain

$$\delta I=\int\Big[\tfrac{1}{2}\mathfrak{G}_{\mu\nu}\delta g^{\mu\nu}+\frac{\kappa}{2}\mathfrak{T}_{\mu\nu}\delta g^{\mu\nu}-\kappa\frac{\partial\mathfrak{F}^{\mu\nu}}{\partial x^\nu}\delta A_\mu+\frac{\kappa}{2}(v_\mu v^\mu-1)\,d\lambda$$
$$+\kappa v^\mu\lambda\sqrt{-g}\,\delta v_\mu+\frac{\kappa\lambda}{2}\sqrt{-g}\,v_\mu v_\nu\,\delta g^{\mu\nu}-\frac{\kappa\lambda}{4}\sqrt{-g}\,(v^\alpha v_\alpha-1)\,g_{\mu\nu}\,\delta g^{\mu\nu}\Big]d\tau_4.$$

*The difference in sign is due to our alternative definition of $F_{\mu\nu}$ (see Eq. [3]).

The condition that I shall be stationary after making use of [18] gives

$$v^\mu v_\mu - 1 = 0, \tag{21}$$

$$k\frac{\partial \mathfrak{F}^{\mu\nu}}{\partial x^\nu} + \lambda v^\mu \sqrt{-g} = 0, \tag{22}$$

$$\frac{\partial \mathfrak{F}^{\mu\nu}}{\partial x^\nu}\frac{\partial \xi}{\partial x^\mu} = 0, \qquad \frac{\partial \mathfrak{F}^{\mu\nu}}{\partial x^\nu}\frac{\partial \eta}{\partial x^\mu} = 0, \tag{23}$$

$$\mathfrak{G}_{\mu\nu} + \kappa \mathfrak{T}_{\mu\nu} + \kappa\lambda \sqrt{-g}\, v_\mu v_\nu - \frac{\kappa\lambda}{4}(v^\alpha v_\alpha - 1)\, g_{\mu\nu}\sqrt{-g} = 0. \tag{24}$$

Equation [22] becomes Maxwell's field equations if we identify the charge-current density as

$$j^\mu = -\frac{\lambda}{k} v^\mu \sqrt{-g}\,. \tag{25}$$

Equations [23] become the field equations for particles in electromagnetic and gravitational fields after using equation [21],* and, finally, equations [23] may be replaced for $\lambda \neq 0$ by

$$v^\mu \frac{\partial \eta}{\partial x^\mu} = v^\mu \frac{\partial \xi}{\partial x^\mu} = 0$$

and give, with the help of [18],

$$v^\mu \left[\frac{\partial}{\partial x^\mu}(A_\nu + k v_\nu) - \frac{\partial}{\partial x^\nu}(A_\mu + k v_\mu) \right] = 0 \tag{26}$$

which are identical with [16] and thus lead back to Lorentz's equations of motion. Thus the action principle gives both the equations of motion and the field equations correctly.

In a subsequent paper we shall discuss the Hamiltonian form of the field equations and give the corresponding action principle.

In conclusion, I wish to thank Professor P. A. M. Dirac for valuable discussions.

REFERENCES

1. Dirac, P. A. M. Proc. Roy. Soc. (London), A, 212: 330. 1952.
2. Einstein, A. and Infeld, L. Ann. Math. 41: 455. 1940.
3. Einstein, A., Infeld, L., and Huffman, B. Ann. Math. 39: 65. 1938.
4. Tauber, G. E. and Weinberg, J. W. Phys. Rev. 86: 621. 1952.
5. Weyl, H. Space, time and matter. Methuen & Co. Ltd., London. 1922.

*λ *plays the role of the mass and thus is identical to the inertial function m defined in Section 2. Hence [25] becomes*

$$j^\mu = -\frac{1}{k} p^\mu. \tag{25a}$$

GAMMA RAYS FROM THE DEUTERON BOMBARDMENT OF BORON 10[1]

By J. T. Sample, G. C. Neilson,[2] G. B. Chadwick,[2] and J. B. Warren

ABSTRACT

Bombardment of B^{10} with 1.4 Mev. deuterons has been found to produce gamma rays of energy 4.46±.04, 4.75±.03, 5.03±.09, 5.35±.05, 6.52±.04, 6.78±.07, 7.29±.04, 8.27±.09, and 8.87±.02 Mev., as measured with a three-crystal pair spectrometer. Tentative assignments to transitions in B^{11} and C^{11} agree well in most cases with the known energy level schemes. No gamma rays of very high energy were observed, even with a single-crystal spectrometer; consequently an upper limit of 10^{-31} cm.^{2} has been placed on the cross-section of $B^{10}(d, \gamma)C^{12}$ at 0.95 Mev. bombarding energy.

INTRODUCTION

Bombardment of B^{10} with deuterons produces simultaneously the mirror nuclei B^{11} and C^{11} through the reactions $B^{10}(d, p\gamma)B^{11}$ and $B^{10}(d, n\gamma)C^{11}$. If the charge symmetry postulate that p–p and n–n forces are equal except for electrostatic forces is correct, and if many-body forces are either negligible or charge independent, then the energy level diagrams of mirror nuclei should be identical in the energies, spins, and parities of the states. The ground states should differ in energy by the n–p mass difference and the Coulomb energy of the proton according to

$$E = (m_n - m_p)c^2 - (3e^2/5R)(A-1) \qquad [1]$$

where

m_n = neutron mass,
m_p = proton mass,
c = velocity of light,
e = proton charge,
$R = 1.45\, A^{\frac{1}{3}} \times 10^{-13}$ cm. is the nuclear radius, and
A = mass number.

The energy level diagrams of B^{11} and C^{11} (2) are shown in Fig. 1 with the ground states at the same height to facilitate comparison of the level spacings. From equation [1] the ground state of C^{11} should be 1.39 Mev. above that of B^{11}; the experimental energy difference is 1.98 Mev. (2). This is by no means an indication that the charge symmetry postulate is incorrect, since the electrostatic term in equation [1] is derived on the assumption of uniform charge distribution throughout the nuclear volume; furthermore, the nuclear radius is not a well-defined quantity.

Unfortunately, there is as yet insufficient information, particularly as to spin and parity assignments, to permit detailed comparison of the two level

[1]*Manuscript received August 12, 1955.*
Contribution from the Department of Physics, University of British Columbia, Vancouver, British Columbia.
[2]*Holder of N.R.C. studentship.*

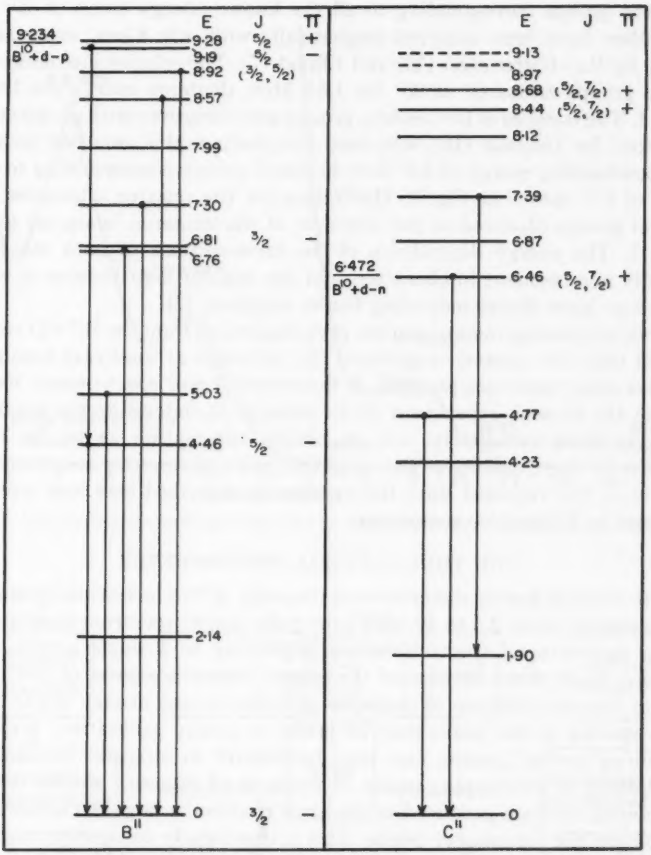

FIG. 1. Energy levels of B^{11} and C^{11}. Transitions shown were found in the present work.

schemes, but the pattern of levels is certainly similar. The first five excited states show a marked resemblance to each other in spacing, with those of C^{11} lying on the average 250 kev. below the corresponding levels of B^{11}. The only certain spin assignment of those shown in Fig. 1 is that of the B^{11} ground state (8). There is, for example, considerable difference between the spin and parity assignments listed by Ajzenberg and Lauritsen (2) and those listed by Jones and Wilkinson (11). The energies of the levels are assigned largely from the measurement of energies of proton and neutron groups from deuteron bombardment of B^{10} (7, 10, 14). Because the energy resolution attainable is poorer for neutrons than for protons, it is possible that some levels are not yet resolved in C^{11}; for example, the 6.46 Mev. level in C^{11} probably corresponds to the 6.76, 6.81 Mev. pair of levels in B^{11}.

Proton groups corresponding to all the known energy levels of B^{11} up to 10.32 Mev. have been analyzed magnetically with only 8 kev. uncertainty in energy by Van Patter *et al.* (14) and Elkind (7). The relative intensities of the proton groups measured at 90° for 1.51 Mev. deuteron energy are listed in Table I. The energies of the neutron groups were measured with an uncertainty of 60 kev. by Johnson (10), who used the photographic emulsion technique. At a bombarding energy of 3.6 Mev. he found groups corresponding to all the levels of C^{11} shown in Fig. 1. His values for the relative intensities of the neutron groups observed in the direction of the deuteron beam are given in Table I. The energy dependence of the cross-sections of both reactions is basically non-resonant in character, and the angular distributions of some of the groups have shapes indicating Butler stripping (2).

Previous investigations of gamma rays originating from the $B^{10}+D$ reactions showed only five gamma transitions (1), although at moderate bombarding energies many more are possible. A three-crystal pair spectrometer has been used in the present experiment in an attempt to determine the gamma-ray spectrum more completely, and to obtain information as to the relative intensity of the transitions. The magnetic pair spectrometer measurements of Bent *et al.* (4), reported since the experiment described here was completed, are listed in Table I for comparison.

THE THREE-CRYSTAL SPECTROMETER

With crystals having dimensions of the order of two inches and gamma rays in the energy range 2.5 to 10 Mev., the pulse height spectrum from a sodium iodide single-crystal spectrometer corresponding to a single gamma energy contains three peaks because of the escape from the crystal of one or both quanta from annihilation of positrons produced in pair events. While the 0.51 Mev. spacing of the peaks may be useful in energy calibration, a spectrum containing several gamma rays may be difficult to interpret because of the multiplicity of overlapping peaks. If neutrons of intensity similar to that of the gamma rays are produced in the same reaction, a large background tends to obscure the gamma-ray peaks. This is due largely to neutron capture by I^{127} in the crystal, which results in the prompt emission of gamma rays in the energy range 4 to 6 Mev., followed by 2.0 Mev. beta decay, or 1.6 Mev. beta decay coincident with a 0.4 Mev. gamma ray. The beta decay half-life is 25 min. This background can cause, through "pile-ups", pulses of magnitude corresponding to 15 Mev. gamma rays. A typical single-crystal spectrum obtained with a 2 in. $\times 1\frac{3}{4}$ in. diam. crystal from deuteron bombardment of B^{10} is shown in Fig. 2.

The three-crystal pair spectrometer, at the expense of a factor of 100 to 1000 in efficiency, completely eliminates the first difficulty mentioned above, and reduces the second to a level tolerable in most experiments. The principle of the three-crystal spectrometer has been discussed by several authors (3, 9, 15). The spectrometer used in the present experiment differs in detail, but not in principle, from those described in the above papers. Figure 3 is a block diagram of the complete spectrometer, excluding the high voltage and "B-plus" supplies.

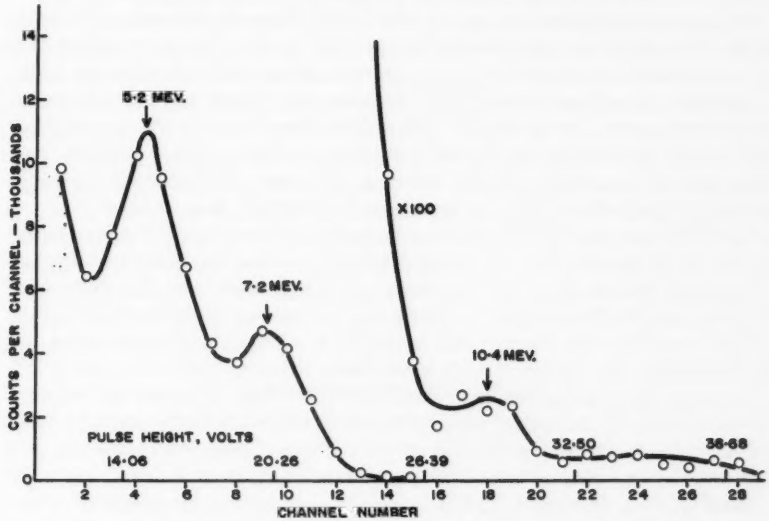

FIG. 2. Single-crystal spectrum from $B^{10}+D$. $E_d = 0.95$ Mev. 230 microcoulombs.

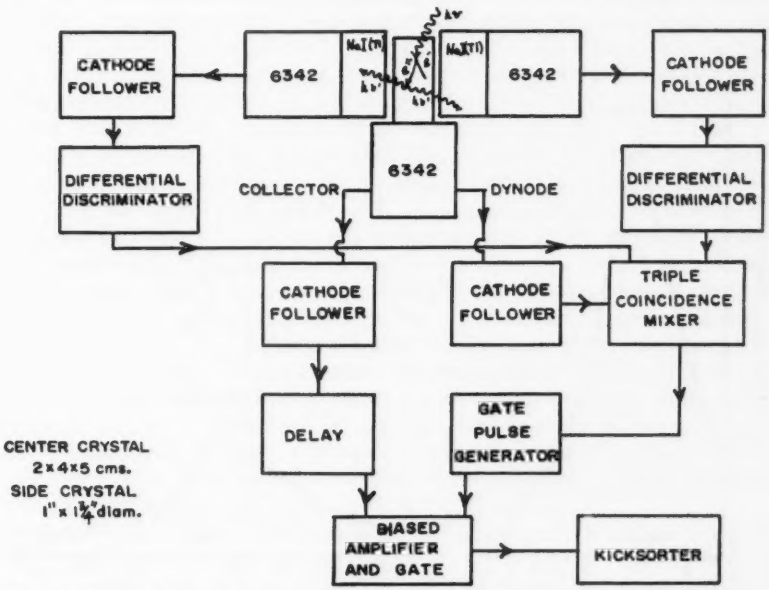

FIG. 3. Block diagram of the three-crystal spectrometer. Power supplies are not shown.

Differential discrimination in each side channel was used to reduce the number of unwanted true coincidences due to the "double Compton" effect (12) and to scattering of single Compton quanta from one side crystal to the other. Accidental coincidences were also, of course, decreased by the differential discriminators, and were further reduced by the use of triple, rather than double, coincidence mixing. In addition, the side crystals were shielded from the target by 5 in. of lead, and all three crystals were shielded from the background of X-rays from the Van de Graaff generator by 3 in. of lead.

The side channel discriminators were adjusted to pass the total energy pulses of 0.51 Mev. quanta by viewing the spectrum of the annihilation radiation from a Na^{22} source with an oscilloscope receiving pulses from the collector of the side channel photomultiplier. With the oscilloscope trace triggered by the output from the side channel discriminator receiving the corresponding last dynode pulse, the discrimination levels were adjusted until only the bright full energy group of pulses was visible on the screen. The one microsecond resolving time of the triple coincidence mixer was sufficiently short to make accidental coincidences negligible, since the permissible counting rate was restricted by the effect of high counting rates on the gain stability of the center channel photomultiplier (6). The coincidence output pulse triggered a univibrator which produced a 30 v., 2 μsec. gating pulse. Center channel pulses were amplified by a Northern Electric No. 1444 amplifier and passed through the gated biased amplifier to a 30 channel Marconi kicksorter. A 1.5 μsec. delay, in the form of 1000 ohm cable, was inserted in the center channel to locate the pulses within the gated interval.

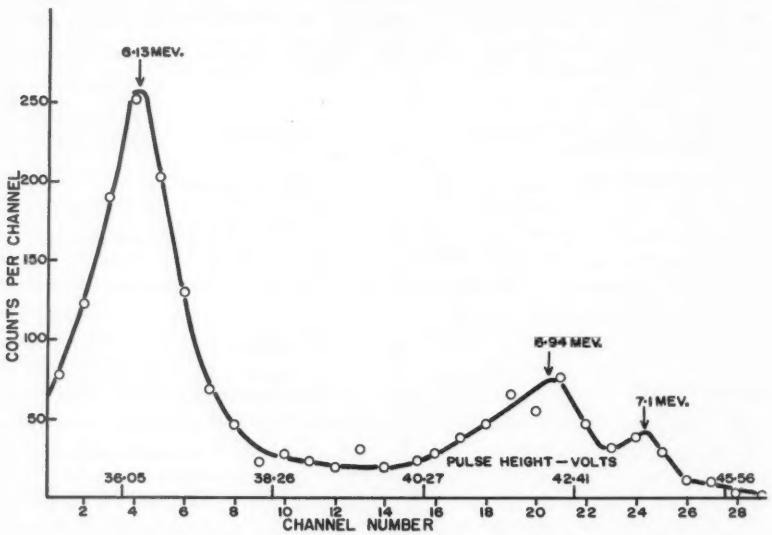

FIG. 4. Spectrum from $F^{19}(p, \alpha\gamma)O^{16}$. $E_p = 0.873$ Mev. Thin target.

The performance of the spectrometer has been very satisfactory; its resolution was found to be about 4% at 6 Mev., as shown by Fig. 4, an energy calibration spectrum of the 6.13, 6.94, and 7.1 Mev. gamma rays from the 0.873 Mev. resonance in $F^{19}(p, \alpha\gamma)O^{16}$.

A resolution of 6.5% was obtained for the 2.62 Mev. line from radiothorium, shown dotted in Fig. 5. Comparison of Fig. 2 with Figs. 5 and 6 shows that the neutron rejection of the spectrometer was very good indeed. The pulse height scales on the various spectra do not agree because different injection points in the center channel circuit for the calibration pulses from a standard pulse generator were tried, to avoid a troublesome slow drift in the gain of the center channel. In the final configuration, although only the center channel crystal and photomultiplier were outside the calibration loop, gain drifts persisted. A correlation between instability of gain and counting rate was found, in agreement with Reference (6).

EXPERIMENTAL PROCEDURE

The targets, kindly supplied by the Isotopes Division, A.E.R.E., Harwell, were enriched to better than 95% B^{10}. Deposited on platinum backings, they were 100 μgm./cm.^{2} thick, or approximately 40 kev. thick to 1.5 Mev. deuterons. They were clamped on a copper support insulated to permit measurement of the beam current. No coolant was used, since some heating was desirable to reduce carbon build-up on the targets. A 3/16 in. diam. beam-defining stop cut from 1/16 in. molybdenum sheet was placed 6 in. from the target. The spectrometer was located at 0° to the deuteron beam, the distance from the target to the center of the center crystal being 13 cm.

By inserting standard pulses at some point in the center channel, in the later runs at the grid of the cathode follower, and adjusting the gain and bias of the Northern Electric amplifier-biased amplifier combination, the desired range of pulse heights was made to cover the 30 kicksorter channels. This setting was checked at the beginning and end of each two hour B^{10} bombardment. Gamma rays of known energy were used for energy calibration, usually those from $F^{19}(p, \alpha\gamma)O^{16}$ (6.13, 6.94, and 7.1 Mev.) and radiothorium (2.62 Mev.). This was repeated at least twice each day, two or more B^{10} runs intervening between calibration runs. To check the linearity of the center channel gain, several other energy points were used occasionally. The center channel could be operated as a single-crystal spectrometer by disabling the gate, permitting determination of the photoelectric peak of the 2.62 Mev. line from radiothorium, and those of the 0.51 and 1.28 Mev. lines from Na^{22}. This was not repeated often, as the linearity was always very good, at least as far as 7 Mev. Checks with the 17.6 and 14.8 Mev. gamma rays from the 440 kev. resonance in $Li^7(p, \gamma)Be^8$ indicated that the gain was linear to 17.6 Mev., but the peaks were broad and asymmetrical because of bremsstrahlung losses and wall effects in the rather small center crystal.

Even though power supply and heater voltages were carefully stabilized and monitored, and the center channel counting rate was kept less than 8000 counts per second by limiting the beam to about five microamperes, small gain drifts

persisted. In analyzing the results, if the peaks in a particular spectrum were abnormally broad, the spectrum was not used in determining the gamma-ray energies. If the peaks of a spectrum were of normal width, but the energies of all gamma rays determined from the peaks deviated in the same direction from the respective mean values of other determinations, the energy scale was "normalized" to the mean value for the energy of the most prominent gamma ray present in the spectrum; this procedure was only necessary for one spectrum retained in the final analysis.

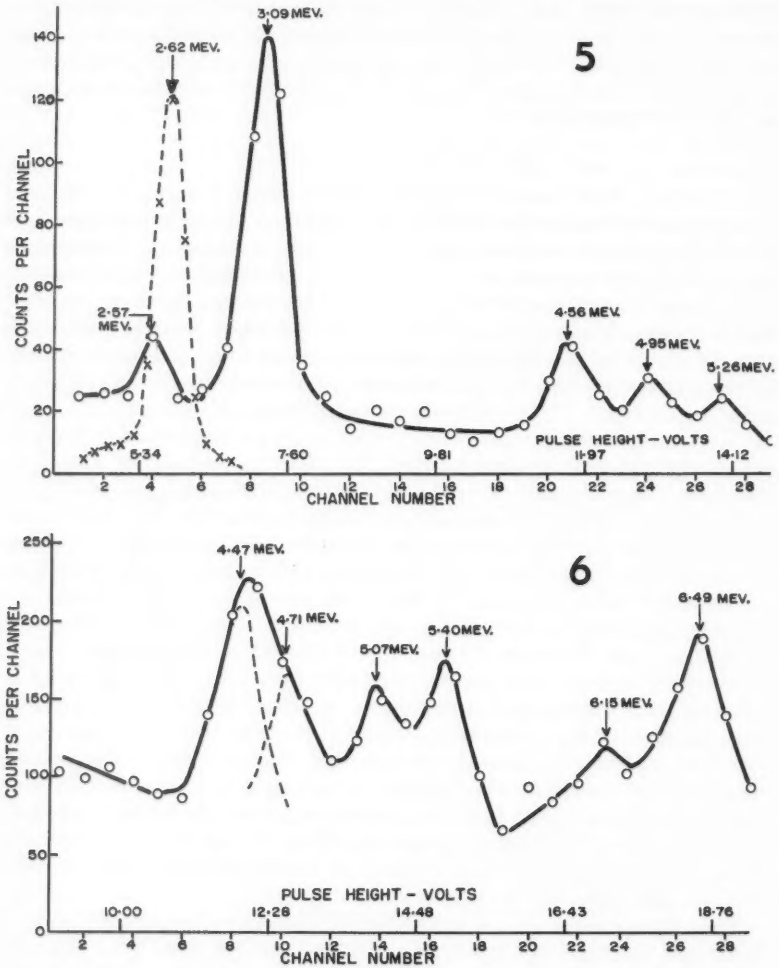

FIG. 5. Spectrum from $B^{10}+D$, 2.0 to 5.5 Mev. E_d = 1.40 Mev. 3300 microcoulombs. The dotted curve is the spectrum from radiothorium.

FIG. 6. Spectrum from $B^{10}+D$, 4.0 to 6.5 Mev. E_d = 1.40 Mev. 11,300 microcoulombs.

RESULTS AND DISCUSSION

Typical spectra, obtained at 0° to the 1.4 Mev. deuteron beam and covering the range of gamma-ray energies from 2 to 9.5 Mev., are shown in Figs. 5, 6, 7, and 8. The peaks are labelled according to actual gamma-ray energy, as

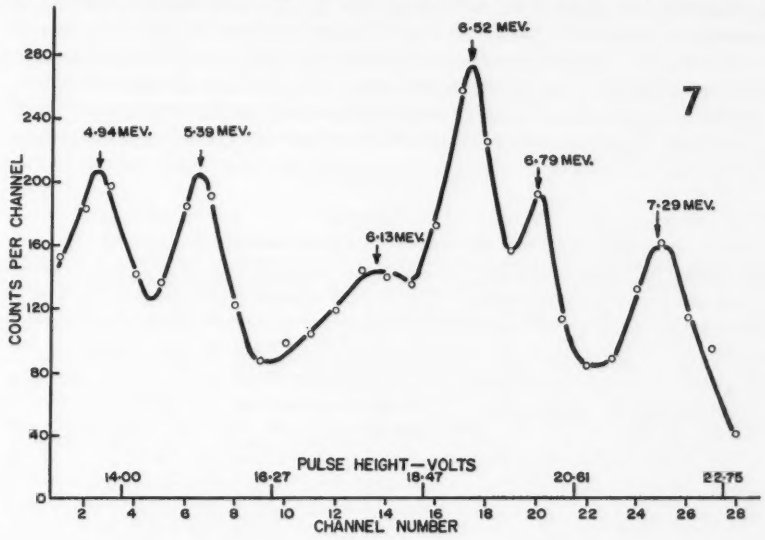

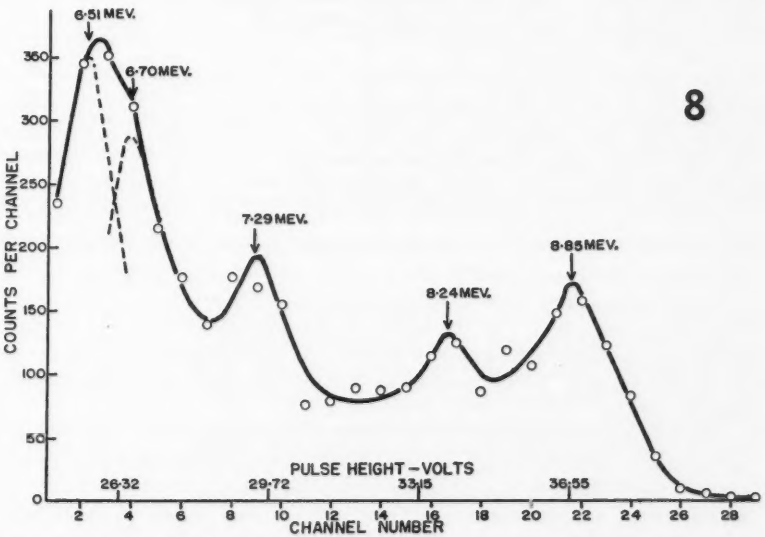

FIG. 7. Spectrum from $B^{10}+D$, 4.8 to 7.5 Mev. $E_d = 1.40$ Mev. 19,300 microcoulombs.
FIG. 8. Spectrum from $B^{10}+D$, 6.5 to 9.5 Mev. $E_d = 1.40$ Mev. 30,000 microcoulombs.

determined from each spectrum, rather than pair peak energy. The integrated beam current for each run is indicated in the captions of the figures. Direct comparison of intensities between the various spectra is only rough, because of the loss of target material during bombardment.

The energies, found by averaging the results from several spectra, and relative intensities of the gamma rays assigned to transitions of B^{11} and C^{11} are listed in Table I. The assignments are indicated by arrows in Fig. 1. The energy errors listed in the table are standard deviations of several determinations of each gamma energy, ranging from three determinations of the 4.75 Mev. gamma ray to twelve of the 7.29 Mev. gamma ray. The measurements of Bent *et al.* (4), listed in Table I for comparison, were corrected for Doppler

TABLE I

ASSIGNMENT OF THE GAMMA RAYS TO LEVELS OF B^{11} AND C^{11}

B^{11}*	PRESENT WORK		BENT et al.(1955)		PROTON GROUPS	C^{11}*	PRESENT WORK		BENT et al.(1955)		NEUTRON GROUPS
	E_γ	I_{rel}	E_γ	I_{rel}	I_{rel}		E_γ	I_{rel}	E_γ	I_{rel}	I_{rel}
0	—	—	—	—	11	0	—	—	—	—	2.2
2.14	—	—	—	—	2.4	1.90	—	—	—	—	0.6
4.46	4.46 ±.04		4.50 ±.10	6.0	6.5	4.23	—	—	—	—	2.8
5.03	5.03 ±.09		5.03 ±.04	4.1	5.5	4.77	4.75 ±.03	6	4.74 ±.04	6.9	2.0
6.76 6.81	6.78 ±.07	6	6.79 ±.04	12	12	6.46	6.52 ±.05	12	6.52 ±.04	12	12
7.30	7.29 ±.04	5	7.32 ±.04	4.1	6.5	6.87	—	—	7.01 ±.06	6	2.0
7.99	—	—	5.87 ±.07	2.8	1.6	7.39	5.35 ±.05	7	—	—	0.4
8.57	8.27 ±.09	4	8.62 ±.07	1.9	1.6	—	—	—	—	—	—
8.92	8.87 ±.02	11	8.98 ±.04	7.2	27	—	—	—	—	—	—
9.19	4.75 ±.03	6	4.74 ±.04	6.9	44	—	—	—	—	—	—
9.28	—	—	—	—	22	—	—	—	—	—	—

shift, whereas the present measurements were not corrected. Doppler corrections for center of mass motion (for 1.4 Mev. bombarding energy and observation at 0°) range from 28 kev. for the 4.46 Mev. gamma ray to 57 kev. for the 8.87 Mev. gamma ray, of the order of the standard deviations. However, several of the neutron and proton groups are emitted predominantly forward (5, 10, 13), tending to reduce the mean Doppler correction of the corresponding gamma rays.

The relative intensities listed in Table I were obtained by measuring the areas under the peaks in the spectra, subtracting a somewhat arbitrary background, normalizing to the integrated beam current, and applying a correction factor for the variation of the pair cross-section with energy. A correction, of the order of 30% for the higher energy gamma rays, due to bremsstrahlung

loss and wall effects in the center channel crystal, has not been applied, since the uncertainties in intensity were of this order. Agreement between successive runs was not good, owing to loss of target under bombardment and to possible variations in the distribution of the deuteron beam on the target, so the intensities from overlapping spectra were normalized by the use of gamma rays common to both. All intensities in Table I, including those of the proton and neutron groups, are normalized to be directly comparable. The gamma-ray intensities of Bent *et al.* (4) were measured for thick targets and 2 Mev. bombarding energy; the difference in conditions perhaps explains why there is only qualitative resemblance to the intensities from the present experiment.

B^{11} TRANSITIONS

The intensities of the proton groups listed in Table I were measured at 90° and 1.51 Mev. bombarding energy (14); because of differences in the angular distributions of the groups, only qualitative comparison with the gamma-ray intensities is possible. The difference in the intensity of the proton group and gamma ray corresponding to the 4.46 Mev. state in B^{11} may be explained by the proposed cascade through this state from the 9.19 Mev. state. Serious discrepancies arise for the three highest states at 8.92, 9.19, and 9.28 Mev. The 8.92 Mev. ground state transition is much weaker than the proton group exciting it, the 9.19 Mev. state decays apparently only by a 4.73 Mev. cascade gamma ray much less intense than the corresponding proton group, and no gamma rays were attributed to the 9.28 Mev. state. In a few early runs, with wider side channel windows, and thus greater efficiency, there was some indication of radiation of energy greater than 9 Mev., but these suffered from poor resolution and gain drifts. The proposed decay scheme of B^{11} does not agree well with that of Jones and Wilkinson (11) from measurements on the reaction $Li^7(\alpha, \gamma)B^{11}$.

The 8.27 Mev. gamma ray has been assigned to the 8.57 Mev. state in B^{11}, although the energy discrepancy is three times the standard deviation of the energy measurements. This discrepancy may arise in part from the low intensity of the radiation, and perhaps from conflicting counts due to 8.87 Mev. photons which fail to produce the full pulse height because of bremsstrahlung loss and wall effects, and produce a peak below the pair peak. A similar effect, though much smaller in proportion, has been observed with the clean 6.13 Mev. gamma ray from $F^{19}(p, \alpha\gamma)O^{16}$.

C^{11} TRANSITIONS

The neutron group intensities in Table I were measured at 0° and 3.4 Mev. bombarding energy (10); the difference in bombarding energy and the strong forward peaking of some of the groups make comparison with the gamma-ray intensities rather hazardous. It has been found at this laboratory (13) that, at 1.5 Mev. deuteron energy, the neutron groups corresponding to states in C^{11} at 6.46 and 4.77 Mev. are much more intense than other groups, with the possible exception of the ground state group which was not under observation. So the 4.75 Mev. gamma ray observed has been attributed in part to the ground

state transition from the 4.77 Mev. state in C^{11} as well as to the 4.73 Mev. transition between the 9.19 and 4.46 Mev. states in B^{11}. The 7.01 Mev. gamma ray attributed by Bent *et al.* (4) to the 6.87 Mev. state of C^{11} was not observed in this experiment. A 5.35 Mev. gamma ray was assigned to the 5.49 Mev. transition between the 7.39 and 1.90 Mev. states analogous to the 5.87 Mev. transition from the 7.99 Mev. state in B^{11} reported by Bent *et al.* (4), although comparison of neutron and gamma-ray intensities is not encouraging.

Four peaks corresponding to gamma-ray energies of 2.57, 3.09, 3.52, and 6.13 Mev. have been observed (Figs. 5, 6, and 7). The 2.57 Mev. gamma ray may be from the 2.38 Mev. transition between the 9.19 and 6.81 Mev. states of B^{11}. Carbon accumulated on the target and beam stop was responsible, through the reaction $C^{12}(d, p\gamma)C^{13}$, for the 3.09 and 3.52 Mev. gamma rays, since their intensities were much smaller from a new target and freshly cleaned stop. The 3.52 Mev. gamma ray, probably from the 3.68 Mev. state of C^{13}, was seen only with very dirty targets, and had about one-fortieth of the intensity of the 3.09 Mev. gamma. The excitation curve of these gamma rays also showed a resonance near 1 Mev. deuteron energy, in agreement with the assignment to C^{13}. The 6.13 Mev. peak may be attributed to the intense 6.12 Mev. gamma ray from the reaction $C^{13}(d, p\gamma)C^{14}$. Using the yield values given in Reference (2) and assuming 1% isotopic abundance for C^{13}, the 3.09 Mev. gamma-ray peak should have an intensity larger by a factor of 170 than that of the 6.12 Mev. gamma ray, allowing for the energy variation of the pair cross-section. The intensity ratio of the two peaks was found by experiment to be approximately 60—fair agreement, considering that the intensity comparison was between different runs, so that the amount of carbon had probably changed. There may be some contribution to this peak from bremsstrahlung losses and wall effects of the 6.52 Mev. gamma ray, as discussed above in connection with the 8.27 Mev. peak.

The relative yields of the 6.12, 6.52, 6.78, and 7.29 Mev. gamma rays were determined at four bombarding energies between 0.8 and 2.2 Mev. The excitation curves, shown in Fig. 9, within the rather poor accuracy of the intensity determinations, rise smoothly throughout this energy range, indicating that the reactions are of a non-resonant type.

No evidence was found, either during the initial single-crystal survey, or in the later measurements with the three-crystal spectrometer, of high energy gamma rays from deuteron capture by B^{10}, leading to excited states of C^{12}. The excitation energy at a deuteron energy of 0.95 Mev. is 26.1 Mev., well above all single-crystal background except cosmic rays. Assuming that a total count three times background corresponds to the smallest detectable gamma-ray intensity, and assuming an efficiency of 20% in order to allow for the severe bremsstrahlung losses and wall effects, this indicates that the cross-section of the $B^{10}(d, \gamma)C^{12}$ reaction is less than 10^{-31} cm.^{2} at 0.95 Mev. bombarding energy.

These results provide additional data on the B^{11} and C^{11} nuclei, and in general confirm the mirror character, although, in addition to those discussed above, there are several conflicting details in the data. The 4.23 Mev. ground

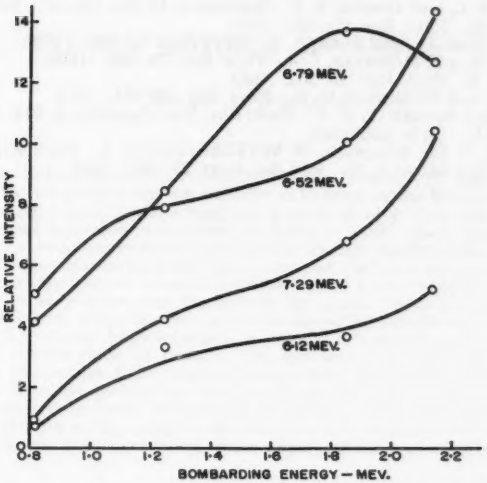

FIG. 9. Yield curves of the 6.12, 6.52, 6.78, and 7.29 Mev. gamma rays.

state transition in C^{11} should have been detectable, since the intensity should have been comparable to that of the 4.46 Mev. transition in B^{11}. The fact that gamma rays at 5.87 and 7.01 Mev. reported by Bent *et al.* (4) were not detected in the present work may be explained by the differences in target thickness and bombarding energy, but this does not explain why they did not detect the 5.35 Mev. gamma ray which was quite evident in the present work. Measurements of the angular distributions of some of the gamma rays, for example those of 6.52 and 6.76 Mev., could aid in comparing the mirror levels. Since it has been found (13) that the neutron groups are strongly peaked forward even at deuteron energies of 1.5 Mev., it is preferable to measure the gamma-ray energies at 90° rather than at 0°, to reduce neutron background. The experiment reported here has demonstrated the usefulness of a three-crystal spectrometer in accurate measurements of gamma-ray energies in an intense neutron flux.

ACKNOWLEDGMENTS

The authors are indebted to Dr. K. L. Erdman and Dr. D. B. James for helpful suggestions during construction of the apparatus. They also wish to thank Mr. J. B. Elliott for aid in constructing the apparatus and operating the Van de Graaff generator. We are grateful to Atomic Energy of Canada Ltd. for financial support during the course of this work.

REFERENCES

1. AJZENBERG, F. and LAURITSEN, T. Revs. Mod. Phys. 24: 321. 1952.
2. AJZENBERG, F. and LAURITSEN, T. Revs. Mod. Phys. 27: 77. 1955.
3. BAIR, J. and MAIENSCHEIN, F. Rev. Sci. Instr. 22: 343. 1951.
4. BENT, R. D., SIPPEL, R. F., and BONNER, R. W. Reported in Ref. (2).
5. BURKE, W. H., RISSER, J. R., and PHILLIPS, G. C. Phys. Rev. 93: 188. 1954.

6. CALDWELL, R. L. and TURNER, S. E. Nucleonics, 12 (No. 12): 47. 1954.
7. ELKIND, M. M. Phys. Rev. 92: 127. 1953.
8. GORDY, W., RING, H., and BURG, A. B. Phys. Rev. 74: 1191. 1948.
9. HOFSTADER, R. and MCINTYRE, J. A. Phys. Rev. 79: 389. 1950.
10. JOHNSON, V. R. Phys. Rev. 86: 302. 1952.
11. JONES, G. A. and WILKINSON, D. H. Phys. Rev. 88: 423. 1952.
12. MANDL, F. and SKYRME, T. H. R. Proc. Roy. Soc. (London), A, 215: 497. 1952.
13. NEILSON, G. C. To be published.
14. VAN PATTER, D. M., BUECHNER, W. W., and SPERDUTO, A. Phys. Rev. 82: 248. 1951.
15. WEST, H. I. and MANN, L. G. Rev. Sci. Instr. 25: 129. 1954.

THE NEW ISOTOPES Cd^{104} AND Ag^{104} [1]

By F. A. Johnson[2]

ABSTRACT

Two new neutron deficient isotopes Cd^{104} (59 min.) and Ag^{104} (27 min.) have been produced by the reaction $Ag^{107}(p, 4n)Cd^{104}$ at 50 Mev. in the McGill University synchrocyclotron and by the subsequent growth of silver from the cadmium. These isotopes have been investigated by means of a 180° spectrograph of high resolution, a lens spectrometer, and a scintillation spectrometer. Chemical methods of identification have also been employed. Ag^{104} has been found to emit a positron spectrum of end point 2.70±.01 Mev. and a γ-ray of 556.2 kev. which is thought to be in series with the positron spectrum. The origin of a γ-ray of energy 118.4 kev. which appears to be converted in palladium is at present unknown. A tentative decay scheme is proposed. Cd^{104} appears to decay primarily by K-capture since no positron spectrum was observed which could be assigned to this isotope. Four γ-rays, of energies 66.7, 83.6, 123.6, and 134.2 kev., have been definitely assigned to this isotope on the basis of K–L differences shown by conversion lines; on the basis of relative L line intensities and K/L ratios the two low energy γ-rays have been shown to represent $M1$ transitions. Other conversion lines were found whose origin and element of conversion are unknown.

1. INTRODUCTION

Various neutron deficient isotopes of cadmium may be produced by proton bombardment of silver. The lowest mass cadmium isotope which is formed depends on the energy of the bombarding protons. Thus when silver (Ag^{107}) is bombarded with protons of energy less than about 20 Mev. the main reaction is $Ag^{107}(p, n)Cd^{107}$, while above 20 Mev. the reaction $Ag^{107}(p, 3n)Cd^{105}$ is initiated; the nucleus Cd^{106} is stable, and the excited product of the $Ag^{107}(p, 2n)Cd^{106}$ reaction is probably too short lived to be observed by the techniques here employed. The product of the $(p, 3n)$ reaction has been discussed in a previous paper (11). As the bombardment energy is further increased to above 30 Mev. the reaction $Ag^{107}(p, 4n)Cd^{104}$ begins to take place, and this paper is concerned with an investigation of the radiations emitted by the isotope Cd^{104} and by its daughter product Ag^{104}.

The Cd^{104} was produced by proton bombardment of metallic silver in McGill University's 100 Mev. synchrocyclotron. All bombardments were carried out at a nominal proton energy of 50 Mev. where the Cd^{104} activity was produced in high yield. The two isotopes Cd^{104} and Ag^{104} were investigated by means of a 180° permanent magnet spectrograph, a lens spectrometer, and a scintillation spectrometer in a manner similar to that used for the investigation of Cd^{105} (11). As in the previous investigation all sources were prepared by evaporation of the active cadmium from the irradiated silver target. Consequently the radiations consisted of a mixture of those emitted by Cd^{104} and by its daughter Ag^{104}, as well as of those emitted by Cd^{105} and Cd^{107} (and by its daughter Ag^{107m}). The previous investigation, however, had served to identify the con-

[1]*Manuscript received August 4, 1955.*
Contribution from the Radiation Laboratory, McGill University, Montreal, Quebec.
Preliminary results have been reported in Paper No. 76, Royal Society of Canada, June Meeting, Quebec, 1952.
[2]*Present address: Defence Research Board, Suffield Experimental Station, Ralston, Alberta.*

version lines, positron spectra, and γ-radiations from Cd^{105}, Cd^{107}, and Ag^{107m}, and thus it was hoped that any new observations could be assigned to the decay chain Cd^{104}–Ag^{104}–Pd^{104}. Analysis of some of the data, however, indicated that the isotope Ag^{103} might also have been present to some extent. The fact that the two cadmium isotopes, Cd^{105} (55 min.) and Cd^{104} (59 min.), had similar half-lives did not complicate the investigation greatly. Assignment of γ-radiations and positron spectra to a particular mass 104 isotope was made where possible on the basis of K–L differences shown by conversion lines, half-life considerations, and chemical methods.

2. PREVIOUS WORK

Cd^{104} has not been reported previously.

The only references to Ag^{104} are very brief and non-specific. Enns (3) found two activities of half-lives 73 and 16 min. after proton bombardment of palladium. These he assigned to Ag^{104} and Ag^{102} respectively. Lindner and Perlman (14) reported a 70 min. activity obtained amongst the spallation products of antimony and concluded that there was "considerable orbital electron capture branching in the decay of this isotope" (assumed to be Ag^{104} or Ag^{102}). Bendel, Shore, Brown, and Becker (1) extracted a 66 min. silver activity from palladium which had been bombarded by 12 Mev. deuterons and found internal conversion lines of energies 530, 550, and 740 kev. They assigned these lines as the K and L lines of a 554 ± 4 kev. γ-ray ($K/(L+M)$ 4 to 7) and the K line of a 764 ± 6 kev. γ-ray respectively, both converted in palladium. No definite assignment was made as to the mass number of the silver isotope involved, but masses 104 and 102 were cited as possibilities. Recently this activity has been assigned to Ag^{103} by Haldar and Wiig (7) who prepared an activity of identical half-life by bombardment of silver with high energy protons. These authors also showed that this isotope decayed by emission of positrons of 1.3 Mev. end point.

3. MEASUREMENTS WITH THE 180° SPECTROGRAPH

The $H\rho$ values and energies of the conversion lines detected in the 180° spectrograph are listed in Table I together with their most probable assignments. Approximate relative intensities of the most prominent lines are also included, these being derived from K/L ratios measured in the lens spectrometer and from visual estimates of the intensities of weak lines observed on the photographic plates. The added binding energies were obtained from the most recent values of X-ray level energies (9). As was pointed out above, the radiations of the higher mass cadmium and silver isotopes were also present in sources prepared at 50 Mev. bombardment energy; only the lines which were found after bombardment of the target at 50 Mev. and which were not found at 30 Mev., see Reference (11), are listed in Table I. Thus the table should contain only those lines emitted in the decay Cd^{104}–Ag^{104}–Pd^{104} (a number of the unassigned weak lines might be due to Ag^{103}). It will be noted that a number of the lines are assigned as being converted in a definite element (as Ag or Pd); this has been done only where both K and L conversion lines were observed. Two doubtful lines are indicated as such.

TABLE I

INTERNAL CONVERSION LINES OF Cd^{104} AND Ag^{104} DETECTED IN 180° SPECTROGRAPH

$H\rho$, gauss-cm.	E, kev.	Assignment		Approximate relative intensity	γ-Energy, kev.
697.3	41.11±0.06	K	Ag	40	66.65
834.9	58.01	K	Ag	500	83.55
854.7	60.65				
870.8	62.83	L_I	Ag	4	66.66
988.7	79.75	L_I	Ag	60	83.58
990.5	80.02	L_{II}	Ag	2	83.57
991.9	80.23	L_{III}	Ag	1	83.61
1009.2	82.85	M_I	Ag	8	83.59
1013.2	83.86	N_I	Ag	2	83.58
1080.5	94.02±0.15	K	Pd	2	118.38
1105.6	98.09	K	Ag	2	123.63
1169.4	108.70	K	Ag	2	134.24
1204.8	114.77	L_I	Pd		118.38
1234.6	119.97	L_{II}	Ag		123.52
1254.3	123.45				
1260.8	124.61				
1294.3	130.63	L_{II}	Ag		134.18
1421.4	154.37				
1441.9	158.32				
1783.0	228.5±0.3				
3032.2	531.8±0.4	K	Pd	7	556.2
3039.6	533.8				
3111.1	552.5	L_I	Pd	1	556.1
3120.7	555.0±0.5				
3138.6	559.7				
3271.6	594.9±0.6				
3292.3	600.5				
3294.1 (?)	600.9				
3308.8	604.8±0.7				
3390.5	626.7				
3399.5	629.1				
3407.4	631.2				
3514.2	659.9				
3532.1 (?)	664.5				
3548.3	669.1±0.8				
3605.6	684.6				
3785.9	733.7				
3821.9	743.6				

Figure 1 is a reproduction of a spectrograph plate taken of the region below $H\rho$ 1100, and shows the most prominent conversion lines which were observed, those due to the γ-rays of energies 66.7 and 83.6 kev. emitted by Cd^{104} (converted in silver). For the 66.7 kev. γ-ray the only L line which was observed was L_I. In the case of the 83.6 kev. γ-ray all three L lines were visible on the original plate, with L_I being very much the strongest; a visual estimate of the relative intensities indicated $L_I:L_{II}:L_{III} = \sim 60:\sim 2:\sim 1$.

Of the lines above $H\rho$ 1100 the most prominent were those of the 556.2 kev. γ-ray emitted in the decay of Ag^{104}. For this γ-ray the K/L_I ratio was visually estimated as 7±3. The energy value obtained for this γ-ray is in accord with values of 550±10 (12) and 560±10 (15) found for a γ-ray in investigations of the decay of Rh^{104}; these latter investigations also serve to confirm the present assignment to mass 104.

Of the weak lines the ones most readily observed were those of energies 94.02

and 98.09 kev., followed by those of energies 108.70 and 123.45 kev. The first three of these were assigned as K lines, and the assumed L lines related to them were so weak that a reliable visual estimate of the K/L ratio could not be made. It would appear that in these cases $K/L > 3$. All other lines were very weak and many could be observed only after repeated exposures of many sources on the same plate.

4. MEASUREMENTS WITH THE LENS SPECTROMETER

4.1 Conversion Lines

The decay of the K conversion lines of the 66.7 and 83.6 kev. γ-rays was measured in the lens spectrometer and values of 62 ± 4 and 58 ± 2 min. respectively were obtained for the half-lives. The decay rate of the K line of the 66.7 kev. γ-ray was subject to a greater uncertainty than that of the K line of the 83.6 kev. γ-ray since the counting rate on the peak was just over twice the rather high background (positron) count in this region. In both cases the L and M conversion lines were so weak that a reliable decay rate determination over a sufficiently long period of time could not be made.

The K/L ratios for these two γ-rays were obtained by planimetric measurement of the areas under the lines; in the case of the L line of the 83.6 kev. γ-ray it was necessary to subtract the small contribution due to the partially resolved M and N lines. For the 66.7 kev. γ-ray this ratio was 10 ± 3, and for the 83.6 kev. γ-ray it was 7.5 ± 1.5. The ratio K_{84}/K_{67} was ~13. These ratios will be referred to later to aid in the assignment of the multiple orders of the γ-rays.

Of the other conversion lines found by means of the 180° spectrograph the only one which could be detected above the intense positron continuum in the lens spectrometer was the K conversion line of the 556.2 kev. γ-ray. Since previous measurements in the 180° spectrograph had indicated that this γ-ray was converted in palladium, a determination of its decay characteristics could give valuable information which would aid in the assignment of half-lives and positron spectra. After subtraction of the positron background under the conversion line the data were sufficient to indicate a 27 ± 4 min. growth and then a 59 ± 4 min. decay. This evidence must be considered along with that provided by the positron spectrum (see below).

4.2 Positron Spectrum

The positron continuum was investigated and found to be complex. This was to be expected owing to the presence of Cd^{105} as well as of the mass 104 isotopes. The first run in the spectrometer showed the already known 1.69 Mev. spectrum of Cd^{105}, and also a new spectrum extending up to 2.7 Mev. This latter spectrum showed growth and in another run a number of points on this continuum were followed for eight hours to establish the decay characteristics. Analysis showed that this spectrum eventually went into a simple 59 ± 2 min. period, and subtraction of the actual counting rate from the extrapolated portion of the final decay curve led to a value of 27 ± 1 min. for the rate of growth. Such a growth and decay curve is shown in Fig. 2. It will be seen that the two straight lines, extrapolated backwards, meet at a point within ±1 min. of the time at which the cadmium was evaporated (chosen as zero time),

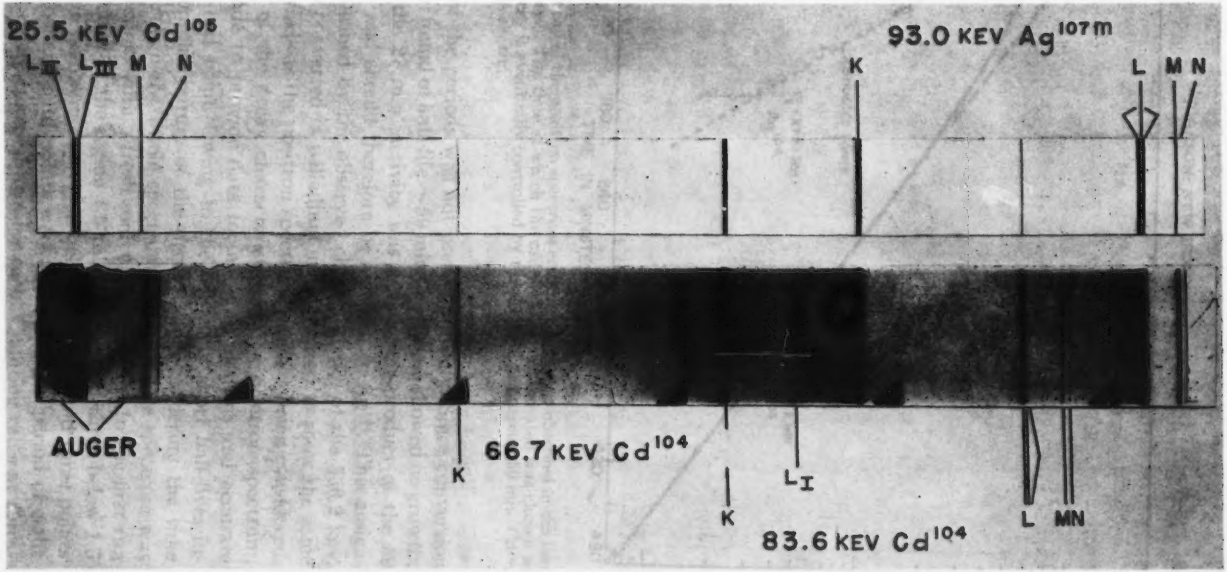

FIG. 1. Spectrograph plates of the region below $H\rho$ 1100 showing the most intense internal conversion lines which were observed. Lower plate overexposed to bring up weak lines.

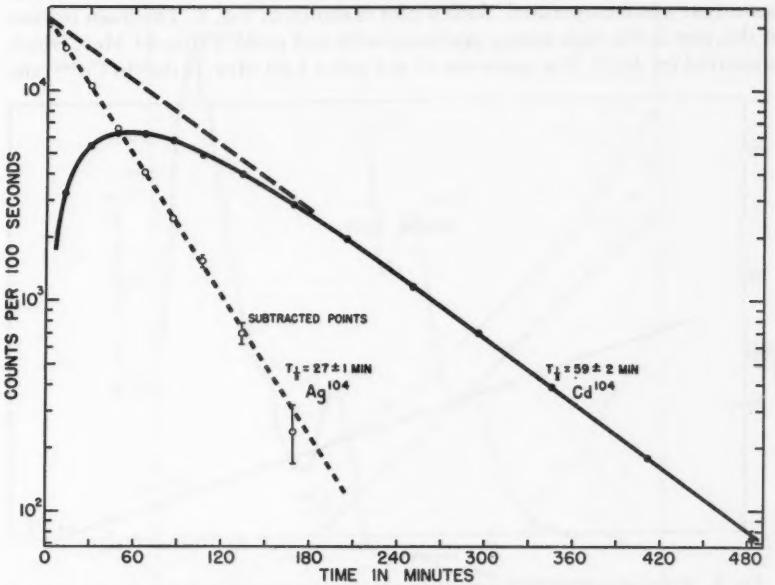

FIG. 2. Growth and decay of the positron spectrum emitted by Ag^{104} as observed in the lens spectrometer (at 1.78 Mev.). The time at which the cadmium was evaporated was chosen as zero time. The rate of decay is eventually controlled by the decay of the parent, 59 min. Cd^{104}. The standard deviation is shown.

indicating that one of the periods was not present initially. Since conversion lines had already been found of half-life ~59 min., and these showed no growth, it was evident that the 27 min. activity was a daughter product of the 59 min. activity (Cd^{104}) and should therefore be assigned to Ag^{104}. This assignment is partially confirmed by the observed characteristics of the 556.2 kev. γ-ray; this γ-ray was converted in palladium and appeared to show the same growth and decay periods as the positron spectrum which is being considered.

With a knowledge of the decay characteristics of the positron spectrum, further runs were made to provide data for a Fermi analysis and accurate determination of the end point. Owing to the relatively short half-lives involved and to the complex nature of the decay, and considering the time necessary to sweep through the whole spectrum, the complete spectrum was investigated in two sections with a fresh source for each run. In the first run many points were counted in the region 1.5 to 3.0 Mev. and three below 1.5 Mev. In the second run points in the region below 1.8 Mev. and three points above 1.8 Mev. were counted. All points were followed for a period of eight hours and growth and decay curves drawn for each. Counting rates at corresponding times were read from these curves in the usual manner. A complete Fermi plot of the whole spectrum was made by combining the two sections and normalizing at the common points. Values of the Fermi function were taken

from the National Bureau of Standards publication AMS 13, and the screening correction was incorporated. Such a plot is shown in Fig. 3. The main feature of this plot is the high energy spectrum with end point 2.70±.01 Mev. which is emitted by Ag^{104}. The spectrum of end point 1.69 Mev. is due to Cd^{105}; the

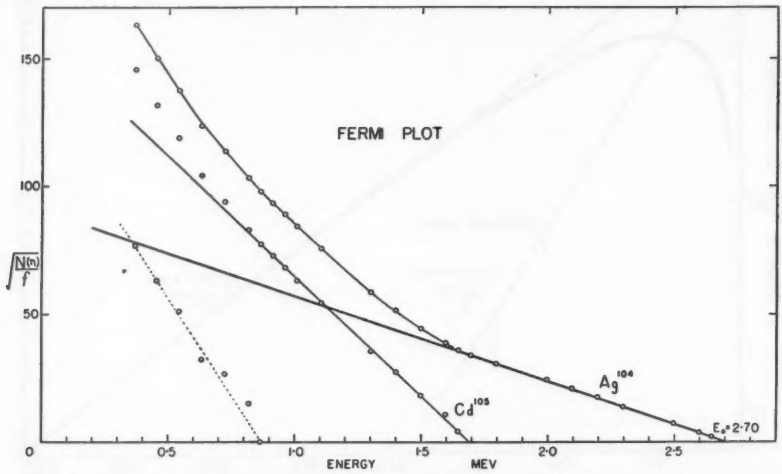

FIG. 3. Fermi plot of positron spectrum emitted by evaporated cadmium source prepared at 50 Mev. The standard deviation for the high energy spectrum is no larger than the plotted points.

upward curvature beginning at about 0.8 Mev. is similar to that found in the investigation of Cd^{105} and cannot be considered to be a new spectrum. This upward curvature was originally (10) interpreted as a positron spectrum of 0.93 Mev. end point and was assigned to Cd^{104} because it did not show the growth and decay characteristics of the Ag^{104} spectrum. Further work, however, established that the general form of the curvature was similar to that found in the spectrum of Cd^{105} (11), and indicated that this spectrum of low energy positrons ought not to be assigned to Cd^{104} or to Ag^{104}. It will be noted that there is no evidence for a spectrum of end point 1.3 Mev. Thus in the decay chain Cd^{104}–Ag^{104}–Pd^{104} only one positron spectrum is evident, that of Ag^{104}.

5. MEASUREMENTS WITH THE SCINTILLATION SPECTROMETER

Further investigation of the gamma radiations was carried out by means of a NaI(Tl) scintillation spectrometer which had been built up by Martin and Breckon (16) and Henrikson (8). A single channel analyzer was used to obtain a pulse height distribution, the source being covered with a 3 Mev. aluminum absorber to absorb all positrons.

In the high energy region no new peaks were found which had not already been established to belong to Cd^{105}. The region below 1.4 Mev. is shown in Fig. 4. The most prominent peaks are those of 1.30 Mev., 930 kev., and 270 kev. already assigned to Cd^{105}; that of 740 kev. which is probably due to a

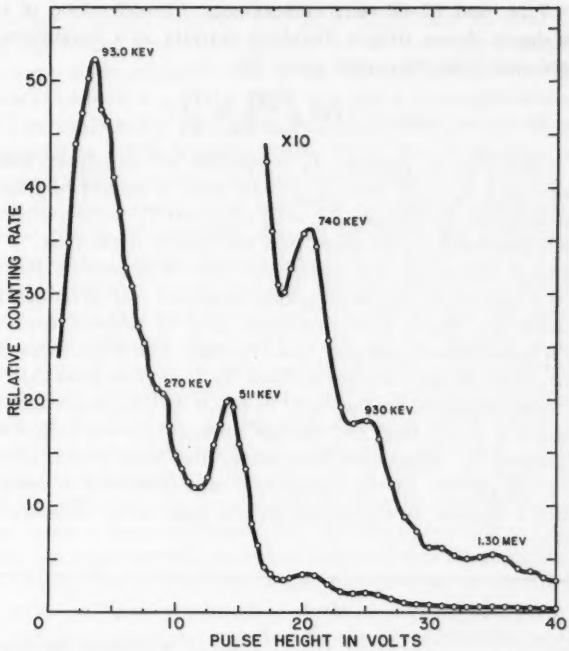

FIG. 4. Scintillation spectrometer pulse height distribution of the γ-rays from Cd^{104}, Ag^{104}, and Cd^{105} (source produced at 50 Mev.). Successive points have not been corrected for half-life.

mixture of the γ-rays associated with the internal conversion lines of energies 684.6, 733.7, and 743.6 kev. listed in Table I; the annihilation radiation at 511 kev.; and the large peak due to the 93.0 kev. γ-ray of Ag^{107m}. In addition the effect of the 556.2 kev. γ-ray of Ag^{104} and possibly of the γ-ray (about 559 kev.) associated with the internal conversion line of 533.8 kev. may be seen as a hump on the high energy side of the annihilation radiation peak. Other slight humps on the curve indicate the presence of other γ-rays, but with the profusion of γ-rays in this region a further analysis was not warranted. The peak assigned to the 93.0 kev. γ-ray appears to show structure, but with the poor resolution in this region nothing definite can be said about the presence of a peak due to the 66.7 or 83.6 kev. γ-rays. The hump on the high energy side of this peak is unexplained but it was also found in a later run after a bombardment at 30 Mev. and so might belong to Cd^{105}, or it might be a scattering effect.

6. CHEMICAL INVESTIGATIONS

In order to verify that the 27 min. activity assigned to Ag^{104} did in fact belong to silver, an attempt was made to isolate it chemically. This was rather important since the gross decay of an evaporated cadmium sample, produced at 50 Mev., showed no signs of such an activity, the decay curve being resolvable

only into 6.7 hr. and 57–60 min. components. Consideration of the laws of radioactive decay shows that a daughter activity is a maximum at a time t_{max} after isolation from its parent given by

$$t_{max} = 1.443 \frac{T_d T_p}{T_p - T_d} \ln \frac{T_p}{T_d},$$

where T_p = half-life of parent, T_d = half-life of daughter. For the case $T_p = 59$ min. and $T_d = 27$ min., $t_{max} = 56$ min. It should be noted that the same t_{max} is obtained for the case $T_p = 27$ min. and $T_d = 59$ min. Evidence has already been presented to the effect that the former is the case.

The chemical procedure was essentially that of dissolving the evaporated cadmium in dilute nitric acid with added cadmium and silver carrier, precipitation of silver by means of hydrochloric acid to remove any active silver which might have been evaporated, and filtration. The filtrate was then allowed to stand for about 55 min. in order to allow Ag^{104} to grow from Cd^{104}, this being about the time necessary for the Ag^{104} to reach its maximum activity. A little silver nitrate was then added and the AgCl precipitate was collected on a filter stick, redissolved in ammonium hydroxide, and then precipitated again by acidification. A portion of the precipitate was dissolved in ammonium hydroxide, and a drop or two pipetted onto a glass slide. This was then dried and counted.

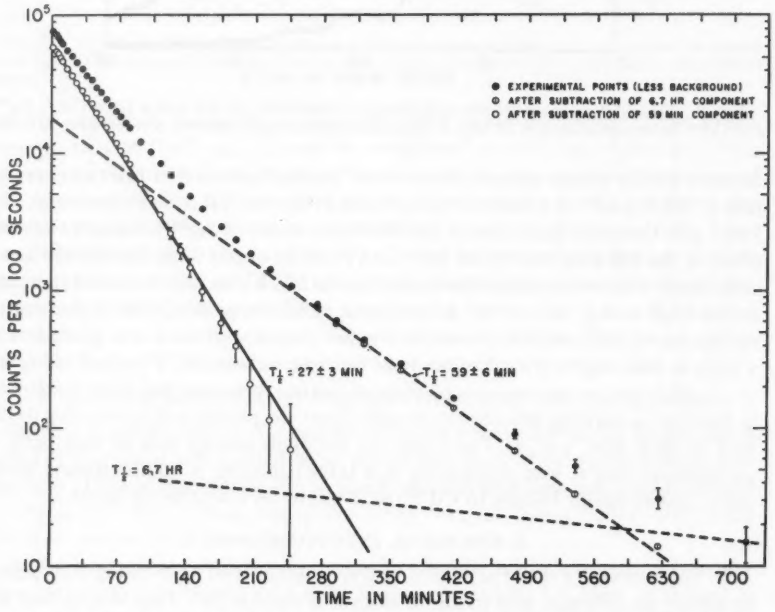

FIG. 5. Gross decay of chemically separated $Ag^{104}Cl$ as measured with an end-window Geiger Counter. The standard deviations are shown for the original points and for the 27 min. component (Ag^{104}).

The gross decay of the silver chloride precipitate, as measured with an end-window Geiger counter, is shown in Fig. 5. The initial 27 min. half-life is in very good agreement with that obtained in the lens spectrometer. Although attempts were made to purify the silver chloride precipitate from the very large excess of cadmium activity, there was still a noticeable amount (usually about 20% as computed at the time of final separation) of a 55–65 min. activity present, as well as a still longer activity. Since this 55–65 min. activity was present in such a large amount, it must be assumed that it was due mainly to a silver isotope (which must grow from the evaporated cadmium). On yield arguments it might be expected that at 50 Mev. the production of Cd^{103} will be appreciable, perhaps greater than that of Cd^{104}, and it is possible that this 55–65 min. activity is due to Ag^{103}. On the assumption that the primary yield of Cd^{103} could be twice that of Cd^{104} at this energy, the presence of this amount of Ag^{103} indicates that Cd^{103} might have a lifetime of the order of 5 to 15 min. Part of this 55–65 min. activity may also be accounted for by the known adsorption property of a silver chloride precipitate for metal ions, as pointed out by Bradt *et al.* (2), but this will be a minor effect. The longest period, as will be seen from the graph, appears to approach a half-life of the order of 6–8 hr. (suggestive of the presence of Cd^{107}). Accordingly, a line of 6.7 hr. half-life was drawn on the assumption that the experimental decay curve approached such a line asymptotically (the fact that the 6.7 hr. line goes through the last experimental point is accidental, this point appears to be low compared to previous points). While the contribution of the 6.7 hr. activity (assumed to be Cd^{107}) is very small, it serves to indicate that some of the cadmium activity may have been adsorbed by the silver chloride, or else that the separation was not complete. Subtraction of this 6.7 hr. component from the experimental points yielded a line of half-life 59 ± 6 min. for the second component of the decay. On the basis of half-life this component could be due to Ag^{103}, as pointed out above, with a small admixture of adsorbed Cd^{105} (55 min.) and Cd^{104} (59 min.).

In connection with the suspected presence of Ag^{103}, it should be pointed out that Ag^{103}, if present, would not affect the determination of the end-point of the Ag^{104} positron spectrum, nor of the half-life of Ag^{104} as measured in the lens spectrometer, since both these determinations depend on data taken beyond the end point of the Ag^{103} positron spectrum at 1.3 Mev. (7). The absence of evidence for the positron continuum of Ag^{103} in the Fermi plot of Fig. 3 does not give conclusive proof that this isotope was not present, since it is expected from K/β^+ ratio considerations that the number of Ag^{103} positrons will be small compared to those of the other isotopes present.

Since Ag^{107} and Ag^{109} both have isomeric states with half-lives of the order of 40 sec. and emit γ-rays of 93.0 and 87.9 kev. respectively, the discovery of a γ-ray of comparable energy, 83.6 kev. (and also converted in silver), raised the question of whether there might be a similar short-lived state of measurable period here also. The fact that Ag^{104} was of even mass made this hypothesis unlikely. Nevertheless, a search was made using a scintillation spectrometer and one channel of a fast counting apparatus (16) available in the laboratory.

The procedure followed was to precipitate out all the silver from a nitric acid solution of the evaporated cadmium in a manner similar to that described previously, and then to do a quick chemical separation of the $Ag^{104}Cl$ precipitate after Ag^{104} had been allowed to grow for varying lengths of time (of the order of a minute). The elapsed time from the separation of the $Ag^{104}Cl$ until counting was started was less than a minute.

Since the γ-ray had an energy of only 83.6 kev. the lower bias level had to be set just above noise level, and it was found that an absorber could not be used over the source. Thus the counting rates obtained were very high in the rather wide channel that was used. The first run gave an initial decay of 21 sec., but subsequent runs gave values ranging from 29 to 42 sec. which seemed to be directly proportional to the time the Ag^{104} was allowed to grow before being precipitated. In all these cases the counting rate decreased by not more than a factor of two in the counting period. Finally, about seven hours after the cyclotron bombardment, when most of the 55 min. Cd^{105} and 59 min. Cd^{104} had died out, the separation procedure was repeated in order to see whether the 44.3 sec. Ag^{107m} could be detected, and consequently if the method was valid. This run was very successful and gave a period of 43 ± 2 sec., with the counting rate decreasing by more than a factor of 10 in the counting period.

These results do not appear to indicate definitely the presence of any activity of half-life 30–60 sec. which could be assigned to a metastable state of Ag^{104}, or in fact of Ag^{105}. It is felt that the periods of 21, 29 sec., etc., which were obtained, could have been due to Ag^{107m} being counted on top of a very high background, the latter causing a pile-up of pulses, or could have been due to deterioration of the photomultiplier dynode voltages caused by the necessarily high counting rates. Also the uncertainty in the measured period might have been caused by a form of temporary fatigue in the photomultiplier itself, such fatigue being known to appear at high counting rates and to disappear again at lower rates. This problem has not been investigated further, but if there is any short-lived activity present, in either Ag^{104} or Ag^{105}, it would appear that it is of a half-life less than 20 or 30 sec.

7. DISCUSSION OF RESULTS

7.1 Mass Assignment

The mass assignment of the 59 min. Cd^{104} rests on considerations of the systematics of nuclei in this region of the periodic table. Cd^{104} is an even–even nucleus only two mass units removed from the stable Cd^{106}. For this reason it is to be expected that this isotope would have a readily measurable period. Cd^{103}, on the other hand, in continuation of the trend Cd^{109} (1.3 yr.), Cd^{107} (6.7 hr.), and Cd^{105} (55 min.), would be expected to have a shorter half-life of the order of 2–20 min. Cd^{102} might be expected to be short-lived.

Rather more substantial arguments may be obtained by consideration of the threshold energies for the $(p, 3n)$, $(p, 4n)$, and $(p, 5n)$ reactions on Ag^{107}. These may be calculated (17) as 22 Mev., 32 Mev., and 43 Mev. respectively. Experimental results indicated that the activity which was assigned to Cd^{104} began to appear at a nominal proton bombardment energy of just above 30 Mev., which would favor an assignment to Cd^{104}.

Since the 27 min. Ag^{104} was observed to grow from Cd^{104}, its mass assignment depends on that of its parent, and very little additional discussion is necessary. One of the isomers of Ag^{106} has a very similar half-life, 24.5 min., but the fact that its positron end point of 2.04 Mev. is very different from the 2.70 Mev. observed for the 27 min. activity assigned to Ag^{104} removes all doubt that the two could have been confused. Also the observed growth, the method of production, and the energetics preclude an assignment to mass 106. The fact that the 556.2 kev. γ-ray assigned to Ag^{104} is probably identical with a γ-ray found in the decay of Rh^{104} (12, 15) also lends support to the proposed mass assignment.

7.2 Multiple Order of γ-Rays

The relative intensities of L_{I}, L_{II}, and L_{III} internal conversion lines, as well as K/L intensity ratios, provide information concerning the multipole order of the γ-ray with which the lines are associated.

To obtain information about the multipole orders of the 66.7 kev. and 83.6 kev. γ-rays use is made of the experimental fact that of the L conversion lines L_{I} was very much the strongest in both cases. Comparison with theoretical L shell ratios (5) indicates that both these transitions are $M1$; this assignment is further confirmed for the 83.6 kev. γ-ray by the fact that the L_{II} line was found to be more intense than the L_{III} line. This assignment is also in accord with graphs presented by Tralli and Lowen (24) concerning the $L_{\mathrm{III}}/L_{\mathrm{I}}$ ratio. Further information is provided by the measured K/L ratios, 10 for the 66.7 kev. γ-ray and 7.5 for the 83.6 kev. γ-ray. Comparison with empirical K/L ratios (6) would appear to confirm that both of the γ-rays represent $M1$ transitions. A detailed examination of theoretical K/L ratios for $M1$ and $E2$ transitions has been made by Swann and Hill (23) who plotted the ratio of Reitz's K conversion coefficients (20) and the total L conversion coefficients of Gellman, Griffith, and Stanley (5). These authors point out that the theoretical K/L ratios show a significant Z dependence, and examination of their plotted curves shows that for the values of Z^2/E (33.2 and 26.5) applicable to the two γ-rays in question a K/L ratio of 7–7.5 might be expected for an $M1$ transition in the region $Z = 49$ (for Ag, $Z = 47$). Such a K/L ratio is within the limits of the experimentally determined ratio for the two γ-rays. Higher multipolarities may be excluded on the basis of both K/L ratio and lifetime.

For the case of the 556.2 kev. γ-ray in Pd^{104} the Z^2/E value is 3.8, and in this range it is difficult to assign the type of transition without ambiguity solely on the basis of the K/L ratio (estimated as $\sim$7). From the curves given by Swann and Hill it will be seen that in the region of small Z^2/E for $Z = 49$ the K/L ratio curves for $M1$ and $E2$ transitions appear to approach each other and to indicate a K/L ratio of $\sim$9. Indeed the observed K/L ratio cannot be used with certainty to eliminate any of the possible multipolarities (6). The fact that of the L conversion lines only L_{I} was observed does not provide a choice between any one of $M1$, $E1$, or $E2$ transitions at this energy (5). Consideration of the observed intensity of the K conversion line of this γ-ray relative to the 2.70 Mev. positron spectrum and of the K conversion coefficient to be expected at this energy (21) indicated that the number of γ-rays amounted to at least 50% (if $E2$) of the number of positrons; hence it is likely that this γ-ray is in

series with the 2.70 Mev. positron spectrum and leads to the ground state of Pd^{104}. Thus in accord with the evidence (6, 22) that the first excited states of even–even nuclei can be expected to have spin 2 and even parity it is reasonable to assign the 556.2 kev. γ-ray as an $E2$ transition. This assignment is also in accord with the observation (18) that, for low Z and high energy, conversion in the L_I shell becomes increasingly important for $E2$ transitions.

For the case of the three remaining γ-rays for which both K and L conversion lines were observed the very low intensity of the conversion lines makes a multipolarity assignment difficult. For the 118.4 kev. γ-ray (converted in palladium) $M1$ or $E1$ assignments are most probable (5). For the 123.6 and 134.2 kev. γ-rays (converted in silver) an $E2$ transition is perhaps likely (5, 18).

7.3 Decay Schemes

Conclusions as to decay schemes may be drawn from considerations of positron spectra, γ-ray intensities, and theoretical predictions. In the decay chain Cd^{104}–Ag^{104}–Pd^{104} it is convenient to start from the stable end product Pd^{104}.

Since Pd^{104} is an even–even nucleus its ground state might be expected to have spin 0 and even parity. The theoretical (4) K-capture to positron ratio for the decay of Ag^{104} is $\sim$0.18, calculated on the basis of the 2.70 Mev. positron spectrum. Thus for Ag^{104} positron emission is the predominant process (except perhaps to very much higher levels) and γ-rays accompanying K-capture to other levels might be expected to be difficult to detect by the techniques employed. As was mentioned above, since the 556.2 kev. γ-ray in the Ag^{104}–Pd^{104} decay is by far the most intense γ-ray which could definitely be assigned as being converted in palladium, it is logical to conclude that it follows positron emission and leads to the ground state of Pd^{104}. The position of the first excited state, 2+, of Pd^{104} at 556.2 kev. compares closely with the corresponding state at 513 kev. in Pd^{106}, and is consistent with the systematics of these states in this region of the periodic table (22). A decay scheme based on these ideas is shown in Fig. 6.

The positron end point of 2.70 Mev. taken in conjunction with the experimentally determined half-life of 27 min. gives a log ft product of 5.4. The f value used here was determined from the graphs given by Feenberg and Trigg (4) and includes the theoretical correction for K-capture. In the absence of further information regarding other modes of decay this figure may be taken as a minimum value for log ft. The apparent absence of other positron spectra or intense γ-rays which could be assigned to this decay would indicate that the log ft value of 5.4 might be expected to be near the correct value. This implies that the transition is allowed; assuming the correctness of the 2+ rule for the first excited states of even–even nuclei, the ground state of the odd–odd nucleus ${}_{47}Ag^{104}_{57}$ may be expected to have spin 1, 2, or 3 and even parity. The absence of any detectable positron emission to the ground state of Pd^{104}, however, indicates that the spin is 2 or 3. On the basis of the shell model of the nucleus (13), the configurations $g_{9/2}$, $p_{1/2}$ or 7/2, and $g_{7/2}$ or $d_{5/2}$ are indicated for the

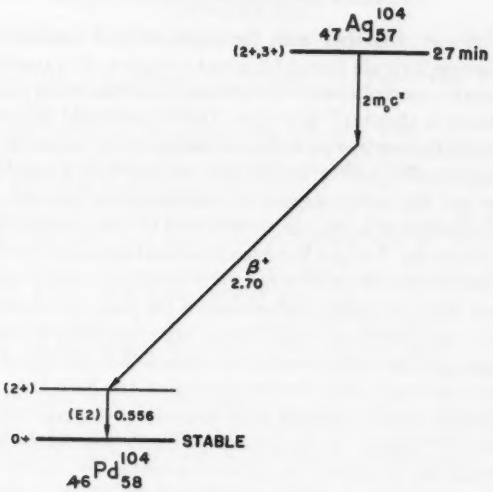

FIG. 6. Proposed decay scheme for Ag^{104}.

odd proton and odd neutron orbitals respectively in $_{47}Ag^{104}_{57}$. The parity assignment of even excludes the $p_{1/2}$ configuration. The remaining configurations can yield spin values of 2 or 3, although a simple application of the empirical rules would favor a spin of 1 $(g_{9/2}-g_{7/2})$ (19).

The decay scheme for Ag^{104}, presented in Fig. 6, is in accord with that proposed for the decay of 44 sec. Rh^{104} (12, 16). The γ-ray of energy 118.4 kev., which was assigned to palladium on the basis of two conversion lines whose separation was equal to the K–L_I separation in palladium, does not fit into the proposed scheme. It may be that this γ-ray represents a transition between two states of higher energy in Pd^{104}, or the K–L_I difference may be fortuitous and the two conversion lines may actually represent K lines of γ-rays converted in silver whose origin and position are at present unknown. The second excited state of Pd^{104} may reasonably be expected to lie at about 1.1–1.2 Mev. (12, 15, 22), and it is possible that one of the high energy conversion lines whose assignment was not obvious might represent a transition from the second to the first excited state in Pd^{104}; a γ-ray which could have represented a transition from this second excited state in Pd^{104} to the ground state was not observed. Since the position of such a second excited state was uncertain it has not been included in the proposed decay scheme.

The apparent absence of a positron transition in the decay of Cd^{104} makes the assignment of spins and parities difficult in any decay scheme which is proposed, and thus provides no corroborating evidence for the 2+ or 3+ state assigned above to the ground state of Ag^{104}. An approximate argument may be used to show that a positron transition in the decay Cd^{104}–Ag^{104} may indeed be expected to be weak and that the γ-rays which were observed probably arise from K-capture. Using the energies of the Rh^{104}–Pd^{104} β^- decay and the

Ag^{104}–Pd^{104} β^+ decay, together with the experimental δ correction term in the semiempirical mass formula found for nearby masses, it is possible to construct approximate mass parabolas and to estimate that the energy available for the Cd^{104}–Ag^{104} decay is about 0.7–0.8 Mev. This value could be in error by almost a factor of two, but nevertheless it shows that positron emission, if not actually forbidden energetically, will be negligible compared to K-capture.

While there are numerous suggested relationships between the energies of the observed conversion lines, the complexity of the γ-ray spectrum and also the possibility that Ag^{103} might have been present to contribute to the observed radiations make it unwise to attempt to construct a decay scheme for Cd^{104}. It will be noted that the energy differences of the pairs of conversion lines 600.5 and 533.8 kev., and 626.7 and 559.7 kev., are very close to the energy of the 66.7 kev. γ-ray, and the differences of the lines 743.6 and 659.9 kev., and 684.6 and 600.5 kev., are very close to the energy of the 83.6 kev. γ-ray. This apparent relationship might indicate that these lines are converted in silver and belong to the Cd^{104} decay. It is also tempting to postulate that the 66.7 and 83.6 kev. γ-rays are in series, as appears possible by virtue of the presence of the weak conversion line of energy 124.61 kev. which, if assumed to be the K line of a γ-ray converted in silver, would give the exact γ-ray energy to be expected for a crossover transition. Many other relationships may be obtained between the observed conversion lines or between γ-ray energies obtained from the conversion lines on the assumption that conversion takes place in silver, but further data will be required to corroborate any decay scheme which might be proposed. As was stated above, some of the conversion lines which were observed might be due to Ag^{103}. There is also the possibility that some of them may represent weak transitions in the decay Cd^{105}–Ag^{105} which were not observed in the previous investigation.

In order to verify and to extend the above decay scheme for Ag^{104} and to obtain more evidence for a scheme for Cd^{104} it would be desirable to perform coincidence experiments, but the very large number of γ-rays in the energy range 500–770 kev. would necessitate the use of rather high resolution. Nevertheless valuable information could be obtained even with moderate resolution, particularly if coincidences were sought between γ-rays and the adequately intense K conversion lines of the 66.7, 83.6, and possibly the 556.2 kev. γ-rays.

ACKNOWLEDGMENTS

The author wishes to thank Dr. J. S. Foster, Director of the Radiation Laboratory, for his interest and encouragement during the course of the investigation, Dr. J. D. Jackson for many helpful discussions, Dr. A. L. Thompson for advice concerning chemical problems, and Drs. W. M. Martin, S. W. Breckon, and A. Henrikson for the use of and advice concerning their scintillation counting apparatus. The facilities and personnel of the Drafting Department of Canadian Aviation Electronics, Ltd., Winnipeg were kindly made available to the author for preparation of the diagrams.

REFERENCES

1. BENDEL, W. L., SHORE, F. J., BROWN, H. N., and BECKER, R. A. Phys. Rev. 90: 888. 1953.
2. BRADT, H., GUGELOT, P. C., HUBER, O., MEDICUS, H., PREISWERK, P., SHERRER, P., and STEFFEN, R. Helv. Phys. Acta, 20: 153. 1947.
3. ENNS, T. Phys. Rev. 56: 872. 1939.
4. FEENBERG, E. and TRIGG, G. Revs. Mod. Phys. 22: 399. 1950.
5. GELLMAN, H., GRIFFITH, B. A., and STANLEY, J. P. Phys. Rev. 85: 944. 1952.
6. GOLDHABER, M. and SUNYAR, A. W. Phys. Rev. 83: 906. 1951.
7. HALDAR, B. C. and WIIG, E. O. Phys. Rev. 94: 1713. 1954.
8. HENRIKSON, A. Thesis, McGill University, Montreal, Que. 1953.
9. HILL, R. D., CHURCH, E. L., and MIHELICH, J. W. Rev. Sci. Instr. 23: 523. 1952.
10. JOHNSON, F. A. Roy. Soc. Can., June Meeting, Quebec, Paper No. 76. 1952.
11. JOHNSON, F. A. Can. J. Phys. 31: 1136. 1953.
12. JORDAN, W. C., CORK, J. M., and BURSON, S. B. Phys. Rev. 90: 862. 1953.
13. KLINKENBERG, P. F. A. Revs. Mod. Phys. 24: 63. 1952.
14. LINDNER, M. and PERLMAN, I. Phys. Rev. 78: 499. 1950.
15. MAEDER, D. and PREISWERK, P. Helv. Phys. Acta, 24: 625. 1951.
16. MARTIN, W. M. and BRECKON, S. W. Can. J. Phys. 30: 643. 1952.
17. METROPOLIS, N. and REITWIESNER, G. Table of Atomic Masses. Argonne Natl. Lab. 1950.
18. MIHELICH, J. W. Phys. Rev. 87: 646. 1952.
19. NORDHEIM, L. W. Revs. Mod. Phys. 23: 322. 1951.
20. REITZ, J. R. Phys. Rev. 77: 10. 1950.
21. ROSE, M. E., GOERTZEL, G. H., SPINRAD, B. E., HARR, J., and STRONG, P. Phys. Rev. 83: 79. 1951.
22. SCHARFF-GOLDHABER, G. Phys. Rev. 90: 587. 1953.
23. SWANN, J. B. and HILL, R. D. Australian J. Phys. 6: 371. 1953.
24. TRALLI, N. and LOWEN, I. S. Phys. Rev. 76: 1541. 1949.

A STANDARD OF MUTUAL INDUCTANCE[1]

By J. T. Henderson and M. Romanowski

ABSTRACT

A primary standard of mutual inductance of the Campbell type has been constructed by the National Research Council to serve as an ultimate standard of reference for electrical quantities in Canada. The electrical value is computed from its measured physical dimensions. A detailed description is warranted in view of its national importance. The value of the standard is $0.010,007,24_8$ henry with an error not larger than 13 p.p.m.

1. DESCRIPTION

Two of the first considerations in making any standard are stability and accuracy. This is particularly true if the objective is to produce a primary standard. Consequently the earlier experience of the National Physical Laboratory and the United States National Bureau of Standards has been followed and both laboratories have been most helpful and co-operative throughout the program. Modifications were made to the original techniques when it seemed probable that the final result would be improved.

The Campbell mutual inductance (3, 4) is represented in Figs. 1 and 2. The primary has two equal single layer coils of 100 turns of bare copper wire wound in a helical groove on a quartz cylinder. The cylinder is roughly 30 cm. diameter, and the windings, having 1 mm. nominal pitch, occupy an axial length of 10 cm. each and are separated by a distance of 20 cm. The secondary has 459 turns of insulated wire wound in a groove in a marble ring the mean diameter of which is approximately 52 cm. The secondary is located midway between the two primary windings and is coaxial with them.

As is well known the main advantage of Campbell's design is that the mean diameter of the secondary coincides with the neutral circle (the circle of zero magnetic field between the primary coils when the latter are excited in series). This means that small errors in physical dimensions of the secondary have relatively small effect on the calculated inductance compared to the effect of similar dimensional errors in the primary.

A marble base, together with marble supports which hold the secondary ring and provide horizontal and vertical adjustment of the latter, completes the instrument. The ends of the electrical leads from the primary coils must be in one straight line within a tolerance of ± 0.1 mm. The inductor is housed in a laboratory having controlled temperature and humidity, and is built without use of magnetic materials and avoiding closed electrical loops or large metallic areas.

Our constructional methods were very similar to those described by the U.S. National Bureau of Standards (6, 7). The primary quartz cylinder, obtained before the war from "Quartz et Silice" (Paris), was lapped to a true cylinder. The thread to hold the primary winding which extends the entire length of the

[1]*Manuscript received August 25, 1955.*
Contribution from the Division of Applied Physics, National Research Council, Ottawa, Canada. Issued as N.R.C. No. 3796.

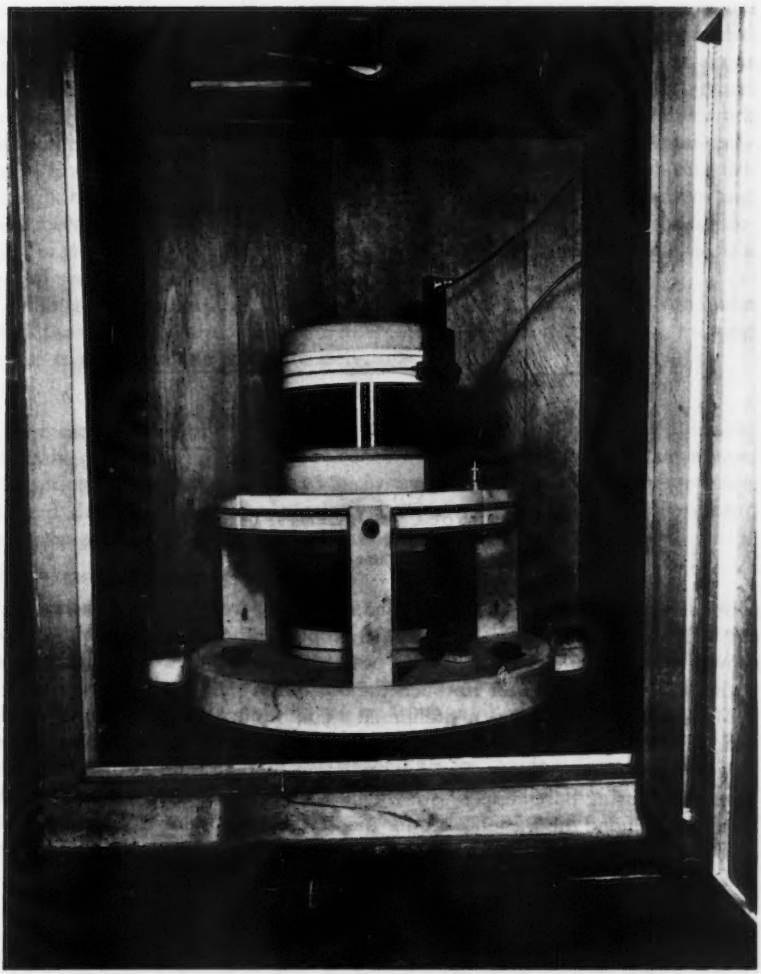

FIG. 1. Primary inductor.

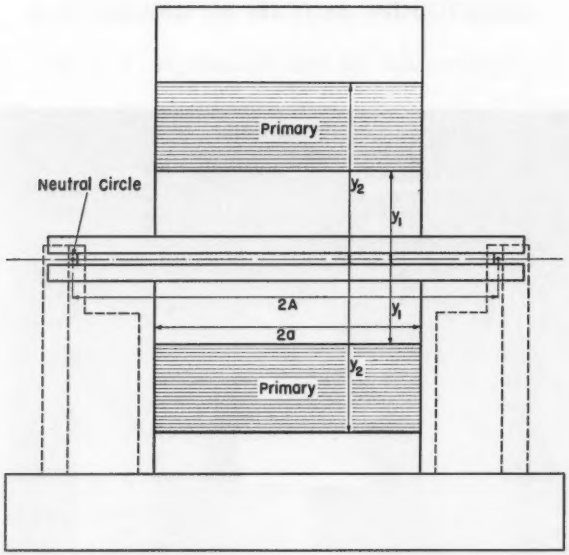

$a = 15{\cdot}098\ 428$ cm. $\quad y_1 = 9{\cdot}996\ 48_5$ cm.

$A = 25{\cdot}760\ 0$ cm. $\quad y_2 = 19{\cdot}993\ 03$ cm.

FIG. 2. Principal dimensions of inductor.

cylinder was also lapped to its final shape starting from an initial helical saw cut 1/100 in. square. The process was stopped when photographic profiles showed that the primary wire would be supported along two generating lines without tendency to roll or to touch the bottom of the groove.

Measurements made on a preliminary coil wound the full length of the cylinder showed there was no optimum position for the final coils, the cylinder being remarkably uniform. The final winding of the two 100-turn coils was then made, using bare copper wire which was drawn through a series of dies. The last diamond die was checked for quality with a Taylor Hobson projector and shown to be circular. Samples of the wire taken from the beginning and end of each primary helix were measured. In addition the relative diameter of the wire was continuously checked during the winding with a Zeiss micrometer. The uniformity of the readings showed there was no significant difference between the diameters of the samples and the helices. (The wire in the helices is carried one half turn beyond the electrical end of the coils to simplify securing the end of the wire.)

The base, the supports for the secondary, and the secondary ring itself were all made in the National Research Council Central Workshops. The measurements on the preliminary coil mentioned above were accurate enough to compute the position of the neutral circle to the precision required to cut the

groove in the secondary ring. The mean diameter of the groove should not differ from that of the neutral circle by more than 0.01 mm., but high grade machine shop practice was quite adequate to achieve this.

We constructed six separate secondary rings to be used with the same primary. Three of these secondaries will yield mutual inductors of 10 mh. nominal value, two of 15.8 mh., and one of 20 mh. All of them can serve as computed standards but at present the best secondary winding giving 10 mh. is taken as the standard. Five secondary forms are constructed of Alabama marble and one form is of Italian marble. The extra secondaries are intended for other work and will not be discussed in detail here. All were wound using the same technique. Each layer of the winding is separated from the next by insulating fish paper 0.005 in. thick and the resulting winding is very uniform, an important point because only the outer wires of each layer can be seen during measurement of the diameter of the coil. Electrically the secondary coils terminate in a coaxial connector.

Although we were using established techniques, the laboratory had to make up all the necessary laps and special micrometers, and to modify many existing gauges to carry out the work precisely.

2. MEASUREMENT

All measurements of the primary coils are required to the highest precision attainable. The limiting factor in the accuracy is probably the fact that we are attempting to define the position of the primary current by measurements made on hard drawn copper wire, a relatively soft material, and any significant improvement can come only from a complete change in approach.

2.1. Diameter of the Primary Coil

A substitution method developed by Moon (12, 13) was adopted. A fixed and a moving anvil of a micrometer are secured diametrically opposite one another on a large invar ring. The moving anvil is motor driven, and is automatically stopped when a predetermined measuring pressure (150 gm.) is reached. A large dial attached to the rotating anvil reads directly in microns and measurements can be repeated with ease and certainty. (See Figs. 3 and 4.)

The reference standard is a quartz end gauge, having optically polished spherical ends, the center of the sphere being the center of the gauge. The gauge is placed in a "Y" shaped support suspended above the primary cylinder. When the invar ring is elevated to pick up the "Y" the quartz end gauge is automatically placed in the same position each time with respect to the micrometer anvils.

The primary quartz cylinder is mounted with its axis nearly vertical immediately below the quartz gauge. The axis is tilted to compensate for the helical angle and this must be allowed for in diameter measurements, but the method has the advantage of keeping the micrometer axis horizontal. Diameters were measured on each wire along four pairs of generating lines at 45° intervals around the cylinder.

The measurements were made in groups of 10 turns each, the time interval being divided into halves, symmetrical with respect to the mid-point. Every

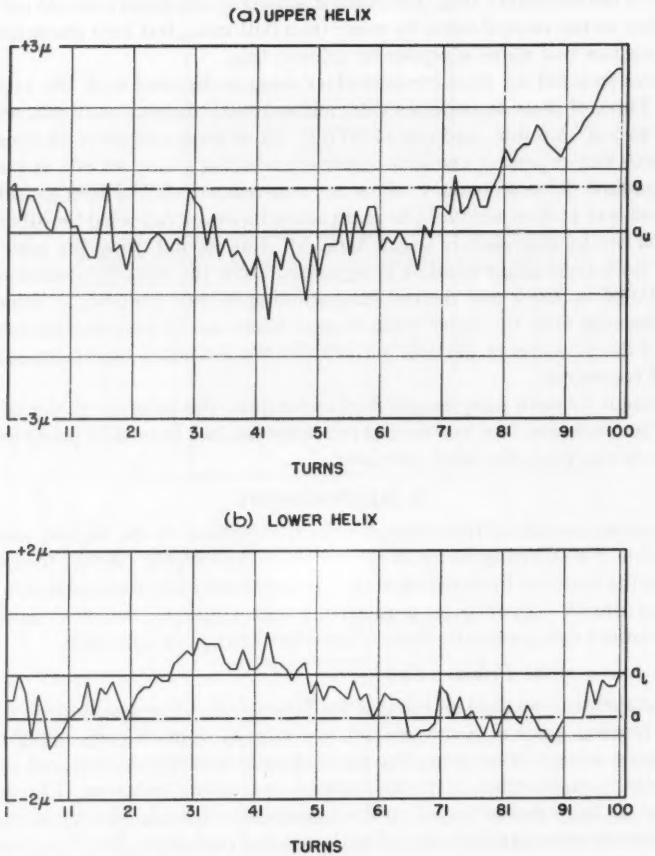

FIG. 3. Radius of individual turns, compared to average radii a_u (upper helix) and a_l (lower helix). "a" the mean of a_u+a_l is that used for inductance computation.

wire was touched three times in the first half and three times in the second half of the group. The cylinder was rotated slightly after each measurement so that the anvils did not touch the wire twice in the same spot. The gauge was measured three times in each half group. The quartz cylinder was turned end for end after the first helix was completed, to facilitate measurement of the other coil.

To minimize thermal effects the whole equipment was enclosed in a box and two thermometers read before and after each set of measurements. Normal agreement between the two was a few tenths of a degree. The change in temperature for a whole day of operation did not exceed one or one and a half degrees. The thermal coefficient of the quartz gauge was found experimentally

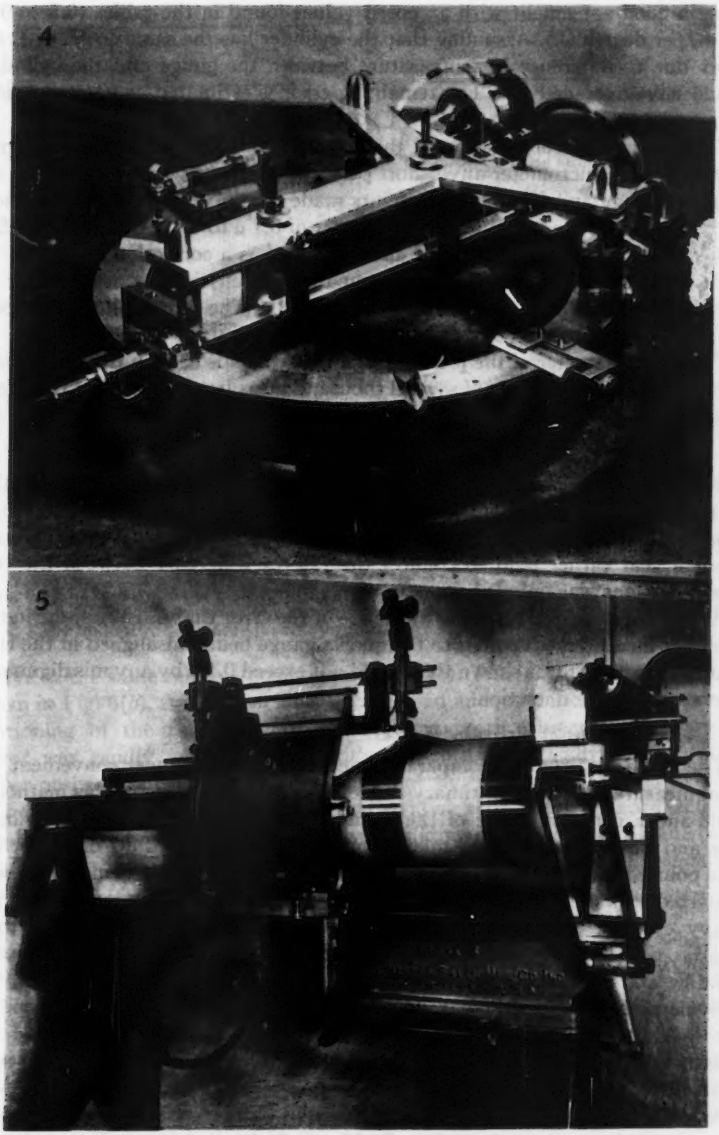

FIG. 4. Ring comparator, showing quartz gauge in its Y-shaped support, which has point line-plane contact with invar ring.

FIG. 5. Longitudinal comparator. The only portion of rider assembly visible is mirror *m* (near right-hand microscope objective).

to be in good agreement with accepted values found in the tables (0.5 to 0.7 p.p.m. per degree C.). Assuming that the cylinder has the same coefficient, all errors due to difference in temperature between the gauge and the cylinder should have averaged out. The remaining error is estimated as not exceeding 0.1 μ to 0.2 μ.

To measure the compression of the copper wire by a pressure of 150 gm. exerted by the micrometer anvil short pieces of the same wire were fixed to an auxiliary gauge and from measurements made by the Interferometry Section the compression was found to be of the order of 0.1 μ to 0.2 μ. The value 0.15 μ was adopted as the most probable and employed as a correction.

The errors arising from the ring comparator itself, insofar as they are of mechanical origin, are of the order of 0.2 μ to 0.3 μ. The sum of all these errors, i.e. all those due to the comparator, amounts to about 0.3 μ to 0.5 μ.

The mean diameter of the primary winding (which is used in the inductance calculations) is the average of several thousand measurements so that the effect of accidental errors on the final result may be considered as very small.

2.2. Length of Quartz Gauge

The length of the quartz gauge used above was measured interferometrically for us by K. M. Baird and given as 0.302,6087 m. The error in the length of the gauge may be estimated as between 0.2 and 0.4 μ. Measurements on this gauge about a year earlier tend to confirm this, as the difference between the two determinations was only 0.1 μ.

At the same time an estimate was made of the error that might appear in the diameter measurement owing to the quartz gauge being misaligned in the ring comparator, but it was shown this would not exceed 0.1 μ by any misalignment that could escape detection.

2.3. Axial Lengths of Primary Helices

The Abbe longitudinal comparator method was found most convenient for axial measurement of the primary helices (Fig. 5). According to this method a scale and a generating line of the cylinder were placed in the same straight line and observed with two microscopes rigidly connected to one another. One pointed the scale while the other pointed the turns of the winding. It was preferred to move the microscopes together in a rigid mounting rather than the heavy cylinder and scale because of obvious difficulty in preserving their relative positions. The distances to be measured were the axial length of each winding and the distance between them.

Some useful preliminary data were obtained by pointing the microscope on the lines of light reflected by the wires from the axial illumination of the microscopes. This method can be relied upon to only a few microns however.

In the precise measurements the definition of the position of the wire was obtained from a mechanical "rider" brought into contact with the copper wire analogous to the system described by C. Volet (11) for similar work on a self-inductance standard. A fine line at K (Fig. 6(a)) defines the center of the wire. CK is of the order 1.5 mm. and the CK should be vertical, so a very sensitive mechanism is necessary to level the rider (or at least ensure that it is

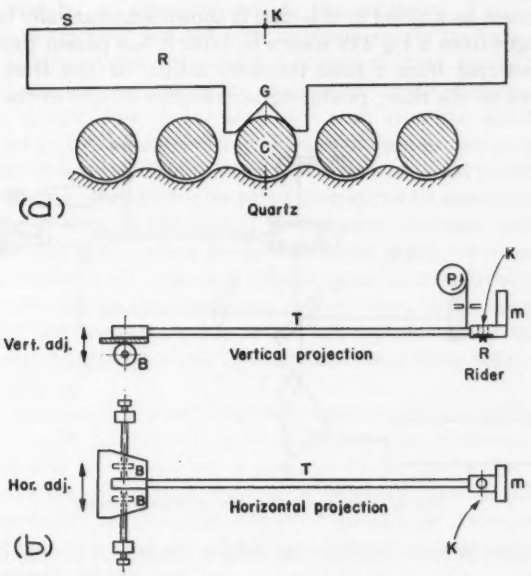

FIG. 6. (*a*) Cross section of rider.
(*b*) Rider adjusting device. A light tube *T* fastened to rider *R* rests on bearings *BB* and *R*. Rider and mirror *m* can be raised by thread over pulley *P*.

always in the same relative position on the wire). The levelling mechanism is shown in Fig. 6(*b*). A sensitive level bubble is an adequate indicator of correct positioning of the rider but for the interferometric observations a small mirror was rigidly fastened to the rider which automatically assumed the proper position when the mirror was set correctly.

The microscopes (Fig. 5) are joined by two invar rods. These rods are secured at one end only to a rigid aluminum casting sliding on the ways of a lathe bed. Checked by autocollimation the ways are straight, horizontally and vertically, to one second of arc.

The distances between turns were determined in terms of the intervals of a 52% Ni length standard, which was calibrated against an invar meter, which is checked periodically against the N.R.C. standard meter, the latter being known directly in terms of the international prototype.

2.4. Interferometric Measurement of Axial Dimensions

A recent improvement by Baird (1) in interferometric technique, materially shortening the observation time required for an optical determination of length, made it practical to apply to these axial measurements. Accordingly a series of measurements of the displacement of the rider were made by K. M. Baird and one of us wherein the displacement was obtained optically. These measurements were simultaneous with those described above. The rider, with its associated errors, is common to both methods.

Baird's system as applied to this case is shown schematically in Fig. 7. The collimated light from a Hg 198 source is, after it has passed through a beam splitter S, reflected from a fixed reference mirror M and from a mirror m rigidly secured to the rider, producing interference fringes in the telescope T.

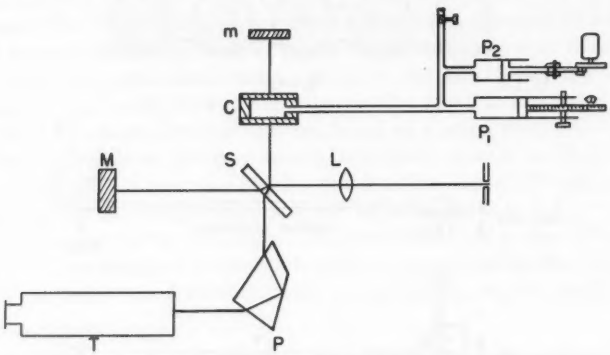

FIG. 7. Schematic diagram of interferometer.

The air pressure in cell C in the path SmS is controlled by the piston P_1. An essential feature of his method is the use of an auxiliary oscillating piston P_2 so that by applying the principle of flicker photometry the optical paths from the two mirrors can be adjusted by P_1 to make the order of interference exactly integral.

The difference in setting of piston P_1 when the mirror m is displaced is an indication of the fraction the displacement exceeds a whole number of half waves. Using three colors (the Hg lines 5461, 5777, 5791) and applying the method of exact fractions (5) the displacement can be accurately and quickly determined. (The required preliminary knowledge of the measured distance to within 2 μ was easily supplied by the comparator measurements.)

In this measurement the beam of light SmS is first made accurately parallel to the direction of travel of the microscopes, then the rider is set on a wire midway between the wires to be measured. The mirror m is set perpendicular to the light beam and then M is adjusted to give sharp fringes of nearly zero order. Now when the rider is moved to the wires whose spacing is required and adjusted so that mirror m produces good fringes, this automatically ensures that the rider is always in the same relative position with respect to the wires and that the engraved line will be in focus in the microscope. Separate settings of M were used to measure the two coils and the spacing between the coils to minimize the broadening of fringes due to long path differences. The greatest path difference in this work was 20 cm.

To ensure stable conditions for the optical measurements the comparator was placed in a separate enclosure inside a temperature-controlled room. An air pump evacuating the hot air produced by the mercury lamp causes a slow exchange of air between the room and the enclosure. The optical measurements

were made first by an observer outside the enclosure. Then, immediately following, the wires were pointed with microscopes. As the later observations lasted only a few minutes the presence of the observer inside the enclosure did not affect the temperature of the comparator or the enclosure. A mercury thermometer placed close to the scale was read after the pointings and all results reduced to 20°C. Temperature changes did not exceed a rate of 0.01°C. in 10 min. and it is reasonable to expect that the reduction to 20°C. gave rise to only very small errors which were partly eliminated by repetition of readings.

The sources of error in the optical measurement include: obliquity of the measured direction with respect to the axis of the helix, tilt of mirror m with respect to the required direction multiplied by the distance to the rider from the center of m, obliquity in the interfering beams from a finite aperture, error in piston setting, and corrections due to the atmosphere. All of these are very small or easily corrected for and it is unlikely that their total contribution exceeds 0.1 or 0.2 μ.

A more serious source of error is due to change of conditions between settings of the rider. It is due both to changes in the dimensions of the comparator and interferometer and to the change in pressure of the gas in the air cell. The latter resulted from differential changes in different parts of the air system caused by insufficient temperature control of the pistons. These effects should produce random errors and the scatter in readings indicates their magnitude. The scatter was of the order of 1 μ.

2.5. Measurement of the Secondary

The diameters of the secondaries were measured in a laboratory comparator against an invar meter bar in a temperature-controlled room. The secondary windings were viewed through radial slots cut at 90° intervals in the marble form. Pointings were made directly on the wire. The radial depth H is deduced directly from pointings made on the inside and outside layer when determining the coil diameter. The axial length (or width) W of the coil was measured with a good hand micrometer. Adequate accuracy for all these dimensions can be obtained in this way.

3. RESULTS

The limit of precision of the Campbell inductor is set by the errors assigned to the measurements of the primary helices, the mean radius a, and the axial distances y_1, y_2.

The mean radius deduced from ring gauge measurements on both helices, corrected for the slight tilt during measurement and for the compression of the wire, is:

$$a = 0.150{,}984{,}28 \text{ m}.$$

When describing the diameter measurement the following errors were included:

Error in comparison of diameter against reference gauge	0.2–0.3 μ
Error due to temperature	0.1–0.2 μ

Error in length of gauge	0.2–0.4 μ
Error in wire diameter	0.1–0.2 μ
Error due to misalignment of gauge	0.0–0.1 μ
Sum of the errors	0.6–1.2 μ

A reasonable conclusion seems to be that even if some small cause of error was overlooked, the upper limit of the total error on the diameter is about a micron and therefore on the radius, half a micron.

The axial measurements, AB (length of lower helix), BC (separation between coils), CD (length of upper helix), are used to determine the distances of beginning and end of the coils from the neutral plane, viz. $y_1 = \frac{1}{2}BC$ and $y_2 = y_1 + \frac{1}{2}(AB+CD)$.

Because of the extra half turn on the wire beyond the electrical end of the winding, these distances could be measured along three lines displaced 90° from one another around the cylinder. The lengths of the two coils agree within 0.6 to 0.7 μ. The individual scale measurements and the interferometric measurements agree to about 0.5 μ. Some of the discrepancy may be due to observational technique and some to slight imperfections in the coil. The systematic part of the error measuring the displacement of the rider is about 0.2 μ and the scatter in individual settings about the same, so one is left with the over-all impression that the rider technique as used here probably defines the position of the wire to about half a micron.

The measurements are:

	Scale	Interferometer	Average
y_1 =	0.1 m.–35.3 μ	0.1 m.–35.0 μ	0.1 m.–35.1$_5$ μ
y_2 =	0.2 m.–70.1 μ	0.2 m.–69.3 μ	0.2 m.–69.7$_0$ μ

so that

$$y_1 = 0.099,964,8_5 \text{ m.},$$
$$y_2 = 0.199,930,3_0 \text{ m.}$$

Considering the maximum deviation of measurement, one arrives at an upper limit for the probable errors of:

$$\text{on } y_1 \text{ about } 0.6\ \mu,$$
$$\text{on } y_2 \text{ about } 1.1\ \mu.$$

The pitch P was taken as uniform. Actually every 10th turn on both helices was measured on one line and no significant departure from the ideal case was observed.

4. CALCULATION OF MUTUAL INDUCTANCE

The value of the inductance is computed from the measured physical dimensions and by assuming a value of permeability *in vacuo*. Jones' formula (10) is used and three corrections were applied to allow for (*a*) the finite cross-section of the secondary, (*b*) the finite diameter of primary wire, and (*c*) the magnetic permeability of the quartz form. Direct measurements by R. Bailey on a small sample taken from the quartz cylinder whose density was 2.1 give a value of $-0.389 \pm 10\%$ for the volume susceptibility.

Jones' formula gives the mutual inductance between a helix and a circle in the plane of the end of the helix, and so must be applied twice for a circle displaced from the end of the helix. Hence

$$M = M_2 - M_1$$

where
$$\underset{i=1,2}{M_i} = 2\pi N_i(A+a)\left[\frac{c}{k_i}(K_i-E_i)+\frac{(A-a)^2}{A+a}\frac{K_i-\Pi_i}{\sqrt{[(A+a)^2+y_i^2]}}\right].$$

Here A = measured diameter of secondary = 0.257,600 m.,
a = measured diameter of primary = 0.150,984,2_8 m.,
y_1, y_2 axial distances from secondary circle to ends of helix = 0.099,964,8_5 m., = 0.199,930,3_0 m.,
pitch = 0.000,999,654_5 m.

K, E, Π are complete elliptic integrals of the first, second, and third kind, to the modulus k and parameter c where k and c are evaluated from the dimensions by:

$$k_i^2 = 4Aa/[(A+a)^2+y_i^2], \qquad c^2 = 4Aa/(A+a)^2, \qquad i = 1, 2,$$
$$N_i = Y_i/P, \qquad (k_i')^2 = 1-k_i^2, \qquad c'^2 = 1-c^2.$$

Bartky (2) gave a method for reducing such integrals to arithmetico-geometrical series (already partly established by L. V. King) and the Bureau of Standards (16) applied the method to the computation of a similar mutual inductance, giving very complete examples.

The computation yields

$$M_2 = 28{,}996.492{,}4 \times 10^{-9} \text{ h.},$$
$$M_1 = 18{,}095.117{,}6 \times 10^{-9} \text{ h.}$$

Hence
$$M = M_2 - M_1 = 10{,}901.374{,}8 \times 10^{-9} \text{ h.}$$

Doubling this because there are two primary coils and multiplying by 460, the original number of turns on the secondary, gives

$$M = 0.010{,}029{,}264{,}8 \text{ h.}$$

One turn less will obviously bring the result closer to 10 mh., but a complete calculation is required for each primary coil to account for the removal of one turn of the secondary because this turn is displaced from the neutral axis and the electrical system is no longer symmetrical. The amount to allow for the removal of the 260th turn is found to be $21{,}801.6 \times 10^{-9}$ h., a value which is smaller by 1.15×10^{-9} h. than simple proportionality would indicate. The true value was checked by means of a second order Taylor expansion with respect to the radius and position of the 260th turn.

Hence our inductance becomes 0.010,007,463,2 h. with the following corrections:

(A) cross-section of secondary $= 155.2 \times 10^{-9}$ h.,
(B) cross-section of primary wire $= 36.3 \times 10^{-9}$ h.,
(C) magnetic susceptibility of quartz $= 23.5 \times 10^{-9}$ h.

The first of these (A) is briefly summarized below, the other two are taken from the accompanying article (15). (B) represents the effect due to non-uni-

form distribution of current in the primary wire; (C) represents the allowance to be made for the difference in magnetic permeability of vacuum and the material in the primary former.

We therefore conclude that the value of the N.R.C. mutual inductor is

$$0.010,007,248_2 \text{ henry.}$$

From the estimates of the errors in a, y_1, y_2 (diameter of primary and axial positions of the coils) we can arrive at an order of magnitude of the resulting error in M by the following simple analogy. Consider two coaxial circles of radius $A = 0.25$ m. and $a = 0.15$ m. located a distance $y = 0.15$ m. from one another. Their mutual inductance μ is 143×10^{-9} h. and

$$\partial\mu/\partial a = +13\times10^{-7} \quad \text{and} \quad \partial\mu/\partial y = -6\times10^{-7}.$$

So that for an error of 0.6×10^{-6} m. on a and 1×10^{-6} m. on y, the relative value

$$\Delta\mu/\mu = 9.7\times10^{-6}.$$

It therefore seems reasonable to believe that the probable error in M is smaller than 10 parts per million from errors in the primary helices.

The radius of the secondary (A) will probably not affect the final result but errors in the dimensions of the cross-section of the secondary coil might produce an error as large as three parts per million.

Summing these linearly we conclude that the error in M is definitely smaller than 13 p.p.m. It is emphasized that in obtaining this number not only is it assumed that circumstances are most unfavorable and all errors act in the same direction but also it is assumed that each individual error has been assigned a relatively large value. Hence 13 p.p.m. is felt to be very definitely an upper limit rather than a probable error.

The effect of temperature on the value of this mutual inductance is very small. Following similar reasoning to that of Dye and Hartshorn (9) the temperature coefficient would be of the order of a few parts in 10^{-7} per degree C. The temperature of the room is now controlled to ±1°C. and a separate enclosure is provided for the inductor so that closer control of its temperature can be arranged.

Direct comparison of this standard with those of other laboratories would be difficult and for the present will depend on the comparison between laboratories of resistances, after the unit of resistance has been determined (14) in terms of the calculated inductance.

5. FINITE CROSS-SECTION OF THE SECONDARY

In Campbell's (4) and Dye's (8) earlier work the effect of a finite cross-section of the secondary was evaluated using a formula due to G. F. C. Searle. Wilmotte (17) further reviewed the problem and obtained an equivalent solution.

Fraser of this laboratory, starting with the assumption that the secondary is composed of a group of concentric circles of different radii and different axial positions and of a number equal to the number of turns in the secondary, arrived at a formula expressed in terms of the number of turns (n_w) in each

layer of the secondary and the number of layers (n_H) in the winding. The total correction for the finite size of the secondary ΔM is given by

$$\Delta M = \frac{1}{24}\frac{\partial^2 M}{\partial A^2}\left[H^2\left(\frac{n_H+1}{n_H-1}\right)-W^2\left(\frac{n_W+1}{n_W-1}\right)\right],$$

a result that is good to the fourth order of small quantities for a symmetrical winding, H and W being the radial depth between centers of the wires, in the inner and outer layers, and the axial width between centers of the exterior wires.

This formula gives equivalent results to those derived from Searle's. Applying Fraser's formula to the present case, where

$$H = 1.09415\times10^{-2}\text{ m.}, \qquad n_H = 20,$$
$$W = 1.04786\times10^{-2}\text{ m.}, \qquad n_W = 23,$$

and $$\partial^2 M/\partial A^2 = -29.675\times10^{-2},$$

we find that

$$\Delta M = -155\times10^{-9}\text{ h.},$$

which represents a relative value of 15.5 p.p.m.

This correction can be in error depending on errors in measurement of the radial (δH) and axial (δW) dimensions of the secondary coil. If these are as large as ±0.05 mm. the resulting error in ΔM can be shown to be as large as 2.7 p.p.m. The dimensions should be somewhat better known than this assumption so that correction to the value of the mutual inductance should be smaller than 3 p.p.m. used above.

ACKNOWLEDGMENTS

The mutual inductance work was started before the war, which greatly delayed it. Work was resumed late in 1949 and completed about a year ago. Many people have had a share in it at one time or another and the product should be considered a co-operative achievement of the laboratory. It is not possible to include here all the names of those who have helped, but we gratefully acknowledge our indebtedness to the late Dr. Charles Moon of the National Bureau of Standards for his most valuable assistance and advice on constructional and measurement methods. Amongst others from N.R.C. we would like to thank Mr. R. Bailey, Dr. K. M. Baird, Mr. J. N. Cairns, Mr. P. Fraser, Miss E. Kennedy, Mr. W. R. Malloch, Mr. B. Rafuse.

We would like to emphasize the contributions of the late Mr. A. J. Grant who was associated with the work for a number of years and we deeply regret that he was unable to see the inductance completed, and that we are deprived of the co-operation of an esteemed colleague.

REFERENCES

1. Baird, K. M. J. Opt. Soc. Amer. 44: 11. 1954.
2. Bartky, W. Revs. Mod. Phys. 10: 264. 1938.
3. Campbell, A. Proc. Roy. Soc. (London), A, 79: 428. 1907.
4. Campbell, A. Proc. Roy. Soc. (London), A, 87: 394. 1912.
5. Chandler, C. Modern interferometers. Hilger Watt, London. 1951. p. 217.
6. Curtis, H. L., Moon, C., and Sparks, C. M. J. Research Natl. Bur. Standards, 16: 1. 1936.

7. CURTIS, H. L., MOON, C., and SPARKS, C. M. J. Research Natl. Bur. Standards, 21: 375. 1938.
8. DYE, D. W. Proc. Roy. Soc. (London), A, 101: 315. 1922.
9. DYE, D. W. and HARTSHORN, L. Natl. Phys. Lab. Collected Researches, 21: 1. 1927.
10. JONES, V. Proc. Roy. Soc. (London), 63: 199. 1898.
11. JOUAUST, R., PICARD, M., and HEROU, R. Bull. soc. franç. élec. 8: 588. 1938.
12. MOON, C. J. Opt. Soc. Amer. 11: 453. 1925.
13. MOON, C. Bur. Standards J. Research, 10: 249. 1933.
14. ROMANOWSKI, M. Can. J. Phys. 30: 631. 1952.
15. ROMANOWSKI, M. and FRASER, P. A. Can. J. Phys. 33: 871. 1955.
16. THOMAS, J. L., PETERSON, C., COOTER, J. L., and KOTTER, F. R. J. Research Natl. Bur. Standards, 43: 291. 1949.
17. WILMOTTE, R. M. Proc. Roy. Soc. (London), A, 107: 716. 1925.

CONSIDERATIONS ON THE PRIMARY WINDING OF THE CAMPBELL STANDARD INDUCTOR[1]

By M. Romanowski[2] and P. A. Fraser[3]

ABSTRACT

The effect of the presence of the quartz cylinder on the mutual inductance of the N.R.C. standard is examined using the expression for the energy of the circuit made of the primary and the secondary connected in series. The analysis and the computation show that the volume susceptibility of the quartz, equal to $-4\pi\times0.39\times10^{-6}$ (in m.k.s. rationalized units), produces a decrease of the mutual inductance of the order of 2 parts in 10^6. In the second section the effect of the finite cross-section of the primary wire is examined. The assumption that the current is concentrated in the central filament of the wire was in several past cases considered as sufficient. The computation given here shows that this effect is not negligible and on the actual N.R.C. standard amounts to 3 or 4 parts in 10^6.

1. EFFECT OF THE MAGNETIC SUSCEPTIBILITY OF QUARTZ

The energy of a circuit C placed in a medium of magnetic permeability μ and carrying a current i is given, in the m.k.s. rationalized system of units, by the following expression

$$W = \tfrac{1}{2}li^2 = \frac{1}{2}\int_\infty (\mathbf{H}, \mathbf{B})\, dv \qquad [1]$$

where l is the self-inductance of the circuit, $\mathbf{H}$ is the magnetic field produced by the current, and $\mathbf{B}$ is the magnetic induction given by

$$\mathbf{B} = \mu\mathbf{H}. \qquad [2]$$

Let us now consider a circuit composed of two practically closed loops C' and C'' interconnected by two parallel conductors (actually they are twisted or concentric). Considering as negligible the effects of these wires, and following the method previously used for self-inductance standards (1) we can write

$$W = \tfrac{1}{2}l'i^2+\tfrac{1}{2}l''i^2+Mi^2, \qquad [3]$$

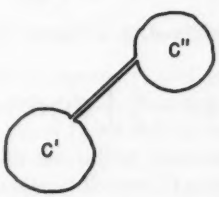

FIG. 1. Interconnected, but practically closed, loops.

[1]*Manuscript received August 25, 1955.*
Contribution from the Division of Applied Physics, National Research Council, Ottawa, Canada. Issued as N.R.C. No. 3795.
[2]*Division of Applied Physics, National Research Council.*
[3]*Former summer student, Division of Applied Physics, National Research Council; now at Department of Physics, University College, London, England.*

l' and l'' designating the self-inductance of loops C' and C'' and M their mutual inductance. Resolving the total magnetic field $\mathbf{H}$ into partial components created by the loops C' and C'' we have

$$\mathbf{H} = \mathbf{H}'+\mathbf{H}'', \qquad \mathbf{B} = \mathbf{B}'+\mathbf{B}''. \tag{4}$$

W may be written in the following form:

$$W = \frac{1}{2}\int_{\infty} ([\mathbf{H}'+\mathbf{H}''], [\mathbf{B}'+\mathbf{B}'']) \, dv,$$

$$W = \frac{1}{2}\left\{ \int_{\infty} (\mathbf{H}', \mathbf{B}') \, dv + \int_{\infty} (\mathbf{H}'', \mathbf{B}'') \, dv + \int_{\infty} (\mathbf{H}', \mathbf{B}'') \, dv + \int_{\infty} (\mathbf{H}'', \mathbf{B}') \, dv \right\}. \tag{5}$$

Comparing [3] and [5] and noticing that the third and the fourth integrals are equal, we have

$$M = \frac{\mu}{i^2}\int_{\infty} (\mathbf{H}', \mathbf{H}'') \, dv. \tag{6}$$

If a portion of space v' has a permeability μ' different from μ, then

$$M = \frac{\mu}{i^2}\int_{v} (\mathbf{H}', \mathbf{H}'') \, dv + \frac{\mu'}{i^2}\int_{v'} (\mathbf{H}', \mathbf{H}'') \, dv', \tag{7}$$

v designating the space outside v'.

Assuming that μ is the permeability of free space (or practically of air), the relation between μ and μ' is

$$\mu' = \mu(1+\kappa), \tag{8}$$

κ being the volume susceptibility of the medium v'. Then

$$M = \frac{\mu}{i^2}\int_{\infty} (\mathbf{H}', \mathbf{H}'') \, dv + \frac{\mu\kappa}{i^2}\int_{v'} (\mathbf{H}', \mathbf{H}'') \, dv'. \tag{9}$$

The second integral is considered as a "correction" due to the susceptibility κ of the volume v',

$$\Delta M = \frac{\mu\kappa}{i^2}\int_{v'} (\mathbf{H}', \mathbf{H}'') \, dv'. \tag{10}$$

This expression is easily extended to the case of several media v', v'', etc.

We will now establish, for a Campbell type mutual inductor, the expression for magnetic field which would be suitable for numerical calculations.

Let us designate by C' one of the primary helices of N turns wound on a cylinder of radius a (Fig. 2). The magnetic induction B' (or the field H') produced by C' will be the same at all points of a circle γ of radius ρ (the helix being considered as equivalent to a current sheet). The mutual inductance between γ and C' is given by the following integral:

$$M = \frac{1}{i}\int_{\gamma} (\mathbf{V}', d\boldsymbol{\gamma}), \tag{11}$$

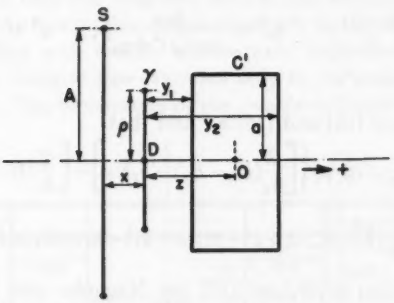

FIG. 2. Relative position of one of the helices (C') and the secondary S of the Campbell inductor. γ is an auxiliary circle used to compute the magnetic field at any point of the space.

i being the current in the helix and $\mathbf{V}'$ the vector potential produced by i at any point of γ. Because of cylindrical symmetry the integration above can be performed and yields

[12] $$V' = Mi/2\pi\rho,$$

V' designating the scalar magnitude of the vector potential. From this finally the field is calculated by the relation

[13] $$\mathbf{H}' = \frac{1}{\mu}\,\mathrm{curl}\,\mathbf{V}'.$$

As coordinates we may choose ρ and z, z being the distance between D and O; then

[14] $$H_\rho' = -\frac{1}{\mu}\frac{\partial V'}{\partial z}, \qquad H_z' = \frac{1}{\mu}\frac{1}{\rho}\frac{\partial}{\partial \rho}(\rho V'),$$

V' being expressed in terms of M and its derivatives. The mutual inductance M is given by the formula of Jones. It is a function of ρ and of the distances y_1 and y_2:

[15] $$M = M_2 - M_1.$$

In the Jones formula [16a] distances y_1 and y_2 are considered as algebraical quantities, a positive direction being (arbitrarily) chosen on the inductor's axis as in Fig. 2. The formula of Jones and its derivatives apply to all positions of D either outside or inside the helix.

[16a] $$M_h = \tfrac{1}{2}\mu\frac{y_h}{P}(\rho+a)\left[\frac{c}{k_h}(K_h - E_h) + \frac{(\rho-a)^2}{\rho+a}\,\frac{K_h-\Pi_h}{\sqrt{[(\rho+a)^2+y_h^2]}}\right],$$

[16b] $$\frac{\partial M_h}{\partial y_h} = \mu\frac{\sqrt{(a\rho)}}{P}\left[\frac{2}{k_h}(K_h - E_h) - k_h K_h\right],$$

[16c] $$\frac{\partial M_h}{\partial \rho} = \frac{\mu}{2P}\,y_h\,c k_h\left[K_h - \frac{a-\rho}{2a}(K_h - \Pi_h)\right],$$

with

$$P = \frac{y_2 - y_1}{N}, \qquad k_h^2 = \frac{4a\rho}{(a+\rho)^2 + y_h^2}, \qquad c^2 = \frac{4a\rho}{(a+\rho)^2},$$

$$c'^2 = 1 - c^2.$$

Combining [14] with [15] and [16] we find that

$$[17] \quad H_\rho' = -\frac{i}{2\pi P}\sqrt{(a/\rho)}\left\{\left[\frac{2}{k_2}(K_2 - E_2) - k_2 K_2\right] - \left[\frac{2}{k_1}(K_1 - E_1) - k_1 K_1\right]\right\},$$

$$[18] \quad H_z' = \frac{ci}{8\pi a\rho P}\{k_2 y_2[K_2(a+\rho) + \Pi_2(a-\rho)] - k_1 y_1[K_1(a+\rho) + \Pi_1(a-\rho)]\}.$$

For the calculation of H_ρ' by [17] the Nagaoka and Sakurai tables are sufficient. A note on them is given at the end of this section.

In an actual Campbell inductor the primary is made of two coaxial helices, nominally identical. The field H' produced by one of them is computed by the formulae [17] and [18]. The total field, i.e. the field produced by both helices, is designated by H_t'; it is a sum of fields $(H_\rho')_t$ and $(H_z')_t$.

The secondary S of a Campbell inductor is a coil of small square cross-section (11 mm. $\times$ 11 mm.) containing 459 turns of wire. The actual calculation of ΔM was made for one single turn lying on the neutral plane of the inductor. Calling A the radius of the secondary and x the distance from its plane to the plane of ρ we have to apply the following formulae where m designates the mutual inductance between S and γ:

$$[19] \qquad m = \mu\sqrt{(A\rho)}\left[\left(\frac{2}{k} - k\right)K - \frac{2}{k}E\right],$$

$$[20] \qquad \frac{\partial m}{\partial x} = -\frac{\mu\rho}{\sqrt{[(A+\rho)^2 + x^2]}}\left[\frac{2AxE}{(A-\rho)^2 + x^2} - \frac{x}{\rho}(K - E)\right],$$

$$[21] \qquad \frac{\partial m}{\partial \rho} = \frac{\mu\rho}{\sqrt{[(A+\rho)^2 + x^2]}}\left[\frac{2A(A-\rho)E}{(A-\rho)^2 + x^2} + (K - E)\right].$$

From these formulae and using the relation $V'' = mi/2\pi\rho$ (V'' being the vector potential created by S at any point of the circle ρ), the values of field H_ρ'' and H_z'' will be established as in [14], i.e.,

$$[22] \quad H_\rho'' = -\frac{i}{\mu 2\pi\rho}\frac{\partial m}{\partial x} = \frac{ix}{2\pi\rho\sqrt{[(A+\rho)^2 + x^2]}}\left[-K + \frac{A^2 + \rho^2 + x^2}{(A-\rho)^2 + x^2}E\right],$$

$$H_z'' = \frac{i}{\mu\rho}\frac{\partial}{\partial\rho}\left(\rho\frac{m}{2\pi\rho}\right) = \frac{1}{2\pi\sqrt{[(A+\rho)^2 + x^2]}}\left[K + \frac{A^2 - \rho^2 - x^2}{(A-\rho)^2 + x^2}E\right].$$

With these expressions we form, in cylindrical coordinates, the expression for ΔM:

$$[23] \qquad \Delta M = \mu\frac{\kappa}{i'^2}\int_{v'}(\mathbf{H}_t', \mathbf{H}'')\, dv'.$$

The volume v' is made up of the volume of the quartz cylinder on which the primaries are wound and of the volume of the marble ring containing the secondary coil. The latter lying in the neutral circle of primary helices, it is

reasonable to expect that the magnetic field in the vicinity of the secondary will be very small.[4] As this marble ring is relatively far from the primaries, the portion of space filled with marble was entirely neglected in our numerical calculation, and the integral was extended only to the volume v' occupied by the quartz cylinder. The dimensions of the quartz cylinder are given in Fig. 3.

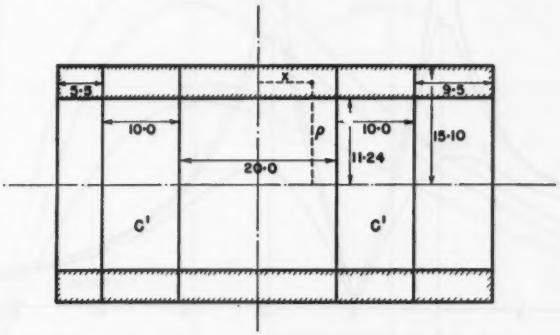

FIG. 3. Cross-section of the quartz cylinder showing points such as (x, ρ) where the magnetic field was actually computed (dimensions in cm.).

(*a*) *Field produced by the primary windings.*—The radial component H_ρ' and the axial component H_z' produced by one helix were computed by formulae [17] and [18] using the following set of values of ρ and x:

$\rho = 0.1125$ m. (inside the quartz, close to the inner surface),
$\rho = 0.1252, 0.1379, 0.1475$ m.,
$\rho = 0.1507$ m. (inside the quartz, close to the outer surface),
$x = 0.15, 0.16, 0.17, 0.18, 0.19, 0.20, 0.21, 0.22, 0.25, 0.30, 0.35, 0.40, 0.50, 0.60$ m.

The results of these computations for the radial and axial components of the *total* field are represented in Figs. 4 and 5.

(*b*) *Field produced by the secondary coil.*—This field being much smaller than the primary field, it was found unnecessary to take as many values of x and to extend the computation beyond $x = 0.30$ m. Results are given in Figs. 6 and 7.

The double integration was made in various preliminary operations by graphical evaluation of areas, and in the final computation also by means of a planimeter. The result was ($i = 1$ amp.):

$$\frac{1}{i^2}\int_{v'}(\mathrm{H}_t', \mathrm{H}'')\,\rho\,d\rho dx d\phi = \frac{1.31\times 10^3}{(4\pi)^2}.$$

The volume susceptibility[5] had been determined experimentally by means of

[4] *In the present application of the standard the current in the secondary is equal to zero. It has no effect on the mutual inductance.*

[5] *In tables actually existing the susceptibility is given in the non-rationalized system. In such a system κ would be equal to -0.39×10^{-6}, i.e. 4π times smaller than in the rationalized system.*

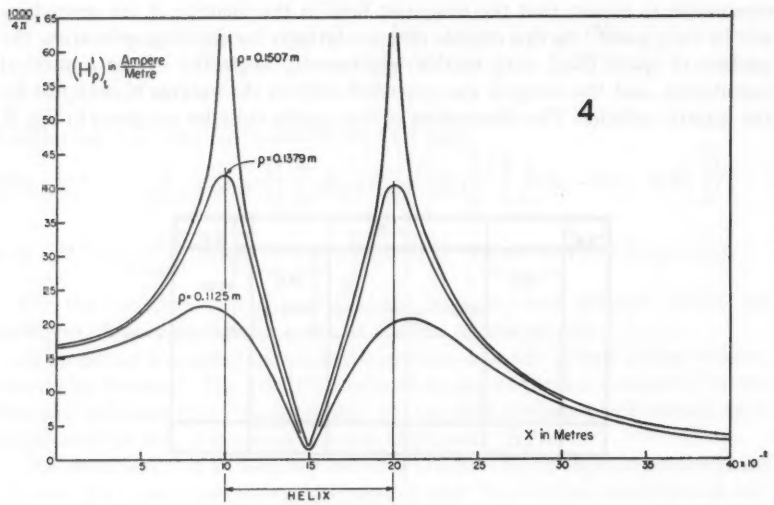

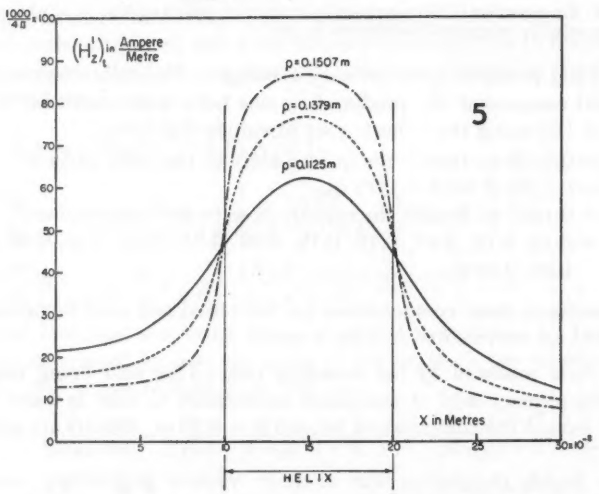

FIG. 4. Radial component of the magnetic field produced by *both* primary helices.
FIG. 5. Axial component of the magnetic field produced by *both* primary helices.

a magnetic balance on a sample of quartz taken from the cylinder and had been found equal to

$$\kappa = -0.39 \times 4\pi \times 10^{-6}.$$

Thus (taking $\mu = 4\pi \times 10^{-7}$):

$$\Delta M = -5.11 \times 10^{-11} \text{ h}.$$

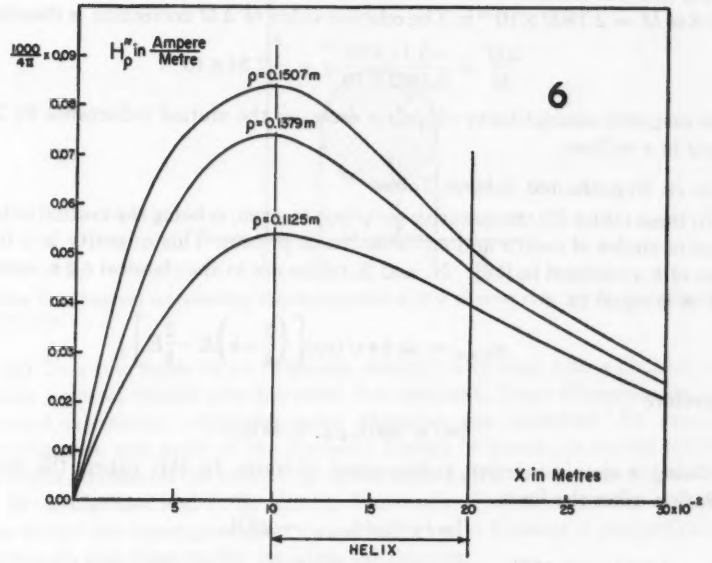

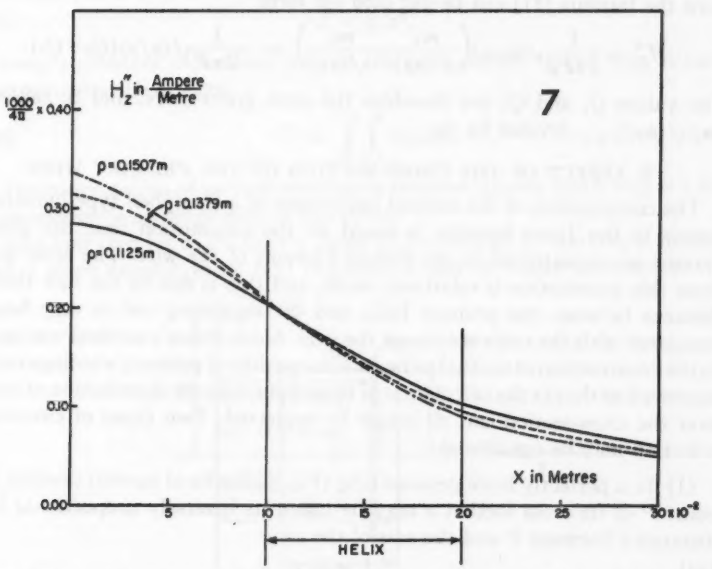

FIG. 6. Radial component of the magnetic field produced by the secondary winding.
FIG. 7. Axial component of the magnetic field produced by the secondary winding.

The mutual inductance between the primary (both helices) and the secondary S is $M = 2.1802\times10^{-5}$ h. The relative value of ΔM correction is therefore:

$$\frac{\Delta M}{M} = \frac{-5.11\times10^{-11}}{2.1802\times10^{-5}} = -2.34\times10^{-6}.$$

The magnetic susceptibility of quartz *decreases* the mutual inductance by 2.34 parts in a million.

Note on Nagaoka and Sakurai Tables

In these tables (2) the quantity $m/\sqrt{(a\rho)}$ is given, m being the mutual inductance of circles of radii a and ρ (Table No. 2, p. 140). This quantity is a function of k as defined in [16]. N. and S. tables are in the classical c.g.s. system, i.e. m is equal to

$$m_{\text{c.g.s.}} = \mu_0 4\pi\sqrt{(a\rho)}\left[\left(\frac{2}{k}-k\right)K-\frac{2}{k}E\right];$$

therefore

$$[m/\sqrt{(a\rho)}]_{\text{c.g.s.}} = 4\pi[Q],$$

Q being a simple number, independent of units. In this paper, the similar relation takes the form

$$[m/\sqrt{(a\rho)}]_{\text{m.k.s.}} = \mu[Q].$$

Now the formula [17] can be put into the form

$$H_\rho' = \frac{1}{2\pi P\mu}\sqrt{(a/\rho)}\left(\frac{m_2}{\sqrt{(a\rho)}}-\frac{m_1}{\sqrt{(a\rho)}}\right) = -\frac{1}{2\pi P}\sqrt{(a/\rho)}(Q_2-Q_1).$$

The values Q_1 and Q_2 are therefore the ones given in N. and S. tables for $[m/\sqrt{(a\rho)}]_{\text{c.g.s.}}$ divided by 4π.

2. EFFECT OF THE CROSS SECTION OF THE PRIMARY WIRE

The computation of the mutual inductance of a Campbell type inductor by means of the Jones formula is based on the assumption that the primary current is concentrated in the central filament of the wire. The error arising from this assumption is relatively small, and this is due to the fact that the distance between the primary helix and the secondary coil is very large as compared with the cross-section of the wire. Since Moon's method was applied to the construction of mutual inductors the quality of primary windings notably improved so that in the calculation of these inductors the distribution of current over the cross-section can no longer be neglected. Two types of current distribution may be considered:

(1) In a perfectly homogeneous ring (Fig. 8) the local current density J in a point P of its cross section σ may be taken as inversely proportional to the distance x between P and the axis of the ring:

[24] $$J = \alpha/x.$$

This expression is rigorously valid only for a true ring (toroid), but it is considered to be a good approximation for a helical conductor of small pitch. Such a distribution is generally called "natural".

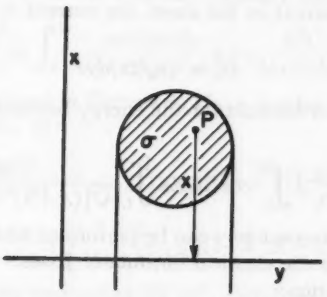

FIG. 8. Diagram representing the cross-section σ of a circular ring, y-axis being its axis of symmetry.

(2) In a ring made of an originally straight wire bent into a circular loop, elastic stresses should also be taken into account. Inner filaments are compressed resistivity, while the outer filaments are stretched. An extensive investigation was made at the National Bureau of Standards on the influence of elastic stresses on the resistivity of wires (3). It is a development of works of P. W. Bridgeman and F. R. Kotter. The result of all these studies is that we can accept the assumption that the resistivity of a filament is proportional to its length, and thus readily establish the relation

[25] $$J = \beta/x^2,$$

β being a constant dependent only on the total current in the ring. It can be computed by the integral

[26] $$I = \int\int_{\sigma} J(x)\, d\sigma.$$

The computation of mutual inductance between a circle and a ring of a finite cross-section is accomplished in two steps.

As a first step let us consider a circle (C_1) of radius A, carrying a current i, and a short current sheet (C_2) of radius x and of length 2λ (Fig. 9). If i_2

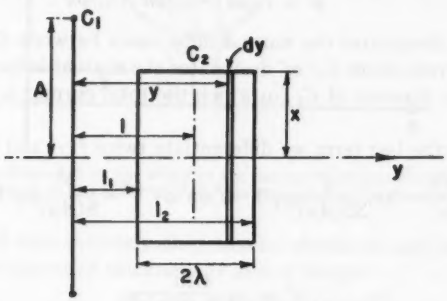

FIG. 9. Relative position of the secondary and the current sheet C_2, the latter being considered as composed of infinitesimal sheets dy.

designates the total current in the sheet, the current in a differential sheet dy will be equal to

$$di_2 = (i_2/2\lambda)dy.$$

Applying the Neumann formula for the energy between i_1 and i_2, we find the following expression:

$$[27] \qquad w = -\mu i_1 i_2 \frac{Aa}{2\lambda} 2 \int_0^{\frac{1}{2}\pi} \cos 2\phi \, d\phi \int_{l_1}^{l_2} \frac{dy}{\sqrt{[(A+a)^2+y^2-4Aa\sin^2\phi]}}.$$

The integration with respect to y can be performed and the remaining expression can be reduced to the classical formula of Jones.

Let us use the notation:

$$f(y) = [y^2+(A+a)^2-4Aa\sin^2\phi]^{-\frac{1}{2}}.$$

It gives

$$\int_{l_1}^{l_2} f(y)\,dy = F(l_2)-F(l_1) = [F(l_2)-F(l)]-[F(l_1)-F(l)]$$

and

$$F(l_2)-F(l) = \lambda f(l)+\frac{\lambda^2}{2}\left(\frac{\partial f}{\partial y}\right)_l+\frac{\lambda^3}{6}\left(\frac{\partial^2 f}{\partial y^2}\right)_l+\ldots,$$

$$F(l_1)-F(l) = -\lambda f(l)+\frac{\lambda^2}{2}\left(\frac{\partial f}{\partial y}\right)_l-\frac{\lambda^3}{6}\left(\frac{\partial^2 f}{\partial y^2}\right)_l+\ldots,$$

and, therefore,

$$\int_{l_1}^{l_2} f(y)\,dy = 2\lambda f(l)+\frac{\lambda^3}{3}\left(\frac{\partial^2 f}{\partial y^2}\right)_l.$$

Terms of higher order are neglected.

The expression for energy becomes

$$[28] \qquad w = -\mu i_1 i_2 2Aa \int_0^{\frac{1}{2}\pi} f(l)\cos 2\phi\,d\phi - \mu i_1 i_2 \frac{1}{3}\lambda^2 Aa \int_0^{\frac{1}{2}\pi}\left(\frac{\partial^2 f}{\partial y^2}\right)_l \cos 2\phi\,d\phi$$

and can be written

$$[29] \qquad w = i_1 i_2 m = i_1 i_2 m' + i_1 i_2 m''.$$

The symbol m designates the mutual inductance between C_1 (circle of radius A) and the current sheet C_2; m' designates the mutual inductance between C_1 and the central filament of C_2 (in which the total current i_2 would be concentrated).

To evaluate the last term we differentiate twice $f(y)$ and find

$$\frac{\partial^2 f}{\partial y^2} = 3y^2\frac{k^5}{32(Aa)^{5/2}}(1-k^2\sin^2\phi)^{-5/2}-\frac{k^3}{8(Aa)^{3/2}}(1-k^2\sin^2\phi)^{-3/2}$$

with

$$k^2 = \frac{4Aa}{(A+a)^2+y^2}.$$

Substituting in [28] we obtain

[30] $$m'' = -\mu\frac{l^2\lambda^2k^5}{16(Aa)^{3/2}}\int_0^{\frac{1}{2}\pi}\frac{\cos 2\phi\, d\phi}{\sqrt{(1-k^2\sin^2\phi)^5}} + \mu\frac{k^3\lambda^2}{24\sqrt{(Aa)}}\int_0^{\frac{1}{2}\pi}\frac{\cos 2\phi\, d\phi}{\sqrt{(1-k^2\sin^2\phi)^3}}.$$

Both integrals can be found in Bierens de Haan Tables (p. 91, Table 58, No. 4 and p. 93, Table 59, No. 4):

[31] $$\int_0^{\frac{1}{2}\pi}\frac{\cos 2\phi\, d\phi}{\sqrt{(1-k^2\sin^2\phi)^5}} = \frac{1}{3(1-k^2)^2k^2}[(2-k^2)(1-k^2)K - 2(1-k^2+k^4)E],$$

$$\int_0^{\frac{1}{2}\pi}\frac{\cos 2\phi\, d\phi}{\sqrt{(1-k^2\sin^2\phi)^3}} = \frac{1}{(1-k^2)k^2}[2(1-k^2)K - (2-k^2)E].$$

They yield the following expression for m'', suitable for numerical computations:

[32] $$m'' = -\mu\frac{k\lambda^2}{24\sqrt{(Aa)}k'^2}\left\{\left[\frac{l^2k^2(2-k^2)}{4Aa} - 2k'^2\right]K - \left[\frac{l^2k^2(1-k^2+k^4)}{2Aak'^2} - (2-k^2)\right]E\right\},$$

where, as usual, k' designates the quantity $\sqrt{(1-k^2)}$.

Complete numerical computations will be found at the end of this note. It may be readily seen, however, that m' is the main term and m'' only a small second-order correction. For inductors like those used as primary standards the correction term m'' is negligible. This will simplify considerably the following computation of the effect of the radial distribution of current.

Let us consider (Fig. 10) a circular ring C_2 of mean radius a, the cross-section being a circle of (small) radius ρ, and carrying the total current i_2. The ring

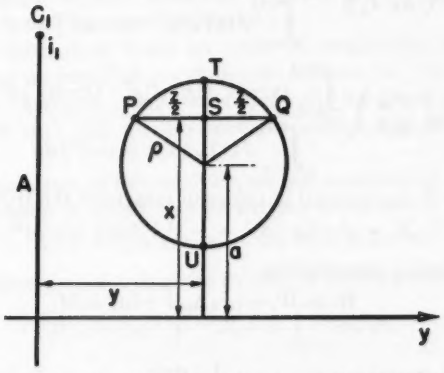

FIG. 10. Diagram showing how the effect of the current distributed over the cross-section of the ring can be reduced to the effect of a current concentrated in the diameter TU.

can be subdivided into infinitely thin coaxial sheets of radii x. The current Δi_2 in one of these sheets of thickness dx and of length

[33] $$PQ = z = 2\sqrt{[\rho^2-(x-a)^2]}$$

is equal to

[34] $$\Delta i_2 = 2J(x)z\, dx = 2J(x)\sqrt{[\rho^2-(x-a)^2]}\, dx.$$

$J(x)$ is considered as a function of the radius of the sheet. Using [29] we have the mutual energy between C_1 and the sheet PQ (m being their mutual inductance):

$$\Delta W = (i_1\,\Delta i_2)m. \tag{35}$$

Let us now assume that Δi_2 flows in a sheet of the same length z but of radius a. The mutual energy ΔW_0 in this case would be equal to

$$\Delta W_0 = (i_1\,\Delta i_2)m_0. \tag{36}$$

The relation between ΔW and ΔW_0 can be expressed by the series

$$\Delta W = \Delta W_0 + i_1\Delta i_2\left[(x-a)\left(\frac{\partial m}{\partial x}\right)_a + (x-a)^2\left(\frac{\partial^2 m}{\partial x^2}\right)_a + \dots\right] \tag{37}$$

of which only first and second order terms in $(x-a)$ will be retained.

Integrating between points T and U gives

$$W = W_0 + i_1\left(\frac{\partial m}{\partial x}\right)_a\int_U^T (x-a)di_2 + \frac{i_1}{2}\left(\frac{\partial^2 m}{\partial x^2}\right)_a\int_U^T (x-a)^2 di_2. \tag{38}$$

Using [34] and its integral

$$i_2 = \int_{a-\rho}^{a+\rho} 2J(x)\sqrt{[\rho^2-(x-a)^2]}\,dx, \tag{39}$$

we obtain

$$W = W_0 + i_1 i_2\left(\frac{\partial m}{\partial x}\right)_a \frac{1}{2}\frac{\displaystyle\int_{a-\rho}^{a+\rho}(x-a)\,J(x)\sqrt{[\rho^2-(x-a)^2]}\,dx}{\displaystyle\int_{a-\rho}^{a+\rho} J(x)\sqrt{[\rho^2-(x-a)^2]}\,dx}$$

$$+ i_1 i_2\left(\frac{\partial^2 m}{\partial x^2}\right)_a \frac{\displaystyle\int_{a-\rho}^{a+\rho}(x-a)^2 J(x)\sqrt{[\rho^2-(x-a)^2]}\,dx}{\displaystyle\int_{a-\rho}^{a+\rho} J(x)\sqrt{[\rho^2-(x-a)^2]}\,dx}$$

Designating by X (as is usual in tables of integrals) the trinomial

$$X = \rho^2-(x-a)^2 = -x^2+2ax+(\rho^2-a^2) \tag{40}$$

and also introducing the notation

$$W = W_0 + i_1 i_2\,\Delta_1 M + i_1 i_2\,\Delta_2 M, \tag{41}$$

we have

$$\Delta_1 M = \left(\frac{\partial m}{\partial x}\right)_a\left[\frac{\displaystyle\int_{a-\rho}^{a+\rho} x\sqrt{X}\,.\,J(x)\,dx}{\displaystyle\int_{a-\rho}^{a+\rho}\sqrt{X}\,.\,J(x)\,dx} - a\right],$$

$$\Delta_2 M = \frac{1}{2}\left(\frac{\partial^2 m}{\partial x^2}\right)_a\left[\frac{\displaystyle\int_{a-\rho}^{a+\rho} x^2\sqrt{X}\,.\,J(x)\,dx}{\displaystyle\int_{a-\rho}^{a+\rho}\sqrt{X}\,.\,J(x)\,dx} - 2a\frac{\displaystyle\int_{a-\rho}^{a+\rho} x\sqrt{X}\,.\,J(x)\,dx}{\displaystyle\int_{a-\rho}^{a+\rho}\sqrt{X}\,.\,J(x)\,dx} + a^2\right]. \tag{42}$$

In both cases, (1) and (2), all integrals involved may be performed using Peirce's or Dwight's Tables. In the case when

$$J(x) = \beta/x^2$$

we obtain after a few elementary transformations

$$\Delta_1 M = \left(\frac{\partial m}{\partial x}\right)_a [\sqrt{(a^2-\rho^2)}-a],$$

[43]

$$\Delta_2 M = \frac{1}{2}\left(\frac{\partial^2 m}{\partial x^2}\right)_a \left[\frac{3a}{2}[a-\sqrt{(a^2-\rho^2)}]-\frac{\rho^2}{2}\right].$$

Both brackets are obviously small and, therefore, only an approximate value for m is required for a correct computation of $\Delta_1 M$ and $\Delta_2 M$. We will assume for this purpose that m in [43] may be taken equal to m_0' (mutual inductance between coaxial circles of radii A and a, y being the distance between their planes):

[44] $$m_0' = -\mu 2Aa \int_0^{\frac{1}{2}\pi} f(y) \cos 2\phi \, d\phi = \mu\sqrt{(Aa)}\left[\left(\frac{2}{k}-k\right)K-\frac{2}{k}E\right].$$

The first derivative of m_0' with respect to a is well known:

[45] $$\frac{\partial m_0'}{\partial a} = \frac{\mu}{r_1}\left[\frac{2A(A-a)}{r_2^2}E+(K-E)\right]$$

with

$$r_1^2 = (A+a)^2+y^2, \qquad r_2^2 = (A-a)^2+y^2.$$

It is easily computed with sufficient accuracy by means of Nagaoka and Sakurai tables for all necessary values of y.

The second term $\Delta_2 M$ being an order of magnitude smaller than $\Delta_1 M$, there is no need to establish an elaborate formula for $\partial^2 m/\partial x^2$. This second derivative was, therefore, computed numerically for three values of y, namely 10, 15, and 20 cm., and all intermediate values were found by graphical interpolation.

As the last operation of this analysis, we will examine the integration [38] of ΔW_0, the expression of which may be written as follows:

[46] $$\Delta W_0 = i_1 \, \Delta i_2 \, m_0 = i_1 \, \Delta i_2 \, m_0'+i_1 \, \Delta i_2 \, m_0''.$$

It is easy to notice that m_0', as given by [44], is independent of x and therefore

[47] $$W_0 = i_1 m_0' \int_{a-\rho}^{a+\rho} di_2 + i_1 \int_{a-\rho}^{a+\rho} m_0'' di_2.$$

The first term is obviously equal to $i_1 i_2 m_0'$ and represents the mutual energy between two coaxial circles of radii A and a, located at a distance y from one another, the circle a carrying the total current i_2 of the ring.

The numerical computation of the second term using any well-known integration method (e.g. Simpson's) would be tedious work, the result of which would add only very little to the actual value of W_0. The value of m_0'' is obviously maximum for infinitesimal sheets having the largest length λ, i.e. $\lambda = \rho$, (sheet through the center of cross section). If, for example, we

calculate m_0' and m_0'' for $A = 25$ cm., $a = 15$ cm., $\rho = \lambda = 0.03$ cm., and $y = 10$ cm. we find

$$[48] \qquad \begin{aligned} m_0' &= 0.145\ \mu\text{h.}, \\ m_0'' &= 0.000{,}000{,}04\ \mu\text{h.} \end{aligned}$$

The error on ΔW_0 in [46], when m_0'' is neglected with respect to m_0', is of the order of 0.3 parts in a million. On the other hand, m_0'' decreases to zero when x approaches $a-\rho$ or $a+\rho$, so that 0.3 p.p.m. appears to be the upper limit of the error on W_0. The second term in [47] was therefore simply assumed to be negligible.

Computation of $\Delta_1 M$ *and* $\Delta_2 M$

The computation was performed using the following dimensions of the primary inductor described above:

$$\begin{aligned} A &= 0.257{,}69 \text{ m.}, \\ a &= 0.150{,}98 \text{ m.}, \\ \rho &= 0.0003 \text{ m.}, \end{aligned}$$

each helix being treated as a set of 100 rings regularly spaced between $y = 0.10$ and $y = 0.20$ m. The computation was simplified by forming groups of turns, associating 10 turns in each group with the mean value of $\partial m/\partial x$ and $\partial^2 m/\partial x^2$. Actually $\partial m/\partial x$ was computed for $y = 0.10, 0.11, \ldots, 0.20$ m. while $\partial^2 m/\partial x^2$ was computed only for $y = 0.10, 0.15, 0.20$ m. Graphical interpolation was used for intermediate values.

y (in m.)	$\left(\frac{\partial m}{\partial x}\right)_a$	Mean for a group	$\left(\frac{\partial^2 m}{\partial x^2}\right)$	Mean for a group
0.10	19.175×10^{-9}	18.4780×10^{-9}	1.07×10^{-9}	0.970×10^{-9}
0.11	17.781	17.1170	0.87	0.805
0.12	16.453	15.8795	0.74	0.690
0.13	15.306	14.7615	0.64	0.600
0.14	14.217	13.7185	0.56	0.535
0.15	13.220	12.7635	0.51	0.480
0.16	12.307	11.8895	0.45	0.430
0.17	11.472	11.6890	0.41	0.385
0.18	10.706	10.3555	0.36	0.340
0.19	10.005	9.6825	0.32	0.310
0.20	9.360		0.30	
		135.7345×10^{-9}		5.545×10^{-9}

The substitution of these values into [43] followed by summation (with respect to turns) gives the following numerical results:

$$\begin{aligned} \Sigma(\Delta_1 M) &= -0.0934\times10^{-9} \text{ h.}, \\ \Sigma(\Delta_2 M) &= +0.0144\times10^{-9} \text{ h.}, \\ \Sigma(\Delta_1 M)+\Sigma(\Delta_2 M) &= -0.0790\times10^{-9} \text{ h.} \end{aligned}$$

With 459 turns in the secondary winding the total correction is

$$-36.26\times10^{-9} \text{ h.}$$

On a mutual inductance of 0.010 h. this represents 3.6 parts in a million.

REFERENCES

1. CURTIS, H. L., MOON, C., and SPARKS, C. M. J. Research Natl. Bur. Standards, 16: 22. 1936.
2. NAGAOKA, H. and SAKURAI, S. Sci. Papers Inst. Phys. Chem. Research (Tokyo), 1922.
3. THOMAS, J. L., PETERSON, C., COOTER, J. L., and KOTTER, F. R. J. Research Natl. Bur. Standards, 43: 291. 1949.

NOTE

A NOTE ON EVIDENCE FOR A 2.158 MEV. LEVEL IN Ni^{60}*

By J. L. Wolfson†

In a study of the radiations from 24.6-min. Cu^{60}, Nussbaum *et al.* (2) have recently observed a 0.85 ± 0.03 Mev. γ-ray in coincidence with the well-known 1.33 Mev. γ-ray transition in Ni^{60}, from which they deduce the existence of a 2.18 Mev. level in Ni^{60}. They have also observed a γ-ray of 2.13 ± 0.04 Mev. which they interpret as a crossover transition from the proposed 2.18 ± 0.02 Mev. level in Ni^{60} to the ground state of Ni^{60}.

A report some time ago by Fluharty and Deutsch (1) of a γ-ray from the decay of Co^{60} with an energy E given by 1.63 Mev. $< E <$ 2.23 Mev., and an intensity of about 10^{-5} per disintegration, lends support to the conclusions of Nussbaum and co-workers. The result of Fluharty and Deutsch was obtained by disintegration studies of H^2 and Be^9, using a source of Co^{60}.

It became of interest to see whether the γ-ray could be detected in a manner which would enable its intensity and energy to be determined accurately. A source of cobalt consisting of a cylinder 1 mm. long and 1 mm. in diameter, irradiated in the NRX reactor to a strength of about 150 mc., was placed in a double lens magnetic β-ray spectrometer adjusted for a line width of 0.83% in momentum at half maximum intensity. The source was oriented with its axis coincident with the magnetic axis of the spectrometer. A uranium converter 20 mgm./cm.^{2} thick and 2 mm. in diameter was affixed to the front of the source without interposition of any absorbing material. The detector consisted of a NaI(Tl) crystal, sufficiently thick to absorb completely electrons of energies less than 3 Mev., coupled to a Dumont 6292 photomultiplier tube by means of a lucite light pipe. By employing pulse height selection in the counting circuit, the background counting rate was reduced to a very low level despite the very intense source used.

The result of a survey in the region above 1.88 Mev. is shown in Fig. 1. The photoelectron line at 2.043 Mev. is interpreted as the K line due to a γ-ray of energy 2.158 ± 0.005 Mev. The energy of the line was determined by comparison with the energy of the K photoelectron line from the 1.33 Mev. γ-ray, using the method of extrapolated high energy edges.

While no attempt was made to observe a corresponding L line, it is nevertheless certain that the line observed does not correspond to the L line of a 2.064 Mev. γ-ray, since a much more intense K photoelectron line would then have been observed at 1.949 Mev. Further, the end point of the Compton electron spectrum occurs at about 1.930 Mev. as expected for a γ-ray of energy 2.158 Mev.

The intensity of the 2.158 Mev. γ-ray was found to be $(1.2\pm0.2)\times10^{-5}$

*Issued as A.E.C.L. No. 243.
†Present address: Jewish General Hospital, Montreal, Quebec.

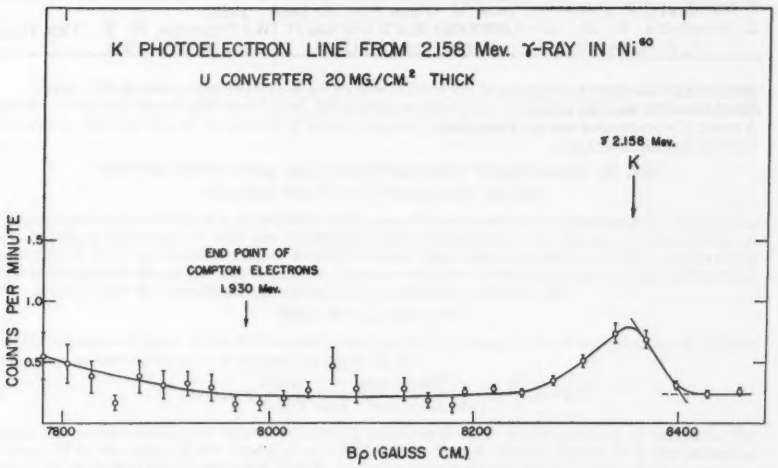

FIG. 1. The secondary electron spectrum of Co^{60} above 1.88 Mev. The line is interpreted as the K photoelectron line due to a 2.158 ± 0.005 Mev. γ-ray. The vertical bars through the experimental points represent standard deviations.

per disintegration, by an intensity calibration of the spectrometer using the 1.38 and 2.76 Mev. γ-rays from a source of Na^{24} in the form of a NaCl crystal of approximately the same dimensions as the Co^{60} source, and similarly situated relative to the U converter.

It seems likely that the 2.158 Mev. γ-ray observed corresponds to the 2.13 ± 0.04 Mev. γ-ray found by Nussbaum *et al.* The latter authors propose an assignment of $2+$ for the 2.158 Mev. level. In this case, the level can be fed only by a 0.346 Mev. γ-ray proceeding from the 2.504 Mev. level in Ni^{60}, since feeding by a 0.656 Mev. β-ray cannot account for more than a very small part of the observed intensity of 1.2×10^{-5} per disintegration. Accordingly a search was made for a 0.346 Mev. γ-ray. This γ-ray was not detected, and an upper limit of 5×10^{-5} per disintegration was found for its occurrence. Because of the high intensity of the Compton electrons, it proved impracticable to search for the 0.826 Mev. γ-ray (corresponding to the 0.85 ± 0.03 Mev. γ-ray found by Nussbaum and co-workers).

It should be pointed out that the author has not demonstrated beyond question that the observed 2.158 Mev. γ-ray proceeds from decay of Co^{60}, and the possibility remains that it is due to some unknown radioactive impurity in the sample. It is felt however that this possibility is rather remote. The source was several months old prior to the experiment, and a search through the literature has failed to indicate a contaminant, with a lifetime of the order of days or longer, which could account for the presence of the 2.158 Mev. γ-ray.

It is a pleasure to acknowledge the helpful discussions and suggestions made by Dr. L. G. Elliott during the course of the work.

1. FLUHARTY, R. G. and DEUTSCH, M. Phys. Rev. 76: 182A. 1949.
2. NUSSBAUM, R. H., VAN LIESHOUT, R., WAPSTRA, A. H., VERSTER, N. F., TEN HAAF, F. E. L., NIJGH, A. J., and ORNSTEIN, L. TH. M. Physica, 20: 555. 1954.

RECEIVED AUGUST 31, 1955.
NUCLEAR PHYSICS BRANCH,
ATOMIC ENERGY OF CANADA LIMITED,
CHALK RIVER, ONTARIO.

Under this heading brief reports of important discoveries in physics may be published. These reports should not exceed 600 words and, for any issue, should be submitted not later than six weeks previous to the first day of the month of issue. No proof will be sent to the authors.

Neutron Scattering and the Frequency Distribution of the Normal Modes of Vanadium Metal*

Slow neutrons incident on a crystalline solid may be scattered either elastically by the crystal as a whole, or inelastically with the production or annihilation of one phonon in the crystal, or inelastically with production and/or annihilation of more than one phonon. For a monatomic crystal composed of atoms which scatter incoherently the incoherent part of the differential cross section (per 4π steradians per atom) for the elastic process is (2)

$$4\pi G_0 = \sigma_{\text{inc}} \exp(-2W) \tag{1}$$

and the incoherent part of the differential cross section for production of one phonon of angular frequency ω_i belonging to one normal mode is (2, 3)

$$4\pi G_{+1} = \frac{\hbar\, \sigma_{\text{inc}}}{6MN} \frac{\exp(-2W)}{\omega_i[1-\exp(-\hbar\omega_i/k_BT)]} \frac{k'}{k} |\mathbf{k}-\mathbf{k}'|^2 \tag{2}$$

where σ_{inc} is the incoherent bound scattering cross section, N is the number of atoms in the crystal, M is the mass of one atom, $\exp(-2W)$ is the Debye–Waller factor, $\mathbf{k}$ is the incoming propagation vector of the neutron, and $\mathbf{k}'$ is the outgoing propagation vector of the neutron.

Equation [2] has been shown to apply to a Debye crystal (2) and to a cubic crystal (3). It also applies to a randomly oriented powder composed of non-cubic crystals, provided the Debye–Waller factor is sufficiently close to unity. The cross section for annihilation of one phonon G_{-1} is simply [2] multiplied by the Boltzmann factor $\exp(-\hbar\omega_i/k_BT)$.

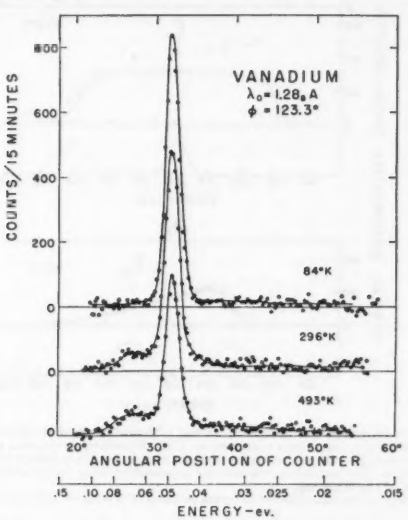

FIG. 1. Counting rate of 0.049$_3$ ev. neutrons scattered at 123° by vanadium at 84°K., 296°K., 493°K., as a function of the setting of the analyzing spectrometer and therefore of the energy. The curves are displaced vertically relative to each other.

*Issued as A.E.C.L. No. 255.

Part of this work was presented at the New York Meeting of the American Physical Society, Jan. 27–29, 1955 (Phys. Rev. 98: 1171. 1955).

The incoming and outgoing energies of the neutron (E and E' respectively) are related to the frequency of the phonon by $|E'-E| = \hbar\omega$. The cross section per energy interval dE' of the outgoing neutron is

$$4\pi G(E')\,dE' = 4\pi G_{\pm 1}\,g(\omega)\,d\omega \qquad [3]$$

where $g(\omega)$ is the frequency distribution of the normal modes without regard to direction or polarization. Measurement of the energy distribution of incoherently scattered neutrons thus provides a method for direct measurement of $g(\omega)$ (3).

Measurement of energy distributions of neutrons scattered by vanadium metal* at several temperatures have been made. Monoenergetic neutrons of mean energy 0.049_3 ev. were scattered symmetrically backwards at an angle of 123° by a slab of vanadium metal 0.35 scattering mean free paths in thickness. The energy of the scattered neutrons was measured by means of a crystal spectrometer, using an aluminum crystal (1). In Fig. 1 the counting rates obtained are shown as a function of the angular position of the counter of the analyzing spectrometer. The energy corresponding to this position is also shown.

At the energy of the incoming neutrons a strong peak is found having a width corresponding to the resolution of the apparatus. This peak decreases with increasing temperature, and a Debye temperature for vanadium of $\Theta_D = 366° \pm 25°$ can be inferred from its temperature dependence using [1] and the Debye model expression (4) for the Debye–Waller factor.

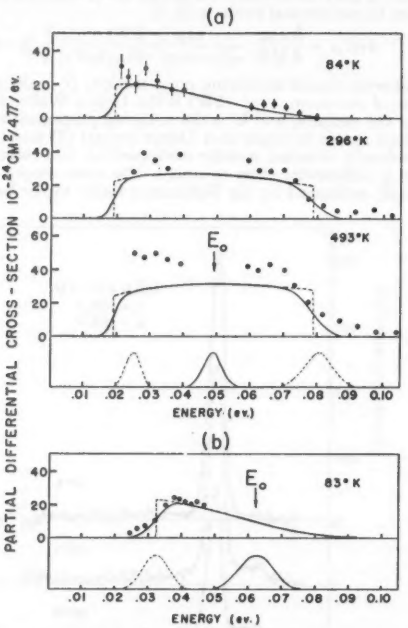

FIG. 2. (*a*) The points represent the measured partial differential cross section of vanadium metal at 84°K., 296°K., and 493°K. for 0.049_3 ev. neutrons scattered at 123°. Standard deviations are shown for the 84°K. cross sections. The solid curves are the one-phonon cross sections computed for a Debye temperature of 348° and folded with the resolution function. The dotted curves are the unmodified cross sections. Estimated resolution functions are shown at the bottom of the diagram.
(*b*) Measured and calculated partial differential cross sections of 0.062_3 ev. neutrons scattered at 95° by vanadium metal at 83°K.

On both sides of the elastic peak inelastically scattered neutrons are observed whose intensity increases with increasing temperature. Converting the counting rates of Fig. 1 to an energy distribution and correcting for the spectrometer efficiency (1) the points of Fig. 2(*a*) are obtained. The cross sections have been put on an absolute basis by using the elastic peaks and equation [1]. In the calculations account was taken of multiple scattering which involved interchange of zero or one phonons.

**Scattering by vanadium is almost completely incoherent* ($\sigma_{coh} = 0.03$ *b.*, $\sigma_{inc} = 5.1$ *b.*).

The upper cutoffs of the spectra imply a Debye temperature of 320°±30°. The lower cutoff could not be obtained because of contamination by the second order spectrum of the analyzing spectrometer. Another spectrum was therefore measured using a higher initial energy (0.062$_2$ ev.) and is shown in Fig. 2(*b*). The low energy end of the spectrum has a cutoff which is sharp within the resolution of the experiment. The location of the cutoff implies a Debye temperature of 350°±20°.

Assuming a Debye frequency distribution

$$g(\omega) = 9N\omega^2/\omega_0^3, \qquad \omega \leqslant \omega_0,$$
$$= 0, \qquad \omega > \omega_0,$$

where $\omega_0 = k_B\Theta_D/\hbar$, the one-phonon spectra were computed for $\Theta_D = 348°$, the weighted mean of the above values. They are shown in Fig. 2 as calculated and as folded with the estimated resolution function of the apparatus. Agreement of the calculated spectra with the measured cross sections is reasonable at the lowest temperature, becoming worse at the higher temperatures. Rough estimates of the cross sections for multiple phonon transfer suggest that the differences probably arise from this process.

The results of these preliminary experiments can thus be satisfactorily accounted for by a Debye model for vanadium. The experiments are being continued under better conditions of intensity and resolution, and it is hoped soon to obtain the essential features of the frequency distribution by this method.

1. Brockhouse, B. N. Phys. Rev. 99: 601. 1955.
2. Cassels, J. M. Progress in nuclear physics. Academic Press, New York. 1950. p. 185.
3. Placzek, G. and Van Hove, L. Phys. Rev. 93: 1207. 1954.
4. Weinstock, R. Phys. Rev. 65: 8. 1944.

Received October 17, 1955.
B. N. Brockhouse
Atomic Energy of Canada Limited,
Chalk River, Ontario.

CONTENTS OF VOLUME 33

Adey, A. W. Diffraction of microwaves by long metal cylinders, 407.

Alexander, T. K. See Heiberg, S. A., 34(L).

Allen, L. J. See Blackwell, J. H., 483.

Archibald, W. J. Field equations from particle equations, 565.

Atwater, H. A., Lang, A. R., and **Chalmers, B.** Some observations of surface phenomena appearing on lead single crystals, 352.

Balazs, N. L. The resolution of four-dimensional vector fields and tensor fields, and its application to electrodynamics, 235.

Bartholomew, G. A., Brown, F., Gove, H. E., Litherland, A. E., and **Paul, E. B.** Capture radiation and neutrons from the bombardment of C^{14} with protons, 441.

Bartholomew, R. M., Boyd, A. W., Brown, F., Hawkings, R. C., Lounsbury, M., and **Merritt, W. F.** The half-life of Cl^{36}, 43.

Bean, D. T. W. See Britton, F. R., 668.

Bedford, R. E. and **Crooker, A. M.** The hyperfine structure of mercury extracted from neutron-irradiated gold, 25.
Correction to: The hyperfine structure of mercury extracted from neutron-irradiated gold, 492(L).

Bell, R. E., Graham, R. L., and **Yaffe, L.** The thermal neutron capture cross section of Au^{198} and the half-life of Au^{199}, 457.

Benson, G. C. See Schreiber, H. P., 534.

Benson, G. C. and **Schreiber, H. P.** A method for the evaluation of some lattice sums occurring in calculations of physical properties of crystals. II, 529.

Bird, J. R. and **Preston, M. A.** A study of nucleon forces with repulsive cores. I. The effect of cores of finite strength, 399.

Blackwell, J. H., Fewer, D. R., Allen, L. J., and **Cass, R. S.** An audio-frequency circuit model of the one-dimensional Schroedinger equation and its sources of error, 483.

Bloom, J. N. See Chatterjee, S. D., 577.

Boyd, A. W. See Bartholomew, R. M., 43.

Boyd, A. W., Brown, F., and **Lounsbury, M.** Mass spectrometric study of natural and neutron-irradiated chlorine, 35.

Britton, F. R. and **Bean, D. T. W.** Long range forces between hydrogen molecules, 668.

Brockhouse, B. N. Neutron scattering and the frequency distribution of the normal modes of vanadium metal, 889(L).

Brown, F. See Bartholomew, G. A., 441; Bartholomew, R. M., 43; Boyd, A. W., 35.

Brown, S. B. See Trainor, L. E. H., 110.

Cass, R. S. See Blackwell, J. H., 483.

Chadwick, G. B. See Sample, J. T., 828.

Chalmers, B. See Atwater, H. A., 352; Elbaum, C., 196.

Chapman, J. H. See Littlewood, C. A., 11.

Chapman, J. H., Davies, K., and **Littlewood, C. A.** Radio observations of the ionosphere at oblique incidence, 713.

Chatterjee, S. D. and **Bloom, J. N.** On diurnal variation in cosmic-ray intensity at Ottawa, 577.

Crooker, A. M. See Bedford, R. E., 25, 492(L).

Crooker, A. M. and **Ross, W. L.** A note on black body radiation, 257.

Cumming, C. The ν_3 infrared band of ammonia, 635.

Currie, B. W. Auroral heights over West-Central Canada, 773.

Currie, B. W. and **Weaver, J. T.** Vertical extent of auroral arcs and bands, 611.

Dauphinee, T. M. An apparatus for comparison of thermocouples, 275.

Davies, K. See Chapman, J. H., 713.

Dirac, P. A. M. Gauge-invariant formulation of quantum electrodynamics, 650.
Note on the use of non-orthogonal wave functions in perturbation calculations, 709.

Dixon, W. R. Energy and angular distributions of photoneutrons produced by 70-Mev. X-rays, 785.

Douglas, A. E. The spectrum of the Si_2 molecule, 801.

Douglas, A. E. and **Møller, C. K.** Predissociations of the $C^{12}O$ and $C^{13}O$ molecules, 125.

Eades, R. G. An investigation of the nuclear resonance absorption spectrum of Al^{27} in a single crystal of euclase, 286.

Elbaum, C. and **Chalmers, B.** The topography of solid–liquid interfaces of metal crystals growing from the melt, 196.

Elliott, L. G., Preston, M. A., and **Wolfson, J. L.** A note on the spin and parity of 2.69 day Au^{198}, 607.

Feldman, T. See Romanko, J., 588.

Feldman, T., Romanko, J., and **Welsh, H. L.** The ν_2 Raman band of methane, 138.

Fewer, D. R. See Blackwell, J. H., 483.

Forsyth, P. A. See Hines, C. O., 609(L).

Forsyth, P. A., Hines, C. O., and **Vogan, E. L.** Diurnal variations in the number of shower meteors detected by the forward-scattering of radio waves. Part II. Experiment, 600.

Forsyth, P. A. and **Vogan, E. L.** Forward-scattering of radio waves by meteor trails, 176.

Fraser, P. A. See Romanowski, M., 871.

Gibbons, J. J. Some exact solutions of the Lorentz invariant problem of the motion of two electric fluids, 819.

Gove, H. E. See Bartholomew, G. A., 441.

Gow, K. V. See Martius, U. M., 225.

Graham, R. L. See Bell, R. E., 457.

Griffiths, G. M. The pulse height distribution from a sodium iodide single crystal scintillation counter and the measurement of gamma ray fluxes, 209.

Gulbis, F. See Keech, G. L., 148(L).

Guptill, E. W., Hoyt, C. K., and **Robinson, D. K.** The velocity and attenuation of sound in solid argon, 397(L).

Hart, J. and **Simmons, D. A.** A note concerning the conductivity of liquid dielectrics, 54.

Hartz, T. R. Radio star scintillations and the ionosphere, 476.

Hawkings, R. C. See Bartholomew, R. M., 43.

Heaps, H. S. The effect of a random noise background upon the detection of a random signal, 1.

The effect of a random noise background upon the detection of a sinusoidal signal, 509.

Hector, F. S. See Meek, J. H., 364.

Heiberg, S. A. See James, D. B., 219.

Heiberg, S. A., James, D. B., and **Alexander, T. K.** The angular distribution of the gamma-rays from the reaction $C^{12}(p, \gamma p')C^{12}$, 34(L).

Heikkila, W. J. and **Hollis Hallett, A. C.** The viscosity of liquid helium II, 420.

Henderson, J. T. and **Mungall, A. G.** The velocity of propagation of electromagnetic waves, 265.

Henderson, J. T. and **Romanowski, M.** A standard of mutual inductance, 856.

Henshaw, D. G. and **Hurst, D. G.** The zero-point kinetic energy of liquid helium, 797.

Herzberg, G. and **Hugo, T. J.** Forbidden transitions in diatomic molecules. IV. The $a'^3\Sigma^+ \leftarrow X^1\Sigma^+$ and $e^3\Sigma^- \leftarrow X^1\Sigma^+$ absorption bands of carbon monoxide, 757.

Hines, C. O. Diurnal variations in the number of shower meteors detected by the forward-scattering of radio waves. Part I. Theory, 493.
See also Forsyth, P. A., 600.

Hines, C. O., Forsyth, P. A., Vogan, E. L., and **Pugh, R. E.** The dependence of meteoric forward-scattering on antenna patterns and orientations, 609(L).

Hollis Hallett, A. C. See Heikkila, W. J., 420.

Hoyt, C. K. See Guptill, E. W., 397(L).

Hugo, T. J. See Herzberg, G., 757; Naudé, S. M., 573.

Hunten, D. M. See Scrimger, J. A., 780.

Hurst, D. G. See Henshaw, D. G., 797.

Husain, A. and **Pickup, E.** Nuclear interaction of K mesons, 260.

Jackson, J. D. On the interpretation of nuclear resonance fluorescence experiments, 575(L).

James, D. B. See Heiberg, S. A., 34(L).

James, D. B., Kubelka, W., Heiberg, S. A., and **Warren, J. B.** The pulse height distribution from boron trifluoride proportional counters irradiated with 4.87-Mev. neutrons, 219.

Johnson, F. A. The new isotopes Cd^{104} and Ag^{104}, 841.

Kaempffer, F. A. Some considerations regarding the principle of phase invariance, 436.

Keech, G. L. and **Gulbis, F.** On anomalies in the absorption of cosmic rays in lead, 148(L).

Kelly, F. M. and **Pearson, W. B.** The rubidium transition at ~180°K., 17.

Krotkov, R. Low energy neutron cross section of manganese, 622.

Kubelka, W. See James, D. B., 219.

Kumar, K. and **Preston, M. A.** Masses of nuclei in isobaric sequences, 298.

Lang, A. R. See Atwater, H. A., 352.

Leachman, R. B. and **Schafer, W. D.** A calorimetric determination of the average kinetic energy of the fragments from U^{235} fission, 357.

Leger, E. G. A panoramic mass spectroscope for kinetic studies, 74.

van de Lindt, W. J. A note concerning forces and torques on spheroidal bodies in cavities, 113.

Litherland, A. E. See Bartholomew, G. A., 441.

Littlewood, C. A. See Chapman, J. H., 713.

Littlewood, C. A. and **Chapman, J. H.** A measurement at Ottawa of the change in height with lunar time of the *E* region of the ionosphere, 11.

Livesey, D. L. A note on nuclear temperatures at low excitation energies, 391.

Lounsbury, M. See Bartholomew, R. M., 43; Boyd, A. W., 35.

Lovejoy, D. R. Surface tension of He^3, 49.

Manchester, F. D. Adiabatic oscillations in liquid helium II, 146(L).

Marr, G. V. and **Nicholls, R. W.** The emission of the 'λ4050 Å' bands and an associated violet continuum in oxyacetylene flames, 394.

Martius, U. M. The initial oxidation of nickel, 466.

Martius, U. M. and **Gow, K. V.** Ferromagnetic domain patterns on single crystals and bicrystals of nickel, 225.

Meek, J. H. and **Hector, F. S.** A recording magnetic variometer, 364.

Melaika, E. A. See Petruska, J. A., 640.

Merritt, W. F. See Bartholomew, R. M., 43.

Michel, W. S. and **Whyte, G. N.** International comparisons of the Canadian primary radium standard, 521.

Miescher, E. Fine structure of NO^+ and NO emission spectra in the Schumann region, 355(L).

Møller, C. K. See Douglas, A. E., 125.

Mungall, A. G. See Henderson, J. T., 265.

Naudé, S. M. and **Hugo, T. J.** The emission spectrum of AlF in the region 1700–2000 Å, 573.

Neilson, G. C. See Sample, J. T., 350, 828.

Nicholls, R. W. See Marr, G. V., 394.

Northover, F. H. Long distance V.H.F. fields. I. Partial reflection from a standard atmosphere, 241.
Long distance V.H.F. fields. II. Refractivity profiles containing "sharp layers", 316.
Long distance V.H.F. fields. III. The case of two elevated layers, 347.

Ogilvie, K. W. The proton component of cosmic rays at aircraft altitudes, 555.
Cosmic-ray experiments with a proton velocity selector, 746.

Paul, E. B. See Bartholomew, G. A., 441.

Pearson, W. B. A method of examining structural changes of metals on deformation in liquid helium: Examination of indium, 473.
See also Kelly, F. M., 17.

Petruska, J. A., Melaika, E. A., and **Tomlinson, R. H.** The fission yields of the cesium isotopes formed in the thermal neutron fission of U^{235} and the neutron absorption cross section of Xe^{135}, 640.

Petruska, J. A., Thode, H. G., and **Tomlinson, R. H.** The absolute fission yields of twenty-eight mass chains in the thermal neutron fission of U^{235}, 693.

Pickup, E. See Husain, A., 260.

Preston, M. A. See Bird, J. R., 399; Elliott, L. G., 607; Kumar, K., 298.

Pugh, R. E. Field theoretical description of the superconducting state, 679.
See also Hines, C. O., 609(L).

Robinson, D. K. See Guptill, E. W., 397(L).

Robinson, R. O. A. The Bethe–Salpeter equation for many-body systems, 369.
α^3 corrections to the ground state of helium, 707(L).

Romanko, J. See Feldman, T., 138.

Romanko, J., Feldman, T., and **Welsh, H. L.** The Raman spectrum of ethane, 588.

Romanowski, M. See Henderson, J. T., 856.

Romanowski, M. and **Fraser, P. A.** Considerations on the primary winding of the Campbell standard inductor, 871.

Ross, W. L. See Crooker, A. M., 257.

Rutter, J. W. See Smith, V. G., 723.

Sample, J. T., Neilson, G. C., Chadwick, G. B., and **Warren, J. B.** Gamma rays from the deuteron bombardment of boron 10, 828.

Sample, J. T., Neilson, G. C., and **Warren, J. B.** Performance of a fast neutron collimator, 350.

Schafer, W. D. See Leachman, R. B., 357.

Schreiber, H. P. See Benson, G. C., 529.

Schreiber, H. P. and **Benson, G. C.** Edge energies of alkali halide crystals, 534.

Scrimger, J. A. and **Hunten, D. M.** The intensity at the bottom of the Fraunhofer *D* lines, 780.

Shaw, E. A. G. On the determination of electromechanical coupling coefficients in a polyresonant piezoelectric vibrator, 504.

Simmons, D. A. See Hart, J., 54.

Smith, V. G., Tiller, W. A., and **Rutter, J. W.** A mathematical analysis of solute redistribution during solidification, 723.

Stacey, F. D. The fluctuating field model of ferromagnetism with particular reference to nickel, 661.

Stoicheff, B. P. High resolution Raman spectroscopy of gases. V. Rotational spectra of allene, allene-d_4, and allene-1,1-d_2, 811.

Tauber, G. E. On equations of motion in general relativity, 824.

Thiessen, G. J. On the efficiency of an acoustic line source with progressive phase shift, 618.

Thode, H. G. See Petruska, J. A., 693; Wanless, R. K., 541.

Tiller, W. A. See Smith, V. G., 723.

Tomlinson, R. H. See Petruska, J. A., 640, 693; Wiles, D. M., 133.

Trainor, L. E. H. and **Brown, S. B.** A note on the X-ray spectrum of a 70 Mev. synchrotron, 110.

Vogan, E. L. See Forsyth, P. A., 176, 600; Hines, C. O., 609(L).

Volkoff, G. M. See Waterman, H. H., 156.

Wait, J. R. Scattering of a plane wave from a circular dielectric cylinder at oblique incidence, 189.

Scattering of electromagnetic waves from a "lossy" strip on a conducting plane, 383.

Wanless, R. K. and **Thode, H. G.** The fission yields of isotopes of xenon and krypton in the neutron fission of U^{235} and U^{238}, 541.

Warren, J. B. See James, D. B., 219; Sample, J. T., 350, 828.

Waterman, H. H. and **Volkoff, G. M.** Nuclear magnetic resonance spectrum of B^{11} in kernite, 156.

Weaver, J. T. See Currie, B. W., 611.

Welsh, H. L. See Feldman, T., 138; Romanko, J., 588.

White, G. K. The electrical resistance of dilute copper alloys at very low temperatures, 119.

White, G. K. and **Woods, S. B.** Thermal and electrical conductivities of solids at low temperatures, 58.

Whyte, G. N. Measurements of spectral and angular distributions of secondary gamma-rays in matter, 96.

See also Michel, W. S., 521.

Wiles, D. M. and **Tomlinson, R. H.** The half-life of Sr^{90}, 133.

Wolfson, J. L. A note on evidence for a 2.158 Mev. level in Ni^{60}, 886.

See also Elliott, L. G., 607.

Woods, S. B. See White, G. K., 58.

Wu, T.-Y. A suggested method for studying the mechanism of energy transfer in collisions, 151.

Yaffe, L. See Bell, R. E., 457.

CORRECTIONS

Vol. 29, 1951. In the paper *The magnetic dipole over the horizontally stratified earth* by James R. Wait, pp. 577–592,

(1) the denominator $2\pi\sigma\rho^4$ in Equation (38) should read $2\pi\sigma\rho^5$,

(2) the + sign preceding the integral in Equation (52) should be a − sign.

Vol. 32, 1954. In *Calculated diffraction patterns of dielectric rods at centimetric wavelengths* by Charlotte Froese and James R. Wait, pp. 775–781, the relation following equation [1] should read

$$\phi_0 = k[\sqrt{(x+x_0)^2+y^2}-x_0].$$

THE PHYSICAL SOCIETY

MEMBERSHIP of the Society is open to all who are interested in Physics.

FELLOWS pay an Entrance fee of £1 1*s*. ($3.00) and an Annual Subscription of £2 2*s*. ($6.00).

STUDENTS: A candidate for Studentship must be between the ages of 18 and 26, and pays an Annual Subscription of 7*s*. 6*d*. ($1.10).

MEETINGS: Fellows and Students may attend all Meetings of the Society including the annual Exhibition of Scientific Instruments and Apparatus.

PUBLICATIONS include the *Proceedings of the Physical Society*, published monthly in two sections, and *Reports on Progress in Physics*, published annually. Volume XVII, 1954, is now available (price 50*s*. ($7.15)). Members are entitled to receive many of the Publications at a reduced rate.

Further information can be obtained from:

THE PHYSICAL SOCIETY

1, LOWTHER GARDENS, PRINCE CONSORT ROAD

LONDON, S.W.7, ENGLAND

REFERENCES—CANADIAN JOURNAL OF PHYSICS

This is to announce a change from the present system of citing references. Beginning in January 1956, reference citations will be unnumbered and will be referred to in the text by the author and date. Authors are requested to follow the new system in all manuscripts submitted henceforth, noting especially the following details.

In the List of References

1. References should be arranged alphabetically according to the names of the authors of the publications.

2. The year of publication should follow the initials of the last author.

3. Citations of work accepted for publication should include the year and place of publication followed by "In press". References to work that has not been published should be given simply as "Unpublished".

4. If two or more publications are listed for the same author or authors, the name(s) of the author(s) should be replaced by a dash in the second and subsequent citations.

5. Two or more publications listed for the same author or authors in the same year should be differentiated by *a*, *b*, etc., following the year.

6. In citations from periodicals the volume number will be printed in bold-face type and thus in the manuscript the number should be underlined by a wavy line.

EXAMPLES:

Atkins, K. R. 1954. Can. J. Phys. **32**: 347.
Dirac, P. A. M. 1947. The principles of quantum mechanics. 3rd ed. Oxford at the Clarendon Press.
——— 1948*a*. Phil. Mag. **39**: 31.
——— 1948*b*. Phys. Rev. **74**: 817.
——— 1952. Proc. Roy. Soc. (London), A, **212**: 330.
Smith, A. B. Unpublished.
Smith, A. B. and Allen, R. O. 1956. Can. J. Phys. In press.
Sumner, J. B. and Somers, G. F. 1944. Laboratory experiments in biological chemistry. Academic Press, Inc., New York, N.Y.

In the Text

The following examples indicate how to refer in the text to citations given in the reference list: (Atkins 1954), (Dirac 1948*a*, *b*, 1952), (Dirac 1947; Smith and Allen 1956), (Smith unpublished). When the names of authors form part of the text, only the date will appear in parentheses, e.g. "Atkins (1954) found . . .".

CANADIAN JOURNAL OF PHYSICS

Notes to Contributors

Manuscripts

(i) ***General.*** Manuscripts, in English or French, should be typewritten, double spaced, on paper 8½×11 in. **The original and one copy are to be submitted.** Tables and captions for the figures should be placed at the end of the manuscript. Every sheet of the manuscript should be numbered.

Style, arrangement, spelling, and abbreviations should conform to the usage of this journal. Names of all simple compounds, rather than their formulas, should be used in the text. Greek letters or unusual signs should be written plainly or explained by marginal notes. Superscripts and subscripts must be legible and carefully placed.

Manuscripts and illustrations should be carefully checked before they are submitted. Authors will be charged for unnecessary deviations from the usual format and for changes made in the proof that are considered excessive or unnecessary.

(ii) ***Abstract.*** An abstract of not more than about 200 words, indicating the scope of the work and the principal findings, is required, except in Notes.

(iii) ***References.*** References should be listed **alphabetically by authors' names,** numbered, and typed after the text. The form of the citations should be that used in this journal; in references to papers in periodicals, titles should not be given and only initial page numbers are required. All citations should be checked with the original articles and each one referred to in the text by the key number.

(iv) ***Tables.*** Tables should be numbered in roman numerals and each table referred to in the text. Titles should always be given but should be brief; column headings should be brief and descriptive matter in the tables confined to a minimum. Vertical rules should be used only when they are essential. Numerous small tables should be avoided.

Illustrations

(i) ***General.*** All figures (including each figure of the plates) should be numbered consecutively from 1 up, in arabic numerals, and each figure referred to in the text. The author's name, title of the paper, and figure number should be written in the lower left corner of the sheets on which the illustrations appear. Captions should not be written on the illustrations (see Manuscripts (i)).

(ii) ***Line Drawings.*** Drawings should be carefully made with India ink on white drawing paper, blue tracing linen, or co-ordinate paper ruled in blue only; any co-ordinate lines that are to appear in the reproduction should be ruled in black ink. Paper ruled in green, yellow, or red should not be used unless it is desired to have all the co-ordinate lines show. All lines should be of sufficient thickness to reproduce well. Decimal points, periods, and stippled dots should be solid black circles large enough to be reduced if necessary. Letters and numerals should be neatly made, preferably with a stencil (**do NOT use typewriting**) and be of such size that the smallest lettering will be not less than 1 mm. high when reproduced in a cut 3 in. wide.

Many drawings are made too large; originals should not be more than 2 or 3 times the size of the desired reproduction. In large drawings or groups of drawings the ratio of height to width should conform to that of a journal page but the height should be adjusted to make allowance for the caption.

The original drawings and one set of clear copies (e.g. small photographs) are to be submitted.

(iii) ***Photographs.*** Prints should be made on glossy paper, with strong contrasts. They should be trimmed so that essential features only are shown and mounted carefully, with rubber cement, on white cardboard with no space or only a very small space (less than 1 mm.) between them. In mounting, full use of the space available should be made (to reduce the number of cuts required) and the ratio of height to width should correspond to that of a journal page (4½×7½ in.); however, allowance must be made for the captions. Photographs or groups of photographs should not be more than 2 or 3 times the size of the desired reproduction.

Photographs are to be submitted in duplicate; if they are to be reproduced in groups one set should be mounted, the duplicate set unmounted.

Reprints

A total of 50 reprints of each paper, without covers, are supplied free. Additional reprints, with or without covers, may be purchased.

Charges for reprints are based on the number of printed pages, which may be calculated approximately by multiplying by 0.6 the number of manuscript pages (double-spaced typewritten sheets, 8½×11 in.) and including the space occupied by illustrations. An additional charge is made for illustrations that appear as coated inserts. The cost per page is given on the reprint requisition which accompanies the galley.

Any reprints required in addition to those requested on the author's reprint requisition form must be ordered officially as soon as the paper has been accepted for publication.

Contents

Page

Note on the Use of Non-orthogonal Wave Functions in Perturbation Calculations—*P. A. M. Dirac* - - - - - - - - - - - - - - - 709

Radio Observations of the Ionosphere at Oblique Incidence—*J. H. Chapman, Kenneth Davies, and C. A. Littlewood* - - - 713

A Mathematical Analysis of Solute Redistribution During Solidification—*V. G. Smith, W. A. Tiller, and J. W. Rutter* - - - 723

Cosmic-ray Experiments with a Proton Velocity Selector—*K. W. Ogilvie* - 746

Forbidden Transitions in Diatomic Molecules. IV. The $a'^1\Sigma^+ \leftarrow X^1\Sigma^+$ and $e^3\Sigma^- \leftarrow X^1\Sigma^+$ Absorption Bands of Carbon Monoxide—*G. Herzberg and T. J. Hugo* - - - - - - - - - - - - - - - 757

Auroral Heights over West-Central Canada—*B. W. Currie* - - - 773

The Intensity at the Bottom of the Fraunhofer *D* Lines—*J. A. Scrimger and D. M. Hunten* - - - - - - - - - - - - - - 780

Energy and Angular Distributions of Photoneutrons Produced by 70-Mev. X-rays—*W. R. Dixon* - - - - - - - - - - - - - 785

The Zero-point Kinetic Energy of Liquid Helium—*D. G. Henshaw and D. G. Hurst* - - - - - - - - - - - - - - - - - - - 797

The Spectrum of the Si_2 Molecule—*A. E. Douglas* - - - - - - - 801

High Resolution Raman Spectroscopy of Gases. V. Rotational Spectra of Allene, Allene-d_4, and Allene-1,1-d_2—*B. P. Stoicheff* - 811

Some Exact Solutions of the Lorentz Invariant Problem of the Motion of Two Electric Fluids—*J. J. Gibbons* - - - - - - - 819

On Equations of Motion in General Relativity—*G. E. Tauber* - - 824

Gamma Rays from the Deuteron Bombardment of Boron 10—*J. T. Sample, G. C. Neilson, G. B. Chadwick, and J. B. Warren* 828

The New Isotopes Cd^{104} and Ag^{104}—*F. A. Johnson* - - - - - - - 841

A Standard of Mutual Inductance—*J. T. Henderson and M. Romanowski* - 856

Considerations on the Primary Winding of the Campbell Standard Inductor—*M. Romanowski and P. A. Fraser* - - - - - - - 871

A Note on Evidence for a 2.158 Mev. Level in Ni^{60}—*J. L. Wolfson* 886

Letter to the Editor:

Neutron Scattering and the Frequency Distribution of the Normal Modes of Vanadium Metal—*B. N. Brockhouse* - - 889

Contents of Volume 33 - - - - - - - - - - - - - - - - - - 892

Printed in Canada *by* University of Toronto Press